The Biophysical and Structural Mechanisms Underlying Mechanosensitivity of the TREK-2 Potassium Channel



Viwan Jarerattanachat

Department of Physics
University of Oxford

A thesis submitted in partial fulfilment of the requirements for the degree of Doctor of Philosophy at the University of Oxford

Wolfson College Michaelmas 2018

Abstract

The mechanosensitive K_{2P} K^+ channels play important roles in a wide range of physiological processes, including touch, balance, pain, and hearing. The ability of these channels to sense changes in pressure within the cell membrane is essential to these processes. However, the structural and biophysical mechanisms underlying this remain unclear. In this thesis, multiscale molecular dynamics simulation techniques were used to investigate the biophysical and structural mechanisms underlying mechanosensitivity of K_{2P} channels. First, how TREK-2 responded to membrane stretch was investigated by simulating TREK-2 embedded in a POPC bilayer subjected to negative pressure (i.e. positive tension). The results show that TREK-2 is intrinsically sensitive to changes in bilayer tension and that the channel switches conformation from the 'Down' state to the 'Up' state in response to membrane stretch. However, although the pressure profile changes symmetrically in both outer and inner leaflets, the structural response of TREK-2 is highly asymmetric. The changes mainly occurred in the lower half of protein. TREK-2 was therefore next examined under asymmetric tension (i.e. tension only applied in one of two leaflets). Interestingly, TREK-2 only responded to positive tension in the inner leaflet indicating it has the ability to distinguish a variety of force directions within the membrane. Since, the mechanisms underlying mechanosensitivity and intracellular pH sensitivity are thought to be similar, I also examined the role of a critical mutation in the proximal C-terminus of TREK-1 (E306A). This revealed that E306A mimics the protonated state and changes the preferred environment of this residue from water to lipid and consequently assists movement up towards the bilayer. In addition, a new force analysis tool was developed to provide more insight into why some K_{2P} channels are mechanosensitive and some are not. Overall, this thesis improves our understanding of the molecular mechanisms underlying the mechanosensitivity of K_{2P} channels and ion channels in general.

Acknowledgement

First of all, I would like to thank my supervisors, Stephen Tucker and Mark Sansom, for their advice, support, and keeping me towards the right direction. Thanks for their patience in explaining and giving me guidance. They both were helpful throughout my DPhil.

Many thanks to Prafulla Aryal for his supervision of someone who is from a physics background and had almost zero knowledge of protein structural biology/biochemistry. He patiently answered my questions even they were often very basic queries about structural biology and electrophysiology. I learnt from him a lot.

Thanks to SBCB members (including former members) for a very good working environment. Special thanks to Jemma for a first day introduction; Tom, Jean, Jan, and Tyler for coding things; Fiona for delicious cakes (which became essential after 6 pm); Anna and Vishal for your sincere help in many aspects.

To family and friends, especially Tong, a lot of thanks for your emotional support and staying by my side during my DPhil.

Last but not least, thanks to DPST for funding and providing career support.

Publications

The following publications resulted from this thesis.

Chapter 3: TREK-2 in a bilayer

1. Aryal P, Jarerattanachat **V**, Clausen MV, Schewe M, McClenaghan C, Argent L, Conrad LJ, Dong YY, Pike ACW, Carpenter EP, Baukrowitz T, Sansom MSP and Tucker SJ (2017) Bilayer-Mediated Structural Transitions Control Mechanosensitivity of the TREK-2 K2P channel. **Structure**. 25:708-718.

2. Nematian-Ardestani E, **Jarerattanachat V**, Aryal P, Sansom MSP & Tucker SJ (2017) The Effects of Stretch Activation on Ionic Selectivity of the TREK-2 K2P K+ Channel. **Channels** 11:482-486.

Chapter 4: Asymmetric response of TREK-2

3. Clausen MV, **Jarerattanachat V**, Carpenter EP, Sansom MSP, and Tucker SJ. (2017) Asymmetric Mechanosensitivity in a Eukaryotic Ion Channel. **Proceedings of the National Academy of Sciences** 114: E8343-E8351.

Table of Contents

Publications ..... **iv**

Table of Contents ..... **v**

List of Figures ..... **x**

List of Tables ..... **xiii**

Chapter 1 Introduction **1**

1.1 Overview **1**

1.2 The Cell membrane **2**

1.2.1 Lipids and self-organisation 2

1.2.2 Phospholipids and Membrane diversity 3

1.2.3 The physical properties of the phospholipid bilayer 5

1.3 Ion channels **6**

1.3.1 Membrane potential, action potential and leak current 7

1.3.2 Ion channel classification 10

1.3.3 K_{2P} family 12

1.3.4 TREK subfamily 14

1.3.5 TREK structure and gating mechanism 15

1.4 Mechanosensitive ion channels **17**

1.4.1 MS channels in different organisms 17

1.4.2 Basic models for the mechanisms of mechanosensitivity 18

1.5 Previous studies of MS channels **20**

1.5.1 Theoretical and thermodynamic overview 21

1.5.2 Studies of Prokaryotic MS channels 23

1.5.3 Eukaryotic MS channels 25

1.6 Overall Perspective and Aims **26**

1.7 Thesis outline and structure **28**

Chapter 2 Theory and Methodology **29**

2.1 Introduction **29**

2.1 Molecular Dynamics Simulation **30**

2.1.1 Theory and algorithm 31

2.1.2 MD simulation scale 38
2.1.3 Multiscale simulation approach 39
2.2 Forcefield and Software engines 39
2.2.1 All-atom and united-atom forcefields 40
2.2.2 Coarse-grained forcefields 41
2.2.3 Water models 42
2.2.4 Software 43
2.3 Limitations 44
2.4 Analytic tools 44
2.5 Simulation methods 47
Chapter 3 MD simulations of TREK-2 in a bilayer 50
3.1 Introduction 50
3.1.1 TREK-2 crystal structures 51
3.1.2 TREK stretch-activation models 52
3.1.3 The truncated TREK-2 crystal construct is mechanosensitive 54
3.1.4 Aims 54
3.2 Computational methods 55
3.2.1 Modelling and MD simulation 55
3.2.2 The development of stretch protocol 56
3.2.3 The influence of hydrophobic mismatch 57
3.3 CG-simulation of TREK-2 in a lipid bilayer 58
3.3.1 Development of stretch protocol 58
3.3.2 Lipids in the fenestration of TREK-2 60
3.3.3 Lipid penetrations during stretch simulation 61
3.3.4 Hydrophobic mismatch effects on TREK-2 62
3.3.5 Changes in the lateral pressure profile of the lipid bilayer 65
3.4 Behaviour of TREK-2 in a stretched bilayer 66
3.4.1 TREK-2 move from the ‘Down’ state to the ‘Up’ state in response to stretch 67
3.4.2 The down to up structural transition 69
3.4.3 Rearrangement of TM2, TM3, and TM4 underlie the stretch-induced structural movements 71
3.4.4 Effects of stretch on selectivity filter and the inner pore cavity 73
3.5 Effect of hydrophobic mismatch on TREK-2 75

3.5.1 A thin bilayer does not drive the down to up transition *per se* 75
3.5.2 Hydrophobic mismatch and structural rearrangements 76
3.6 Discussion 77
3.6.1 Limitations and accuracy of the CG simulations 77
3.6.2 Lipids in the fenestration 78
3.6.3 Stretch and thin bilayer simulations 79
3.6.4 Stretch activation model and selectivity filter 79
3.7 Summary 80
Chapter 4 The response of TREK-2 to asymmetric increases in bilayer tension . 81
4.1 Introduction 81
4.1.1 Asymmetric activation in MS channels 82
4.1.2 Shape sensitivity of TREK-2 83
4.1.3 Planar bilayer experiments 84
4.1.4 Aims 85
4.2 Computational methods 87
4.2.1 Monolayer tension induced protocol 87
4.3 Asymmetric bilayer tension 89
4.3.1 Development of asymmetric protocol 89
4.3.2 Asymmetric tension pressure profiles 91
4.4 Asymmetric structural response of TREK-2 93
4.3.1 TREK-2 structural changes in response to asymmetric membrane tension 93
4.3.2 Monolayer tension or bilayer torque? 94
4.3.3 Structural rearrangement induced by the asymmetric bilayer torsion protocol 97
4.3.4 Structural integrity of the selectivity filter 99
4.5 Discussion 100
4.5.1 Bilayer mismatch under NPAT and NPT 100
4.5.2 Monolayer/Bilayer tension induced by asymmetric protocols 100
4.5.3 Bilayer curvature induced by asymmetric tension. 101
4.6 Summary 102
Chapter 5 Investigation of the effect of the E306A mutation on TREK-1 pH sensitivity 103
5.1 Introduction 103
5.1.1 Internal pH sensitivity and mechanosensitivity of TREK-1 104

5.1.2 Internal pH sensitivity in the TREK subfamily 104
5.1.3 TREK-1 crystal structures 104
5.1.3 Aims 105
5.2 Computational methods 106
5.2.1 Modelling 106
5.2.2 MD simulation 108
5.3 Stability of the TREK-1 structure in a lipid bilayer 109
5.3.1 Secondary structure of proximal C-terminus 111
5.3.2 Re-modelling of the TREK-1 proximal C-terminal structure 112
5.4 Influence of E306A mutation 115
5.4.1 Role of E306A in pH TREK-1 sensitivity 115
5.4.2 E305A does not change the local interaction. 115
5.4.3 E306A mutation and stretch activation 117
5.5 Discussion 119
5.6 Summary 120
Chapter 6 Non-Bonded Force Distribution Analysis 121
6.1 Introduction 121
6.1.1 Perspectives and hypothesis 122
6.1.2 Available analysis tools 123
6.1.3 Theory 125
6.1.4 Aims and direction 126
6.2 Development and implementation of NB-FDA 127
6.2.1 Setting up 129
6.2.2 Pre-calculation 130
6.2.3 Calculation and statistical analysis 131
6.2.4 Output 132
6.3 Protein-lipid interaction 133
6.3.1 NB-FDA and traditional lipid contact analysis 133
6.3.2 General protein-lipid interactions in TREK-2 and TWIK 136
6.3.3 State dependent protein-lipid interaction 139
6.3.4 Force sensing residues 139
6.4 Internal protein interactions 141
6.4.1 TREK-2 and TWIK-1 internal networks 142
6.4.2 The unique network in the non-mechanosensitive TWIK-1 channel 143

6.4.3 Unique network of the TREK-2 ‘down-like’ state and the ‘up-like’ state 145
6.4.4 Correlation of motion and allosteric pathway 148
6.6 Discussion 149
6.6.1 Advantage and disadvantage of NB-FDA 149
6.6.2 Cut-off sensitivity of contact analysis 150
6.6.3 Statistical approaches 150
6.6.5 Future work..... 151
6.7 Summary 152
Chapter 7 Summary 153
7.1 Stretch activation model 153
7.2 Asymmetric response in membrane tension 154
7.3 Intracellular pH sensitivity of TREK-1 154
7.4 Internal protein interactions..... 155
7.4 Further work..... 156
7.5 Conclusion 158
List of abbreviations..... 159
Bibliography..... 160

List of Figures

Figure 1.1 Structure of cell membrane and lipids.. 4

Figure 1.2 Cell electricity. 9

Figure 1.3 Voltage-gated ion channel (VIC) superfamily 11

Figure 1.4 K_{2P} family. (A) The topology of K_{2P} channels....13

Figure 1.5 Regulation of TREK channels....14

Figure 1.6 Structure of TREK channels and gating mechanism....16

Figure 1.7 MS mechanism models....19

Figure 1.8 Simple patch-clamp scheme.. 20

Figure 1.9 Thermodynamics of ion channels and force from lipid principle....23

Figure 1.10 Structures of MS channels....25

Figure 2.1 Multi-scale computational simulations....30

Figure 2.2 Bonded interactions....32

Figure 2.3 Periodic boundary condition 37

Figure 2.4 Diagram describing MD simulation. 38

Figure 2.5 MD simulation scale 39

Figure 2.6 TIP3P water model. Bonds, and angle are parameterised and defined 43

Figure 3.1 TREK-2 crystal structures. 51

Figure 3.2 Stretch-activation models.. 53

Figure 3.3 The CG-system in various applied tension....59

Figure 3.4 An alignment of CG-TREK-2 and CG-TWIK when subjected to tension. 60

Figure 3.5 Lipids in the CG-TREK-2 fenestration 61

Figure 3.6 Lipid penetration during the stretch simulation. 62

Figure 3.7 Bilayer distortion caused by hydrophobic mismatch....64

Figure 3.8 Structural changes caused by hydrophobic mismatch 65

Figure 3.9 Lateral pressure profiles of lipid bilayers 66

Figure 3.10 TREK-2 move from the 'Down' state to the 'Up' state 68

Figure 3.11 Lack of structural changes in the non-mechanosensitive TWIK-1 69

Figure 3.12 Changes in TERK-2 structure during the stretch simulation. 70

Figure 3.13 The TREK-2 structural alignment and cross-sectional area.....71

Figure 3.14 Movement of the lower section of the TMs 72

Figure 3.15 Sequential movement of the TMs.....72

Figure 3.16 Ions-water occupancy in the selectivity filter.....74

Figure 3.18 The selectivity filter is relatively stable during the stretch 75

Figure 3.19 TREK-2 in thin bilayer during the simulation 76

Figure 3.20 The structural rearrangements of TREK-2 in thin bilayers 77

Figure 4.1 Asymmetric structural changes in response to membrane stretch 82

Figure 4.2 Bilayer torque and protein shape sensitivity 83

Figure 4.3 Asymmetric functional response of TREK-2 to positive and negative pressure. 86

Figure 4.4 Monolayer tension induced protocol. 87

Figure 4.5 Asymmetric protocol in CG-simulation. 90

Figure 4.6 Pressure profiles of asymmetric bilayers 92

Figure 4.7 Snapshots of TREK-2/bilayer systems using the asymmetric protocol.....93

Figure 4.8 Structure changes induced by asymmetric tension 94

Figure 4.9 Clockwise bilayer torque vs. positive monolayer tension 96

Figure 4.10 Order parameter of POPC sn-1 acyl chains 96

Figure 4.11 Structural rearrangements induced by asymmetric bilayer tension 98

Figure 4.12 Selectivity filter structure under the asymmetric protocol.....99

Figure 4.13 Monolayer tension and bilayer torque scheme. 102

Figure 5.1 The TREK-1 crystal structures and simulation model 107

Figure 5.2 The Cα-RMSD comparison with the initial crystal structure (5VK5) 110

Figure 5.3 Snapshots of TREK-1 110

Figure 5.4 The secondary structure of C-terminus 111

Figure 5.5 Re-modelling of the TREK-1 proximal C-terminal structure.....113

Figure 5.6 The stability of the re-modelled TREK-1 113

Figure 5.7 Snapshot of re-modelled TREK-1 at 200ns. 114

Figure 5.8 The local interactions about residue 305 and 306. 116

Figure 5.9 Structure overlay at 200 ns of the simulations 117

Figure 5.10 Effect of E306A mutation on lipid bilayer. 118

Figure 6.1 The difference between TREK and TWIK channel 123

Figure 6.2 Bonded and Non-Bonded forces in MD simulations 125

Figure 6.3 Global NB-FDA algorithm. 128

Figure 6.4 diagram describe read/call of non-bonded parameters. 129

Figure 6.5 NB-FDA internal data structure. 130

Figure 6.6 Diagram of the pre-calculation and forces calculations. 131

Figure 6.7 diagram of periodic boundary condition. 132

Figure 6.8 Lipid contact analysis. 134

Figure 6.9 Lipid contact analysis and NB-FDA 135

Figure 6.10 General Protein-lipid interaction of TREK-2 137

Figure 6.11 General Protein-lipid interaction of TWIK-1. 138

Figure 6.12 Protein-Lipid state dependent interaction. 140

Figure 6.13 TREK-2 Internal protein network 141

Figure 6.14 TREK-2 and TWIK-1 internal network. 143

Figure 6.15 TM4 network of TREK-2 and TWIK-1. 144

Figure 6.16 Venn diagram represents TREK-2 network 146

Figure 6.17 The network that changes during stretch protocol. 147

Figure 6.18 Network changing during stretch simulation 149

Figure 6.19 Force distribution in lipid bilayer. 151

List of Tables

Table 1.1 Physical properties of Phospholipid bilayers. 6

Table 2.1 CG-simulation parameters.....48

Table 2.2 All-atom simulation parameters.....49

Table 3.1 CG- Bilayer thickness.....64

Table 4.1 Simulation system details. 89

Table 5.1 Secondary structure of TREK-1.....112

Table 5.2 Secondary structure of re-modelled TREK-1. 114

Table 6.1 Technical details.....128

Chapter 1
Introduction

1.1 Overview

The ability of a cell to sense a change in pressure is essential for its survival. It has an important role in a wide range of other processes. In bacteria it is essential for the control of osmotic balance and to prevent cell lysis caused by osmotic shock[1]. In plants, it is involved in their ability to sense touch, gravity, as well as osmotic homeostasis [2]. In mammalian cells it plays an important role in many different sensory processes, e.g. touch, balance, hearing, blood pressure regulation, and pain signalling[3–5] with defects in this ability often proving fatal.

It is well-known that senses that detect physical stimuli often require the conversion of these signals into electrical signals by ion channel proteins embedded in cell membrane. The channels that respond to changes in pressure are called mechanosensitive (MS) channels but understanding how these proteins function at the molecular level is challenging[6]. This thesis uses a computational approach to this problem by using molecular dynamics simulations to study the mammalian MS channels TREK-1 and TREK-2. In particular, it examines their mechanism of action from a structural perspective with reference to new structures of these channels and detailed electrophysiological studies which have examined their functional properties.

1.2 The Cell membrane

Ion channels are embedded within the lipid bilayer that forms the cell membrane. In order to understand the structural basis of their behaviour it is essential to understand the biological and physical properties of the bilayer. The cell membrane is an indispensable cellular component. In addition to physically separating the cell from its external environment, it also controls the movement of substances, including charged ions, into and out of the cell. Its composition was first described by the 'fluid mosaic model'[7,8] consisting of two lipid layers (the bilayer) made up of different lipids with embedded molecules such as cholesterol and proteins (**Figure 1.1A**).

1.2.1 Lipids and self-organisation

Lipids are biological molecules that are soluble in nonpolar solvents. Normally, they are small hydrophobic or amphipathic molecules. There are 8 types of lipids defined by their structural characteristics: fatty acyls, glycerolipids, glycerophospholipids, sphingolipids, saccharolipids and polyketides, sterol lipids, and prenol lipids [9], however, only glycerophospholipids are described in this thesis. Glycerophospholipids or phospholipids are a key component of the lipid bilayer. They have a phosphate group and glycerol as their core (**Figure 1.1B**), and consist of 2 main parts: a polar head group and a non-polar hydrocarbon tail, thus forming an amphiphilic structure. This particular structure makes lipids experience complex hydrophobic and hydrophilic forces within the membrane and underlies various forms of self-organisation e.g. liposome, micelle, and bilayer sheet (**Figure 1.1D**). These forms depend on the geometry of lipid molecule[10,11]. Cylindrical shape lipids tend to form a bilayer, whereas conical shape lipids are likely to form a micelle. Almost 250 years of detailed studies, from Benjamin Franklin's 'oil on water' experiment in 1774 to more recent biophysical studies[12,13] now provide us with a solid knowledge of lipids and the bilayer they form. The structural and biophysical properties of lipids are well described in various reviews [9,14,15]. However,

many aspects of their functional properties remain unclear, in particular their role in many physiological processes and how their behaviour influences ion channel function.

1.2.2 Phospholipids and Membrane diversity

Phospholipids are grouped based on the chemical structure of their polar head group (**Figure 1.1B & C**). Common phospholipids include Phosphatidylcholine (PC), Phosphatidylethanolamine (PE), Phosphatidylserine (PS), Phosphatidylinositol (PI), Phosphatidic acid (PA), and Phosphatidylinositol phosphate (PIP). These lipids exist in varying amounts in biological membranes[15] and also have different lengths of acyl chain[16]. In addition, the cell membrane is asymmetric because the composition of the inner and outer leaflets is sometimes different. In most cell membranes, amount of Phosphatidylcholine is >50% [15]. This lipid self-assembles as a planar bilayer because of its cylindrical shape. Other lipids (e.g. PE, PS, PA and lysolipid) that have either an inverse-conical or a conical geometry are also important as they can modify bilayer properties by inducing curvature in the bilayer. This of particular importance as it alters the mechanical properties of the bilayer and will influence the activity of mechanosensitive ion channels (see Chapter 4 for more details).

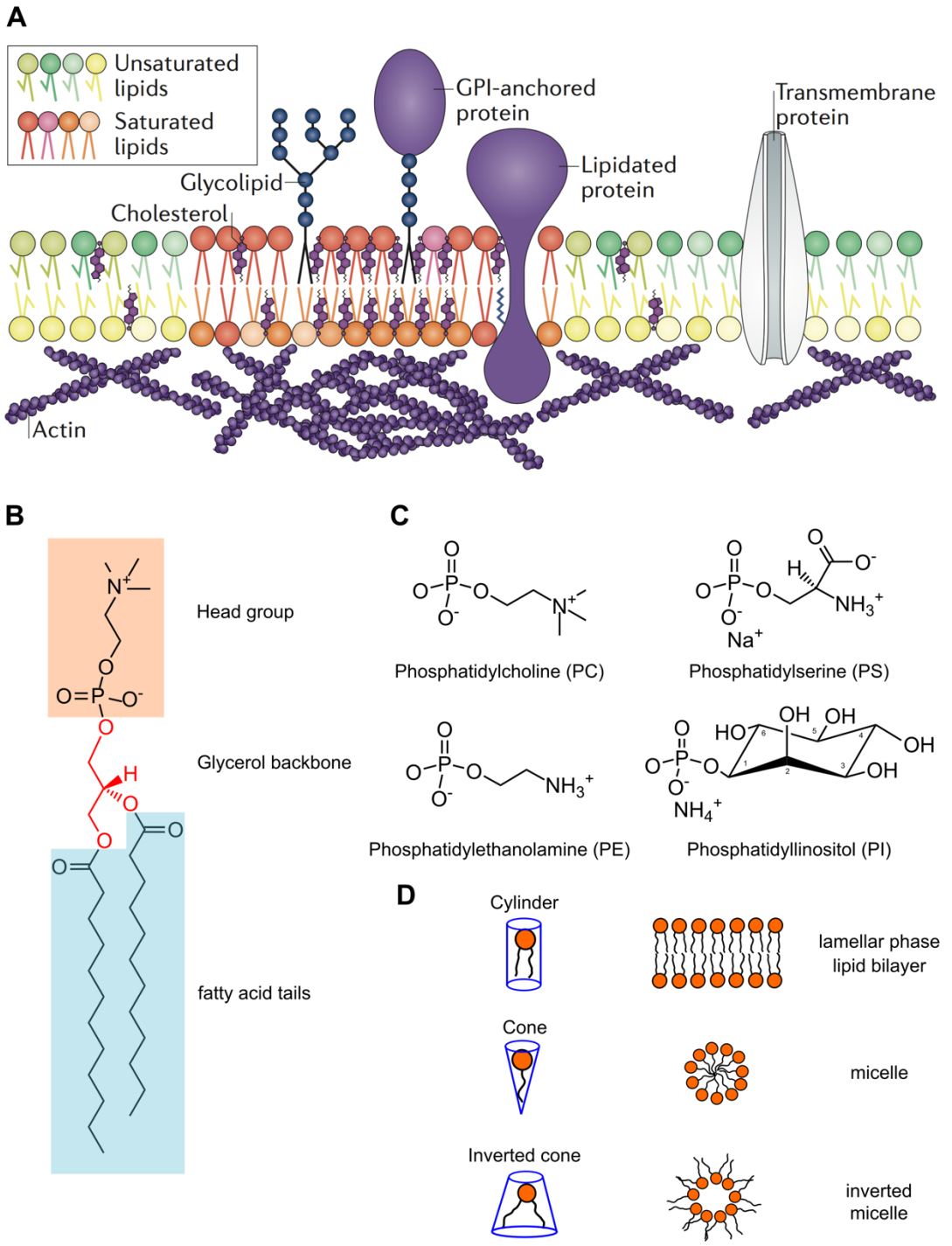


Figure 1.1 Structure of cell membrane and lipids. *(A) structure of cell membrane. (B) lipids (C) phospholipid head groups (D) lipid self-organisation. The figure 1A is taken from*[17] *with Springer Nature permission.*

1.2.3 The physical properties of the phospholipid bilayer

The typical physical attributes of a bilayer that define their functional properties are their lateral area per lipid (APL), bilayer thickness, lipid diffusion coefficient, viscosity, as well as phase behaviour and overall mechanical properties (e.g. area elastic modulas, Young's modulus). The properties of the lipid bilayer therefore depend on its lipid composition and the chemical structure of these lipids. For example, long acyl-chains result in a thicker bilayer, and because the saturated lipid tail order parameter is higher than for unsaturated lipids this will affect the phase transition temperature and overall fluidity of the membrane. This makes each type of bilayer have its own unique properties, but experimentally measurement of these properties is very difficult. Various techniques, approaches, and tools have therefore been developed to address this, but one of the most tractable are computational studies that attempt to mimic the chemical structure of the membrane and its dynamic behaviour. This is a particularly powerful approach as it allows these properties to be compared with experimental results. More details of these approaches are described in Chapter 2. A comparison of the physical properties of DLPC, DMPC, DPPC, DSPC, and POPC bilayers are shown in **Table 1.1**. The influence of these properties on proteins embedded within the bilayer, in particular mechanosensitive ion channels, will be discussed later in section 1.5.

Table 1.1 *Physical properties of Phospholipid bilayers, area per lipid (APL), bilayer thickness (B_L) and area elastic modulas (K_a).*

	293K		**303K**		**323K**		**333K**		**298 K**
	APL (Å²)	B_L (Å)	APL (Å²)	B_L (Å)	APL (Å²)	B_L (Å)	APL (Å²)	B_L (Å)	K_a (N/m)
DLPC	59.6	33.0	60.8	32.6	64.8	31.0	65.9	30.7	-
DMP	Gel		59.9	36.7	63.3	35.2	65.7	34.2	0.21
DPPC	Gel		Gel		6.1	39.0	65.0	38.1	0.21
DSPC	Gel		Gel		Gel		63.8	42.2	0.21
POPC	62.7	39.8	64.3	39.1	67.3	37.9	68.1	37.7	-

The data is taken from[18,19]*. The standard deviations in area per lipid and bilayer thickness are less the 1.4 and 0.8, respectively. In addition, area elastic modulas of DOPC (18:1 Δ9) is 0.30 N/m* [19].

1.3 Ion channels

Ion channels are pore-forming proteins embedded in lipid bilayer where they control the movement and relative permeability of ions across the cell membrane. The study of ion channels has undergone a very long journey, see [20,21] for more details. As early as the mid 17th century when the term *ion channel*, let alone *membrane* or *cell* did not exist, Jan Swammerdam studied signal propagation between nerve and muscle by performing experiment on dissected frog legs [22]. This gave rise to the idea of an *animal electricity* and the true electrical nature of the nerve was established with the experiments of Luigi Galvani in 1790s [23]. He demonstrated that nerve tissues respond to external stimuli by generating electric signals, later called 'action potentials'. These signals result from the accumulation of charges on the external or internal surface of muscle or nerve cells. Simultaneously with the development of better instruments for the measurement of electrical signals, the understanding of cell electricity was improved. After the initial discovery that an electro-chemical gradient could be generated by differences in ion concentrations across a semi-permeable barrier was proposed by Nernst in 1889 [24], Alan Hodgkin and Andrew Huxley published their now famous model of how the action

potential works in neurons[25]. Their model proposed that membrane electricity is controlled by passive ion fluxes caused by electro-chemical gradients, thus indicating that ion-selective pathways must exist across the membrane. The existence of ion channels was confirmed in the 1970s with the development of methods for the recording of currents through single channel[26]. These studies found that the ions move through protein pores rather than lipids[27,28] and were also able to exhibit selectivity between potassium and sodium ions[29].

1.3.1 Membrane potential, action potential and leak current

At rest, a living cell membrane potential is maintained at approximately -70 mV (interior is negatively charged compared to outside). This potential is generally described by Nernst equation[24], equation 1.1, and fulfilled by Goldman–Hodgkin–Katz voltage equation[30] (i.e. Goldman equation), equation 1.2. The equations basically explain that the potential caused by the difference of ion concentrations between intracellular and extracellular side of the membrane. This condition is maintained by Sodium-Potassium (Na^+/K^+) pump, and ion channels (**Figure 1.2A**). Na^+/K^+ pumps require energy (i.e. ATP) to be functional, whereas ion channels do not.

$$V_e = \frac{RT}{zF} \ln \frac{[ion]_{out}}{[ion]_{in}} \tag{1.1}$$

, where V_e is a potential for the given ion, $[ion]_{out}$ and $[ion]_{in}$ are the extracellular and intracellular ion concentration, R is gas constant, T is temperature, F is Faraday constant, and z is the valence of the ion.

$$V_m = \frac{RT}{F} \ln \frac{P_K[K^+]_{out} + P_{Na}[Na^+]_{out} + P_{Cl}[Cl^-]_{in}}{P_K[K^+]_{in} + P_{Na}[Na^+]_{in} + P_{Cl}[Cl^-]_{out}} \tag{1.2}$$

, where V_m is membrane potential, P is permeability with subscribe letter note for a corresponding ion, [ ] refers the ion concentration with subscribe letter note for

extracellular or intracellular site, R is gas constant, T is temperature, and F is Faraday constant.

In response to stimuli, an action potential is generated (**Figure 1.2B**). This is started by gating of sodium channels that allow Na^+ ions move into the cell; therefore the membrane becomes depolarised (i.e. increase in positive charges inside the cell). This depolarisation continuously occurs until the sodium channels inactivate, then the voltage-sensitive potassium channels become activated to allow K^+ ions to leak out from the cell, and repolarise the membrane back towards the resting membrane potential. This dynamic is described by the Hodgkin and Huxley[25] model (**Figure 1.2C**). The system of membrane and ion channels is considered as circuit that membrane and ion channels are represented by capacitor and resistors, respectively. The total current (i.e. the membrane current (I_m)) is the summation of capacitive current (I_C), sodium current (I_{Na}), potassium current (I_K), and leak current (I_L), equation 1.3. Their currents are described by Ohm's law and can be written as equation 1.4.

$$I_m = I_C + I_{Na} + I_K + I_L \tag{1.3}$$

$$I_m = C_m \frac{dV}{dt} + g_{Na}(V_m - E_{Na}) + g_K(V_m - E_k) + g_L(V_m - E_L) \tag{1.4}$$

, where V_m is membrane potential, C_m is membrane capacitance. g and E are conductance and Nernst potential of a corresponding ion/ ion channel. The last term this equation indicates the exitance of leak current which is primarily responsible for setting membrane potential when the system is in the resting state ($\frac{dV}{dt} = 0,\ E_{Na} \sim V_m,\ E_K \sim V_m$), I_C, I_{Na} and I_K are absent.

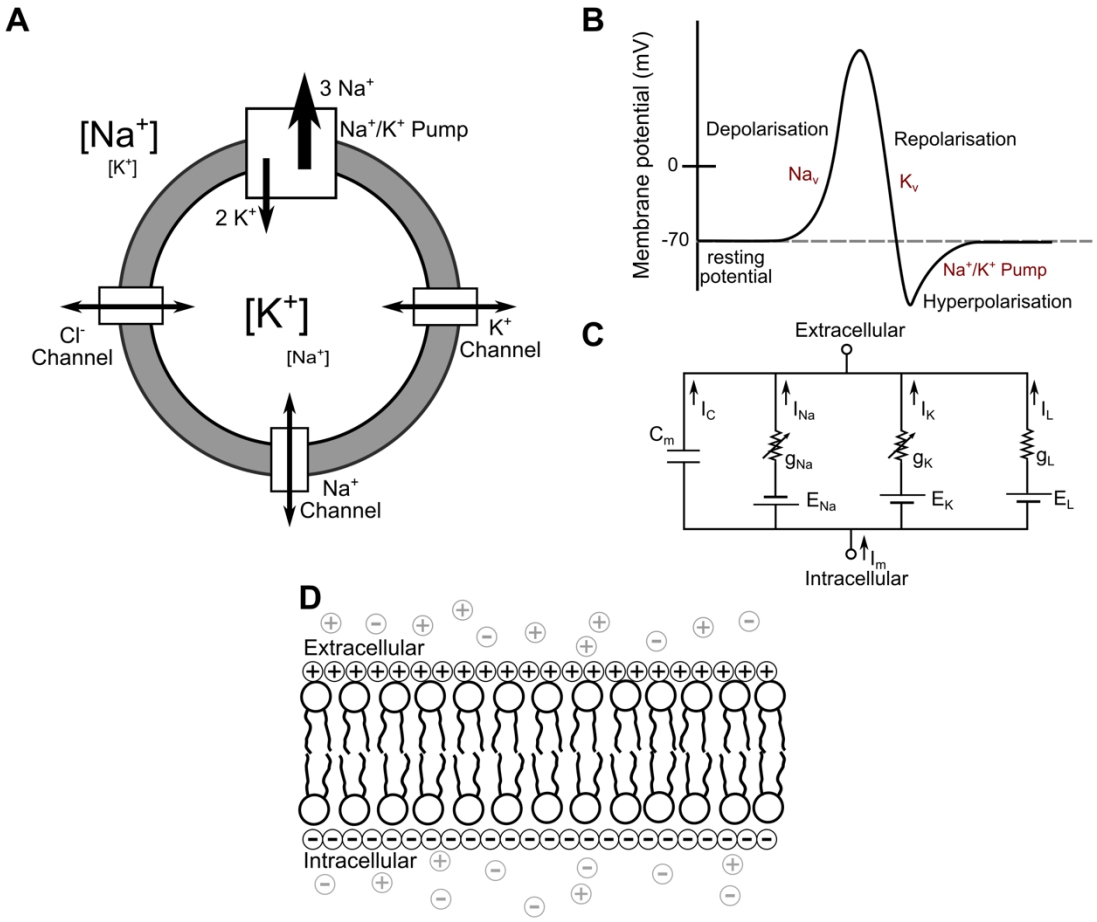


Figure 1.2 Cell electricity. *(A) Simplified model of cell. (B) Action membrane potential. (C) Hodgkin and Huxley circuit model. Cell membrane and ion channels were represented by capacitor and resistors respectively. (D) The figure illustrates how charges distribution about cell membrane and makes it act as a capacitor.*

1.3.2 Ion channel classification

The diversity of ion channels found in cells is very high. There are many different types of channel that can be classified according to their selectivity, structure, sequence, functions and their mechanisms of regulation or 'gating'[31]. Fortunately, there are many available databases that provide sequence annotations and group them into superfamilies, families and subfamilies (e.g. SUPERFAMILY[32] and pfam[33]). Furthermore, there are structural classification databases (e.g. SCOP [34]) and systematic name databases (HUGO)[35]. This thesis mainly addresses K^+ selective channels, in particular the K_{2P} subfamily of K^+ channels, and focuses on the members of this subfamily that are mechanosensitive, i.e. that are regulated by changes in membrane tension. More detailed descriptions of other types of ion channels can be found either in text books [31,36] or in reviews [37] and so are not discussed in detail here.

The K_{2P} family belongs to the superfamily of voltage-gated ion channels which has >140 members [38] and consists of the Na_v, Ca_v, K_v, K_{Ca}, CNG, HCN, TRP, TPC, K_{ir}, and K_{2P} families (**Figure 1.3**). The common ancestor of this superfamily is probably a channel very similar to the prokaryotic potassium channel, KcsA. This simple K^+ channel is typically used as a traditional model because its overall transmembrane topology and selectivity filter sequence (TVGYG) are highly conserved amongst both prokaryotic and eukaryotic K^+ channels. Moreover, it was the first K^+ channel that its structure was solved using x-ray crystallography[39]. Detailed studies of KcsA have therefore provided much of our current understanding of K^+ selectivity [40], ion permeation [41] and gating mechanism [42,43]. Furthermore, it was used as the base model for many early homology models of many related K^+ channels [44,45] including even the TREK-1 and TREK-2 members of K_{2P} family that form the focus of this thesis [46].

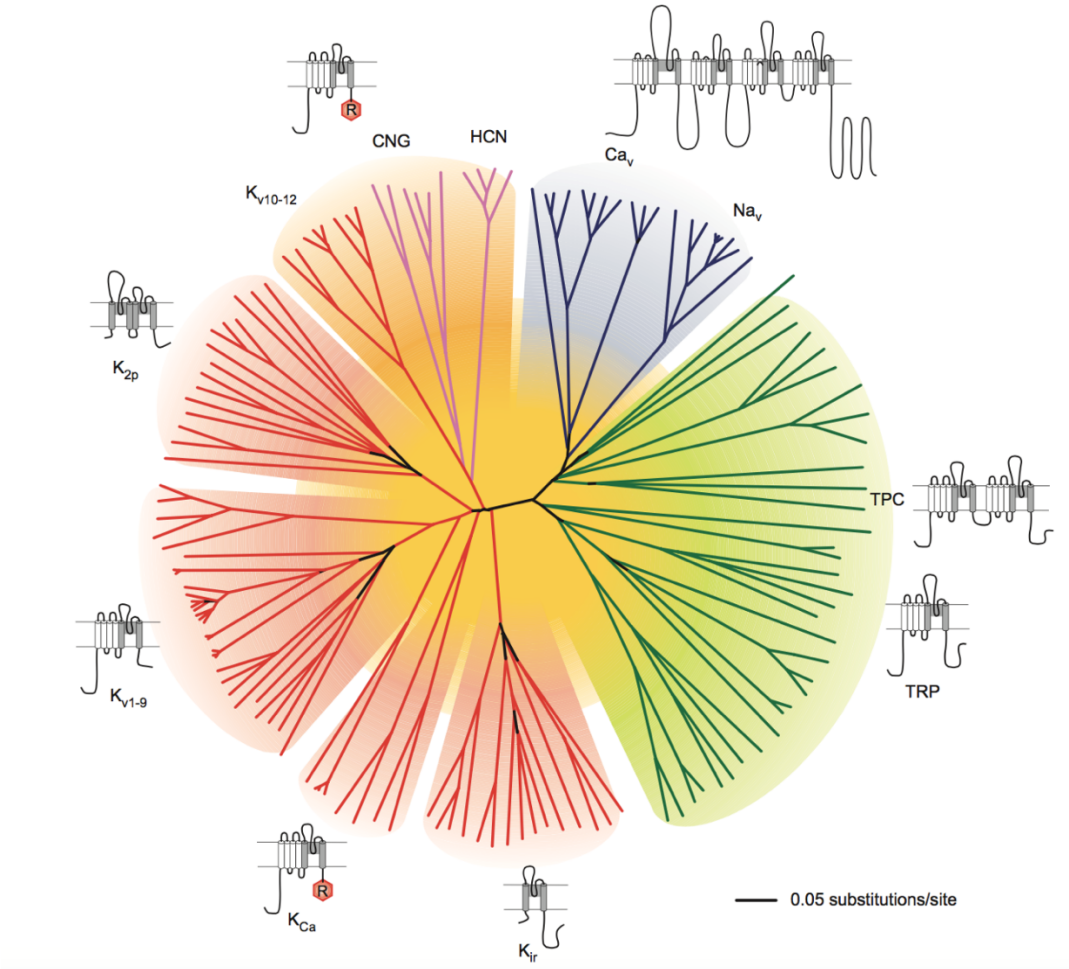


Figure 1.3 Voltage-gated ion channel (VIC) superfamily. *Profiles are based on hidden Markov models (HMMs). The figure is reused from* [38]. *Reprinted with permission from AAAS.*

1.3.3 K_{2P} family

In contrast to a KcsA, the K_{2P} family is a group of mammalian K^+ channels that assemble as dimers rather than tetramers. Each subunit has 4 transmembrane helices and two pore domains (2P/4TM) i.e. two pore-forming domains per monomer[47,48]. Otherwise, their overall architecture is similar to other members of the K^+ channel superfamily (**Figure 1.4A**). K_{2P} channels play a role in the K^+-selective leak background current and are sensitive to diverse forms of physical and chemical stimuli. The first member of this family, TWIK1, was cloned in 1996 [49] with a further 14 cloned quickly afterwards [50–59]. These 15 members of this family, encoded by the *KCNK* genes, are divided into 6 subfamilies based on sequence similarity and shared functional properties [47] (**Figure 1.4B**) :

i) Tandem of P domain in a Weak Inward rectifying K^+ channel (TWIK): TWIK-1 ($K_{2P}1.1$), TWIK-2 ($K_{2P}6.1$), and $K_{2P}7.1$

ii) TWIK-related K^+ channel (TREK): TREK-1 ($K_{2P}2.1$), TREK-2 ($K_{2P}10.1$), and TWIK-related arachidonic acid activated K^+ channel (TRAAK, $K_{2P}4.1$)

iii) TWIK-related alkali-activated sensitive K^+ (TALK): TALK-1 ($K_{2P}16.1$), and TALK-2 ($K_{2P}17.1$)

iv) TWIK-related acid-sensitive K^+ (TASK): TASK-1 ($K_{2P}3.1$), TASK-2 ($K_{2P}5.1$), TASK-3 ($K_{2P}9.1$), and TASK-5 ($K_{2P}15.1$)

v) TWIK-related halothane-inhibited K^+ (THIK): THIK-1 ($K_{2P}13.1$), and THIK ($K_{2P}12.1$)

vi) TWIK-related spinal cord K^+ (TRESK): TRESK ($K_{2P}18.1$).

Since only members of the TREK subfamily are mechanosensitive, only these channels are described in this thesis. Details of the others can be found in a number of comprehensive reviews [3,47,48].

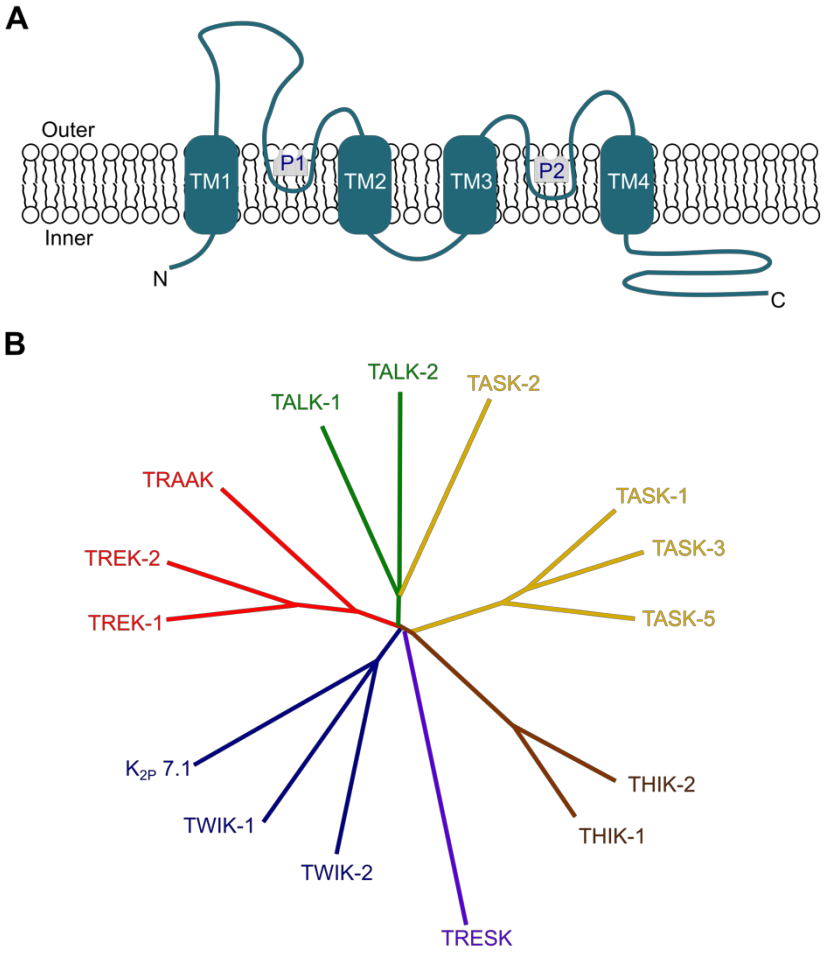


Figure 1.4 K_{2P} family. *(A) The topology of K_{2P} channels. There are 2 subunits which contains 4 transmembrane helixes and two pore domains (2P/4TM). (B) K_{2P} subfamilies and their members. The mechanosensitive K_{2P}(s) are shown in red (TREK/TRAAK)*

1.3.4 TREK subfamily

TREK channels have complex regulatory properties; they are activated by many chemical and physical stimuli e.g. lipids, membrane tension, temperature, voltage, and pH [47,60]. The first member of this subfamily to be identified was TREK-1 [61] followed by TRAAK [55] and was completed with the cloning of TREK-2 [56,62]. TREK-1 is highly expressed in central nervous system (CNS) [63] whereas TREK-2 expression is relatively low in these tissues, nonetheless it is highly expressed in pancreas and kidney [56,62]. However, under physiological conditions, TREK channels are thought to provide the greatest contribution to the resting K^+ current in Dorsal Root Ganglion (DRG) neurons in the spinal cord (TREK-2, 69%; TRESK-like, 16%; TREK-1-like, 12%; TRAAK-like, 3%)[64]. TRAAK is also expressed in Trigeminal Ganglia (TG) neurons that innervate the face and mouth. TREK channels exhibit polymodel regulation. They are activated by many stimuli such as pressure, heat, voltage, acidification, polyunsaturated fatty acids (PUFAs) **Figure 1.5**. More intensive details about their expression, regulation and physiological properties can be found in a number of reviews [3,60,65–67].

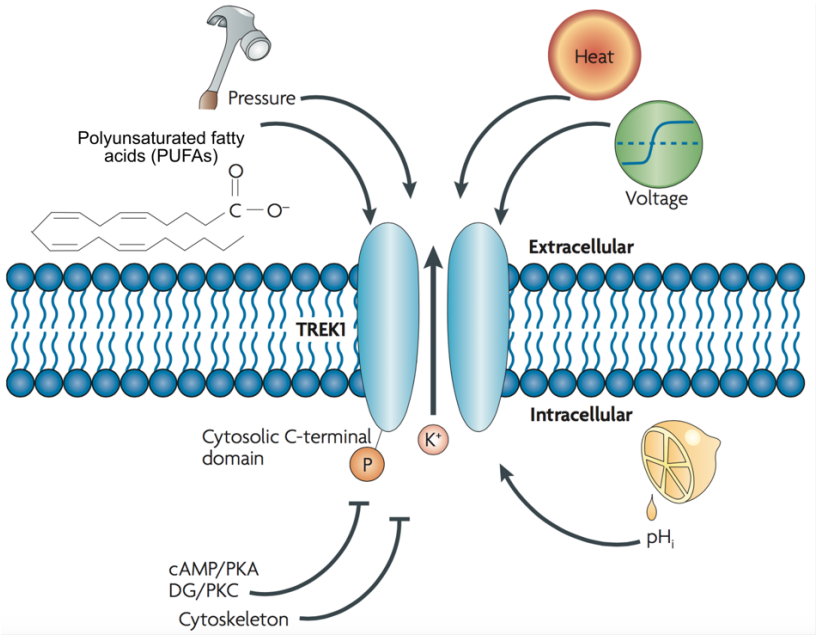


Figure 1.5 Regulation of TREK channels. *TREK channels exhibit polymodel regulation. They are activated by many stimuli such as pressure, heat, voltage, acidification, polyunsaturated fatty acids (PUFAs). (Figure is adapted from review by Honoré [60] with a Springer Nature permission.)*

1.3.5 TREK structure and gating mechanism

The first 3D structure of a TREK subfamily channel became available in 2012 when the x-ray crystal structures of the TWIK-1[68] and TRAAK[69] channels were published simultaneously (**Figure 1.6A**). Previous electrophysiological studies of TREK channels had found that the intracellular pathway to the selectivity filter was physically open even when the channels were in the closed state[70], it was therefore no surprise that the structure of these channels did not demonstrate a classical helix-bundle-crossing gate as seen in most other K^+ channels, including KcsA. This suggested a fundamental difference between the gating mechanism of TREK channels and KcsA.

KcsA has a physical gate at the lower entrance to the pore formed by the four pore-forming helices that create a helix cross-bundle. This gate is thought to be opened and closed by conformational changes of the transmembrane (TM) helices [71] whereas TREK channels were proposed to be gated either within their selectivity filter (similar to C-type inactivation seen in voltage-gated K^+ channels), or within the cavity just below the selectivity filter (e.g. by hydrophobic gating) (**Figure 1.6B & C**). These principles are thought to be shared by other members of the K_{2P} family and several different models have been proposed e.g. direct filter-gating as seen in TREK-1 and other K_{2P}(s)[70], hydrophobic gating in TWIK-1[72], and direct lipid-block of the permeation pathway as proposed from the crystal structures of TRAAK[73]. The relative contribution of these possible gating mechanisms is still debated but the general consensus is that the primary gate in K_{2P} channels exists within the selectivity filter and that this may be allosterically controlled by movement of the TM helices, but without constriction of the lower entrance to pore[70,74].

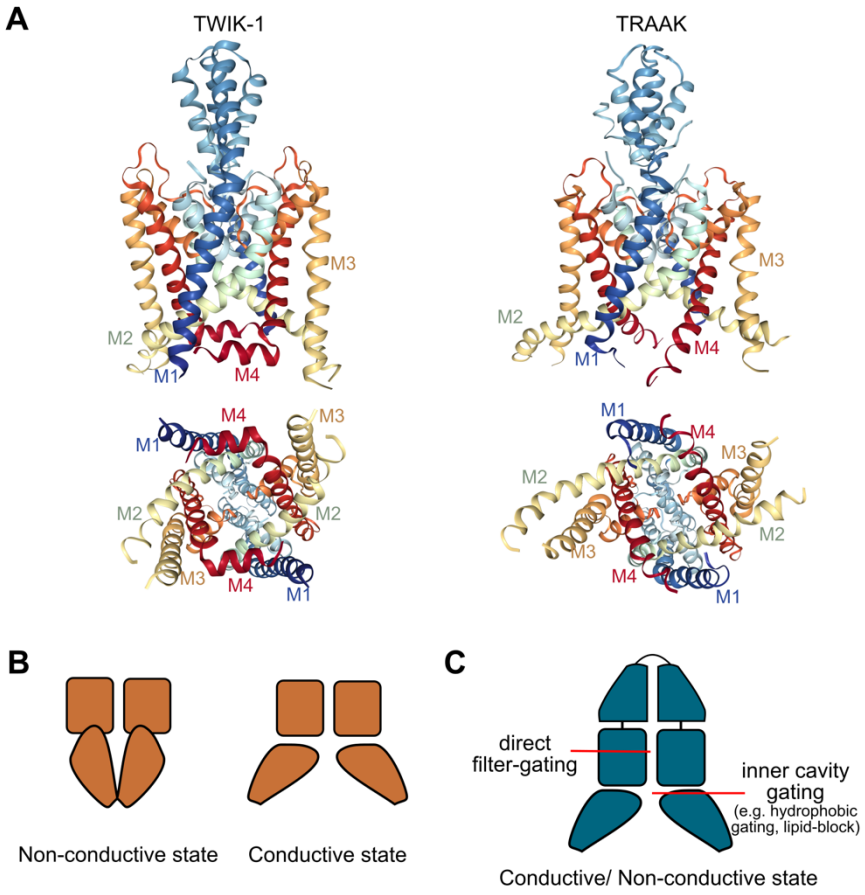


Figure 1.6 Structure of TREK channels and gating mechanism. *(A) Crystal structure of TWIK-1 (left, PDB ID: 3UKM) and TRAAK (right, PDB ID: 3UM7). The intracellular pathway to the selectivity filter was physically open. (B) KcsA gating mechanism. KcsA has a physical gate at the lower entrance to the pore formed by the four pore-forming helices that create a helix cross-bundle. (C) TREK-2 channel gating mechanism. TREK channels were proposed to be gated either within their selectivity filter, or within the cavity below the selectivity filter (e.g. by hydrophobic gating, lipid-block etc.). Structures are rendered by NGL viewer*[75].

1.4 Mechanosensitive ion channels

Mechanosensitive (MS) (stretch-gated, stretch-activation, or membrane tension-gated) ion channels are activated by mechanical or physical forces. The idea of MS channel originally came from the study of mechanosensory neurons [76] but were only first directly characterised in 1984 [77] using patch-clamp experiments. A channel is identified as a MS channel if it is activated by mechanical force (i.e. pressure) which below membrane-lytic tension during the experiment (i.e. patch-clamp recordings) [78,79]. True MS channels only respond to mechanical forces in the lipid bilayer plane and do not respond to perpendicular hydrostatic pressure [80,81]. Although MS channels can be activated by cell volume[82], they are subtly different from volume-sensitive ion channels which often sense changes in Ca^{+} ionic strength[83]. In addition, patch clamp experiments[84] were designed to clarify these two stimuli (cell volume vs. membrane stretch) and shown that they are different. Therefore, overall cellular channel activity is independently controlled by cell volume and membrane stretch[78,83,84]. The possible explanation for this is force distribution and reorganisation of cytoskeleton.

1.4.1 MS channels in different organisms

MS channels are expressed in all cells both of prokaryotic and eukaryotic origin. In bacteria, they play a relatively simple role by preventing cell swelling and death by lytic tension. There are three main family of prokaryotic MS channels: Large-Conductance MS Channel (MscL), Small-Conductance MS Channel (MscS), and Mini-Conductance MS Channel (MscM). These channels, especially MscL and MscS, have been extensively used to study the general mechanisms underlying MS channel behaviour (as described in section 1.4). In eukaryotes, the role of MS channels is more complex because they are involved in many physiological processes. In plants, there are MscS-like, but not MscL-like MS channels [2] where their functions are not just limited to the control of osmotic pressure, but are involved in water transport, pollination and as

gravitational sensors. Mammalian MS channels are even more complex, because they involve in a wide-range of complex physiological processes (including touch, balance (proprioception), hearing, and the sensation of pain). Consequently, defects in their function can give rise to disease, and MS channels have the potential to be exploited as drug targets[85]. In addition to the TREK MS channels, other well-known mammalian MS channels include the DEG/ENaC channels, certain members of the TRP family, and the PIEZO channels (see section 1.5.3 for details). Interestingly, further examples of novel MS channels are even still being cloned right now e.g. the recently identified OSCA/TMEM63 channels[86].

1.4.2 Basic models for the mechanisms of mechanosensitivity

Currently, there are two main models for the molecular mechanising of mechanosensation (**Figure 1.7**). The first model is the 'force-from-filament' (or tethered) model. This model states that channel is activated by force from physically attached filaments (e.g. the cytoskeleton, or extracellular matrix)[87]. This model was originally suggested from the hair cell, sensory receptor in the ear, studies which showed the connection between MS channels and the cytoskeleton [88,89]. The second model is the 'force-from-lipid' (FFL) (or direct) model which proposes that channels are directly activated by forces from their surrounding lipids [90,91]. This model is well supported by the extensive studies of the prokaryotic MS channels that can be activated by amphipaths or by direct activation by membrane tension when reconstituted into lipid bilayer without supported cytoplasmic or extracellular elements [92,93].

For eukaryotic MS channels, studies of purified TREK-1 and TRAAK reconstituted in lipid bilayer [94,95] demonstrate that TREK channel activation only requires the lipid bilayer and does not require the cytoskeleton i.e. they are intrinsically mechanosensitive. Piezo channels also only require the lipid bilayer for stretch activation [96,97]. In addition to these two basic mechanisms of mechanosensing a third model has also been proposed.

This indirect model suggests that force transmitted from supported filaments to a lipid bilayer then activate the channel via the membrane [91,98]. For the purposes of this thesis, only the force-from-lipid principle and its relation to the TREK channels is described in detail and further information regarding these other mechanism can be found in various reviews [91,98–100].

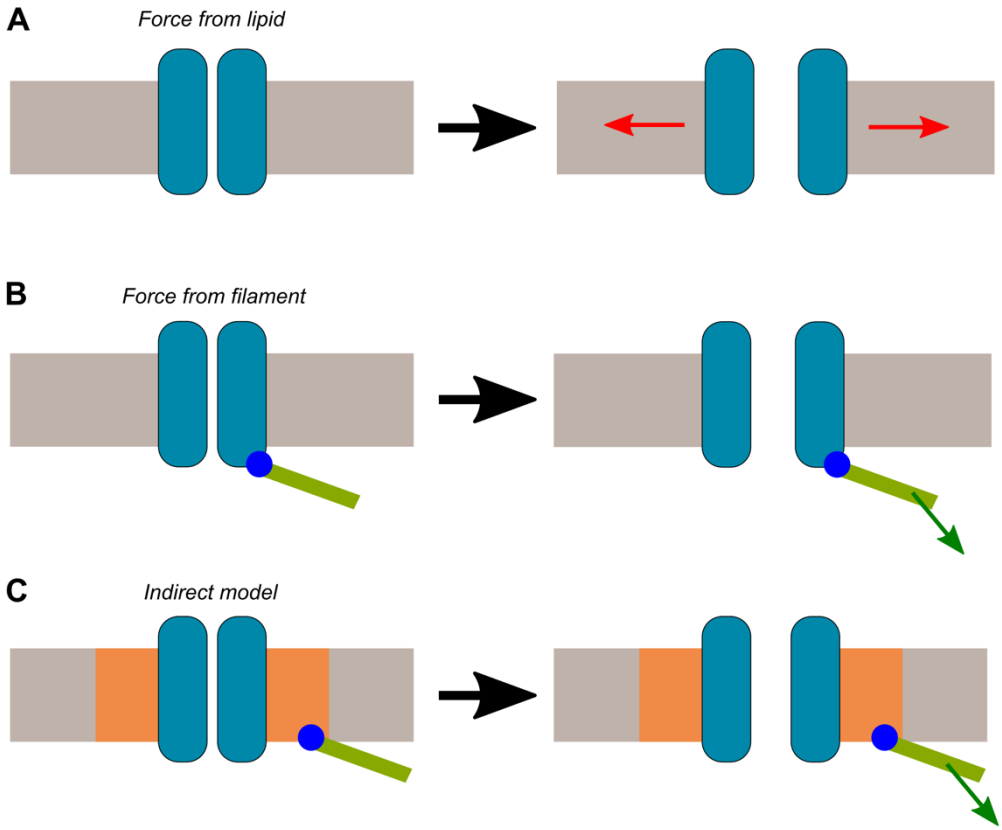


Figure 1.7 MS mechanism models. *(A) 'Force from lipid'. The channels are directly activated by forces from their surrounding lipids. (B) 'Force form filament'. channel is activated by force from physically attached filaments. (C) 'Indirect model'. Force transmitted from supported filaments to a lipid bilayer then activate the channel via the membrane.*

1.5 Previous studies of MS channels

Since their initial discovery in prokaryotes, MS channels have been extensively studied and so there are many available reviews [6,78,79,98,101–108]. This section only provides relevant background information for this thesis and summarises what is already known from these previous studies.

Patch-clamp technique is commonly used to study MS channels. Bilayer tension is created by applying either positive or negative pressure into the lipid patch therefore creating the pressure gradient across the bilayer. The simplified situation is shown in the **Figure 1.8**. As a result, the bilayer curves itself in response to this pressure gradient. The average membrane tension (T) can be computed from Laplace's Law, equation 1.5.

$$T = P\frac{r}{2} \tag{1.5}$$

,where P is the pressure across the membrane and r is the radius of the bilayer curvature.

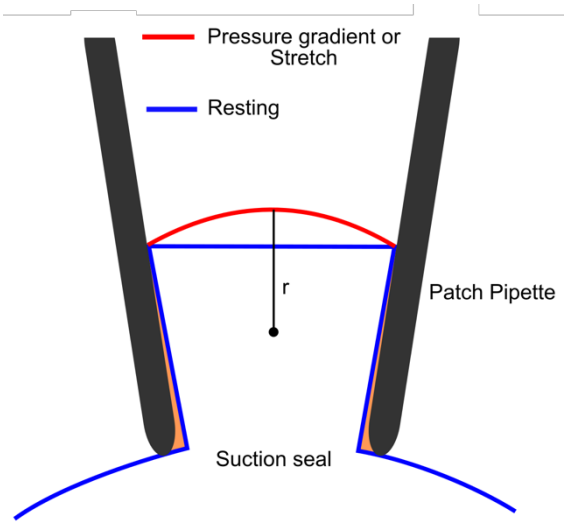


Figure 1.8 Simple patch-clamp scheme. *The blue and red line represent bilayer when it was in resting state and subjected to pressure gradient (or stretch), respectively. The orange shade between patch pipette glass and the bilayer represents gigohm seal. The bilayer curve itself in response to stretch. The average membrane tension can be computed from Laplace's Law.*

1.5.1 Theoretical and thermodynamic overview

To understand the mechanism of MS channels, the theoretical explanation of how MS channels work has to be developed from a particular prospective. Generally, thermodynamic models of ion channels describe the states of ion channels by their energy, equation 1.6. The more stable state has lower energy than the other states. In the two-state model which channel can only be either in 'close' and 'open' state (**Figure 1.9A**), At rest, the close state is more stable than the open state. However, when channels are being activated by stimuli, the energy landscape is perturbed by an increase in entropy as increase in number of microstates (equation 1.7), thus the open state has lower energy than the close state (i.e. open state is now more stable than close state). This event is called 'gating'.

$$\Delta G = \Delta H - T\Delta S \tag{1.6}$$

$$S = k_B \ln \Omega \tag{1.7}$$

, where G is Gibbs free energy, H is enthalpy, T is temperature, S is entropy, Ω is number of microstates, and k_B is Boltzmann's constant.

According to the *force-from-lipid* (FFL) model, MS channels sense forces directly from the lipid bilayer (i.e. 'work' is created by force from lipid). This can be occur via 3 different routes [109–111] (**Figure 1.9 B-D**): (i) a change in the in-plane area (area sensitivity), (ii) a change in protein body angle (shape sensitivity), and (iii) a change in hydrophobic length (length sensitivity). These changes can be independent [109] or can occur together [112–114]. Rather confusingly, these three forms are sometimes referred to by slightly different name in the literature and mostly depends on whether it is being examined from the protein or lipid bilayer perspective. However, they generally refer to the approximately same idea and mechanism. Generally, these models assume that a protein is in a conical or cylindrical shape and lipid bilayer is a fluid elastic sheet.

Area sensitivity refers to a change in protein in-plane area when the channel switches between its different conformations i.e. closed or open. This mechanism is also sometimes referred to as footprint or bilayer dilation. The channel increases its in-plane area in response to increases in applied bilayer tension in an attempt to minimise this change in energy.

Shape sensitivity refers to a change in protein shape or tilt angle in response to bilayer curvature or midplane bending. This includes the curvature caused by lysophospholipids (LPC) and poly-unsaturated fatty acids (PUFAs). The influence of bilayer curvature on MS channels will be discussed more in Chapter 4.

Length sensitivity is the change caused by mismatch between the protein and the bilayer hydrophobic thickness/length. Decreases in bilayer thickness result in reduction in gating energy. However, the Wiggins model[114], which is in agreement with MscL experimental data [115], shows that this behaviour has a parabola (x^2) shape, therefore if the bilayer is too thin, it may result in the opposite effect.

Further work[113] also obtained three distinct protein diffusion-versus-applied membrane tension (D-vs-σ) patterns. These refer to gating by dilation, tilt, and combinations of both dilation and tilt.

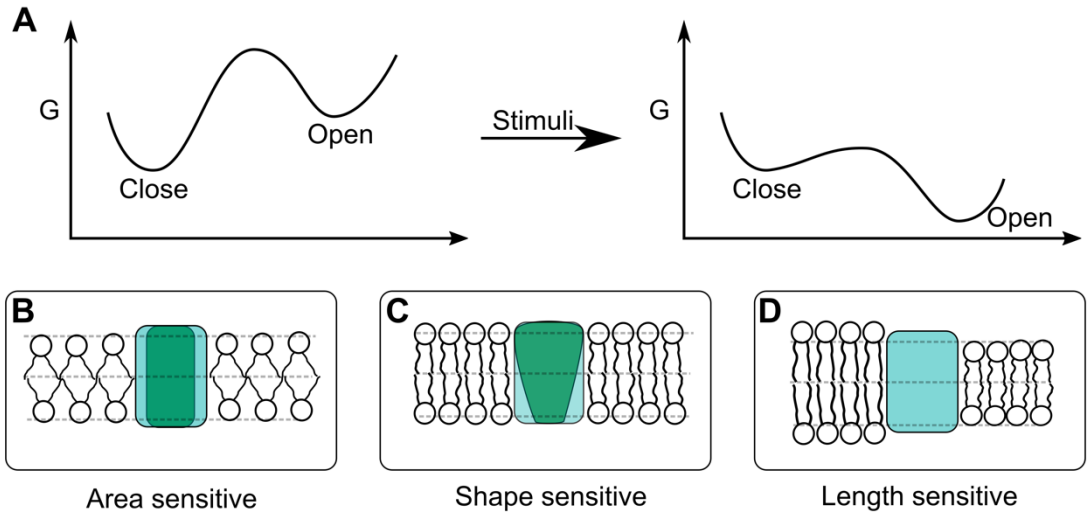


Figure 1.9 Thermodynamics of ion channels and force from lipid principle*. (A) Thermodynamics of ion channel, G is Gibbs free energy. At rest, the close state is more stable (lower energy) than the open state, whereas, when subjecting under stimuli, the open state is more stable than the close state. (B) Area sensitive. A change in protein in-plane area when the channel switches between its different conformations (C) Shape sensitive. a change in protein shape or tilt angle. (D) Length sensitive. The change caused by mismatch between the protein and the bilayer hydrophobic thickness*

1.5.2 Studies of Prokaryotic MS channels

Bacterial MS channels has been studied for many decades, especially the MscL and MscS channels. Initially, their study started with patch clamp experiments[116] that observed a stepwise increase in current as the transmembrane pressure was increased. The principle function of these channels is to maintain cell integrity when they are expose to osmotic changes [117]. The first cloned MS channel is MscL[118] and the first structure was of MscS in 2002[119]. The reconstitution of MscL[118] and MscS[120,121] in pure lipid bilayer system suggested that they only require a lipid bilayer for their mechanosensitive activity and are therefore intrinsically mechanosensitive.

MscL was reconstituted in lipid bilayers with various thickness and then studied using a combination of electrical recordings of channel activity and electron paramagnetic resonance (EPR) spectroscopic [115]. This demonstrated that thin bilayers shift the $P_{1/2}$ value of activation to the left (i.e. make it easier to open) without significantly changing the single channel conductance. However, the hydrophobic mismatch induced by

membrane thinning alone is not sufficient to fully open the channel. The same study [115] also investigated the effect of LPC on the MscL gate and found that LPC open the channel when externally applied, whereas symmetrically applied LPC did not open the channel. In addition, they found that PE lipid had the opposite effect of LPC. This was in agreement with the effect of different lipid headgroups on MscL gating [122] which discovered that PE lipid increases the threshold for channel activation by tension by altering the biophysical properties of a membrane. In parallel, the structural rearrangement of MscL during gating had also been studied [123] and demonstrated that a movement of the TM helices and increase in pore radius during activation. Nonetheless, the effect of conical LPC was then further studied using a combination of functional experiments and MD simulation [124] and this suggested that the action of LPC was different from applied tension. Another study of the amphipathic N terminus of MscL [125] also showed that this part of the protein was involved in stabilising the closed state and coupling to the membrane. Further simulation studies of MscL[126] provided evidence that the protein changed its shape during gating in a way that could induce a contribution of ~30 k_BT on the gating energy. As for MscS, it was shown that, in comparison to MscL, it has a different protein-lipid interaction pattern[127] and unlike MscL, MscS gating does not appear to be significantly affected by bilayer thickness and/or hydrophobic mismatch. In contrast, cholesterol and LPC have a much larger effect on MscS than on MscL thus suggesting that these proteins individually have their own characteristic set of lipid-protein interactions.

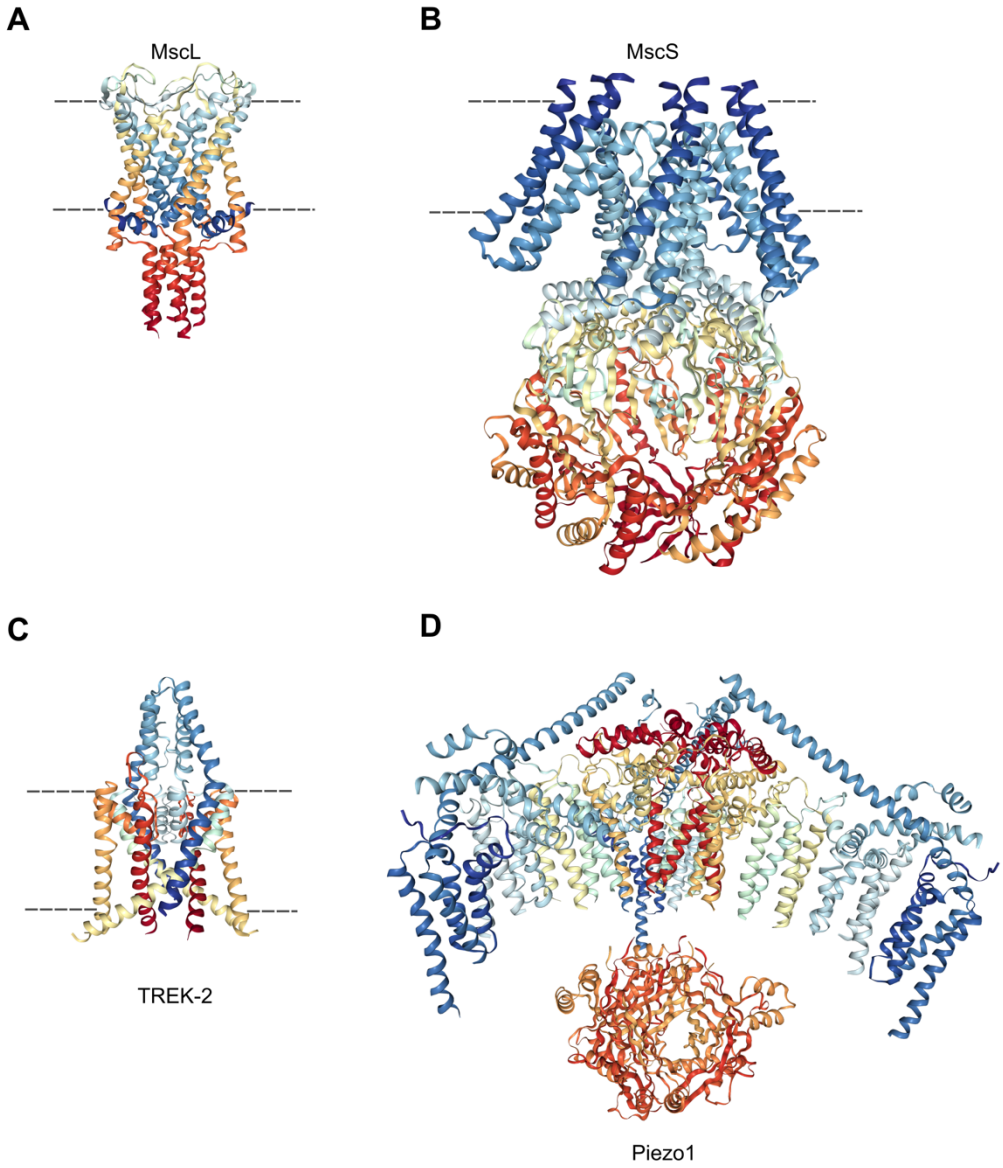


***Figure 1.10 Structures of MS channels**. Structure of (A) MscL (PDB ID: 2OAR), (B) MscS (PDB ID: 2OAU), (C) TREK-2 (PDB ID: 4XDJ), (D) Piezo-1 (PDB ID: 6BPZ). The dash lines indicate bilayer regions. Structures are rendered by NGL viewer[75].*

1.5.3 Eukaryotic MS channels

Eukaryotic MS channels include the TREK family of K^+ channels, the Na^+ selective DEG/ENaC channels and the non-selective TRP and PIEZO channels (**Figure 1.10**). However, only TREK and PIEZO channels have solidly supported evidence that they are intrinsically MS channels[96,102,104,128]. This thesis only examines the TREK family of

channels and further information regarding PIEZO channels can found in the following reviews [129,130].

At the start of this thesis, our understanding of the mechanisms underlying TREK mechanosensitivity where highly incomplete, especially when compared to the extensive studies of prokaryotic MscL channels. The basic mechanosensitivity of TREK channels was first demonstrated in the late 1990s [56,131,132] and later studies confirmed that this was an intrinsic property, i.e. only required the lipid bilayer [94,95]. In comparison to MscL, the tensions required to gate TREK channels open are relatively low (e.g. 0.5-4 mN/m for TRAAK) and the channels remain active until the membrane breaks [73], but in addition to applied tension, adding LPC lipid or arachidonic acid also opens TREK channels[133] indicating that they may share similar mechanisms of action with their prokaryotic cousins.

At the end of 2014, two stretch-activation models were suggested based on the different crystal structure conformations of TRAAK[73,134]. These two models contradicted with each other. The Mackinnon group model[73] suggested that activation involved movement from the 'down' conformation to the 'up' conformation of the channel, whereas the model from Minor group [134] suggested the opposite movement, i.e. from up to down. At that same times, crystal structures of TREK-2 simultaneously became available in both the down and up states [135] and initial studies from our group supported the down to up model of activation for this channel. This was the point in time that this thesis started.

1.6 Overall Perspective and Aims

Although the stretch-activation models were presented, they were only based on the comparison of two relatively static crystal structures. Furthermore, these channel structures were removed from their surrounding environment, i.e. the lipid bilayer. Many studies have shown that the lipid bilayer is important for ion channel function [92,114,136,137] and it is clearly critical for the FFL model of activation. Yet due to

the difficulty of studying its role, it was often ignored and referred to as '*the elephant in the room*' [107]. In this thesis, I have therefore attempted to take a more dynamic approach to studying the conformational changes of the TREK-2 channel located in a lipid bilayer and investigating how its response to membrane stretch can be examined using MD simulation. The initial aims of this thesis were to answer the following questions:

i) Is the stretch-activation model the 'down to the up' state transition or the 'up to the down' state transition?

ii) Are there any bilayer properties that play a significant role on stretch-activation?

These two questions formed the starting point of this thesis and following this there were also further questions that arose from determination of a new structure of the TREK-1 channel with an extended c-terminal domain that was not visible in the earlier structures [138].

iii) If the protein shows an asymmetric response in change of shape, then will it respond differently to asymmetric changes in membrane tension?

iv) How does intracellular pH sensitivity affect TREK channel activity and how is this related to mechanical activation?

v) How are the mechanical forces which activate the channel distributed across all the molecules in the system? What do the protein-lipid and intra-protein interactions look like, and can this be used to understand why some structurally related K_{2P} channels are not mechanosensitive?

1.7 Thesis outline and structure

This thesis aims to study the mechanosensitivity of TREK-2 from a structural and biophysical prospective. The outline of the thesis chapters are as follows:

Chapter 1 Introduction This presents the thesis aims, and related background knowledge.

Chapter 2 Theory and Methodology describes and explains the background theory of molecular dynamics (MD) simulations as well as other related theories and tools.

Chapter 3 MD simulations of TREK-2 in bilayer, our extensive understanding of the bacterial MS channel, MscL, was adapted and applied to study TREK-2. Its mechanosensitivity in a symmetrically tensioned bilayer is examined by MD simulation along with the potential role of hydrophobic mismatch condition.

Chapter 4 The response of TREK-2 to asymmetric increases in bilayer tension, after investigating TREK-2 under symmetric tension, its asymmetric response in protein shape is examined.

Chapter 5 Investigation of the effect of the E306A mutation on TREK-1 pH sensitivity, this examines the relationship between intracellular pH sensitivity and mechanosensitivity in TREK-1 and the specific role of mutations that affect both properties.

Chapter 6 Non-Bonded Force Distribution Analysis, this describes the development of an analysis tool that focus on protein-lipid interaction and internal protein interactions. This tool was also applied on TREK-2 and TWIK to observe the relative changes in interaction during the stretch-activation.

Chapter 7 Summary of the thesis.

Chapter 2
Theory and Methodology

2.1 Introduction

Molecular dynamics (MD) simulation is a powerful computational technique which has made a strong impact as demonstrated by the award of the 2013 chemistry Nobel prize. In parallel with the rapid development of computing technology, it has therefore become an effective technique used in structural and molecular biology to study interactions of biomolecules (i.e. enzymes, proteins, DNAs, lipids). This chapter describes the basic concept of MD simulation including its essential component (the forcefield) and also information on relevant software. Since this study is performed using the GROMACS package along with the Martini, and CHARMM36 forcefields, these particular topics will be emphasised. Limitations and how to evaluate/interpret simulation results alongside experimental results also will be discussed. Finally, the parameters used in this study will be summarised.

2.1 Molecular Dynamics Simulation

Molecular dynamics (MD) simulation is a classical approach which considers an atom or a group of atoms as a bead or particle and uses classical mechanics to describe the interactions and motions of the set of atoms. These approximations effectively improve computing performance designed for big system such as biomolecules. Apart from MD, other simulation techniques are also available at different levels of description (**Figure 2.1**). These techniques have their own advantages and disadvantages in a particular situation. The aim of the current study is to understand the behaviour of a mechanosensitive TREK K^+ channel in a fully hydrated lipid bilayer KCl solution. This system consists of ~150,000 to ~200,000 atoms. Furthermore, the principal target behaviours are expected to show in a few hundred nanosecond time scale since it has already been shown in the MscL studies[139,140]. Therefore, MD simulation is an appropriate tool.

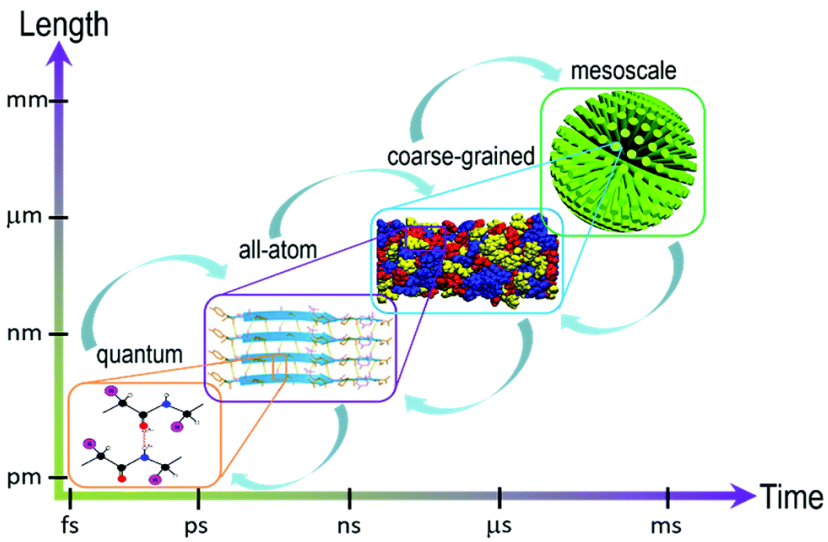


***Figure 2.1 Multi-scale computational simulations**. Diagram shows time scale-system size which is corresponding to each computational scale. Picture is reproduced from Yuan and et al.[141] with permission from the PCCP Owner Societies.*

2.1.1 Theory and algorithm

Atomic interactions. In MD for biological molecules, an atom or a group of atoms is usually considered as a particle/bead. The interactions between atoms are described by potential energies which fall into 2 categories: bonded and non-bonded, equation 2.1. Bonded potentials represent interactions of atoms within a molecule, typically not further than 4 atoms (or 4-body interactions i.e. dihedral), (**Figure 2.2**). They are bonded, angle, and dihedral, equation 2.2. In addition, there is a special type bonded interaction called '*improper dihedral*'. This is used to restrain atoms in plane or prevent handedness transition of a chiral configuration.

$$U = U_{bonded} + U_{non-bonded} \tag{2.1}$$

$$U_{bonded} = \frac{1}{2}k_{ij}^{b}\left(r_{ij} - b_{ij}\right)^2 + \frac{1}{2}k_{ijk}^{\theta}\left(\theta_{ijk} - \theta_{ijk}^{0}\right)^2 + k_{\varphi}(1 + \cos(n\varphi - \varphi_s)) + \frac{1}{2}k_{\xi}\left(\xi_{ijkl} - \xi_0\right)^2 \tag{2.2}$$

Each term is bond, angle, dihedral, and improper dihedral term, respectively. k_{ij}^{b}, k_{ijk}^{θ}, k_{φ} and k_{ξ} are the associated constants. In the dihedral, n is multiplicity which indicates number of minima in 2π radius of a rotation. Equation 2.2, all interactions, excluding dihedral, are shown in harmonic type which the standard and simple form. There are others type that can be used to represent some specific interaction, for example, alkane proper dihedrals may be described by Ryckaert-Bellemans function[142].

Non-bonded potentials represent long-range interactions which, generally, are Coulomb (electrostatic) and Lennard-Jones (van der Waals), equation 2.3.

$$U_{bonded} = \frac{1}{4\pi\varepsilon_0}\frac{q_i q_j}{\varepsilon_r r_{ij}} + 4\epsilon_{ij}\left(\left(\frac{\sigma_{ij}}{r_{ij}}\right)^{12} - \left(\frac{\sigma_{ij}}{r_{ij}}\right)^{6}\right) \tag{2.3}$$

The first and second terms are Coulomb and Lennard-Jones (LJ) potential, respectively.

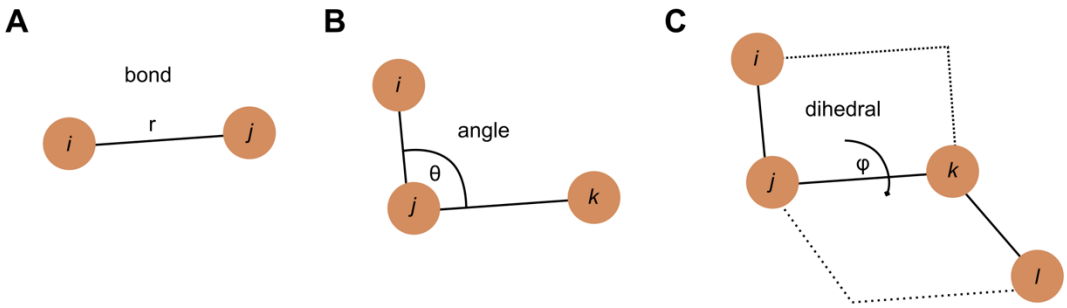


Figure 2.2 Bonded interactions.

Force calculation and equation of motion. The motion of an atom is described by the Newton equation, equation 2.4. To compute an acceleration and update coordinates of atom *i*, summation of forces on an atom *i* ($\sum \boldsymbol{F}_i$) is need. The calculation is done by using equation 2.5 and 2.6 where $\boldsymbol{F}_{ij}$ is force on an atom *i* from any atom *j*.

$$\sum \boldsymbol{F}_i = m\boldsymbol{a}_i = m\ddot{\boldsymbol{x}}_i \tag{2.4}$$

$$\sum \boldsymbol{F}_i = \sum_j \boldsymbol{F}_{ij} \tag{2.5}$$

$$\boldsymbol{F}_{ij} = -\nabla U \tag{2.6}$$

Integration algorithm. An updated coordinate is computed by integrating the acceleration. Although, computationally, there are many available numerical approaches for integration algorithms, there are two widely used algorithms for biomolecular simulations which are leap-frog and velocity Verlet [143], which is a variant of Verlet algorithm[144] (see Berendsen[145] for discussion regarding to integration algorithm). The leap-frog algorithm determines velocities and positions at time *t* using following equations.

$$\boldsymbol{v}\left(t + \tfrac{1}{2}\Delta t\right) = \boldsymbol{v}\left(t - \tfrac{1}{2}\Delta t\right) + \Delta t\boldsymbol{a}(t) \tag{2.7}$$

$$\boldsymbol{r}(t + \Delta t) = \boldsymbol{r}(t) + \Delta t\boldsymbol{v}\left(t + \tfrac{1}{2}\Delta t\right) \tag{2.8}$$

Velocity Verlet works in different way. It does not require the previous half-step velocities as shown in equation 2.9 and 2.10.

$$\boldsymbol{r}(t+\Delta t) = \boldsymbol{r}(t) + \Delta t\boldsymbol{v}(t) + \frac{1}{2}\Delta t^2\boldsymbol{a}(t) \quad (2.9)$$

$$\boldsymbol{v}(t+\Delta t) = \boldsymbol{v}(t) + \frac{1}{2}\Delta t[\boldsymbol{a}(t) + \boldsymbol{a}(t+\Delta t)] \quad (2.10)$$

Leap-frog algorithm is the default integration for GROMACS[142]. Without temperature and pressure coupling, these two algorithms will generate identical trajectories. However, with a starting point given both coordinates and velocities, the trajectories will be different. This because they treat the velocities in different way.

Integration time step and constraints. Integration time step (Δt) determines the physical time in each integration loop. It is an important parameter and should be smartly chosen since it affects MD performance. The common rule is to choose the largest as possible, nonetheless it should be smaller than one fifth of bonded-oscillational period. This make it limited to a small femtosecond-step since the O-H bond oscillation period is 9.1 fs (estimated under CHARMM36 forcefield, others may be slightly different). To speed up the simulation, constraint algorithms were developed. These confine bond geometry of given bonds, thus allowing larger integration time steps. There are three widely-used algorithms: SHAKE[146], LINCS (Linear Constraint Solver)[147], and SETTLE[148]. In this thesis, LINCS and SETTLE were used. LINCS is more stable, faster, and flexible than SHAKE [142]. SETTLE is applied to water molecules by default for fixed point water model, see section 2.2.3.

Particle mesh Ewald (PME) and cut-off. Computing non-bonded electrostatic forces is computational expensive because they are pair-wise and long-range forces. For the system of N particles, the number of interactions is NxN which is a huge number. Therefore, the cut-off approach has been employed to reduce number of interactions. Nonetheless, hard and non-buffered cut-off results in artefacts (energy drift and loss of interactions) and lead to accumulated error for long simulation. Verlet buffer cut-off scheme[142] is used in this study. It uses a buffered pair list which is created at neighbour

search steps. In addition, the number of interactions is reduced to $N \log N$ by PME method[149]. Charges are represented by a Gaussian distribution then applied to grids. After that they are subjected to the Fourier transformed for a summation in a k-space. The potential at the grid points (in real space) is obtained by inverse transformation. Using PME with the Verlet cut-off scheme shifts a small energy to zero at the cut-off. This small shift is neglected when system is neutral (net charge equals to 0)[142].

Temperature coupling and Pressure Coupling are used to control the temperature and pressure of a system. The widely algorithm are Berendsen (T- and P-coupling) [150], Nose-Hoover (T-coupling) [151,152], Velocity-rescale (T-coupling) [153], Parrinello-Rahman (P-coupling) [154], Martyna-Tuckerman-Tobias-Klein (MTTK P-coupling). This study used the Berendsen, Velocity-rescale, and Parrinello-Rahman algorithms.

Berendsen (or weak-coupling)[150] uses the first-order kinetics and the external heat bath with the given temperature (T_0) or pressure ($\boldsymbol{P}_0$) to correct the system temperature (T) and pressure ($\boldsymbol{P}$), equation 2.11 and 2.12.

$$\frac{dT}{dt} = \frac{T_0 - T}{\tau} \tag{2.11}$$

$$\frac{d\boldsymbol{P}}{dt} = \frac{\boldsymbol{P}_0 - \boldsymbol{P}}{\tau_p} \tag{2.12}$$

The system pressure is changed by scaling box vectors with matrix μ_{ij} at every n_{PC} step, equation 2.13.

$$\mu_{ij} = \delta_{ij} - \frac{n_{PC}\Delta t}{3\tau_p}\beta_{ij}\{P_{0ij} - P_{ij}(t)\} \tag{2.13}$$

, where $\boldsymbol{\beta}$ is the isothermal compressibility of the system.

According to equation 2.11 and 2.12, temperature and pressure change exponentially with a time constant τ and τ_p, respectively. This prevents large fluctuations in temperature or volume and make a system slowly adjust to the target temperature. As a result, Berendsen is recommended during the equilibration process. However, it does

not reproduce proper fluctuations in energy and volume, because it suppresses thermal fluctuation of the system. Note, this error is scaled by $^1/_N$, therefore it is not significant in very large system[142].

Velocity-rescale[153] is a temperature coupling and, now, occasionally used for production runs instead of Berendsen. It directly rescales velocities of particles and adds a stochastic term that corrects kinetic energy. Thus, it reproduces the canonical ensemble. Using this algorithm, velocities of each particle are rescaled with a factor (λ), equation 2.14, in every given step (n_{TC}).

$$\lambda = \left[1 + \frac{n_{TC}\Delta t}{\tau_T}\left\{\frac{T_0}{T(t-\frac{1}{2}\Delta t)} - 1\right\}\right]^{1/2} \tag{2.14}$$

This factor ranges from 0.8 to 1.25, mostly closer to 1 in normal. In this case τ is not equal to τ_T, nonetheless $\tau = 2C_v\tau_T/N_{df}k$, where C_v is the total heat capacity, k is Boltzmann's constant and N_{df} is the total number of degrees of freedom.

Parrinello-Rahman[154] is a pressure coupling which is widely used in production runs. It is strongly recommended to use Berendsen in the equilibration then switch to Parrinello-Rahman, because it may cause large fluctuations and crash the system if the starting point is far from the equilibrium[142]. In theory, it gives correct NPT ensembles whereas Berendsen does not. The Parrinello-Rahman barostat describes simulation box (matrix $\boldsymbol{b}$) motion as equation 2.15.

$$\frac{d\boldsymbol{b}^2}{dt^2} = V\boldsymbol{W}^{-1}\boldsymbol{b}'^{-1}(\boldsymbol{P} - \boldsymbol{P}_0) \tag{2.15}$$

, where V is box volume and $\boldsymbol{W}^{-1}$ is determined the strength of the coupling and calculated by equation 2.16, where L is the largest box matrix element and $\boldsymbol{\beta}$ is the isothermal compressibility.

$$(\boldsymbol{W}^{-1})_{ij} = \frac{4\pi^2\beta_{ij}}{3\tau_p^2 L} \tag{2.16}$$

Restraints can be considered as an additional virtual bond term. They are typically used to restrain atoms in the simulation. In other words, it locks a particle's position, distance, angle, or dihedral during the simulation. In general, a particle is restrained by harmonic potential with a force constant, for example positional restraint, equation 2.17. The applications of restraints are to reduce the degrees of freedom in the equilibrium state, or to keep protein structure close to its original crystal structure.

$$U_{pr}(\boldsymbol{r}_i) = \frac{1}{2} k_{pr} |\boldsymbol{r}_i - \boldsymbol{R}_i|^2 \tag{2.17}$$

, where k_{pr} is a positional restrain constant and $\boldsymbol{R}_i$ is a reference position.

Periodic boundary condition (PBC) is an approach to solve the boundary artefacts or edge problems i.e. the missing interactions at the border (**Figure 2.3A**). It generates virtual system images surrounding the actual system (**Figure 2.3B**) so that atoms at the edges interact with these virtual images.

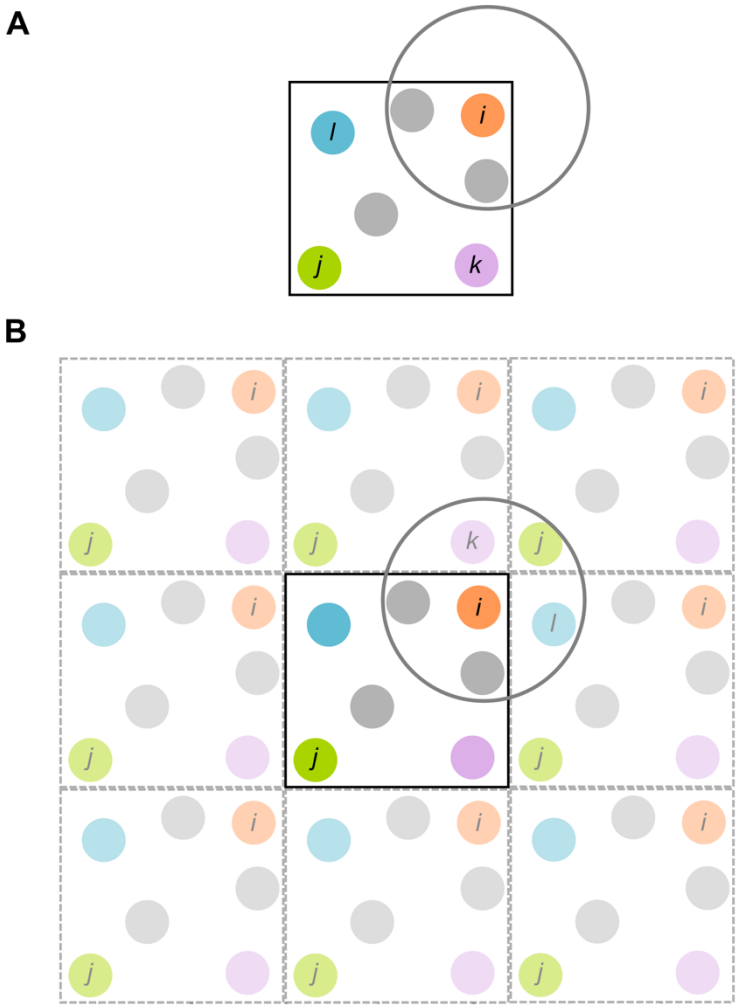


Figure 2.3 Periodic boundary condition. *(A) edge problem of an atom i, interactions (i-j, i-k, i-l) are missing. (B) PBC applied in 2D, now, there is no missing interaction. Images are shown in fade.*

In summary, MD simulation generates the movement of atoms in the simulation system by solving Newtonian equations. Forces can then be calculated from the potential and both temperature and pressure coupling involved to control the system temperature and pressure. The auxiliary-algorithms/approaches (i.e. cut-off, PME, constraint, restraints, and PBC) help to improve MD performance and to speed up the simulation. The MD algorithm is summarised and shown in (**Figure 2.4**).

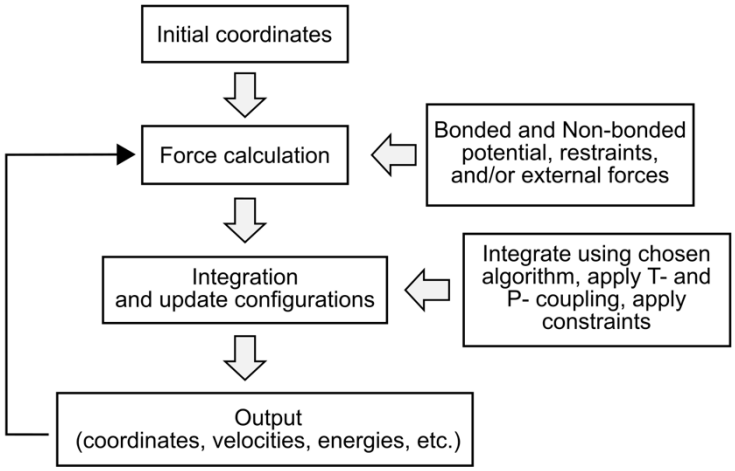


Figure 2.4 Diagram describing MD simulation.

2.1.2 MD simulation scale

MD simulations can be performed on 3 different scales: all-atom, united atom, and coarse-grained (**Figure 2.5**). In all-atom (AT) system, all particles are explicitly represented including hydrogen atoms. In united-atom, hydrogen atoms in hydrocarbon chains are implicit. In hydrocarbon chains, they are grouped with the carbon atom. For example, CH_3 is only represented in one bead instead of 4 beads. In coarse-grain (CG) models, usually 3-4 heavy atoms, not hydrogen atoms, are group into a bead. Each scale has its own advantages and disadvantages. AT simulation is thought to be the most accurate, but is computationally expensive. The simulation at this scale is usually used for an investigation of small molecules or specific interactions (e.g. protein-lipid), because hydrogen interactions which are very important interactions for biomolecules, are explicitly shown. United-atom is mostly applied to lipids. It balances between accuracy and performance. In addition, there is a combination of all-atom protein and united-atom lipid[155,156] which is designed to speed up the study of protein in lipid environments, but which mainly focuses on the protein[157]. CG simulation performance is very fast for many reasons. For example, it reduces the number

of particles, hence, number of interactions. It also uses larger integration time step (2 fs for AT, 20-40 fs for CG).

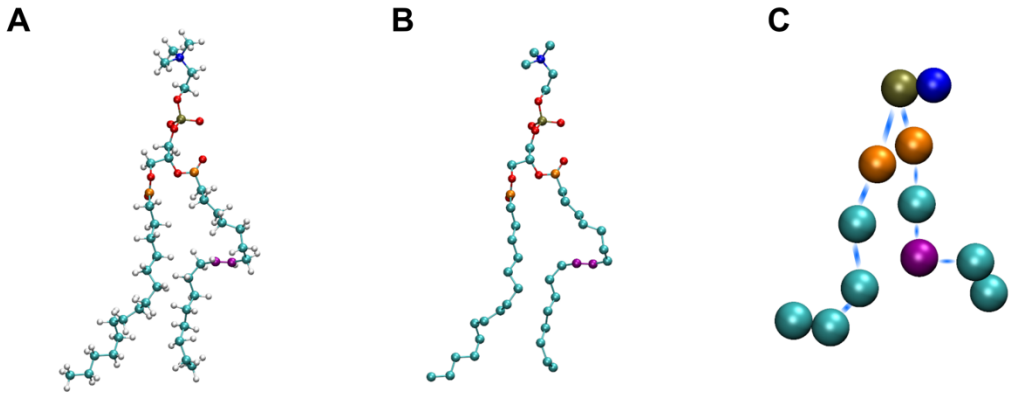


Figure 2.5 MD simulation scale. *A POPC lipid in (A) all-atom, (B) united atom, (C) coarse-grained representation.*

2.1.3 Multiscale simulation approach

In a study, more than one MD simulation scales can be used. This is the so-called multiscale simulation approach. The combination can be either simultaneously performed together (hybrid)[158] or performed in a serial manner (the same pipeline), for example perform the equilibration stage in CG than convert to AT for the production run[159,160]. The latter approach had been used in this thesis where it was used to speed up the equilibrium process and also for screening purposes.

2.2 Forcefield and Software engines

The forcefield is an essential part of any MD simulation study as it provides the chemical details from which reliable potential energies can be determined. It is basically a set of parameters that describes the molecular interactions. In other words, the forcefield contains all the constants that used to calculate the forces. The details of how a forcefield works depends on the software. Software, here, refers to a package which includes the integration engine, preparation tools and any related analysis tools.

2.2.1 All-atom and united-atom forcefields

Currently, the best-known and widely used all-atom and united-atom forcefields are Amber[161,162], CHARMM[163], OPLS[164], and GROMOS[165,166]. They are available for most of the different softwares but there is no easy written rule for how to choose a specific forcefield. However, these forcefields were tested in different aspects such as lipid bilayers[167–169], protein-lipid interactions[170], protein[167,171,172], disordered and folded protein[173–177], peptide insertion energy[178], fluid phase simulation[179]. Generally, Amber, CHARMM, OPLS-AA are popular among protein simulations, whereas GROMOS is for lipid. The current study has been done by using the CHARMM36 forcefield because it has a suitable performance in membrane protein studies which require well-established parameters in both protein[180] and lipid[181,182]. Details of each forcefield, particularly in CHARMM, are described in the following. Others are also covered in a number of reviews[167,183–185].

Amber (Assisted Model Building with Energy Refinement) refers to either a MD package (see section 2.2.4) or a forcefield family. Amber forcefield currently outstanding members are ff94[186], ff98SB[161], ff03[187], ff14SB[162], and GAFF[188]. Amber is widely in the MD field, especially for proteins, enzymes, DNA, and drug development. Small molecule simulations are possible by GAFF that automatically generate their input topologies. A more general overview can be found in the literature[161,189].

OPLS (Optimized Potentials for Liquid Simulations), originally, is parameterised to fit experimental data of liquids. Currently, it is a forcefield family that is available for many of biomolecules (i.e. lipids, protein) and has members in both all-atom (OPLS-AA)[190,191] and united-atom (OPLS-UA)[192,193]. The latest version is OPLS-AA/M[164]. It also has an ability to perform hybrid simulation such as an all-atom protein with united-atom lipids. This make OPLS forcefield is used in membrane protein simulation which is particularly focus on a protein inner pore, but not protein-lipid interaction (e.g. hydrophobic gating).

GROMOS (Groningen Molecular Simulation package), like Amber, refers to both forcefield and associated MD software. It is a united-atom force field parameterised to reproduce thermodynamic properties of small molecules. The current version is GROMOS97, which is developed based on GROMOS87. It contains 43A1-S3[194], 43A2, 45A3[195],45A4[196] , 53A5[165], 53A6[165], 54A7[197], and recently 54A8[166] parameter sets. These sets have different optimisation target, for example 45A3 is for an application to lipid aggregates, 45A4 is for DNA.

CHARMM (Chemistry at Harvard Macromolecular Mechanics) is also the name of forcefield and associated MD software. It is developed based on quantum calculations and experimental data on small molecules. Apart from CHARMM19 which is a united-atom, CHARMM is an all-atom forcefield. The lasted version in CHARMM36m (C36m)[163], which is still called as CHARMM36. The difference between C36m and CHARMM36 (C36)[198] is a correction map (CMAP) which is initially employed in CHARMM22[199] to fix ϕ and φ backbone torsion angle. This change improves an accuracy on the simulation of protein secondary structure. Instead of harmonic angle potential (see equation 2.2), Urey-Bradley potential, equation 2.18, is used by CHARMM forcefield. It is an angle vibration of a triplet atoms (*i*-*j*-*k*) represented by harmonic potential on the angel (θ_{ijk}) and atom *i*-*k* distance (r_{ik}).

$$U_{Urey-Bradley}(\theta_{ijk}) = \frac{1}{2}k_{ijk}^{\theta}(\theta_{ijk} - \theta_{ijk}^{0})^2 + \frac{1}{2}k_{ijk}^{UB}(r_{ik} - r_{ik}^{0})^2 \qquad (2.18)$$

When k_{ijk}^{UB}, Urey-Bradley constant, is equal to 0, $U_{Urey-Bradley}$ is identical to a harmonic bond angle.

2.2.2 Coarse-grained forcefields

Coarse-graining is a practical way to reduce the degrees of freedom in a system. To achieve this, small numbers of atoms are grouped together and represented by single beads/particles. This is done by various methods (e.g. conserving free energies,

conserving distribution, conserving forces). The coarse-grained forcefield used in this thesis is the Martini forcefield[200]. Protein and lipid parameters are available and tested for this forcefield.

Martini[200–202] is the coarse-grained forcefield parametrised by using conserved free energies method and four-to-one mapping. There are only 18 bead types divided into 4 bead type groups, Q (charged), P (polar), N (nonpolar), C (apolar) with additional special type S (ring). These groups have letters denoting hydrogen-bonding capabilities and degree of polarities. Unlike all-atom where $\epsilon_{ij}$and σ_{ij} in LJ-potential fully depend on atom type i and j, Martini assigns only 10 levels of interactions with difference interaction strength (ϵ_{ij}), whereas σ is set to 6.2 Å. This length is scaled down to 4.3 for ring-ring interactions. Coulomb interaction is also scaled down by dielectric constant (ε_r) of 15. Note, there is a lipid topology changes in 2015[203]. This change reduces number of beads in *sn-2* (Oleic acid) of POPC from 5 beads to 4 beads, which is more reasonable, and their bead types were changed. Therefore, the 2015 POPC model has 12 beads instead of 13 beads, see **Figure 2.5**.

2.2.3 Water models

The water models refer to how water is represented. It is integrated as a part of forcefield and plays important roles in MD simulation since the majority of most bio-systems is water. Using an inappropriate water model may cause unnatural behaviour in simulation such as protein unfolding[204]. There are two ways to represent water in a simulation: implicit and explicit. Explicit water can provide maximum detail, but is computationally expensive. On the other hand, implicit water, represented as a dielectric continuum, is fast but provide less detail. Typically, each forcefield has an associated water model which are parameterised together, such as GROMOS and SPC(single point charge), OPSL-AA and TIP4P, Amber and TIP3P. In CHARMM, the TIP3P explicit water model is commonly used. TIP3P (transferable intermolecular potential with 3 points) is

a 3 points rigid fixed-charge water model in the 'TIPn' N-point model class, and first suggested by Jorgensen in 1981[205]. Its model is based on the geometry of a water molecule in gas phase (**Figure 2.6**). The other models in class are TIP4P[206] (4-point model with an additional negative charge toward hydrogen) and TIP5P[207] (5-point model with the addition of two negative charges at the position of lone-pair electrons). Further information regarding to other models can be found in the reviews/studies[208,209].

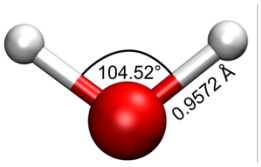


***Figure 2.6 TIP3P water model**. Bonds, and angle are parameterised and defined. Note, these values may be changed during forcefield development.*

2.2.4 Software

Currently, the popular MD packages are GROMACS[210], NAMD[211], Amber[212] including AmberTools, LAMMPS[213], and newly developed OpenMM[214]. These packages are still active, and the latest updates can be found on their official website. Like the different forcefields, there are no written rules to select specific software, but unlike forcefields, although the results of these software are not identical, there is no significant difference between packages. Recently, there was a comparison between these software using the SAMPL5 dataset[215]. The reasons for using GROMACS in this thesis are: (i) it is a free package, (ii) it has been developed for many years and still active, (iii) the CHARMM forcefield is available within it, (iv) it is fast (parallel-CPUs and GPU-accelerated are available), and (v) it provides useful tools. GROMACS is an MD engine developed in Groningen based on the GROMOS87 forcefield in 1990s[142]. Historically, the development of GROMACS and GROMOS have different priorities because, GROMOS itself is mainly focussed on the forcefields whereas GROMACS is only focused on improvements in the software.

2.3 Limitations

Although MD simulation is a powerful technique, it has limitations. These limitations are caused by the classical molecular mechanic (MM) approach, parameterisations, and related computational techniques. First, MD cannot simulate chemical interaction like bonded and unbonded behaviour. This is an obvious limitation from classical MM that represents bonded interactions on the basic of harmonic potential. One can use QM/MM[216,217] which a hybrid between quantum mechanics and molecular mechanics instead. Second are forcefield limitations: availability and accuracy. To simulate a complex system, one needs topologies of all relevant molecules. Accuracy can be either affected by bonded/constrain within molecule itself, such as protein secondary prediction[173], or from non-bonded interaction balance, i.e. the balance between protein-, lipids-, and water/ions- interactions. These interactions were parametrised separately and combined by using combination rules. The influence of these are demonstrated as protein-lipid interactions have to be re-balanced to capture transmembrane helix-helix association[218]. Apart from that, computational limits still remain that make simulation of large system sizes (i.e. complex membranes, or large proteins) impossible to achieve within a reasonable timescale. In addition, the polarisable forcefields (i.e. CHARMM-Drude[185,219], AMOEBA[220,221], Amberff02[222]) are more accurate[185,223], but also extremely computationally expensive.

2.4 Analytic tools

This section describes how to obtain some of the properties and related measurements from proteins and bilayers. MD simulation generates a time series of a set of atoms coordinates, velocities, energy, and forces. This series is called an MD trajectory. Analysis can be relatively simple such as distance between 2 atoms/molecules which is done by basic math, or complex ones such as grid-based calculation, Voronoi diagrams,

or clustering algorithms. In addition, there are visualised packages that display 3D representations of an MD trajectory such as VMD[224] and Pymol[225]. The majority of these MD tools require only the coordinates from the MD trajectory. Standard tools are normally included in the MD software, for example GROMACS has gmx tools to calculate distance, mass or electron density, RMSD, and etc. MD analysis tools are also available in Python packages such as MDAnalysis[226,227] and MDTraj[228]. The following only shows standard and common forms of analysis, related specific ones will be discussed in each particular chapter. Other information is available in the lipid[169] and protein publications[229].

Root mean square deviation (RMSD) is an average distance between atoms (normally C_α atoms) and their reference positions (e.g. initial crystal structure). It is computed by equation 2.19 and refers to how much the given structure is close to the reference structure; 0 means the two structures are identical. In addition, it is also a standard tool to check whether protein structure is in an equilibrium, when the RMSD is converged. This analysis is available in many of protein-related software including GROMACS, Pymol[225], VMD[224], MDAnalysis[227].

$$\text{RMSD} = \sqrt{\frac{1}{n}\sum_{i=1}^{n} d_i^2} \tag{2.19}$$

, where d_i is the distance between two atoms.

Contact analysis is the analysis that counts the number of atoms (normally phosphorus atom of lipid head group) within a cut-off distance around a given residue. This is a traditional method to identify local protein-lipid interaction sites. Data can be compared with crystal structure if a lipid-like density is solved, and interpreted with ion-mobility spectrometry–mass spectrometry (IM-MS)[136]. This analysis is available with the GROMACS package and MDAnalysis.

Area per lipid (APL) refers to the lateral (in-plane) area occupied by a lipid. It is either roughly calculated by dividing the simulation box area by the number of lipids in leaflet or more accurately by using the Voronoi algorithm. The latter method is now popular as increases in membrane complexity become more common. The available software is APLvoro[230]. APL is measured using a combination of X-ray and neutron scattering[231].

Bilayer Thickness is computed by either averaging bilayer axis (z-axis) distance between phosphorus atoms in each leaflet, calculating peak-to-peak distance of the bilayer density (mimics neutron scattering). Note, bilayer thickness is different from hydrophobic thickness which is normally refers to the average distance of the first carbon atoms in tails between each leaflet. Bilayer thickness can be measured by using X-ray, neutron scattering[18]. In addition, atomic force microscope (AFM) with supported lipid bilayer also can be used[232].

Order parameter refers to orientations of lipid tails. It is calculated by using equation 2.20, to mimic he deuterium - nuclear magnetic resonance (NMR) experiments[233]. A high value means the lipid is in an ordered phase, while a low value indicates that the lipid is disorder. There is a problem to obtain unsaturated lipid order parameters because it is not possible to compare the result when a double-bond is located with an experiment result. This problem was recently solved by Piggot[234]. Apart from NMR, a lipid order/disorder phase can be visualised by using AFM[232].

$$S = \frac{1}{2}\langle 3\cos^2\theta - 1\rangle \tag{2.20}$$

, where θ is an angle between bilayer axis (aka, z-axis) and chain segment vector (vector from C_n to C_{n+1}).

Bilayer Pressure Profile represents how forces are distributed in a lipid bilayer. It was first presented by Cantor[19] and later developed[235] before being applied to MS study [126,236]. The recently developments were done by Vanegas[237]. In brief, it uses the Irving-Kirkwood-Noll (IKN) procedure to compute 3D local stress tensor based on Hardy

stress ($\boldsymbol{\sigma}$) definition. The lateral pressure (P_L) is calculated by using equation 2.21 and 2.2. In addition, the bilayer tension (γ) is an integral of the lateral pressure along bilayer normal, equation 2.23.

$$P_{ij} = -\sigma_{ij} \tag{2.21}$$

$$P_L(z) = \frac{P_{xx}(z)+P_{yy}(z)}{2} - P_{zz}(z) \tag{2.22}$$

$$\gamma = -\int P_L(z)dz \tag{2.23}$$

2.5 Simulation methods

All simulations were performed by using GROMACS packages, version 4[238] for Chapter 3 and 4, and version 5[239] for Chapter 5. All-atom simulations were performed under CHARMM36 forcefield for protein [198] (later updated to CHARMM36m[163] in Chapter 5) and lipid [181,182]. CG-simulations were run using Martini2.2[200]. Periodic boundary conditions are applied in all three dimensions. CG and all-atom simulation parameters were set according to Table 2.1 and 2.2, respectively. All systems are neutral as described in the PMF and cut-off sub-section. Pictures are rendered by VMD[224] and Pymol[225].

Table 2.1 *CG-simulation parameters*

	GROMACS 4	**GROMACS 5**
integration time step	20 fs	
Cut-off scheme	Group	Verlet
Verlet buffer tolerance	-	0.005 kJ/mol/ps
neighbour list cut-off	1.3 nm	1.0 nm
coulomb type	Shift	reaction-field
coulomb modifier	Potential-shift-Verlet	
r coulomb	1.2 nm	1.2 nm
dielectric constant	20	15
Fourier grid space	-	
vdw type	Shift	cut-off
vdw modifier	Potential-shift-Verlet	
r vdw switch	0.9 nm	0 nm
r vdw	1.2 nm	1.1 nm
T coupling	Berendsen	V-rescale
T coupling period (τ_T)	1 ps	
Ref. Temp.	310K (POPC), 323K (DPPC, DMPC, DLPC)	
P coupling	Berendsen	Berendsen (equilibrium), Parrinello-Rahman (production)
P coupling Type	semi-isotropic	
compressibility	5×10^{-6} bar^{-1}	3×10^{-4} bar^{-1}
P coupling period (τ_P)	4 ps (Berendsen), 8 ps (Parrinello-Rahman)	
Ref. Pressure	1 bar in xy-plane, 1 bar in z-axis	
constrains	none	
constrain-algorithm	-	

Changes of these parameters are according to suggestion from official Martini forcefield website. Change in GROMACS version accompanies with change in lipid topology[203]*. This changes POPC representation from 13 beads into 12 beads.*

Table 2.2 *All-atom simulation parameters*

	GROMACS 4	**GROMACS 5**
integration time step	2 fs	
Cut-off scheme	Verlet	
Verlet buffer tolerance	0.005 kJ/mol/ps	
neighbour list cut-off	1.0 nm	1.2 nm
coulomb type	PME	
coulomb modifier	Potential-shift-Verlet	
r coulomb	1.0 nm	1.2 nm
dielectric constant	1	
Fourier grid space	0.12 nm^{-1}	
vdw type	cut-off	
vdw modifier	Potential-shift-Verlet	force-switch
r vdw switch	0 nm	1.0 nm
r vdw	1 nm	1.2 nm
T coupling	V-rescale	
T coupling period (τ_T)	0.1 ps	
Ref. Temp.	310K (POPC), 323K (DPPC, DMPC, DLPC)	
P coupling	Parrinello-Rahman	
P coupling Type	semi-isotropic	
compressibility	4.5×10^{-5} bar^{-1}	
P coupling period (τ_P)	1 ps	
Ref. Pressure	1 bar in xy-plane, 1 bar in z-axis	
constrains	all-bonds	h-bonds
constrain-algorithm	LINCS	

Changes are suggested by GROMACS 5 manual [240].

Chapter 3
MD simulations of TREK-2 in a bilayer

3.1 Introduction

Although MS channels have been studied for many decades, most of our knowledge is based on studies of bacterial MS channels such as MscL or MscS and the mechanisms underlying activation of eukaryotic MS channels is still unclear[98]. Two different structural models for stretch-activation of MS K_{2P} channels were suggested based on sets of TREK crystal structures[73,134,135]. However, these models conflicted with each other regarding the structural changes induced in response to increased membrane tension. One model suggests there is a 'down to up' structural transition whereas the another suggests an 'up to down' movement. There was also an additional model which suggested that these up/down movements influenced lipid accessibility to the pore and that direct lipid occlusion of the pore was the main mechanism of mechanogating[73]. This emphasised the difficulties involved in ion channel functional annotation when crystal structures are solved in the absence of their native bilayer environment. In this chapter, MD simulation has been used to investigate the influence of the lipid bilayer on TREK-2 stretch-activation using recently solved crystal structures of TREK-2[135] in different conformations. To examine the effect of membrane, tension the MscL membrane stretch protocol and hydrophobic mismatch concept were employed and adapted.

3.1.1 TREK-2 crystal structures

There are two conformations of TREK-2: the 'up' and the 'down' state[135]. The major difference between them is in the lower section of the TM2, TM3, and TM4 helices (**Figure 3.1**). In the down state (PDB ID: 4XDJ with a resolution of 3.8 Å), these helices project toward cytoplasm, whereas, in the up state (PDB ID: 4BW5 with a resolution of 3.2 Å), these helices move further up toward to the bilayer centre. These movements are consequences of the kink of TM4 with a hinge around a conserved glycine (G312) and hinges in TM2 at G201 and G206. In agreement with previous evidence[70] that the selectivity filter is accessible in both the open and closed states, the cytoplasmic entrance to the pore remains physically open in both conformations. In addition, lipid binding sites were also observed in these structures, (**Figure 3.1**).

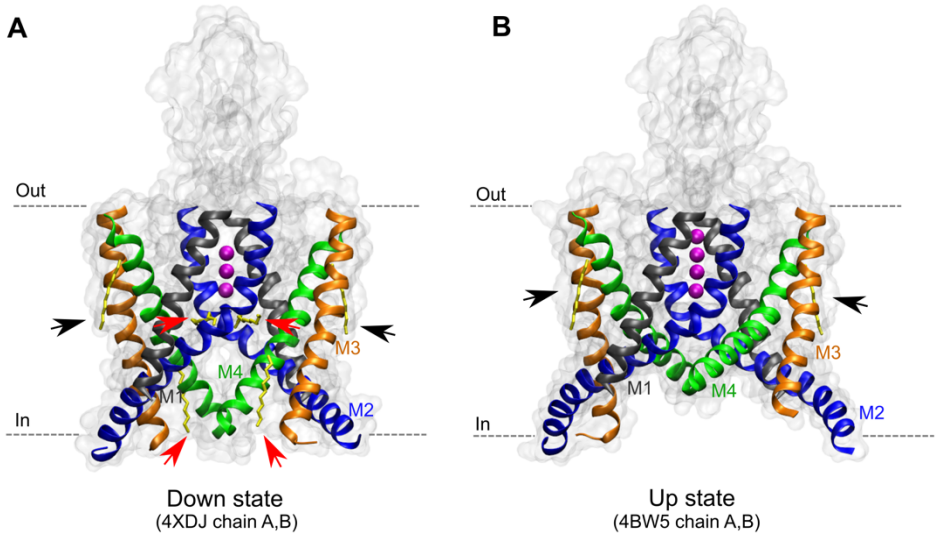


Figure 3.1 TREK-2 crystal structures. *The crystal structures of TREK-2 in (A) the down state (PDB id 4XDJ) and (B) the up state (4BW5). These two structures are quite similar; the major differences are in the lower section of the structure. In the down state, TM2, TM3 and TM4 project toward cytoplasm whereas, in the up state, they move upwards. In addition, there are three ions in down state and four ions in the up state suggesting different conductive states with the down state as the non-conductive state, and the up state the conductive state. There are lipid binding sites presented in the structures (arrows): 6 in the down state and 2 in the up state. The red arrows indicate the state dependent binding lipids. Some are present in the down state, but absent in the up state.*

3.1.2 TREK stretch-activation models

At the start of this current study in 2014, there were suggestions of three different stretch-activation models[73,134,135]. The Mackinnon group[73] solved the structure of TRAAK in two different states: conductive (an 'up' state) and non-conductive (a 'down' state). The conductivity of these two states was inferred by occupancy of K^+ ions in the selectivity filter: there were three ions in non-conductive state, whereas there were four ions in conductive state. Interestingly, in the non-conductive 'down' state, there was an existence of lipid-like densities in the inner cavity of the pore that physically blocked the ion conduction pathway. Based on these observations and additional electrophysiology studies, they suggested the 'down to up' structural transition for stretch-activation (**Figure 3.2A**). However, this model also suggests that it is the lipid tails which directly block the pore and that they access the pore through side cavities (fenestrations) which only exist when the channel is in the down state; in the up state, these fenestrations disappear because TM4 kinks upwards to seal the fenestration gap between TM2 and TM4. Interestingly, at the same time, the Minor group[134] also solved structures of TRAAK in the up state. However, they suggested an opposite model involving an 'up to down' transition (**Figure 3.2C**). This was based on the fact that they solved crystal structures of two mutant channels containing activatory mutations (W262S and G124I)[69] which were found to be in the down state. Shortly afterwards, Dong and *et al.*[135] presented crystal structures of TREK-2 in the same two conformations: the 'down' and the 'up' state and similar to the MacKinnon group proposed that the 'down' state represented a non-conductive state and the 'up' state a conductive conformation. Together with an additional data from electrophysiological studies and co-crystallisation with a state-dependent blocker (Fluoxetine, i.e. 'Prozac'), this study also suggested a 'down to up' mechanism of mechano-activation, however, it

also questioned the proposed role of lipids directly blocking the channel pore in the down state.

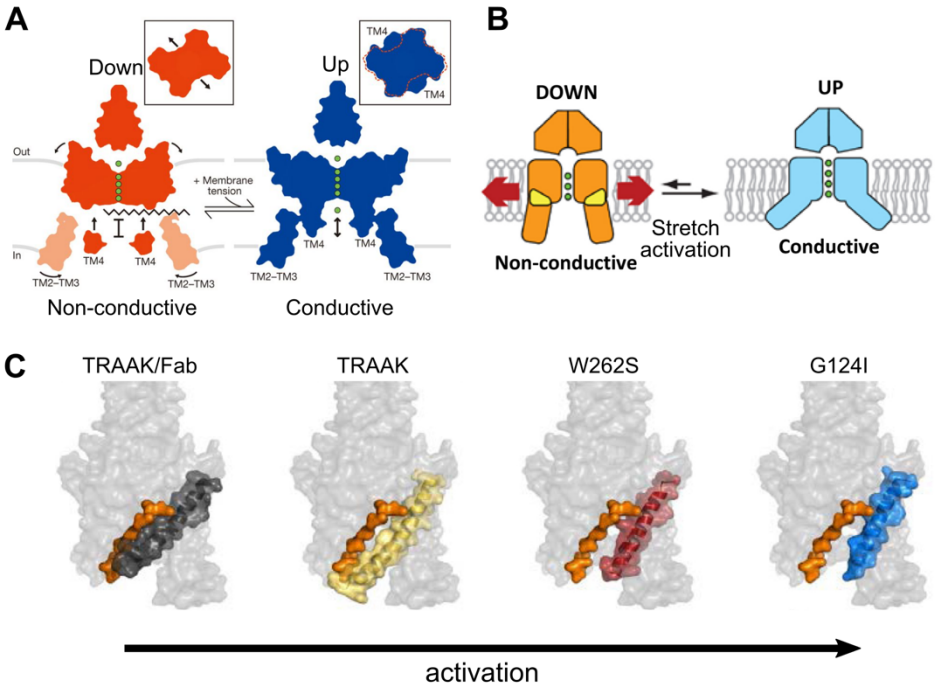


Figure 3.2 Stretch-activation models. *(A) The 'down to up' transition with lipids block model*[73]. *The model shows the kink of TM4 that make itself moves upward and seals the fenestration then therefore prohibiting lipid tails to entre and allowing ions move through the pathway. (B) The model of the 'down to up' transition with gating at selectivity filter*[135]. *The model suggests the 'down to up' transition in response to stretch and ions are gated at the selectivity filter. (C) The 'up to down' transition model*[134]. *The model shows the relation between the channel activation and the position of TM2 (orange) and TM4 (TRAAK/Fab: grey, TRAAK: yellow, W262S: pink, G124I: blue). Figures A and C are taken from*[73,134] *with Springer Nature permissions. Figure B is taken from*[135] *with permission from AAAS.*

3.1.3 The truncated TREK-2 crystal construct is mechanosensitive

The crystal structures of TREK-2 and TRAAK channels only contain the TM helices and the pore domains. The disordered C-terminal domain was truncated in these constructs to facilitate crystallisation and the structures solved are therefore truncated structures. However, functional studies of truncated TREK-1 and TRAAK proteins shows that they retain their mechanosensitivity when reconstituted into lipid bilayer[95]. In addition, the truncated TREK-2 (residue 67-340) used by Dong *et al*[135] for crystallisation also was mechanosensitive when either expressed in *Xenopus* oocytes [135] or when the purified protein was reconstituted into a lipid bilayer[241]. This meant that the truncated structure solved by crystallisation was suitable for studying the mechanism of mechanogating in MD simulations due to its intrinsic mechanosensitivity.

3.1.4 Aims

Although the availability of these crystal structures and the stretch-activation models they proposed represented an advance in our understanding of how mammalian MS channels work, these models ignored the potential contribution of their native environment, i.e. the lipid bilayer. In this chapter, the roles of lipid on stretch-activation were investigated using MD simulation and a multiscale approach. Systems of TREK-2 in a lipid bilayer were systematically simulated under member stretch. In addition, the effects of hydrophobic mismatch were studied by performing a set of simulations of TREK-2 in various bilayer thickness.

3.2 Computational methods

3.2.1 Modelling and MD simulation

The simulation model of the TREK-2 'down' state was taken from chain A and B of the 4XDJ structure[135] (with a resolution of 3.8 Å) and the missing residues completed (Chain A: S150-S154, F226-Q230; Chain B: N149-S154, R227-V231, N292-Y295) using the data from chain C and D. The MODELLER program[242] was also used to model the remaining missing parts (S150-S154). The TREK-2 'up' state (PDB id: 4BW5) was completed using the same protocol. A system of TREK-2/bilayer consisting of a TREK-2 embedded in POPC bilayer was initially created by performing a 100 ns CG simulation of bilayer self-assembly with Martini2.2 forcefield[200]. During this process, the protein was subject to backbone positional restraints with a harmonic force constant of 1,000 kJ $mol^{-1}nm^{-2}$. In addition, in all CG-simulations, an elastic network with harmonic force constant of 1,000 kJ mol^{-1} nm^{-2} was applied to protein atom pairs of distances 5 to 7 Å to keep the stability of the protein secondary structure[243]. The CG production run was 900 ns. Then, the system was converted into an all-atom system using CG2AT[159]. The all-atom system contained TREK-2 with 240 lipids (122, 119 molecules in upper and lower leaflet, respectively), ~25,000 TIP3P water molecules and 150 mM KCl.

All simulations in this chapter were performed using GROMACS 4[238] with the parameters shown in Table 2.1 and 2.2. The simulation is at least 100ns of each system. In brief, all-atom simulations were carried in NPT ensemble with temperature set to 310 K. The pressure was semi-isotropic with 1 bar in the x-y plane and the z-directions. The temperature and pressure coupling are v-rescale thermostat[153] and Parrinello-Rahman barostat[154]. The electrostatic interaction was treated using PME[149]. The Charmm36 forcefield[198] was used. Simulations were repeated with different random velocities.

3.2.2 The development of stretch protocol

To investigate the influences of membrane-stretch on TREK-2, the stretch protocol was adapted from MscL simulation studies[139,140]. However, because MscL gates at higher pressures (near membrane-lytic tensions) compared to TREK-2 which is gated open at lower pressures, the amount of applied pressure had to be adjusted. This was done by performing a series of 1 μs CG simulations with various applied negative pressures in the x-y plane. In other words, pressure in x-y plane were set to -80, -65, -50, -20, and -5 bar; the pressure in the z-direction was 1 bar in all simulation. During stretch simulations, the protein elastic network was modified and used only the network that was present in both the up and the down state. This was to ensure that protein was able to move between these two states. The lowest pressure with the following criteria was chosen: (i) retention of lipid bilayer structure, (ii) TREK-2 shows significant structural movement, (iii) the movement occurs in an acceptable timescale (i.e. ~100ns) and (iv) no PBC problem presented in the simulation with a given size of simulation box. Therefore, see section 3.3.1, pressures of -50 bar and lower were chosen and applied in all-atom simulations. In addition, a similar system containing TWIK-1 (PDB id 3UKM), a non-MS K_{2P} channel, in POPC bilayer was also simulated using the same method. In parallel to section 3.2.3, my colleague, Dr Prafulla Aryal performed a set of all-atom simulations including simulations at -30, -20, and -5 bar. The results of these simulations were analysed by both of us.

3.2.3 The influence of hydrophobic mismatch

The influence of hydrophobic mismatch is well established in MscL[115], whereas its role in TREK channels was still unknown. The simulations of a TREK-2 in thin bilayer were preformed to investigate this influence. First, the CG-systems were built and simulated to observe whether they show any structural transition signals. The candidate bilayers (in order of decreasing thickness) were DSPC (18-21:0), POPC (~16:0, ~18:1), DPPC (15-18:0), DLPC (12-15:0), and DHPC (8-11:0) bilayer. The systems were prepared by lipid-exchange, using an in-house script that adds/removes beads in the lipid tails. Then 1 μs simulations were performed using the parameters in Table 2.1. After structural changes were observed (section 3.3.4) all-atom simulations of DMPC (14:0) and DLPC (12:0) systems were prepared. Note, CG-DLPC can be mapped into both of AT-DLPC and AT-DMPC. The all-atom initial coordinates were generated using CHARMM-GUI[244–247] and performed at 323 K to maintain bilayer fluidity. The simulations were run for 500 ns and repeated with random velocities. Note, at the time this was done, CG2AT did not support other CHARMM lipids apart from POPC. Currently, a more efficient way is to perform CG simulation than convert it to all-atom using either CG2AT[159] or the Backward protocol[160].

3.3 CG-simulation of TREK-2 in a lipid bilayer

The modelled TREK-2 channel contained a total of 521 amino acids and is not considered a big protein, however it includes a large extracellular 'cap' domain. The stretch protocol used was expected to result in an expansion in the xy-plane and a contraction in z-direction of the simulation box. This therefore required use of a large simulation box in the z-direction that contains more water than usual thus resulting in an expensive computational cost. Therefore, the simulations of TREK-2 in a lipid bilayer were initially performed in CG. In these simulations, with a system of the same size, CG simulation performance achieved ~1 μs/day whereas, all-atom simulation performance was only ~10 ns/day. The aims of performing CG simulations were to serve as a quick test for a stretch protocol for TREK-2, and to exam whether hydrophobic mismatch had any influence on the movement of TREK-2. This was done because a previous study[127] showed that MscL was affected by bilayer thickness, whereas MscS was not. I therefore wished to investigate any possible effects of bilayer thickness using CG simulations before performing long (computationally expensive) all-atom simulations.

3.3.1 Development of stretch protocol

The series of CG simulations with various applied negative pressures were performed. Note, according to equation 2.22 and 2.23, a negative pressure in xy-plane will result in a positive bilayer tension. The simulation study of MscL[140] required -100 bar to open the MscL in the bilayer. Negative pressures of -80 (P-80), -65 (P-65), -50 (P-50) were therefore initially tested, then -20 (P-20) and -5 (P-5) later added to investigate TREK-2 behaviour at much lower tensions. The snapshots of P-80, P-65, and P-50 are shown in **Figure 3.3**. In all three system, the structural movement of TREK-2 was clearly observed within 100 ns. However, in P-80, the lipids were unable to retain their bilayer structure, and deformed into a 2D-micelle. In contrast, the bilayer structure was not

affected in P-65 and P-50. At this point, P-50 was chosen and later used in all-atom simulations. The P-20 and P-5 protocols also showed movement of TM2 and TM3, but this was relatively small compared to the movements caused by P-50 (**Figure 3.4**). As a control, the same P-50 protocol was also applied to the related, but non-MS TWIK-1 channel. However, it showed no structural changes (**Figure 3.4**). This implied that the structural changes observed during the simulations were unique for MS K_{2P} channels.

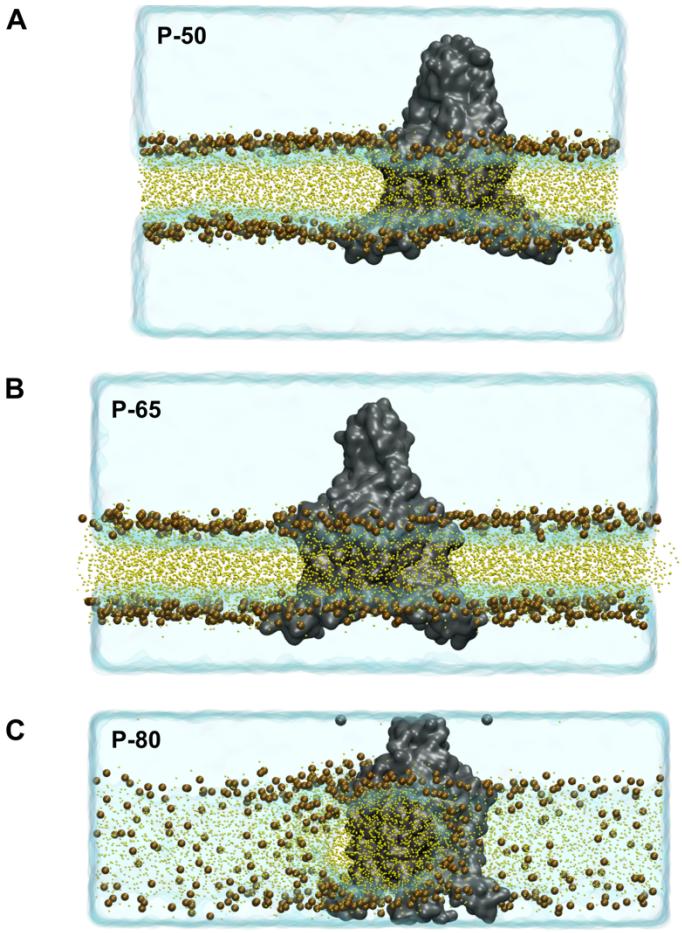


Figure 3.3 The CG-system in various applied tension. *The structural transition of TREK-2 were clearly observed in these three applied pressures: (A) P-50 (B) P-65 and (C)P-80. However, only P-50 and P-65 were able to remain its bilayer structure. The P-80 caused the bilayer deformation into 2D micelle.*

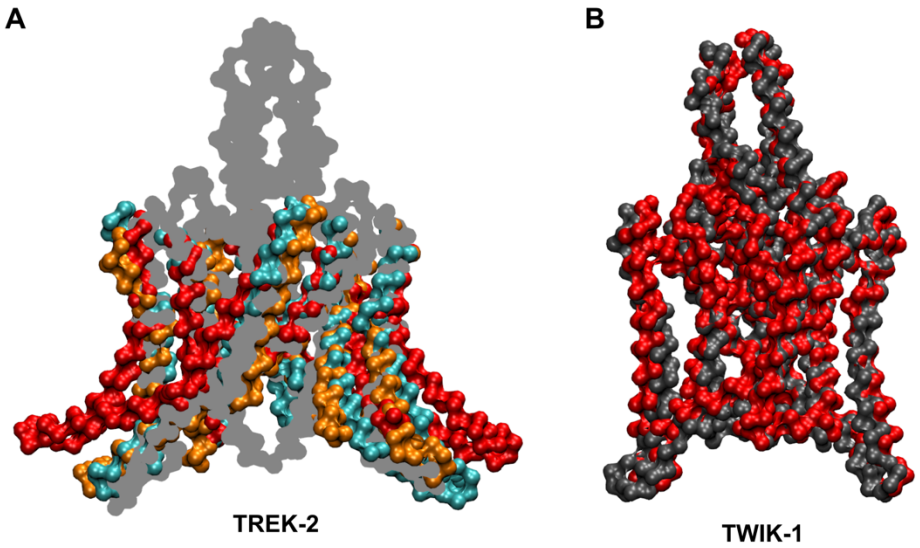


Figure 3.4 An alignment of CG-TREK-2 and CG-TWIK when subjected to tension. *(A) CG-TREK-2 in P-5 (cyan), P-20 (orange) and P-50 (red). The grey shadow indicates the 'down' state. The P-50 protocol clearly drives structural movement of TREK-2. The P-20 and P-5 protocols also produced a movement of TM2 and TM3, but much smaller to the one caused by P-50. (B) TWIK-1 in no-stretch (grey) and stretch with P-50 (red). No significant difference was observed between these two situations.*

3.3.2 Lipids in the fenestration of TREK-2

During the bilayer self-assembly process which the TREK-2 were subjected to backbone restraints, there were two lipids moving into the fenestration in the down state (**Figure 3.5**). This behaviour of the lipids was examined to see if it was an artefact from bilayer self-assembly by removing the lipids and then performing the simulation when the bilayer was formed. The lipids indeed entered at the gap formed between the TM2 and TM4 helices (i.e. the side fenestrations). These lipids only entered in the down state and were stable during the production run. However, without positional restraints applied on the protein (i.e. when the protein was allowed to move) no lipids entered the fenestrations. This suggested that the presence of these lipid may be an artefact resulting from the restrained protein movement. This behaviour was further investigated later in all-atom simulations, see section 3.4.4.

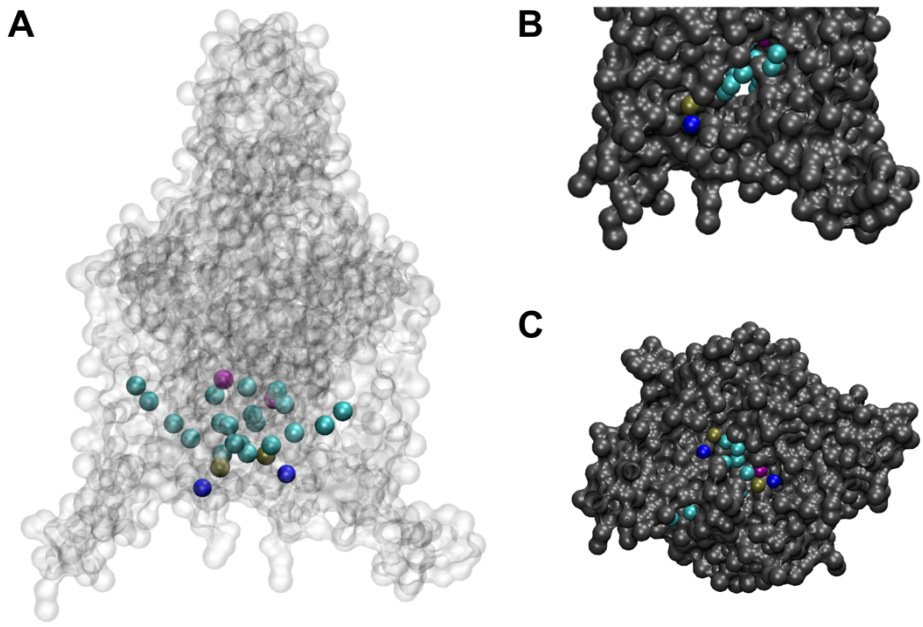


***Figure 3.5 Lipids in the CG-TREK-2 fenestration**. (A) Two lipids (represented as spheres) were found in the fenestration; the protein is shown in ghost. (B) Side view and (C) bottom view; the lipids are represented in spheres and the protein as grey surface.*

3.3.3 Lipid penetrations during stretch simulation

Since we observed lipids in the fenestration that may correspond to the Mackinnon model of mechano-activation i.e. direct occlusion of the pore by lipid tails[73], the behaviour of these lipids under stretch was studied in more detail. The last frame of the TREK-2 down state in a POPC bilayer production run was used as a starting point of another CG stretch simulation. Pressures of -5, -20, and –50 bar were applied using the protocols described in section 3.2.2. These CG-simulations showed that although pressures of –20 and –50 were able to drive structural changes in the TREK-2 down state, only –50 bar was able drive the lipids out of the fenestration, however, this required more than 0.5 μs to occur (**Figure 3.6**).

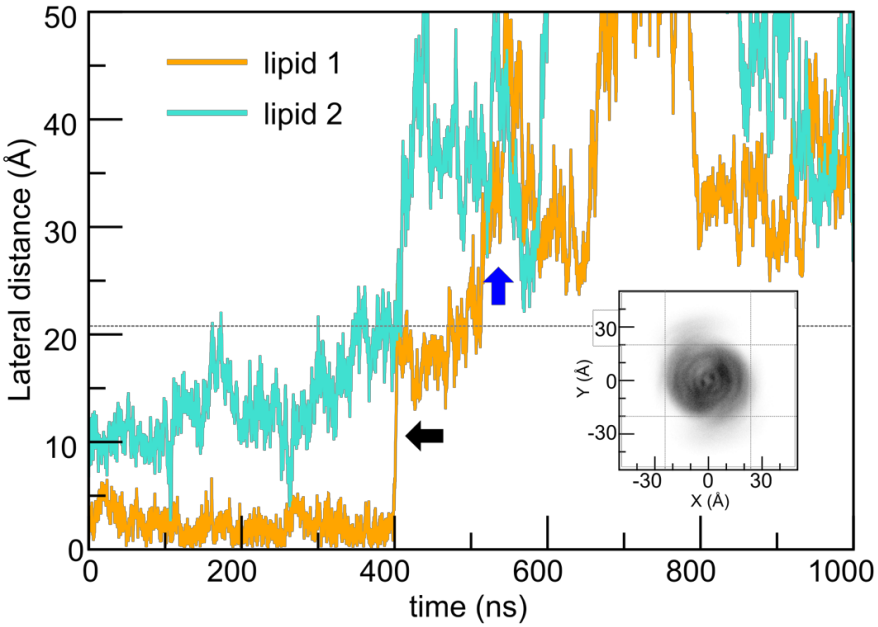


Figure 3.6 Lipid penetration during the stretch simulation*. The figure shows the lateral distance (i.e. distance in xy-plane) between the penetrated lipids and protein centre of mass. The dash line indicates protein radius from its centre of mass. Initially, the lipids were located in the centre of the protein and then were driven out by the applied pressure of –50 bar. They started to move ~400ns (black arrow) and were completely moved out at ~500 ns (blue arrow). The inset is a protein density indicating that the protein core excluding the TM2-TM3 tip has ~20 Å radius.*

3.3.4 Hydrophobic mismatch effects on TREK-2

To investigate the influence of hydrophobic mismatch on TREK-2, CG-simulations of a TREK-2 in DSPC (18-21:0), POPC (15-18:0, ~18:1), DPPC (15-18:0), DLPC (12-15:0), and DHPC (8-11:0) bilayer were performed. The influence of the protein itself was first invested by restricting movement of protein with positional restraints. **Figure 3.7** shows the resulting bilayer deformation caused by the rigid protein (i.e. protein with backbone positional restraints). When the protein was in the down state, both DHPC and DLPC had extension deformation around the protein, whereas DSPC had compression deformation. There was no deformation of the bilayer produced by POPC and DPPC since their hydrophobic heights are about the same as the hydrophobic length of the down state protein. For the up state, bilayer deformation in the thinnest DHPC still remained, whereas it was decreased in DLPC. In contrast, the compression

deformation in DSPC was even more increased. There was no significant change in POPC and DPPC bilayer deformation.

After the protein was allowed to move (by removal of backbone restraints), significant structural movements were only seen when it was embedded in DLPC and DSPC, however these did not represent full down/up transitions and were in opposite directions (**Figure 3.8**). Note, the elastic network of the TREK-2 up state was modified in the same way as described in section 3.2.2 to allow the up to down state transition. The TM2, TM3 and TM4 helices of the down state in the DLPC bilayer all moved further towards the membrane, whereas these helices in the up state in the DSPC bilayer moved down to the cytoplasm. This implied that hydrophobic mismatch has the potential to play a role in the energetics of the structural transitions that occur in TREK-2 in response to membrane stretch.

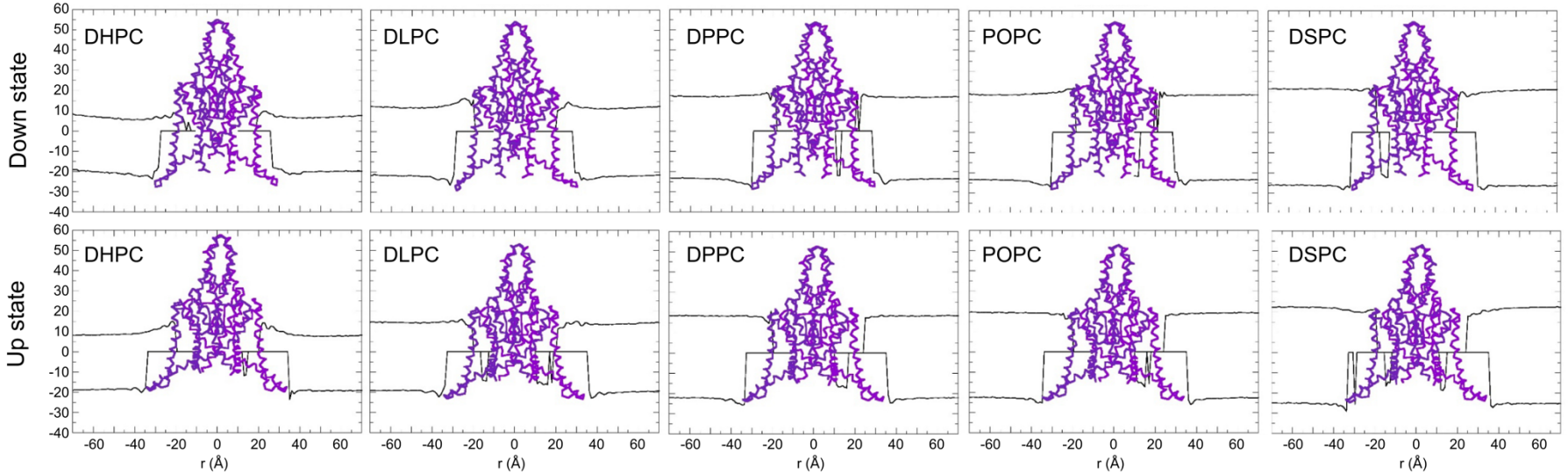


Figure 3.7 Bilayer distortion caused by hydrophobic mismatch. *This figure shows the bilayer extension deformation (i.e. bilayer thickness increase about the protein) in DHPC and DLPC surrounding the TREK-2 down state. This deformation of DLPC decreased when TREK-2 was in the up state. The compression deformation (i.e. bilayer thickness decrease about the protein) was shown in the DSPC bilayer when surrounding the TREK-2 up state. This deformation of DSPC decreased when TREK-2 was in the down state. There was no significant bilayer deformation for DPPC and POPC because their hydrophobic height more closely matches TREK-2.*

Table 3.1 *CG- Bilayer thickness*

Bilayer	Down state		Up state	
	Other (Å)	Around protein (Å)	Other (Å)	Around protein (Å)
DHPC	26	32	27	35
DLPC	36	39	34	36
DPPC	40	44	41	42
POPC	42	46	42	44
DSPC	48	48	48	46

These values are approximated.

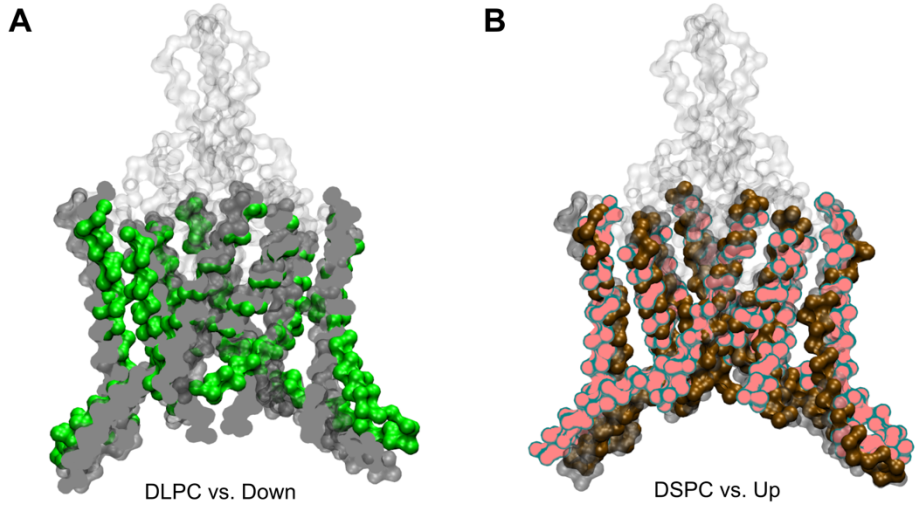


Figure 3.8 Structural changes caused by hydrophobic mismatch. *The figure shows the structural alignment of TREK-2 in (A) DLPC and (B) DSPC bilayer. (A) TREK-2 in DLPC bilayer (green) compared with the TREK-2 down state (grey shadow) and TREK-2 in POPC (black transparent). TREK-2 in a DLPC bilayer shows the significant movement in the position of the TM2-TM3 tip, whereas TM4 has the same position as when it was in POPC bilayer. (B) TREK-2 in a DSPC bilayer (brown) compared with the TREK-2 up state (red shadow). This shows a small downward movement TM2, TM3 and TM4.*

3.3.5 Changes in the lateral pressure profile of the lipid bilayer

When proteins are embedded in lipid bilayers, they are subjected to a variety of forces that change when the membrane is stretched. Lateral pressure profiles (LPPs) of various lipid bilayers were therefore calculated using the method developed by Vanegas[237] with 1 Å grid size and averaged over last 4,000 frames (800 ns) of the CG-simulations. In general, a symmetric bilayer results in symmetric LPP along the bilayer normal (z-axis), **Figure 3.9**. There are four main parts within this profile formed by water, the charged headgroup, the lipid-water interface and the lipid tails. Theoretically, the balance of all these interactions makes the profile in the water region equal to 0. Therefore, this region was used as an indicator of whether the LPPs were calculated using enough sampling frames. The LPPs are shown in **Figure 3.9** where the decrease in positive pressures within the bilayer core (lipid tail) occurred with increasing bilayer tension, whereas changes in acyl chain length resulted in a shift in the peak to peak distance, but no other significant changes in terms of amplitude.

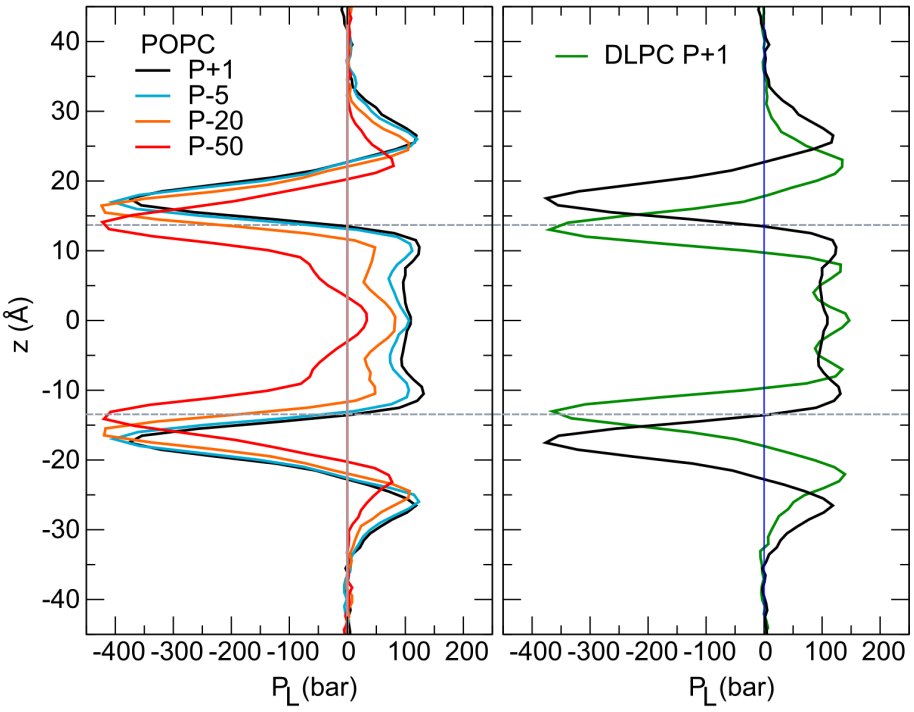


Figure 3.9 Lateral pressure profiles of lipid bilayers. *Lateral pressure profiles (P_L) in an absence of protein in a POPC bilayer with various applied pressures (left) and a thinner bilayer (right). An increase in pressure results in a negative shift of the overall profile. The major change is a decrease in the positive pressure at the bilayer core. A small decrease in peak-peak distance indicates decrease in a bilayer thickness. The dashed line is a guideline to compare the POPC bilayer with P-50 and DLPC bilayer, because they both had the same thickness. The change in hydrophobic length in the DLPC bilayer only shifts the peak-peak distance. The magnitude of P_L was still the same.*

3.4 Behaviour of TREK-2 in a stretched bilayer

Although these CG simulations show that structural movement of TREK-2 occurs when the membrane is stretched and in bilayers of different thickness, they do not provide much additional insight due to the lack of atomistic detail. Therefore, to improve understanding about these transitions, all-atom systems of the TREK-2 down state in a bilayer with the applied pressures of –50, -30, -20, -5 and +1 bar were performed for at least 100 ns using the protocols described in section 3.2.2. As a control, simulations of the non-MS channel TWIK-1, and TREK-2 in the up state were also run using the same P-50 protocol. From this point onwards, the results from all-atom simulations using CHARMM36 forcefields are shown and discussed. We found that the bilayer thickness

of POPC bilayers with stretch protocols of P+1, P-5, P-20, P-30, and P-50 were ~39.2, ~37.9, ~35.6, ~33.5, and ~30.1 Å, respectively. Also, we found that stretch increased the area per lipid by ~1x, ~1.1x, ~1.2x, and ~1.35x for the P-5, P-20, P-30, and P-50 protocols, respectively. Note, all the work in this section (3.4) was performed and analysed jointly by me and my PDRA supervisor, Dr Prafulla Aryal.

3.4.1 TREK-2 move from the 'Down' state to the 'Up' state in response to stretch

The RMSDs of Cα atoms for the TM helices were computed to determine whether the changes observed during these simulations were the 'down to up' transition. The RMSDs were computed using the crystal structures of the down and the up state as the reference structures and are shown in **Figure 3.10A**. These revealed that during the no-stretch (P+1) simulation, TREK-2 remained closer to the down state, whereas it significantly moved away from the down state and simultaneously went closer to the up state when it was subjected to a pressure of -50 bar (P-50). This transition occurred within ~100 ns at P-50. However, it was also seen with the P-20 protocol, but occurred much more slowly within ~500 ns. In addition, we observed that the up state structure was stable when subjected to P-50 protocol (**Figure 3.10B**) i.e. no further movement occurred. Moreover, there was no significant structural movement in the non-MS TWIK-1 channel, even with the P-50 (**Figure 3.11**) suggesting that effects on TREK-2 were specific.

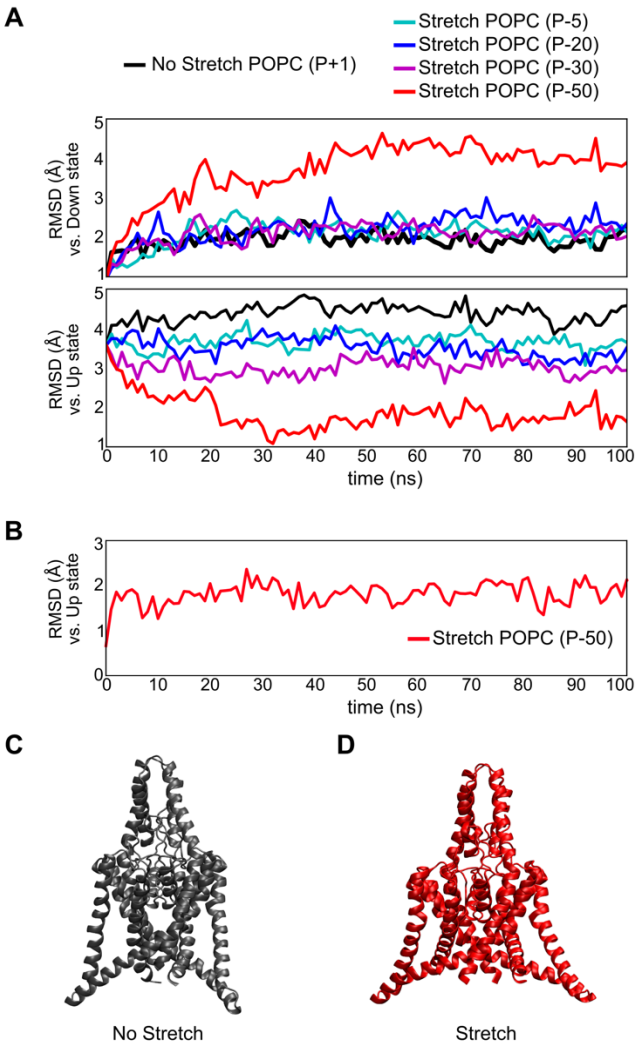


Figure 3.10 TREK-2 move from the 'Down' state to the 'Up' state. *(A) Cα-RMSD of the TREK-2 down state trajectories compared with the down state and the up state. Only the TREK-2 under P-50 showed a significant 'down to up' structural transition. It moved away from the down state and closer to the up state. (B) Cα-RMSD of the TREK-2 up state with P-50 compared with the up state. The TREK-2 up state was stable with ~2 Å RMSD which is about the same value as the down state RMSD was in P+1. (D-E) A snapshot of TREK-2 at 100 ns in (D) no-stretch and (E) stretch bilayer. The figure is adapted from*[241].

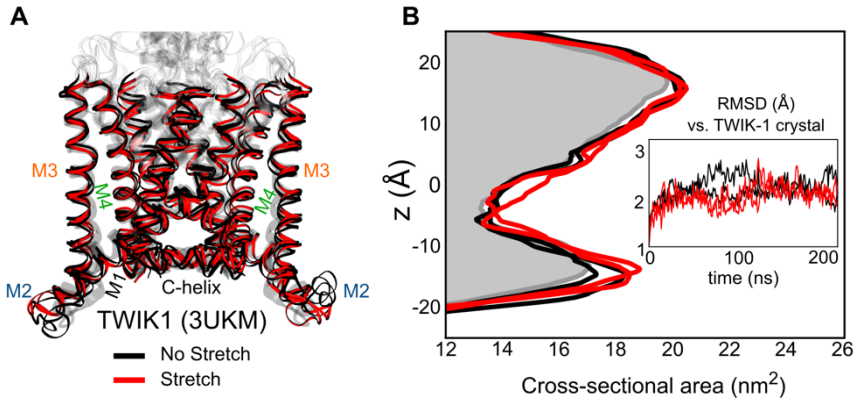


Figure 3.11 Lack of structural changes in the non-mechanosensitive TWIK-1*. (A) Alignment of the TWIK-1 in no-stretch and stretch bilayer. (B) Cross-sectional area of TWIK-1 in no-stretch and stretch simulation. An inset is Cα-RMSD of the TWIK-1 trajectories compared with the initial crystal structure. These indicate that there is no significant change in the structure of TWIK-1. The figure is adapted from*[241].

3.4.2 The down to up structural transition

In response to membrane stretch, TREK-2 moved from the down to the up state. This transition occurred via several discrete changes (**Figure 3.12**). They are (i) the bow-like TM2 tilt angle increases by 10º, (ii) the distance between the tip of TM2-TM3 (F226-F226 distance) increases ~10 Å, (iii) TREK-2 twists with an additional 8º twist in TM2 and 10º twist in TM4, (iv) an increase in the size of the inner pore, (v) TM4 kinks ~20º about the conserved glycine hinge (G312), and (vi) the fenestration closes (i.e. decrease in the P198-G324 distance).

As shown in **Figure 3.13**, these changes mainly occur in the lower section of the protein which result in an increase in cross-sectional area of ~4-5 nm^2. The expansion is in agreement with the changes seen by comparing the crystal structures, and by functional studies which predicted an estimated change in cross-sectional area of ~4-5 nm^2 within the membrane[248]. The rigidity of the upper part is also a likely consequence of the fact that TREK-2 has to maintain the integrity of its K^+ selective filter which is located in the upper half of the protein.

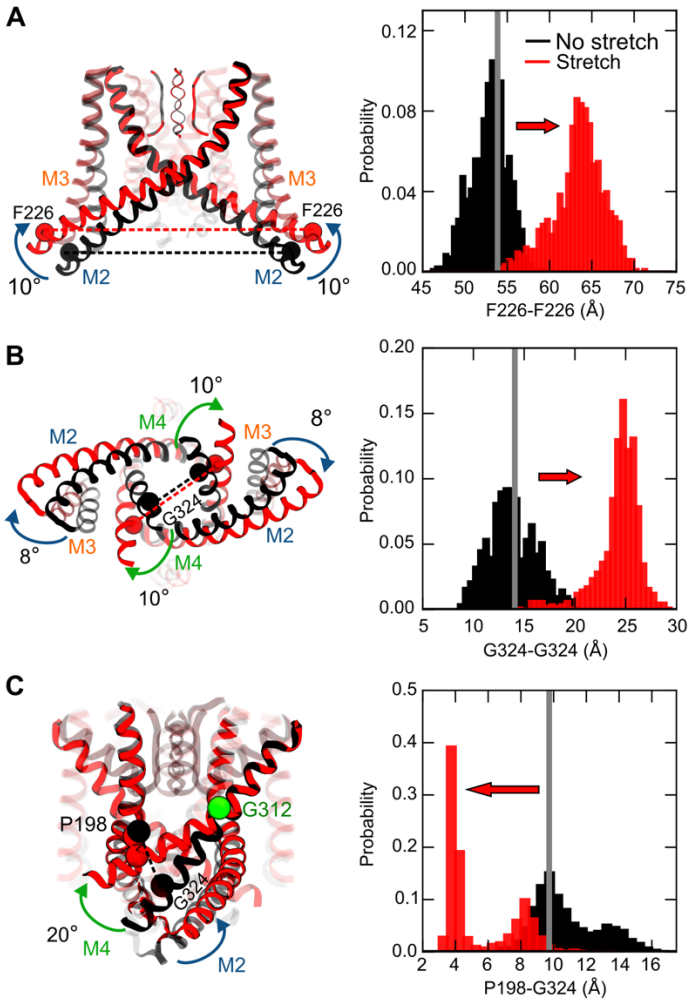


Figure 3.12 Changes in TERK-2 structure during the stretch simulation. *Left: graphical presentations of changes during stretch simulation, black: no-stretch red: stretch. Right: Distribution of a given distance during stretched (red) and unstretched simulations (black). The vertical grey lines indicate the distances in the down state. The histograms were sampled every 1 ns. (A) Stretch increases the tilt angle of the bow-like TM2 helices by 10° and also increases the distance between F226 residues between two subunits by >10 Å. (B) The bottom view of the channel shows an additional 8° twist in M2 (blue arrow) and 10° twist in M4 (green arrow). The distance between G324 residues on M4 also increased as shown in the distributions. (C) The side view shows that membrane stretch caused the 20° kink at the conserved glycine hinge (G312; green dot) in TM4. The subsequent movement of TM4 towards M2 closes and seals the side fenestration. Distance distributions show closure of the fenestration upon membrane stretch (measured between G324 on M4 and P198 on M2 of the adjacent chain). The figure is reused from*[241].

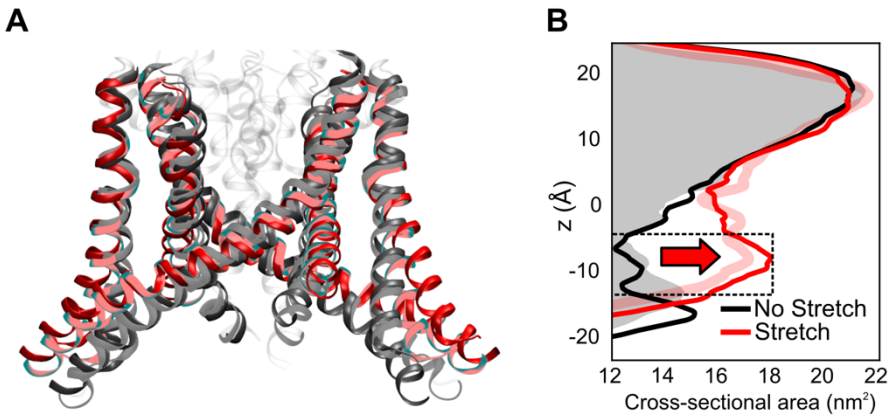


Figure 3.13 The TREK-2 structural alignment and cross-sectional area. *(A) an alignment of the TREK-2 no-stretch (black), the TRKE-2 stretch (red), the down state (grey shadow) and the up state (red shadow) shows that the TREK-2 no-stretch is closer to the down state, whereas the TREK-2 stretch is closer to the up state. (B) The structural movement from the down to the up-like state made a cross-sectional area increases by 4-5 nm^2 in response to membrane stretch.*

3.4.3 Rearrangement of TM2, TM3, and TM4 underlie the stretch-induced structural movements

The structural change from the down to the up state during simulation involves major changes in the lower section of the TM2, TM3, and TM4 helices which reorganise themselves in response to bilayer stretch. To understand these complex rearrangements, three distances representing these interactions were defined. There were (i) the "fenestration" distance between G324 and P198 in another subunit, (ii) the "Zipper" distance W326 to R237, and (iii) the "Expansion" distance between M322 and G212 (**Figure 3.14**). The result of these changes is shown in **Figure 3.15**. First, TM3 and TM4 have to "unzip" (i.e. an increase in W326-R237 distance). This unzipping then allows the expansion between TM4 and TM2 and reorientation of F244. Finally, the lower section of TM4 moves up to seal the fenestrations. Repeated simulations indicated these movement for the two subunits were independent and stochastic (i.e. there is no relation between the subunits).

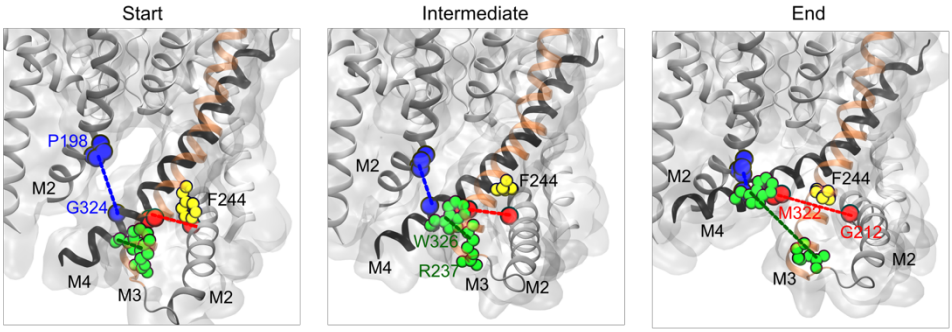


Figure 3.14 Movement of the lower section of the TMs. *The three distances were defined to understand the sequential movement of TM2, TM3, and TM4. They were (i) the "fenestration" distance between G324 and P198 in another subunit (blue), (ii) the "Zipper" distance between W326 to R237 (green), and (iii) the "Expansion" distance between M322 and G212 (red). The F244 residue is shown as a yellow sphere. The figure is reused from* [241].

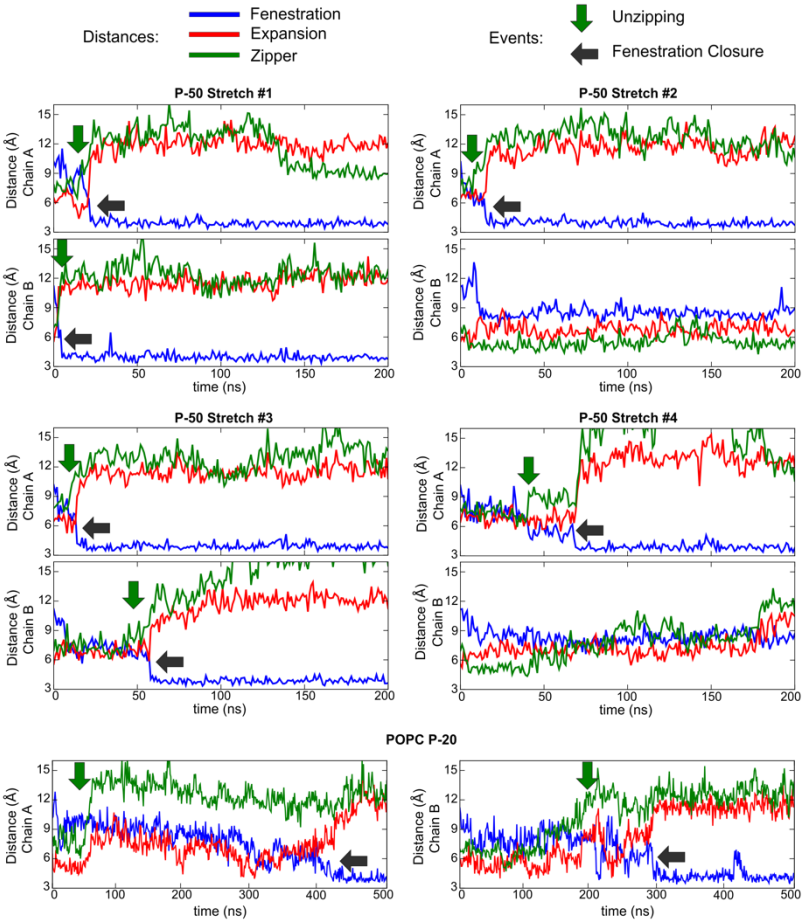


Figure 3.15 Sequential movement of the TMs. *This figure shows changes in the fenestration (blue), expansion (red) and zipper (green) distances over time for the 4 stretch simulations at -50 bar and a stretch simulation of -20 in a POPC bilayer. Profiles for both chains A and B within each TREK-2 channel are shown. Green arrows indicate the 'unzipping' event of the interactions. The black arrows indicate full closure of the fenestration. All repeats show that 'unzipping' always occurs first then the expansion and end up with the closure of the fenestration. The figure is adapted from*[241].

3.4.4 Effects of stretch on selectivity filter and the inner pore cavity

Although there were no major changes in the upper part of protein, some changes in ion occupancy were observed during the stretch simulation (**Figure 3.16 & 3.17**). There was a transition between S1 and S0 sites in the no-stretch simulations whereas in the stretch simulations, ion occupancy decreased at S0 site, and increased at S1 site. During the no-stretch simulations (2 of 4 repeats), there was also penetration of lipid tails into the fenestration which caused partial dehydration of the cavity. These lipid penetration events did not occur in the stretch simulations. These demonstrate that membrane stretch affects ion occupancy of the selectivity filter and also hydration of the inner pore. However, I found that the structure of selectivity filter remained relatively stable during the stretch simulations (**Figure 3.18**). The average Cα-RMSD of the selectivity filter (P1: TIGYGN; P2: TVGFGD) with and without membrane stretch is 0.586 ± 0.265 Å and 0.517 ± 0.112 Å, respectively. These indicate that this part of the protein maintained its initial structure and there was no significant effect caused by membrane stretch on the backbone structure of the selectivity filter.

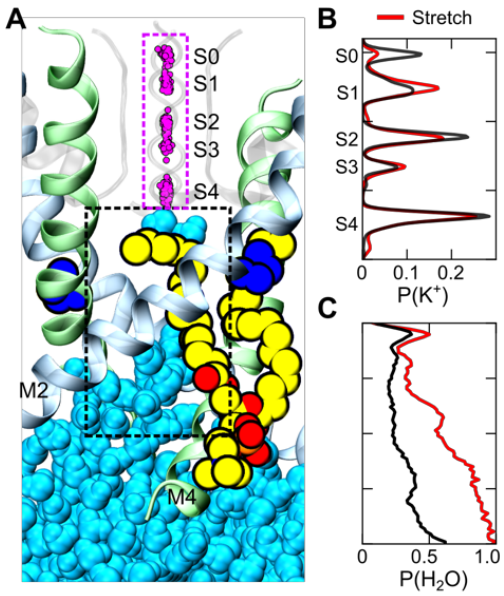


Figure 3.16 Ions-water occupancy in the selectivity filter. *(A) a snapshot of a selectivity filter and the cavity during a no-stretch simulation. The multi-frame of ions within S0-S4 binding site are shown in the small purple spheres. The lipid is shown in yellow; red spheres are oxygen atoms. As shown in this figure (and also figure 3.17), there is a POPC lipid tail penetration into the protein fenestration. This does not occur in the stretch simulation. (B) Ion occupancies at S0-S4 binding site calculated by counting the number of ions then normalised and fit with kernel density (Gaussian distribution). It shows changes in S0 and S1 site occupancy caused by membrane stretch. (C) Water density in the cavity (0 means no water and 1 means bulk water). Membrane stretch increases water occupancy in the cavity. The figure is adapted from*[241].

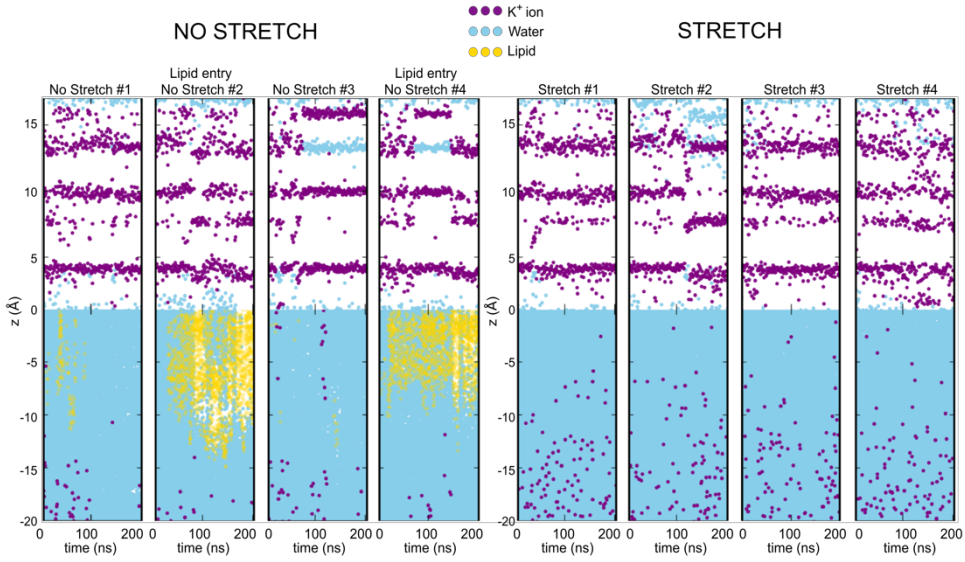


Figure 3.17 The selectivity filter and the cavity during simulations. *This figure shows K^+ ions(purple), water (cyan), and lipid tails (yellow) in the selectivity filter and the lower cavity during the no-stretch and stretch simulations. In 2 of 4 no stretch simulations, there was a lipid penetration into the protein cavity and subsequent dehydration. This does not occur in the stretch simulations. The figure is reused from* [241].

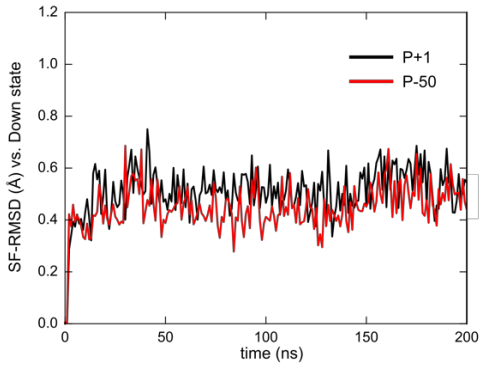


Figure 3.18 The selectivity filter is relatively stable during the stretch. *The Cα-RMSD of the selectivity filter (P1: TIGYGN; P2: TVGFGD). There is no significant different between the no-stretch (P+1, black) and stretch (P-50, red) simulations. In both cases, the filter was stable with ~0.5 Å difference from the initial down state structure.*

3.5 Effect of hydrophobic mismatch on TREK-2

In my previous CG simulations, the DLPC bilayer has the ability to drive the down to up structural change in TREK-2. Hence, this was further investigated in an all-atom simulation. In CG, the DLPC lipid is able to map onto both all-atom DMPC (14:0) and DLPC (12:0). Thus, all-atom simulations of TREK-2 embedded in both DMPC and DLPC bilayer were performed using the protocol described in section 3.2.3. These simulations were performed for 500ns. The DMPC and DLPC bilayer thicknesses are ~35 Å and ~31 Å, respectively.

3.5.1 A thin bilayer does not drive the down to up transition *per se*

The structural change of TREK-2 when embedded in the DMPC and DLPC bilayer was observed during the simulation. However, Cα-RMSD of the TM helices compared with the up state (**Figure 3.19**) indicated that, in this case, the protein did not move toward the up state. The Cα-RMSD of TREK-2 embedded in the DMPC bilayer, remained stable (~3 Å and ~4 Å) compared to the down state and the up state, respectively. In contrast, the Cα-RMSD of TREK-2 in DLPC continuously increased over time in both cases (**Figure 3.19**). This indicates that a thinner bilayer by itself is unable to drive

movement of TREK-2 from the down state to the up state. Moreover, the DLPC bilayer drives the protein into new conformations which are neither the down and the up state.

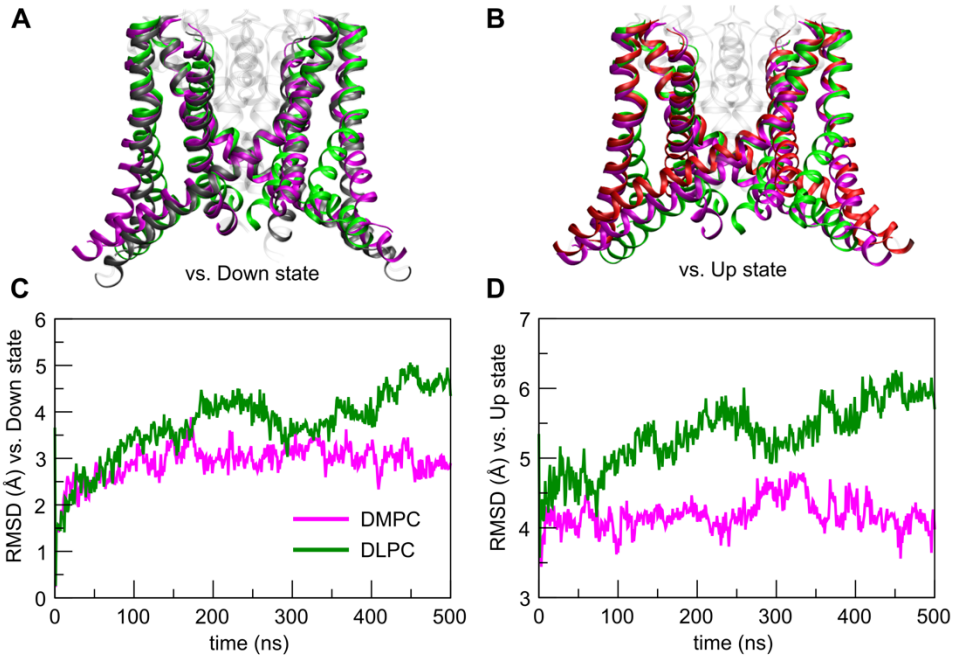


Figure 3.19 TREK-2 in thin bilayer during the simulation. *(A-B) Alignments of TREK-2 in DMPC (magenta) and DLPC (green) with (A) the down state (black) and (B) the up state (red). (C-D) The Cα-RMSD of the TM helices compared with (C) the down state and (D) the up state. The thinner bilayers drive TREK-2 into the new conformations which are not neither the down and the up state. These indicate that a thinner bilayer by itself does not drive the TREK-2 down to up transition. The DLPC bilayer has more influence compared to the DMPC bilayer.*

3.5.2 Hydrophobic mismatch and structural rearrangements

Although the down to up structural transition cannot be observed during simulation of TREK-2 in DLPC, the movements in this thinner bilayer were analysed using the previously defined distances (fenestration, expansion, and zipper). During the 500 ns, in both of DMPC and DLPC, there was no neither an 'unzipping' event nor any expansion during the simulations (**Figure 3.20**). The TREK-2 chain A showed some potential of 'unzipping', but the simulation was not extended beyond 500 ns (~5 weeks wall-clock computational time). Structurally, TREK-2 appeared more stable in the DMPC bilayer than in the DLPC bilayer since the Cα-RMSD continuously increased when in DLPC implying that DLPC simulation was not fully converged. However, it is

not worth to extend this simulation until it was equilibrated because the RMSD clearly demonstrated that opposite motion of the protein. In this case, other options are accelerated MD techniques[249] (e.g. Metadynamics[250]). Nonetheless, replica exchange[251,252] (i.e. parallel tempering) may not suitable for simulating TREK channels because its thermal sensitivity.

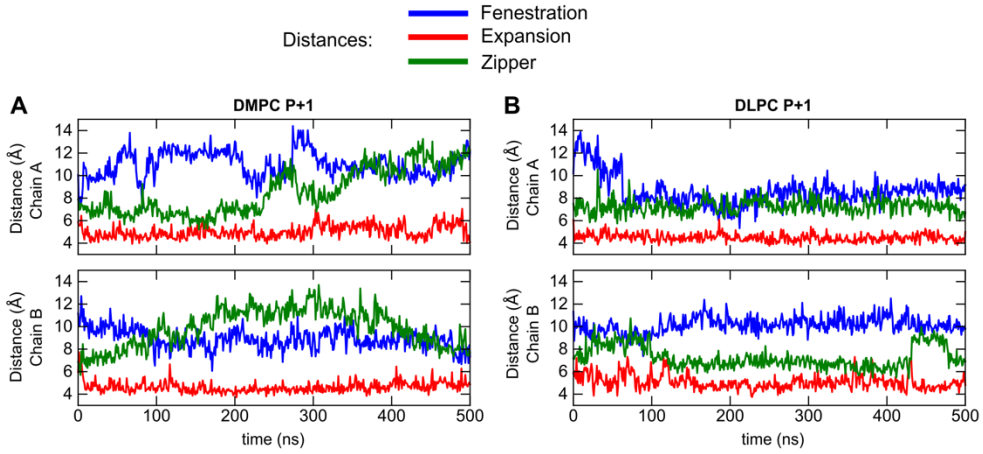


Figure 3.20 The structural rearrangements of TREK-2 in thin bilayers. *The figure shows changes in the fenestration (blue), expansion (red) and zipper (green) distances over time for the DMPC and DLPC simulations. Profiles for both chains A and B within each TREK-2 channel are shown. During the 500 ns, there is no neither 'unzipping' event nor expansion. The fenestrations remained open throughout the simulations.*

3.6 Discussion

3.6.1 Limitations and accuracy of the CG simulations

In the current study, the CG-simulation was used only as an initial testing engine because of its limitations. The interactions in CG were not good for many reasons. For example, Coulomb and VDW were treated by *shift* which smoothly makes potentials become zero beyond the cut-off. Importantly, the hydrogen bond is very difficult to represent in CG simulation, therefore protein secondary and tertiary structures (which are mainly stabilised by hydrogen bonds) were not stable without elastic network, a set of harmonic bonds. However, with elastic network the protein was partially rigid, and

we needed to be careful when examining this structural transition in detail. In this case, there were links connected between TM2 and TM4 helices. These links prevented the downward movement of the TM4 helices, therefore prohibited the up to down structural transition. In addition, the accuracy of CG simulation is acceptable to show overall structural transitions but was unable to accurately identify the down to up transition. This is because the accuracy of TM4 helices position is not good enough since its elastic network was heavily modified to allow the movement of lower section of TM4 helices. Then, only electrostatic and VDW potential were responsible for helix-helix interactions.

3.6.2 Lipids in the fenestration

In CG-simulations, lipids penetrated into the TREK-2 fenestration when the protein was kept rigid in the down state. As shown in **Figure 3.5**, it was not only lipid tails that entered, indeed whole lipid molecules (including headgroup) were found in the middle of protein and these physically blocked the ion conduction pathway, although not in the way originally proposed by Mackinnon. Interestingly, this was not observed in the flexible CG-down state simulation. In addition, in the no-stretch all-atom simulation, I observed that the lipid tails penetrated into the fenestration, but not the whole lipid molecule (**Figure 3.16 & 3.17**). From previous studies[70,253], the intracellular accessibility of the selectivity filter to quaternary ammonium ion blockers is not affected by mechanoactivation and is state-independent. Furthermore, our colleagues found that Rb^+ (used as the permeant ion) could activate the channel in an unstretched membrane thus indicating free unobstructed access to the selectivity filter gate[241]. Therefore, the observation of the whole lipid molecules in the CG-protein down state is probably an artefact of the rigidity of the protein.

3.6.3 Stretch and thin bilayer simulations

The simulations reveal that membrane stretch can drive the down to up transition of TREK-2, but that membrane thinning by itself does not. Although membrane thinning also occurs during the stretch simulation, this result was not necessarily as surprise because the MscL channel is not solely activated by thinner bilayer[115]. Comparing these two situations, the bilayer thickness of DLPC bilayer and POPC bilayer with P-50 were close together (~31 Å and ~30 Å) as seen in the **Figure 3.9** where the large negative peaks were in about the same region. The major differences in their bilayer lateral pressure profile are the negatively shifted overall profile and decrease in positive pressure at the bilayer core using the P-50 pressure protocol. Nevertheless, the influence of bilayer thinning on TREK-2 gating energy/pressure still merits further investigation to see if it can reduce the threshold for mechanoactivation of TREK-2.

3.6.4 Stretch activation model and selectivity filter

The current study shows that TREK-2 switches from the down state to the up state in response to membrane stretch and is in agreement with two previous models[73,135]. Although there was the penetration of the lipid tails into the fenestration, these lipid tails did not exhibit horizontal entry as suggested for the lipid occlusion model[73]. In addition, the model does not explain how the down state can be gated open in the absence of membrane tension[254] and why quaternary ammonium can access to the selectivity filter in both the down and the up state[70,253]. Moreover, our study of Rb^+ activation revealed unobstructed access to selectivity filter in the absence of membrane stretch. Also, in recent simulation studies[255] of TREK-2 with a constant electrostatic field a difference in conductance was determined from the down and the up state that was also affected by membrane tension. These studies emphasise the complexity of the role the selectivity filter plays in channel gating mechanism.

3.7 Summary

In this chapter, MD simulation techniques were used to investigate the dynamic behaviour of TREK-2 in a lipid bilayer when subjected to applied pressure and hydrophobic mismatch. First, the stretch protocol was developed based on previous MscL mechanoactivation protocols using a CG-simulation approach and then applied to an all-atom simulation. Both our CG and all-atom simulation results supported the down to up structural transition as a model for stretch activation. The structure of TREK-2 rapidly changes from the down state to the up-like state in response to membrane stretch. Importantly, TWIK-1, non-MS channel, did show any significant structural movement when subjected to the same protocol. The all-atom simulations of TREK-2 in DMPC and DLPC bilayers indicate that a thinner bilayer alone is unable to drive the down to up structural transition. Consistent with the 'force from lipid' principle, the lateral bilayer pressure profile also shows that the stretch protocol affects the bilayer properties, especially by producing a decrease in the positive pressures at the bilayer core as a consequence of the overall decrease in lipid density (i.e. increase in area per lipid).

Chapter 4
The response of TREK-2 to asymmetric increases in bilayer tension

4.1 Introduction

The role of mammalian MS channels is not just to prevent cell swelling. Instead they are involved in many complex physiological responses and so are designed by nature to sense quite varied forms of mechanical stimuli. However, the mechanisms underlying this complexity are still unclear. In the previous chapter, TREK-2 response under symmetric tension conditions were investigated i.e. where the tension in the inner and outer leaflets were the same condition. But it was also found that the protein itself responded with an asymmetric expansion in cross-sectional area with the majority change occurring only in the lower half of the protein i.e. the part that is in the inner leaflet. Asymmetric change like this is referred to as "shape sensitivity"[109]. One thermodynamic prediction of this is that it may allow an embedded protein like an ion channel to sense changes in tension within individual leaflets of the bilayer and respond accordingly. In this chapter, I created an asymmetric protocol to change bilayer tension in a particular leaflet and applied this to TREK-2. This protocol was designed to generate asymmetric bilayer tension and asymmetric forces on the protein to investigate whether changing the bilayer tension in the inner leaflet alone was enough to cause a structural change in TREK-2 from the down to the up state. These results were also compared to parallel functional (electrophysiological) studies in which TREK-2 was subjected to asymmetric membrane tension.

4.1.1 Asymmetric activation in MS channels

It is well established that small compounds such as anaesthetics or lysolipids (LPC) can activate MS channels by influencing membrane properties such as curvature and changes in the pressure profile[93,115,122,133,256]. Importantly, these compounds only activate MS channels when added asymmetrically into a bilayer (i.e. when added into only one of the two leaflets). CG-simulation studies of bilayers with added LPC have demonstrated that this conical lipid can significantly induce bilayer curvature, and asymmetrically affect the pressure profile[257]. In addition, in that study it was found that the degree of pressure profile perturbation is determined by the lipid packing factor, not the local curvature.

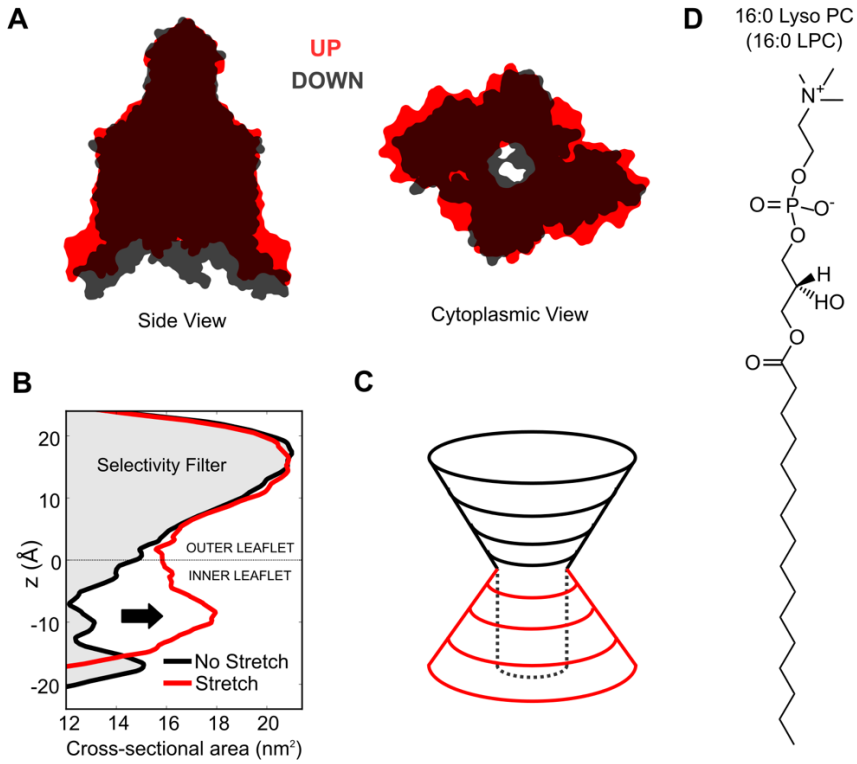


Figure 4.1 Asymmetric structural changes in response to membrane stretch. *(A) Overlay of a surface representation of the TREK-2 down state (black) and the up state (red). (B) The change in cross-sectional area of TREK-2 in a stretched and unstretched bilayer. The changes occur mostly in the lower part of the protein and illustrates the difference in cross-sectional area of these two conformations. (C) Cartoon representation of the change in protein shape and cross-sectional area. It changes from a funnel-like shape (black-dot line) when in a non-stretched bilayer to a more symmetrical shape (red) in a stretched bilayer. The upper part of the protein remains relatively constant to maintain the structural integrity of the selectivity filter. (D) Chemical structure of 1-palmitoyl-2-hydroxy-sn-glycero-3-phosphocholine (16:0 LPC).*

4.1.2 Shape sensitivity of TREK-2

From the results shown in Chapter 3, when TREK-2 was examined under symmetrical membrane tension it moved from the down state to the up-like state in response to symmetrical membrane stretch. Interestingly, the majority of the structural changes that happen in this transition only occur in the lower part of the protein changing the shape of the channel protein from conical-like shape into a more symmetrical, cylindrical-like shape (**Figure 4.1**). Thermodynamically the protein behaviour is regarded as 'shape sensitive'[109] and came from the study of LPC used to activate MscL[115]. Markin and Sachs suggested that the asymmetric distribution of the conical LPC between the inner and outer leaflets induced a force they called bilayer torque[109] (**Figure 4.2**). They further suggested that MS channels can either exhibit 'one-sided' shape activation (i.e. when the protein is activated by one direction of torque but inactivated in the other direction) or 'two-sided' shape activation (i.e. where it can be activated by changes in both directions).

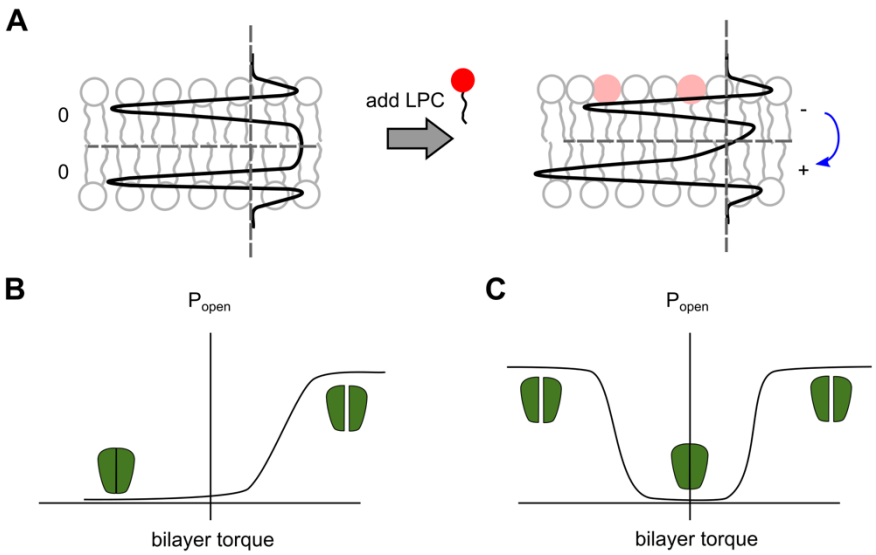


Figure 4.2 Bilayer torque and protein shape sensitivity. *(A) Cartoon representation describes how LPC lipids effect bilayer pressure profile. Plus (+), minus (-) and zero (0) signs indicate monolayer tension. Blue arrow shows bilayer torque which is defined as difference in monolayer pressure. (B-C) MS channel shape activation. (B) 'One-side' shape activation, channel is only activated by one direction of torque and inactivated in an opposite direction. (C) 'two-side' shape activation, channel can be activated by torque in both directions.*

Previous electrophysiological studies of TREK channel function initially suggested that they exhibited one-sided shape activation as they only seemed to respond to increased negative pressure (not increased positive pressure) in patch-clamp recordings[133,258,259]. However, there was a possible discrepancy in the pressure activation of purified and reconstituted TREK-1 proteins. Brohawn *et al*. shown that human TRAAK and zebrafish TREK-1 have similar response to both positive and negative pressure[95]. In contrast, the reconstituted mouse TREK-1 protein appeared to be activated even in the absence of pressure and was actually inhibited by positive pressure[94]. The reasons behind this unusual behaviour and the discrepancy between laboratories was not clear, although possibility was that the orientation of the human TRAAK and zebrafish TREK-1 became mixed upon reconstitution into bilayers, whereas the mouse TREK-1 was uniform when reconstituted. These observations highlight the difficulty and complexity of both performing and interpreting pressure-sensitivity in functional experiments, something that has been previously highlighted[4].

4.1.3 Planar bilayer experiments

In parallel with this current study, Michael Clausen, a post-doctoral researcher in the Tucker lab, reconstituted purified TREK-2 proteins into giant unilamellar vesicles (GUVs) and used a planar patch clamp system to examine their functional response to membrane tension[260]. It was found that under these conditions, TREK-2 oriented randomly when reconstituted but these orientations could be easily distinguished due to their asymmetric conductances at positive and negative voltages (i.e. their rectification). A typical recording of these GUVs (symmetrical 200 mM K^+, -80 mV) shows two main single channel conductances of: ~305 pS and ~155 pS arising from channels in opposite orientations. The relative orientation of these channels was confirmed by application of tetrapentylammonium (TPA) which only blocks from the inside of the channel, or by ruthenium red which blocks channels the extracellular side[70,261]. Using this approach,

the study demonstrated that TREK-2 activation by pressure was orientation-dependent i.e. its response to the different types of curvature induced by either positive or negative pressure were different (**Figure 4.3**)[260]. It was found that when two oppositely oriented channels were examined in the same bilayer, the 'inside-out' channel was activated by increases in negative pressure, whereas no activation observed when it was subjected to positive pressure. Importantly, the simultaneous inverse response was observed in the channel in the opposite orientation. This result therefore demonstrated that TREK-2 channels do in fact exhibit a functionally asymmetric response to changes in membrane tension.

4.1.4 Aims

Having demonstrated that TREK-2 can functionally respond to asymmetric changes in bilayer tension the aim of this study was to determine if we could see structural changes in TREK-2 in response to asymmetric changes in tension. To achieve this, I developed an asymmetric stretch bilayer protocol that generates monolayer tension in a particular leaflet and then applied this to TREK-2.

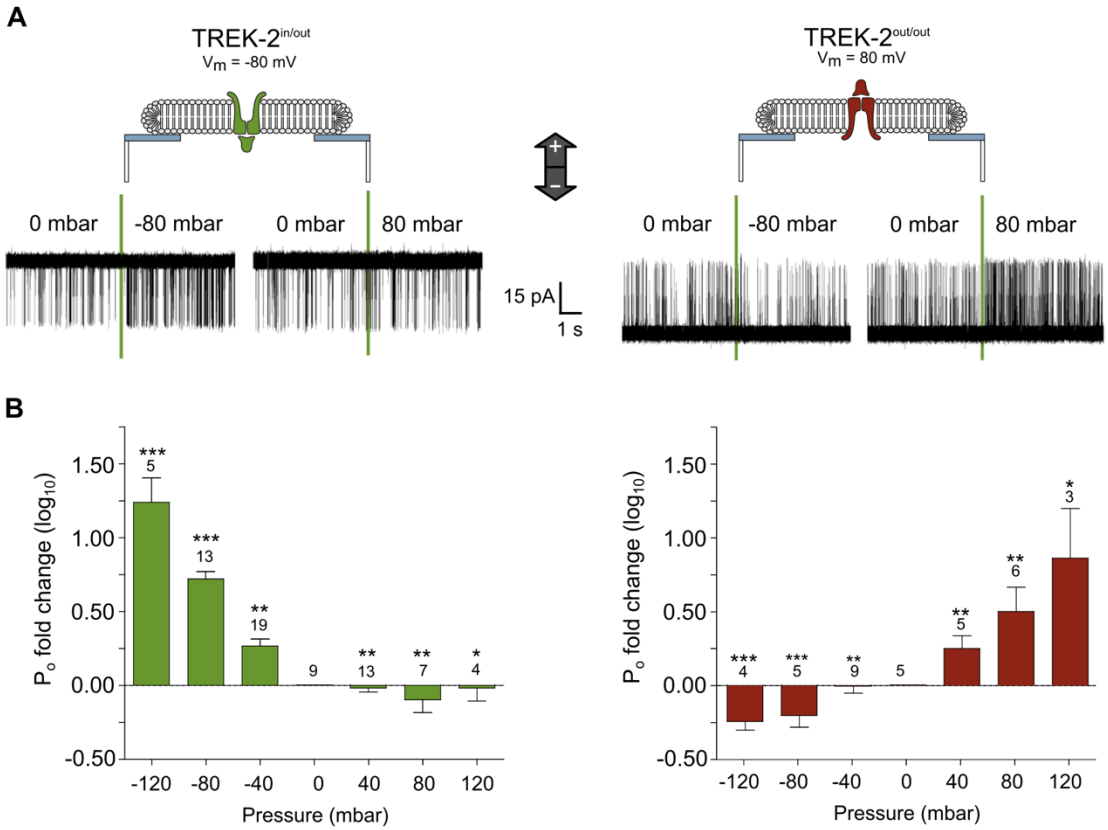


Figure 4.3 Asymmetric functional response of TREK-2 to positive and negative pressure. *(A) A bilayer with single channels (left: inside-out, right: outside-out orientation) were stimulated by pressure of 0 and ± 80 bar. (B) The mean log_{10} fold change in open-probability (Po) for each channel orientation is shown in response to various pressure changes from −120 to +120 mbar. The values above each error bar indicate the number of independent replicates, and error bars represent SEM. Asterisks represent the significance of difference between the two orientations at opposite pressures: ***P ≤ 0.001, **P ≤ 0.01, *P ≤ 0.05 (two-way unpaired t test). The inside-out channel was activated by increase in negative pressure, whereas no equivalent activation observed when it was subjected to positive pressure. The figure is reused from*[260].

4.2 Computational methods

Since this chapter is an extension of the work from Chapter 3, the starting structure was taken from the last frame of a 200 ns unstretched simulation of the TREK-2 down state in a POPC bilayer. In this chapter, the simulations were performed in the NPAT ensemble which is constant in the number of particles, pressure, area, and temperature. The 1 bar semi-isotropic pressure was controlled by a Parrinello-Rahman barostat with compressibility of 0 in xy-plane and 4.5 x 10^{-5} bar^{-1} in the z-direction. This means pressure was not controlled in the bilayer plane. The asymmetric bilayers without the protein were also simulated to obtain the bilayer pressure profiles. In addition, simulation of the bilayer with a 35% mismatch (to the original APL) in an NPT ensemble was performed in order to compare the difference between these two ensembles.

4.2.1 Monolayer tension induced protocol

Using the relationship between area per lipid (APL) and bilayer tension as shown in Chapter 3 (i.e. the increase in area per lipid with increasing bilayer tension) as a guide, monolayer tension was simulated a particular leaflet using the NPAT ensemble by creating a mismatch in the APL between leaflets. In other words, the number of lipid molecules in each leaflet was varied in the fixed xy-plane simulation box (**Figure 4.4**).

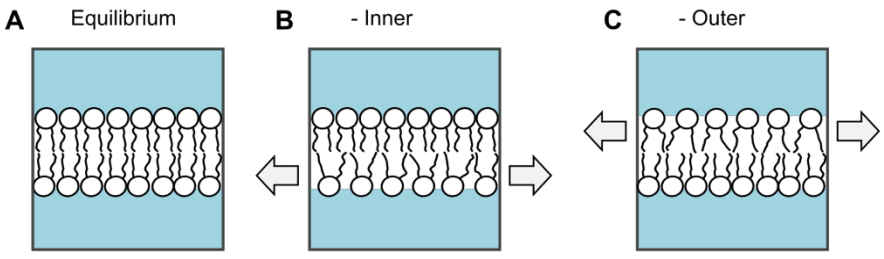


Figure 4.4 Monolayer tension induced protocol. *Cartoon representation describes how the protocol works. First, the bilayer is in equilibrium (A) (i.e. no tension). Then either removing lipids in the inner (B) or outer (C) leaflet creates a positive tension in the leaflet. This tension is caused by lipid rearrangement.*

From the results in Chapter 3, the P-50 protocol which drives the down to up structural transition, increases the APL by ~35%, thus a mismatch in APL of ~35% was used to mimic this situation and then tested using a CG-simulation. Lower percentages of mismatch (i.e. 10%, 25%, 35%, and only applied to the inner leaflet) were also simulated in CG, see section 4.3. The results suggested that the effect of -35% inner leaflet mismatch was the most pronounced, therefore it was used in the all-atom simulations. The equilibrium APL was obtained by performing a 200-ns equilibrium NPT ensemble simulation of the TREK-2 down state (PDB ID code 4XDJ). This was already done in the previous chapter. Therefore, the last frame of this simulation was then used as the initial structure for 200 ns NPAT ensemble simulations after randomly removing (or adding) lipids in the relevant leaflet. Lipids were added by gradually increasing their number and performing energy minimisation to avoid an infinite force on the atom(s). Lipid deletion in a particular leaflet creates a positive monolayer tension (equivalent to negative pressure in bilayer plane), in contrast, adding lipids creates a negative monolayer tension. Simulations were repeated with different randomly removed lipids and random velocities. The system details are shown in **Table 4.1**.

Table 4.1 *Simulation system details.*

System		Ensemble	TREK-2	#repeats	#lipids (outer)	#lipids (inner)
CG	25%	NPAT	without	1	225	169
	35%	NPAT	without	1	225	146
	35%	NPT	without	1	225	146
	-10% Inner	NPAT	with	1	285	254
	-25% Inner	NPAT	with	1	285	213
	-35% Inner	NPAT	with	1	285	185
	-35% Outer	NPAT	with	1	183	282
AT	-35% Outer	NPAT	with	2	77	119
	-35% Inner	NPAT	with	2	122	79
	+16%* Outer	NPAT	with	1	141	119

Minus and plus sign indicate removing and adding lipid molecules in particular leaflet. *The lipid was added into the outer leaflet with 16% which was already met the limit, see section 4.3.2.

4.3 Asymmetric bilayer tension

4.3.1 Development of asymmetric protocol

From the results in Chapter 3, the P-50 protocol increased the area per lipid by ~35%, thus this value was used as the mismatch in these asymmetric simulations. However, it was first tested using CG-simulations to ensure that the bilayer structure was still stable, and also examine the possibility of inducing a structural transition. Lower mismatch percentages (-10% and -25%) were also investigated to see if it was possible to decrease the tension and still induce a structural transition within a reasonable timescale. The simulations revealed that TREK-2 underwent significant structural changes when it was subjected to the -35% inner protocol (**Figure 4.5A & B**). The overlay of structures shows the movement of the TM2, TM3 and TM3 helices in the lower section of TREK-2 when subjected to this -35% protocol. Moreover, the Cα-RMSD of the TM-helices significantly moved away from the down state. In contrast, there was no significant structural changes induced by the other protocols as their Cα-RMSDs were similar to

TREK-2 in no stretch bilayer (P+1). Also, the bilayer structure itself was stable when subjected to -35% inner or -35% outer protocol (**Figure 4.5C & D**).

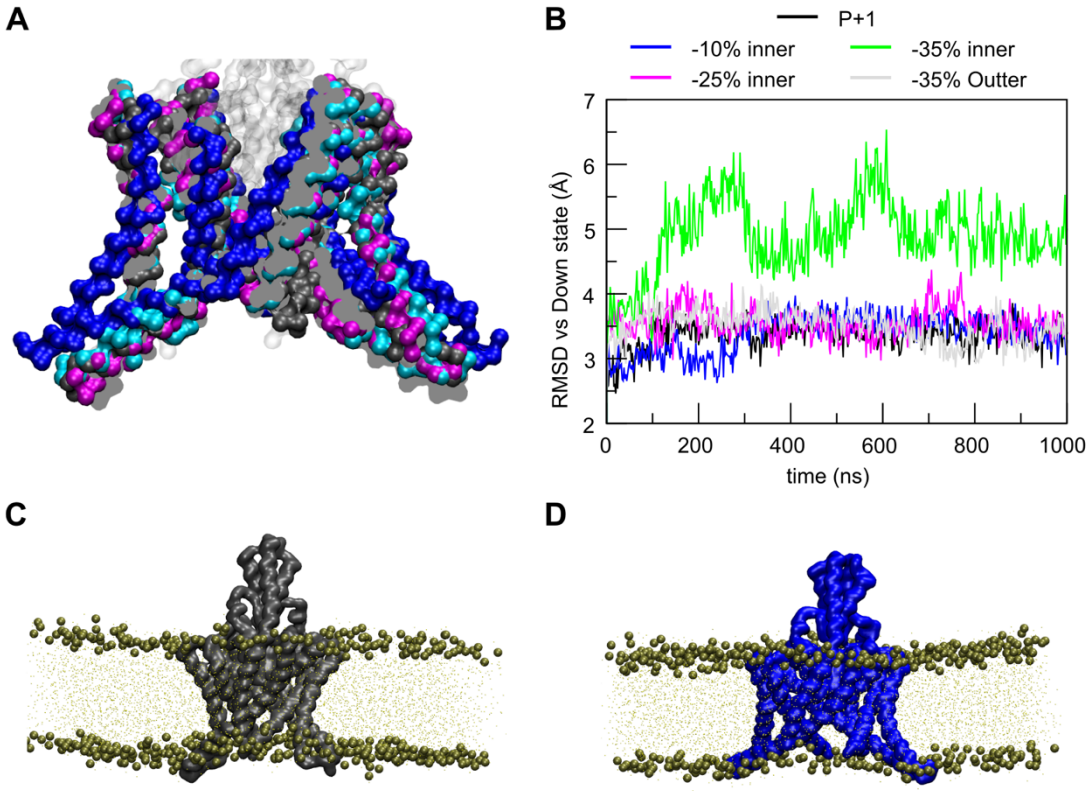


Figure 4.5 Asymmetric protocol in CG-simulation. *(A) Structural alignment of TREK-2 in a bilayer when subjected to P+1 (grey shadow), -35% outer (grey), -35% inner (blue), -25% inner (magenta), and -10% inner (cyan) protocols. (B) Transmembrane helices Cα-RMSDs compared with the down state. The -35% inner protocol has the most pronounced influence and can drive a down to up-like state transition. (C-D) Snapshot of the TREK-2/bilayer system under (C) -35% outer and (D) -35% inner protocols. The overall bilayer structure is stable when subjected to either -the 35% outer or -35% inner protocol.*

4.3.2 Asymmetric tension pressure profiles

Asymmetric bilayers without the channel protein were also simulated to obtain the bilayer pressure profiles. In addition, the bilayer simulation with 35% mismatch in an NPT ensemble was performed to compare the difference between these two ensembles. The pressure profiles were calculated using the same method as described in Chapter 3. Note the smaller size of the bilayer (i.e. simulation box) because it was unnecessary to use a large simulation box without protein - this has no effect on the pressure profile. As expected, the pressure profiles of the asymmetric bilayer were asymmetric along the z-axis (**Figure 4.6**) and the positive pressure at the bilayer core decreased as the mismatch percentages increased. But importantly, this only decreased in the leaflet where the lipid molecules had been removed (i.e. inner leaflet). Interestingly, the positive pressure at the core of the other leaflet increased slightly. In addition, there was a small shift in negative peak-peak distance. This indicates that there may be energetic coupling between two leaflets. Comparing NPAT and NPT ensembles, the coupling effect was even stronger because the xy-plane was free to relax and managed to achieve a pressure of +1 bar. Despite these mismatches between leaflets no curvature was observed to occur during the simulations.

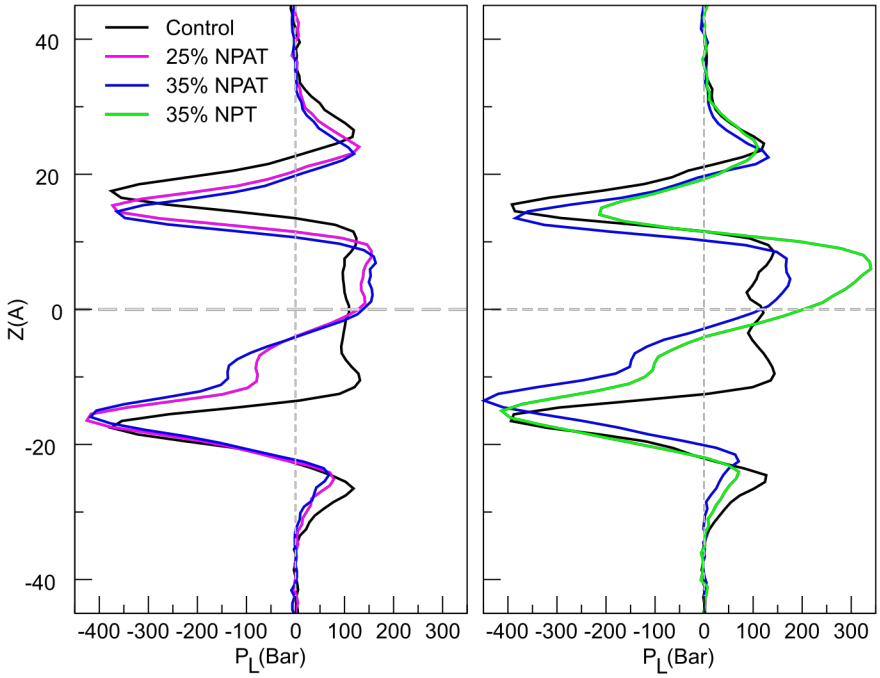


Figure 4.6 Pressure profiles of asymmetric bilayers. *(A) Pressure profile of a bilayer with various mismatch percentages. The positive pressure at the bilayer core decreased as the mismatch percentages increased. This only occurred in the leaflet where the lipid molecules had been removed (i.e. inner leaflet). There is a slight increase in the positive pressure at the core of the other leaflet. In addition, there is a small shift in negative peak-to-peak distance (i.e. bilayer hydrophobic thickness). (B) Pressure profile of bilayer with 35% mismatch in NPAT and NPT ensemble. The coupling between two leaflet present stronger impact under NPT ensemble.*

4.4 Asymmetric structural response of TREK-2

Since, in CG-simulation, the 35% mismatch was the most pronounced, this was used to set up the all-atom simulations. Similar to the CG simulations, this asymmetric protocol did not cause any major disturbance in bilayer structure (i.e. bilayer was still stable), **Figure 4.7A**.

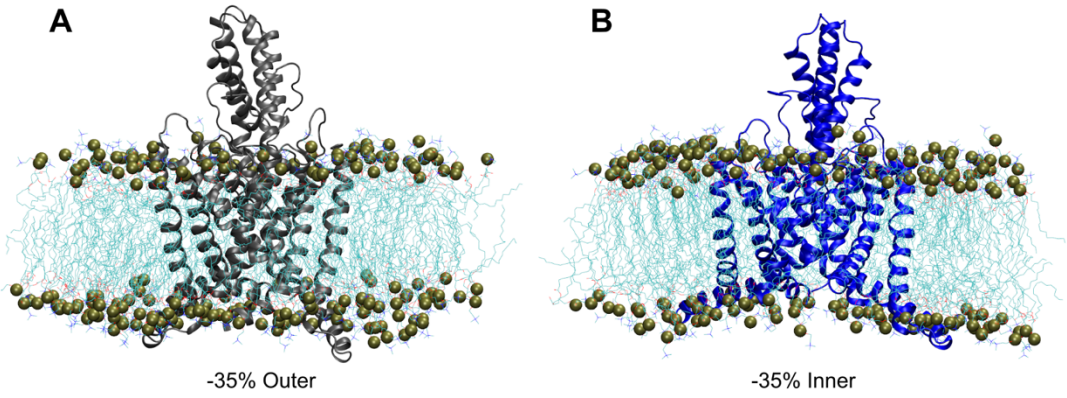


Figure 4.7 Snapshots of TREK-2/bilayer systems using the asymmetric protocol. *(A-B) Snapshots of TREK-2/bilayer system when subjected to (A) -35% outer and (B) -35% inner protocols. The bilayer structures under these two protocols were stable. Importantly, the structures of TREK-2 clearly show that it changes structure differently in response to monolayer tension in each leaflet.*

4.3.1 TREK-2 structural changes in response to asymmetric membrane tension

To identify the down to up transition, Cα-RMSDs of the TM helices were computed; the 'down' state and the 'up' state were used as the reference structures (**Figure 4.8**). These RMSDs clearly demonstrate that the protein only moved from the down state to the up-like state when subjected to positive tension in the inner leaflet. In contrast, the protein with the -35% outer protocol moved away from the up state. This emphasises the observation that TREK-2 has one-sided shape activation.

Lipid occupation of the fenestrations was observed in 1 of the 2 repeats of the -35% inner stretch protocol and it has been shown that physical occupation of these sites can sometimes prevent or slow movement of the channel towards the up state (where the fenestrations are closed) [241]. Therefore, to ensure that lipid occupation of these

fenestrations is not responsible for the failure of the -35% outer protocol to drive the down to up structural transition, lipids in these sites were removed, and the simulations extended for another 200 ns. The Cα-RMSDs (**Figure 4.8**) indicates that although the binding lipids were removed, the Cα-RMSDs did not move closer to the up state. In contrast, the RMSD of the -35% inner protocol continued to move closer to up state.

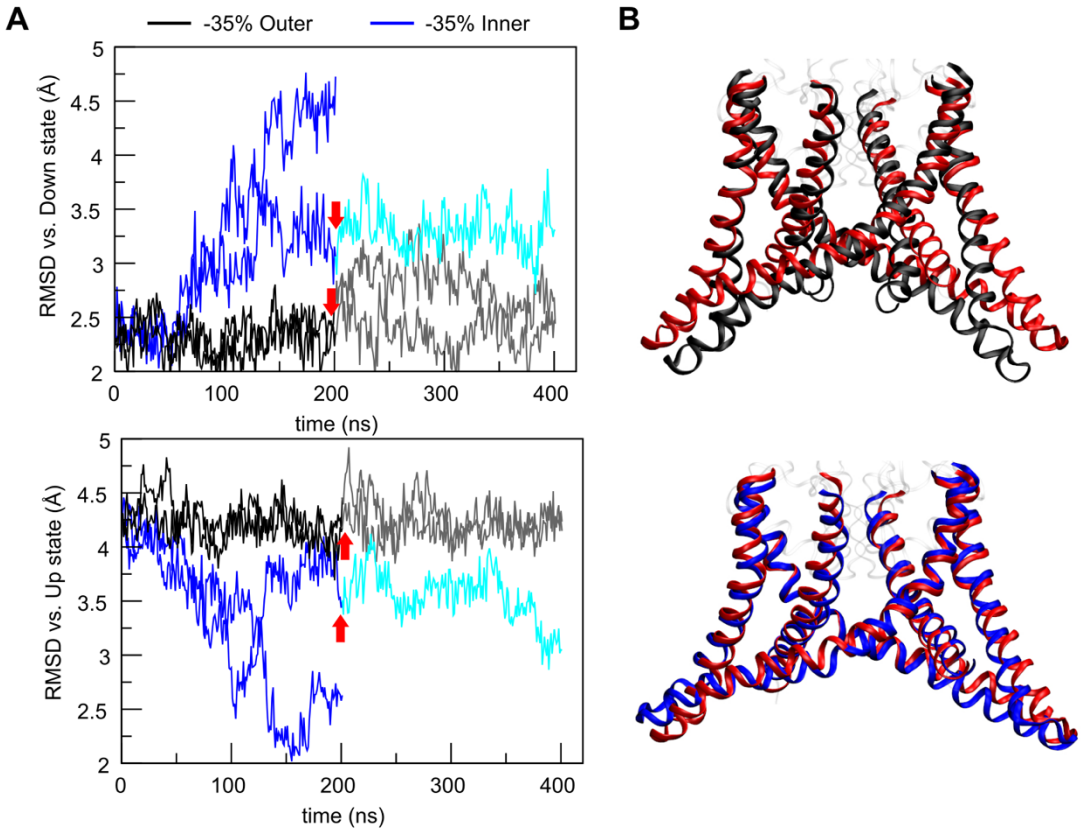


Figure 4.8 Structure changes induced by asymmetric tension. *(A) Cα-RMSDs of TM helices compared with the down and up state. The arrow indicates when the binding lipids were removed. Similar colour indicates repeats. (B) Structural alignment of the simulated structures at the last frame with the up-state induced by symmetrical stretch (represented in red and taken from Chapter 3). Black is TREK-2 in -35% outer protocol, red when is in -35% inner protocol. TREK-2 with -35% inner protocol moved away from the down state and closer to the up state, whereas with -35% outer protocol, it remains close to down state. These emphasise that TREK-2 ca responds to asymmetric changes in tension.*

4.3.2 Monolayer tension or bilayer torque?

The asymmetric protocol induces monolayer tension in a particular leaflet, consequently creating bilayer torque. Removing lipids in the inner leaflet creates a positive tension in the inner leaflet thus therefore results in a clockwise bilayer torque. However, a similar

direction of torque can be also created by adding lipids in the outer leaflet to creating a negative monolayer tension. To mimic this, lipid molecules were directly added into the outer leaflet by gradually increasing their number and performing energy minimisation. This is to prevent to system from blowing up due to infinite force on atoms. Nevertheless, only 19 lipid molecules (equivalent to +16%) were managed to be added, because the bilayer started to become unstable, especially at the edges (**Figure 4.9**). The lipids in the outer monolayer became more ordered whereas the lipids in the inner leaflet remained disordered (**Figure 4.10**). Importantly, despite this change in membrane torque, there was no down to up-like transition observed during this 500 ns simulation (**Figure 4.9D**).

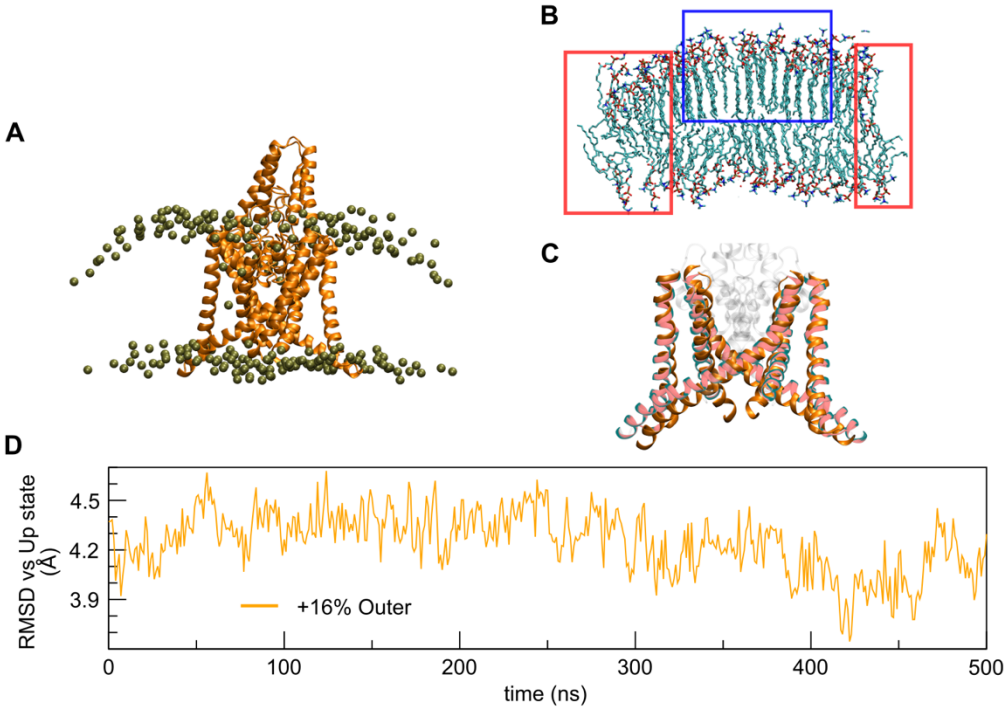


Figure 4.9 Clockwise bilayer torque vs. positive monolayer tension. *The lipid was added into the outer leaflet (+16% outer) to mimic the bilayer torque caused by the -35% inner protocol. (A) TREK-2 in a bilayer with +16% outer protocol. Lipid phosphorous atoms are shown in brown spheres. (B) The bilayer when subjected to +16% outer protocol. The protein is hidden for clear visualisation. The lipids in the middle of outer monolayer (blue frame) were ordered whereas the lipids in the inner leaflet were disordered. Importantly, at the edges (red frames), the bilayer structure was unstable. (C) Overlay of structure at the last frame of this protocol (orange) and the up state (red shadow). (D) Transmembrane helices Cα-RMDS compared with the up state. The RMSD indicates no movement to the up state despite the change in torque.*

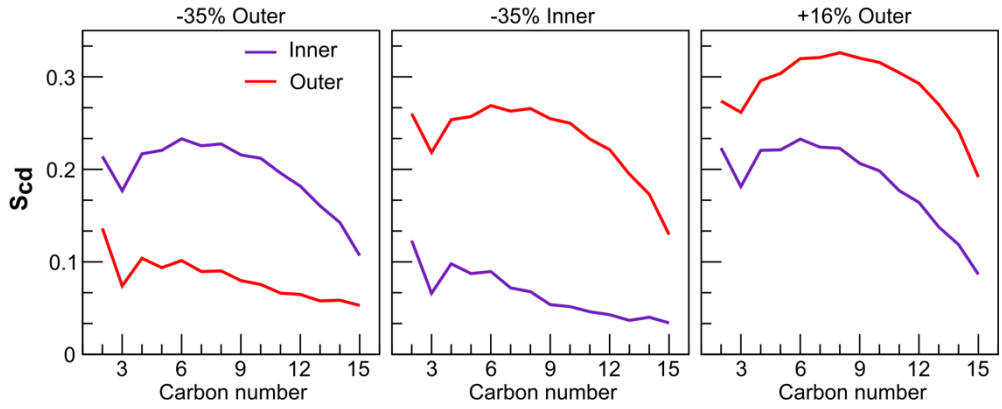


Figure 4.10 *Order parameter of POPC sn-1 acyl chains. The order parameter decreased in the leaflet that lipid molecules were removed. On the other hand, it increased when lipid molecules were added.*

4.3.3 Structural rearrangement induced by the asymmetric bilayer torsion protocol

To better quantify the structural rearrangements that occur during these movements, the previously defined distances used in the symmetrical stretch protocols were calculated i.e. the “fenestration”, “Zipper”, and “Expansion” distances (see Chapter 3.4.3). Similar to the P-50 protocol, the structural rearrangement in symmetrical stretch, this starts by a ‘unzip’ between TM3 and TM4 followed by expansion of TM2 helix and ends by closure of the fenestration (**Figure 4.11**). The kinetics of this process appear slightly different to that which occurred during symmetrical stretch, e.g. in the #1 chain B, the expansion gradually increases over time, but importantly the sequence of events are similar and the -35% outer protocol did not cause any significant movement in the lower part of the protein i.e. there was no increase in zipper and expansion distances, and the fenestration remained open.

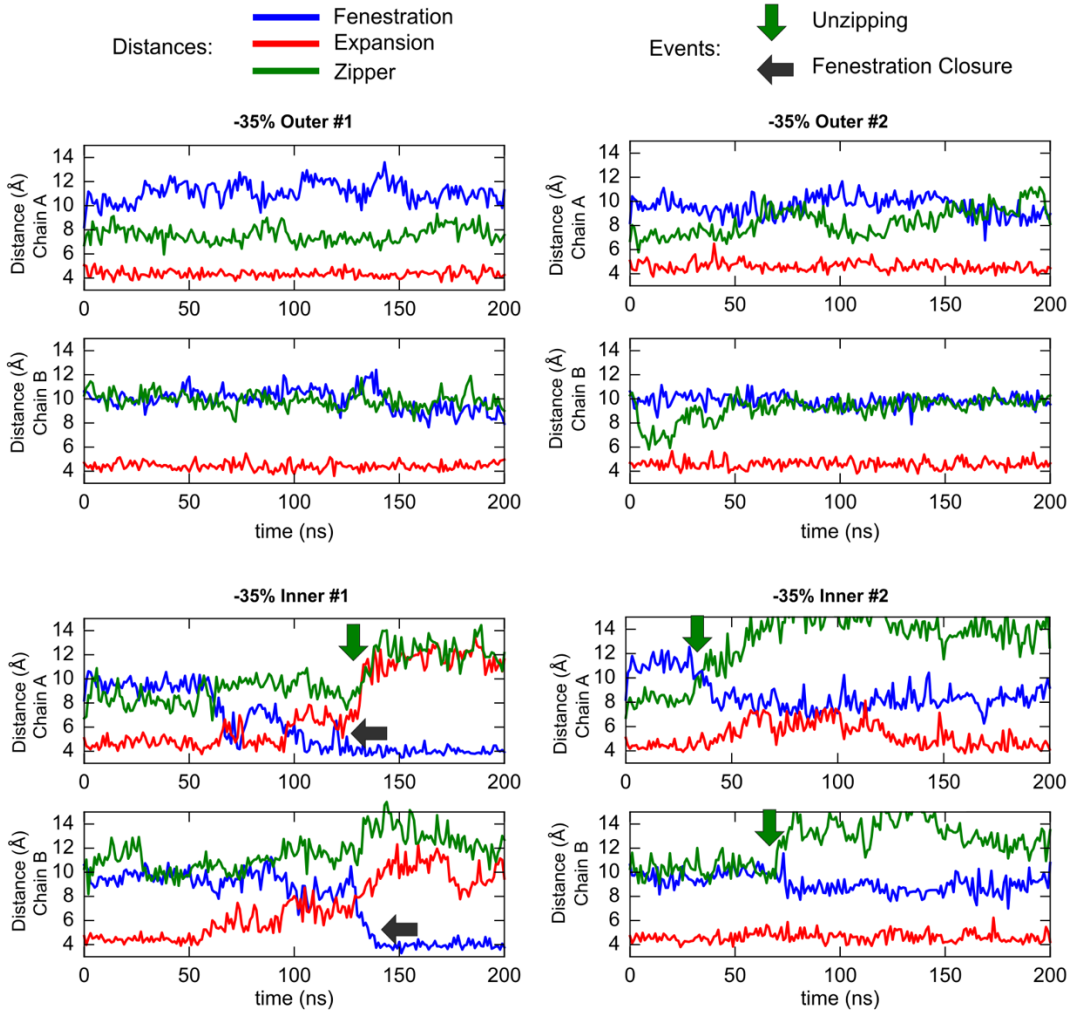


Figure 4.11 Structural rearrangements induced by asymmetric bilayer tension. *The figure shows changes in the fenestration (blue), expansion (red) and zipper (green) distances over time for the 2 of -35% outer simulations and 2 of the -35% inner simulations. Profiles for both chains A and B within each TREK-2 channel are shown. Green arrows indicate the 'unzipping' event of the interactions. The black arrows indicate full closure of the fenestration.*

4.3.4 Structural integrity of the selectivity filter

To investigate any effect of asymmetric tension on the selectivity filter, the Cα-RMSDs of the selectivity filter (P1: TIGYGN; P2: TVGFGD) were compared with the down state. The average RMSD caused by -35% inner protocol is 0.533 $\pm$ 0.095 Å which is slightly higher than the one of -35% outer protocol (0.475 $\pm$ 0.081 Å). However, as shown in **Figure 4.12A**, both -35% outer and -35% inner protocols do not have any significant influence on the structure of selectivity filter.

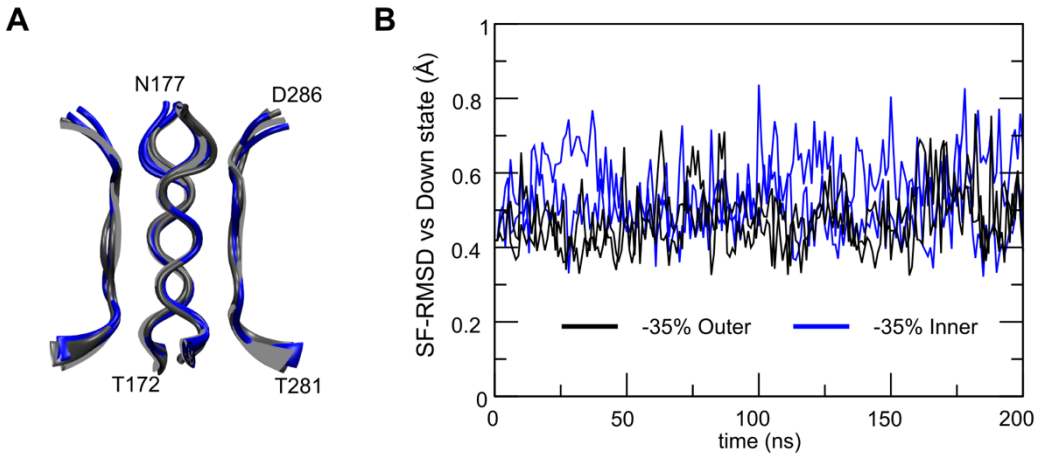


Figure 4.12 Selectivity filter structure under the asymmetric protocol. *(A) An overlay of TREK-2 selectivity filter in -35% outer (black), -35% inner (blue) and the down state (grey shadow). There is no significant difference between these structures. (B) Cα-RMSDs of selectivity filter (P1: TIGYGN; P2: TVGFGD) compared with the down state indicate that no significant difference between them.*

4.5 Discussion

4.5.1 Bilayer mismatch under NPAT and NPT

Although these asymmetric protocols did not cause bilayer deformation, they changed many of the bilayer physical properties. For example, a decrease in bilayer hydrophobic thickness as shown by the decrease in the pressure profile peak-to-peak distance. Lipid tail order parameters (**Figure 4.10**) also decreased as consequence of increasing the area per lipid, however, this increased when lipids were added (i.e. decrease in area per lipid). In NPAT ensemble, these changes were mainly restricted to the monolayer that was subjected under the protocol. In contrast, the bilayer in NPT was changed in both leaflets. This is not a surprise because the coupling between two leaflets in NPT ensemble has previously been shown by the simulation studies[262,263]. These indicate that the monolayer coupling between leaflet is stronger in the NPT ensemble. This difference is because in the NPAT ensemble the bilayer plane (xy-plane) is fixed in the simulation box, allowing changes in the lateral pressure. Whereas in NPT, the simulation box is allowed to adjust itself to maintain the pressure of +1 bar, therefore both leaflets must cooperate to achieve this.

4.5.2 Monolayer/Bilayer tension induced by asymmetric protocols

The monolayer/bilayer tensions can be obtained using equation 2.23 which is basically integration of the lateral pressure profile along the bilayer normal. The NPAT 35% mismatch protocol induced 30.84 mN/m monolayer tension in the leaflet where the lipid molecules were removed and -2.92 mN/m in the other. The bilayer tension is 27.92 mN/m. This is compared to the P-50 protocol which created ~50.2 mN/m bilayer layer tension (~25.1 mN/m in each leaflet). Apparently, the 35% protocol induced higher tension in the lower leaflet, but full structural changes occurred in only one of the two simulations compared to 4 of 4 for the symmetrical P-50 simulations. This might be

explained by the rate of applied tension. The P-50 protocol rapidly increases bilayer tension, whereas the asymmetric -35% protocol gradually created tension. In NPT, the monolayer tension is 26.03 mN/m in one leaflet and -29.83 in the other resulting in an overall bilayer tension of -3.80 mN/m. Theoretically, this should be 0. This small difference may be caused by the relative efficiency of the pressure coupling.

4.5.3 Bilayer curvature induced by asymmetric tension.

Simulation of bilayer curvature is a computational challenge, especially for all-atom simulation, because it requires a large system. Yoo and Cui [257] managed to simulate CG-simulations of bilayer curvature induced by the conical LPC. Their system size was ~40nm × ~40nm × 9 nm with ~2000 lipids molecules. In this study, bilayer curvature was evident in the +16% outer protocol **(Figure 4.8B)**, although this curvature was caused by lipid raft with ordered lipids clustering at the centre of the bilayer and disordered lipid at the edges. Nevertheless, this indicates that using this protocol to create bilayer curvature may be possible.

4.5.4 Monolayer tension and bilayer torque

The +16% outer protocol which mimic the bilayer torque caused by the -35% inner protocol did not make TREK-2 move closer to the down state. The difference between these two is the -35% inner protocol induced negative pressure in the inner leaflet therefore shifted the positive pressure at the bilayer core into the negative pressure. In contrast, the +16% outer protocol created positive pressure in the outer leaflet (**Figure 4.13)**. These imply that rather than bilayer torque, the monolayer positive tension in the inner leaflet itself plays the major role in producing the structural transitions seen in TREK-2.

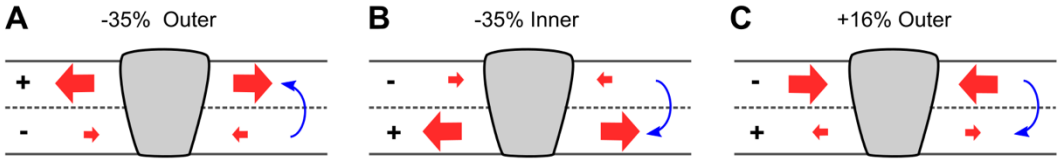


Figure 4.13 Monolayer tension and bilayer torque scheme. *Monolayer tension and bilayer torque induced by (A) -35 outer, (B) -35% inner and (C) +16% outer protocol. Red arrows indicate pressure in each leaflet. Plus and minus sign represent positive or negative tension. Blue arrows indicate bilayer torque. Removing lipids creates negative pressure thus positive monolayer tension in a particular leaflet. In the other hand, adding lipids induces positive pressure therefore negative tension. Both -35% inner and +16% outer protocols create clockwise torque but caused by different tensions. Only the -35% inner protocol was able to drive the down to up structural transition in TREK-2.*

4.6 Summary

In this chapter, the asymmetric bilayer tension protocol was developed and applied on the TREK-2 channel. The results showed that the TREK-2 has asymmetric structural (and functional) response when subjected to asymmetric bilayer tension. The 'down to up' structural transition only occurred in response to positive tension in the inner leaflet, but not in the outer leaflet. The negative tension in the outer leaflet, which is mimic bilayer torque caused by positive tension in the inner leaflet, also did not drive the transition. Together, these structural (and functional) results highlight the ability of a eukaryotic MS channel to sense a complex and diverse range of forces distributed in the cell membrane.

Chapter 5
Investigation of the effect of the E306A mutation on TREK-1 pH sensitivity

5.1 Introduction

The mechanisms underlying the mechanosensitivity of TREK channels are thought to be related with those that control the sensitivity of the channels to changes in intracellular pH[131,264]. Therefore, to understand how TREK channels respond to intracellular acidification may also improve our knowledge of their mechanosensitivity. Unfortunately, the available crystal structure of TREK-2 lacks information about the structure of proximal C-terminus where the H^+ sensing residue (E306) is located[264]. However, towards the end of this thesis a new structure became available that contain this region for related TREK-1 MS channel. Within the TREK subfamily, TREK-1 shares 63% overall identity TREK-2, and 45% identity with TRAAK[56,66]. Like TREK-2, it also exhibits polymodel regulation, in particular, activation by increasing intracellular H^+. This chapter describes a MD simulation study of the structural mechanisms underlying TREK-1 internal pH sensitivity based on this new TREK-1 crystal structure[138] and also a corrected version of that structure that was released towards the very end of completing the work in this chapter.

5.1.1 Internal pH sensitivity and mechanosensitivity of TREK-1

Although TREK-1 exhibits polymodal activation (including membrane tension, temperature, and acids), only internal pH and membrane stretch sensitivity will be discussed in this chapter. Descriptions of the other mechanism of regulation can be found in many of TREK reviews[3,46,60,66,265] and in Chapter 1. In patch-clamp studies[131], intracellular acidification (pH 5.0) activated TREK-1. It was also found that pressure, in the form of membrane stretch, activated the channel. These properties appear linked because an increase in acidification decreases the amount of pressure required for activation. The same study[131] showed that the deletion of the N-terminus does not affect pH sensitivity or mechanosensation, whereas deletion of the C-terminus does. Further truncation studies revealed the importance of proximal C-terminal region in both pH- and mechano-activation. Site-directed mutagenesis [264] then identified E306 in the proximal C-terminus (G293-A343) as the proton sensor for an internal pH activation. Interestingly, there was no significant further effect of membrane stretch on the E306A mutant. Further studies from the Honoré group [266] suggested that a positive charge region close to this E306 residue was also important for interaction with the membrane.

5.1.2 Internal pH sensitivity in the TREK subfamily

In the TREK subfamily, the C-terminal region is critical for the internal pH sensitivity of TREK-1 and TREK-2, but not TRAAK [131,267]. The proximal C-terminal regions of TREK-1 and TREK-2 are highly conserved, especially the S_{300}KKTKEE_{306}VGE [56,61]. The equivalent residue in TREK-2 (E337) is also responsible for intracellular pH activation [267,268].

5.1.3 TREK-1 crystal structures

The first x-ray crystal structure of TREK-1 (PDB id: 4TWK) with 2.6 Å resolution was presented in the 'up-state'[269]. As expected, the overall structure of this TREK-1 is very

similar to the structure of TREK-2 (PDB id: 4BW5) [135] and TRAAK (PDB id: 3UM7)[69] and it also lacked the proximal C-terminus, see Chapter 1 for more detail. Recently several other structures of TREK-1 were solved [138]. All of them were presented in the 'up-state' with resolutions up to 3.1 Å for an apo structure (PDB id: 5VK5), **Figure 5.1A**. These structures were particularly interesting because they included the extra C-terminal domain from W295 to V321 that was absent from the recently previous TREK-2 structure [135]. This allows a more detailed investigation about critical role of this region as many studies have shown it plays a key role in TREK-1 activation [132,266,268,270] by pH, phospholipids, polyunsaturated fatty acids, and by membrane stretch.

5.1.3 Aims

Although it is known that the E306 residue plays a critical role in TREK-1 intracellular pH sensitivity, the precise structural mechanisms are still unclear. This chapter examines how the E306A mutation may influence TREK-1 intracellular pH- and mechano-sensitivity by using MD simulation.

5.2 Computational methods

5.2.1 Modelling

The TREK-1 apo structure (PDB id :5VK5) [138] was completed by introducing the missing loop (I114 to V124) in subunit A by cloning the same region from the subunit B. All mutations (K84R, Q85E, T86K, I88L, A89R, Q90A, A92P, N95S, S96D, T97Q, N119A, S300A, E306A) were mutated back to the wild type configuration using PyMol mutagenesis wizard [225]. The structure was modified to make it symmetric, detail in **Figure 5.1**. The TREK-1 chimera, **Figure 5.1B**, has S35 to V321 in each subunit; the topology of S300 to V321 was taken from the subunit A. All missing heavy atoms were added before setting up the protein topology. A TREK-1 molecule was embedded in POPC lipid bilayer using insane.py [203]; the amount of lipid in each leaflet is equal to 207 molecules. This prevents asymmetric response of TREK-1 since this behaviour of TREK-2 have been shown in Chapter 4. The system was fully hydrated with 150 mM KCl. Each all-atom system consists of 44,000 water molecules in 12.1×12.1×13.1 nm simulation box; the total number of particles is ~200,000 particles.

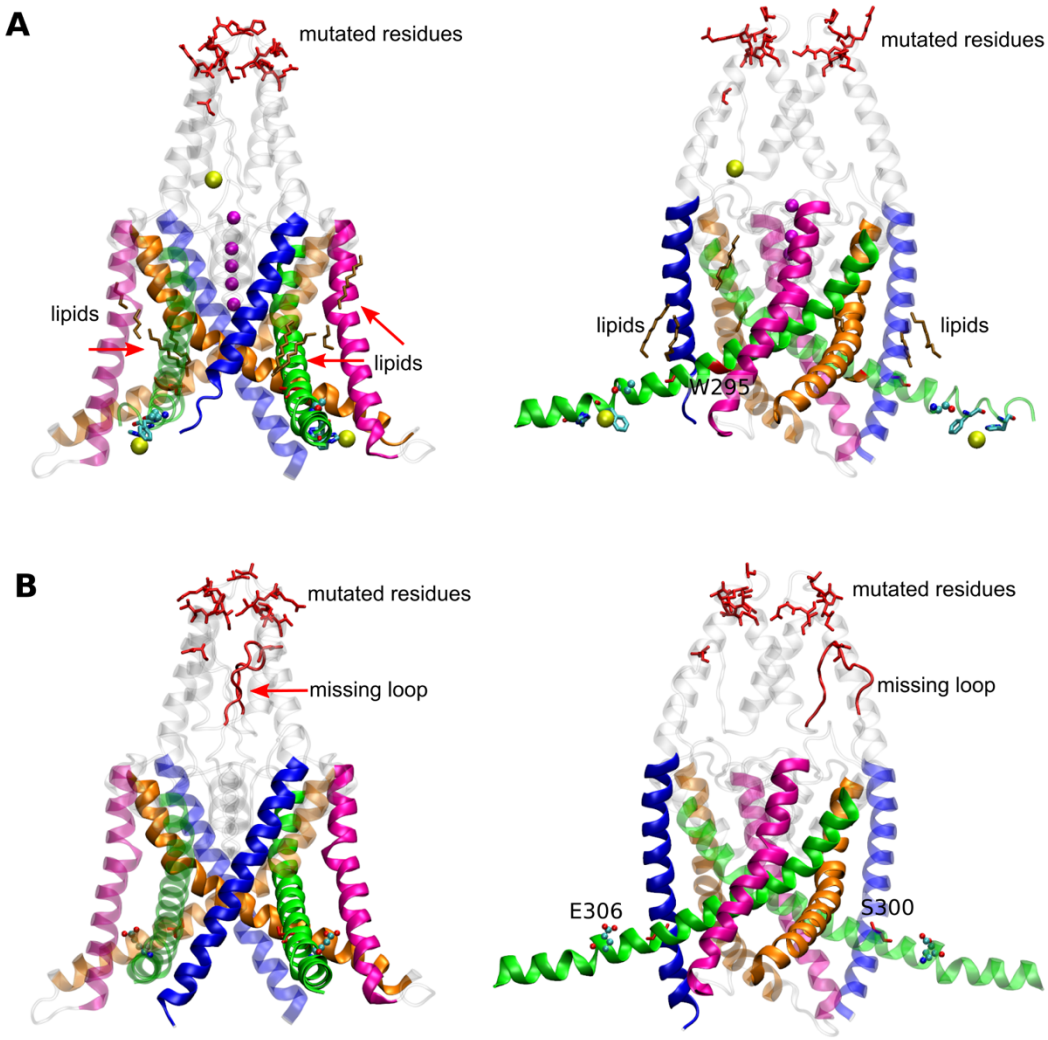


Figure 5.1 The TREK-1 crystal structures and simulation model. *(A) The TREK-1 crystal structure (PDB id :5VK5) has 6 K^+ and 3 Cd^+ (show in purple and yellow spheres) and binding lipids (show in brown sticks). The protein is coloured by the TM domain; subunit B is transparent. W295 and the missing loop (I114 to V124) are highlighted in red. The structure beyond W295 are only solved this new TREK-1 structure [138]. All mutated residues are shown in red sticks. This excludes E306A which show in small spheres. Since the length of TM1 and TM4 of each subunit is different. TM1 of subunit A is shorter than TM1 of subunit B. TM4 of subunit A is longer than and has different topology from TM4 of subunit B. Therefore, the structure was modified to make it symmetric before performing the simulation. (B) The simulation model of TREK-1 after symmetrisation. Both subunits are identical.*

5.2.2 MD simulation

All simulations in this chapter were done using GROMACS 5. Because there are changes in simulation control parameters when moving from GROMACS 4 to GROMACS 5, all changes and the parameters used in this chapter are shown in **Table 2.1 and 2.2** in Chapter 2. In brief, the NPT ensemble with temperature was 310 K using the v-rescale algorithm [153]; the pressure controlled by the Parrinello-Rahman barostat [154] was set to semi-isotropic with 1 bar in x-y plane and z-directions. The electrostatic interaction was treated using PME [149]. Newly developed force field Charmm36m [163] was used in this chapter.

The TREK-1/bilayer systems were equilibrated by performing 1μs CG simulation and then converted to all-atom using the backward protocol [160]. A series of short simulations without LINCS constraint and small integration time step had been conducted to equilibrate the hydrogen atoms; there are i.) 10,000 steps with 0.2 fs integration time, and ii.) 10,000 steps with 0.5 fs integration time. All protein heavy atoms were restrained during these hydrogen equilibrations. After that, the simulation was run for 2 ns with protein heavy atom restraints followed by 10ns simulation with protein Cα restraints to fully equilibrate the system. After the equilibrium process, at least 200 ns production run was simulated. The simulations were repeated with random initial coordinate and velocity. For comparisons, the simulations of E305A and the protonated state of E306 were performed.

5.3 Stability of the TREK-1 structure in a lipid bilayer

Before investigating the influence of E306A, the stability of TREK-1 in the bilayer was first determined by running 200 ns simulations of the 'up state' TREK-1 in a POPC bilayer. The Cα-RMSD of the TM domains, selectivity filter, and C-terminus Cα atoms were compared with the initial crystal structure that was first released (5VK5). As shown in **Figure 5.2**, initially the TM domain RMSDs moved away from the initial structure, after ~25 ns it became stable at ~1.5 Å. This indicates that this TM region is stable in the POPC bilayer. There are the minor movements of TM2 and TM4. There is no structural transition from the 'up state' to the 'down state' and no significant difference between WT and E306A (**Figure 5.3**). The change in selectivity filter is relatively small (~0.5 Å) for 3 of 4 the simulation (1 of 2 for WT and 2 of 2 for E306A). The largest RMSD of SF is ~1.25 that caused by the flip of G146 and G255 in subunit B. There is no large expansion observed in the selectivity filter. However, the RMSDs of C-terminus were relatively large since there were only ~20 amino acids in this region. This indicates that the structure appeared to be unstable in this region as it had been clearly observed in the simulation.

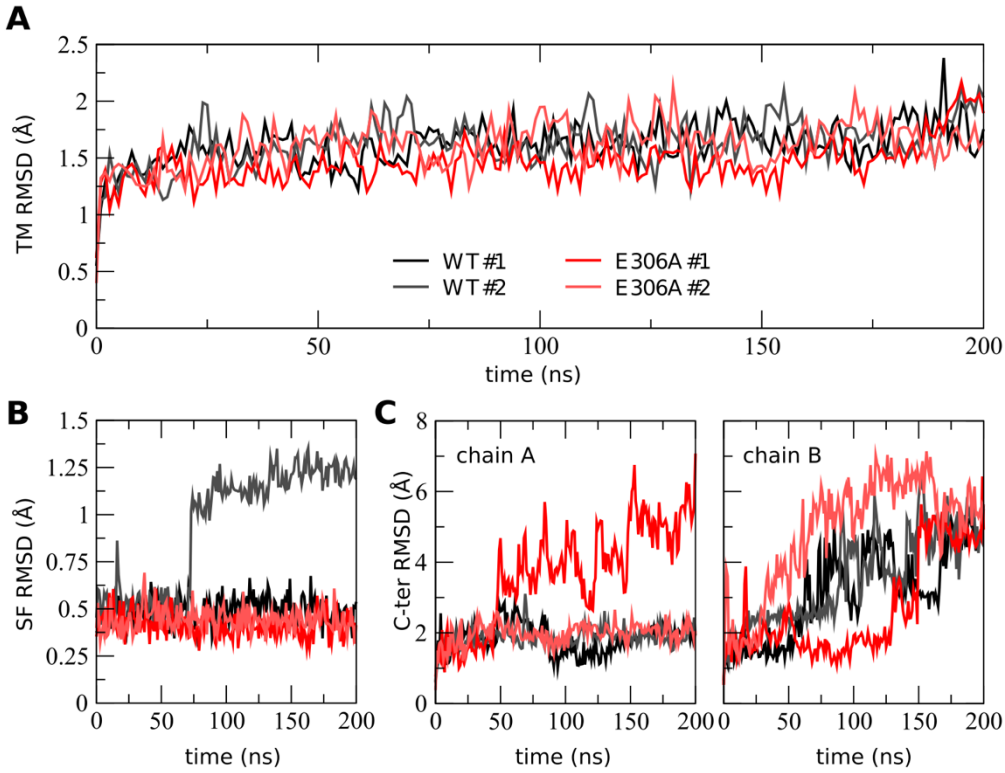


Figure 5.2 The Cα-RMSD comparison with the initial crystal structure (5VK5). *(A) Cα-RMSD of transmembrane domain. The RMSDs of all simulation are stable about 1.5 Å indicates that the TM regions are stable. (B) RMSDs of selectivity filter (SF). Most of them are stable at 0.5 Å. The large RMSD at ~1.25 Å caused by the movement of G146 and G255 in subunit B. and (C) RMSD of C-terminal region for each subunit separately. The RMSDs (even at 2 Å) are relatively large for ~20 amino acids.*

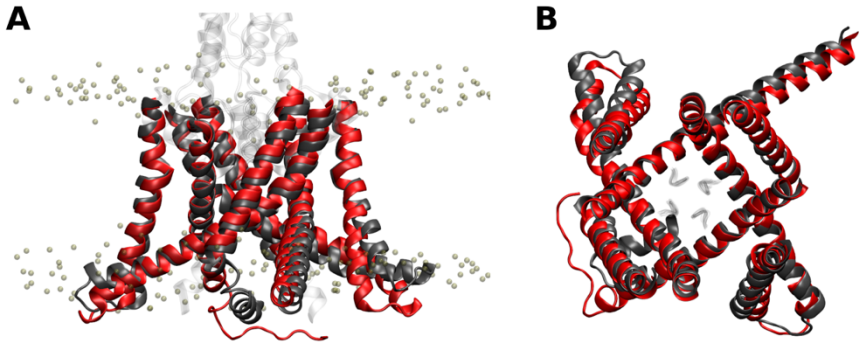


Figure 5.3 Snapshots of TREK-1. *(A) front view (B) top view. The WT represents in black, whereas E306A represents in red. At 200 ns, only minor differences were observed, nonetheless there was no significant between the two structures.*

5.3.1 Secondary structure of proximal C-terminus

There are 3 crystal structures (PDB id: 5VK5, 5VKN, 5VKP) where the proximal C-terminal region is resolved [138], nonetheless their secondary structures were not in perfect agreement with each other. Some of them have 'α-helix – π-helix – α-helix' structure, but some of them have an unfolded structure (**Figure 5.4 & Table 5.1**). The MD simulation result suggests that the 'α-helix – π-helix – α-helix' structure is unstable, especially at the π-helix (after E306) where the unwrapping occasionally occurred. There are 3 suggested structures from the simulation (**Figure 5.4**): i) 'continuous α-helix' (2 of 8), ii) 'α-helix – turn – α-helix' (3 of 8), and iii) unfolded (3 of 8). The differences between these three structures start after the residue 306. However, the E306A mutation had no effect on the structural preference. Since this C-terminus is significant for protein-lipid interaction [266], before deeply investigating the influence of the E306A mutation, we decided to investigate the potential secondary structure in more detail.

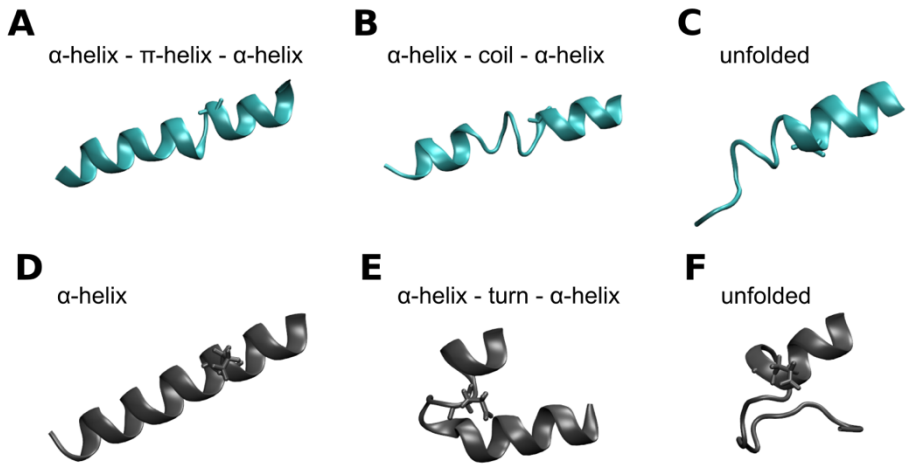


***Figure 5.4 The* secondary structure of C-terminus.** (A-C) Structures of C-terminus presented in the crystal structures: (A) *'α-helix – π-helix – α-helix', (B) 'α-helix – coil – α-helix', and (C) unfolded.* (D-F) Structures of C-terminus suggested from MD simulations: (D) *'α-helix' (2 of 8), (E) 'α-helix – turn – α-helix' (3 of 8), and (F) unfolded (3 of 8). Note that there are 4 simulations and TREK-1 has 2 subunits, thus there are 8 subunits.*

Table 5.1 *Secondary structure of TREK-1.*

System	Subunit	
	A	**B**
WT#1	*αH*	*HTH*
WT#2	*HTH*	*UF*
E306A#1	*UF*	*HTH*
E306A#2	*αH*	*UF*
5VK5	*HPiH*	*UF*
5VKN	*HTH*	*UF*
5VKP	*HPiH*	*HTH*

HPiH is 'α-helix – π-helix – α-helix', αH is 'α-helix', HTH is 'α-helix – turn – α-helix', and UF is unfolded.

5.3.2 Re-modelling of the TREK-1 proximal C-terminal structure

After close examination of the electron density in the new TREK-1 structures, it was suggested by our colleagues in the Structural Genomics Consortium (SGC) that the C-terminus should be a 'continuous α-helix' because this structure allows E309 to interact with Cd^{+} which is more reasonable than the F310 interaction in the original structure (**Figure 5.5**). With help from these colleagues, I re-modelled C-terminal topology of the TREK-1 WT and E306A and simulated 3 repeats of each configurations in the POPC bilayer using the same method as described in section 5.2. The overview of the stability and the structural transition is similar with the previous result (**Figure 5.6**). The RMSD of TM domain compared with the initial structure was also stable at ~1.5 Å. Although the TM4 of WT, in a simulation (1 of 3), clearly moved more toward to cytoplasm compared to E306A (**Figure 5.7**), there was no structural transition and significant change in SF observed during 200 ns (**Figure 5.6A, B & Figure 5.7**). However, the re-modelled C-terminal structure now also appeared to be stable as it remains the α-helical in most of the simulation (3 of 6 for WT, 4/6 of E306A). In some of the simulations the unfolding events start from the end of C-terminus (3 of 6 for WT, 2 of 6 for E306A), see Table 5.2. Interestingly, after contacting the original authors of this structure with

these observations, the 5VK5 PDB was superseded by a new 'corrected' PDB file, 6CQ6, which has the 'continuous α-helix' in C-terminus. The re-modelled TREK-1 TM Cα-RMSD compared with this new structure is 0.316 Å

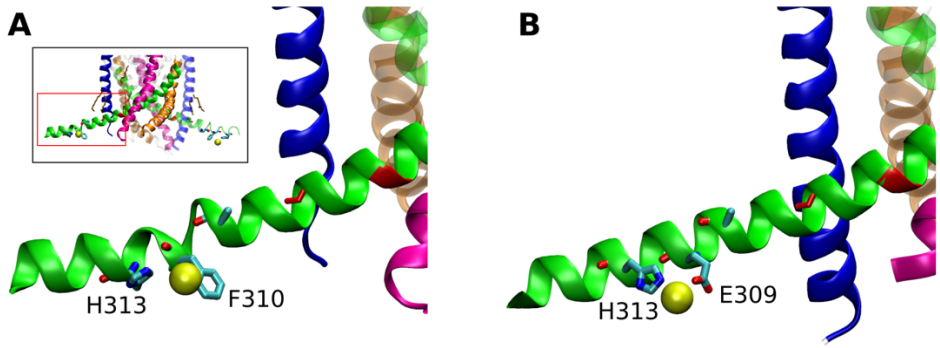


Figure 5.5 Re-modelling of the TREK-1 proximal C-terminal structure. *(A) The TREK-1 apo structure (PDB id: 5VK5), (B) The re-modelled C-terminal based on 5VKP. The re-modelled structure has more reasonable E309 interaction with the Cd^{+}.*

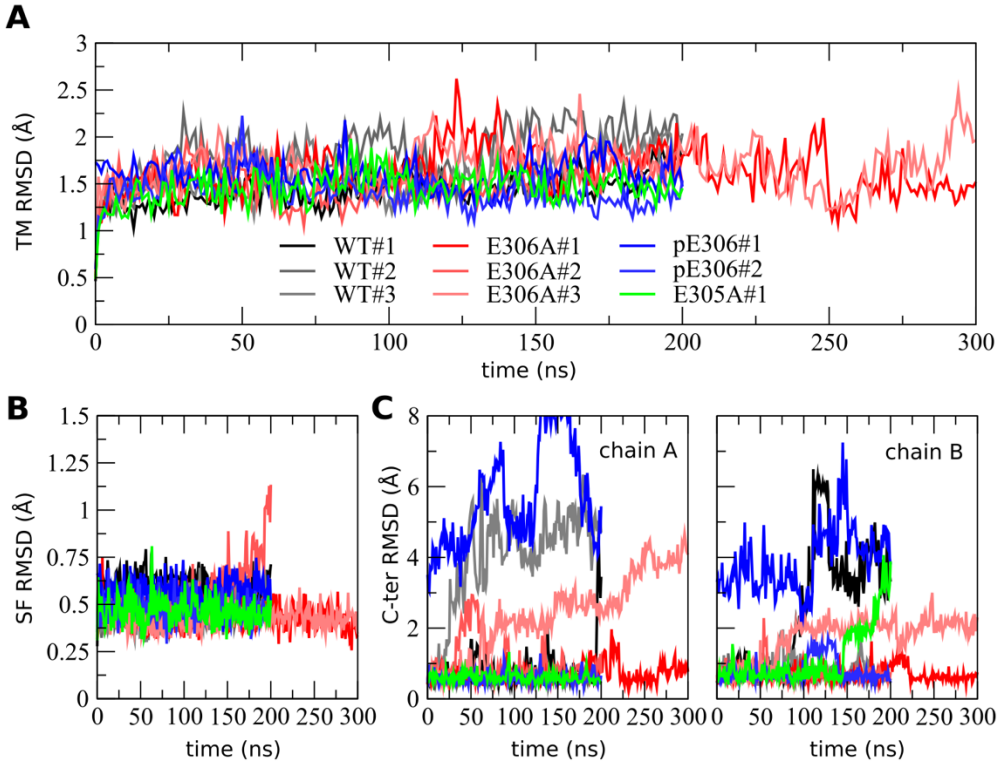


Figure 5.6 The stability of the re-modelled TREK-1. *(A) RMSD of transmembrane domain Cα atoms. The TM regions are stable since RMSDs are stable about 1.5 Å. (B) Cα-RMSDs of selectivity filter. Most of them are stable at 0.5 Å. The large RMSD at ~1 Å caused by the movement of G146 in subunit B. and (C) Cα-RMSD of C-terminal region for each subunit separately. The RMSDs decreases from ~2 Å from previous set of simulations to ~0.5 Å indicates that this re-modelled C-terminal structure is stable. The large RMSDs caused by the unfolding events at the end of C-terminus.*

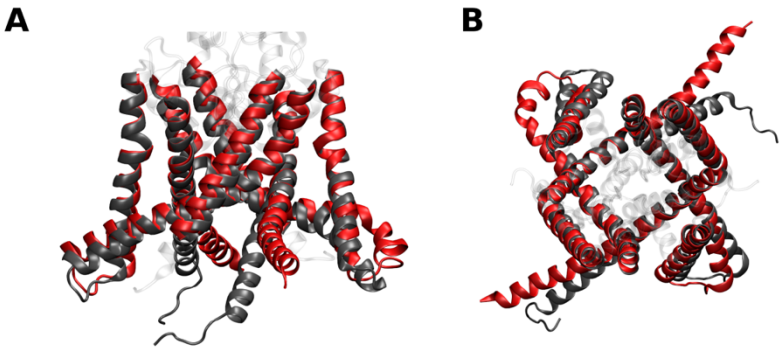


Figure 5.7 Snapshot of re-modelled TREK-1 at 200ns. *(A) front view, (B) side view. In a simulation, there are significant difference in TM4 between WT (black) and E306A (red). However, there is no 'up to down' transition observed.*

Table 5.2 *Secondary structure of re-modelled TREK-1.*

System	Subunit		Unfold	
	A	B	A	B
WT#1	*UF*	*UF*	ALA314	ALA314
WT#2	*αH*	*αH*	-	-
WT#3	*UF*	*αH*	ARG311	-
E306A#1	*αH*	*αH*	-	-
E306A#2	*αH*	*αH*	-	-
E306A#3	*UF*	*UF*	GLU316	TRP317
pE306#1	*UF*	*UF*	ARG311	ARG311
pE306#2	*αH*	*αH*	-	-
E305A#1	*αH*	*HTH*	-	-

HPiH is 'α-helix – π-helix – α-helix', αH is 'α-helix', HTH is 'α-helix – link – α-helix', and UF is unfolded. The unwrapping event started at the end of C-terminus and ended as the residues shown in the table.

5.4 Influence of E306A mutation

Although there is no significant difference between WT and E306A as both remain in the 'up state', the TREK-1 simulations show a very interesting result for the E306 residue and its interaction with its surrounding environment.

5.4.1 Role of E306A in pH TREK-1 sensitivity

The E306A mutation changed interaction from water to lipid. As shown in **Figure 5.8A**, the E306 has a first-shell water interaction about 1.7 Å. However, in E306A, this interaction peak disappears since alanine prefers to interact with lipid rather than water. This also affected the position of the residue in the bilayer (**Figure 5.8B**). E306 remained closer to the water, whereas A306 moved toward to bilayer centre (**Figure 5.9**). This may therefore influence the 'down to up' structural transition of TREK-1 as it may help to lock TREK-1 in the 'up state'. Since E306A is designed to mimic the protonated state of E306, the protonated form of E306 simulation was run with the same protocol, as described in section 5.2. The protonated E306 (pE306) does not have exactly the same result as E306A, nonetheless they have the same trend. Protonation of E306 causes the interaction to shift from water to lipid and positions its residue more toward to bilayer centre. However, the effect of this neutralisation is not strong as the E306A.

5.4.2 E305A does not change the local interaction.

At the proximal C-terminus, there are 2 glutamates located next to each other (E305 and E306). However, only E306A has a significant effect on the TREK-1 pH activation, whereas E305A does not [264]. Therefore, as a control for our observation, we simulated TREK-1 with the E305A mutation using the method in section 5.2. Interestingly, although the E305A eliminates the first-shell of water interaction (**Figure 5.8A**), the

interaction does not shift from water to lipid. In contrast to A306, the A305 is still close to water (at ~2 Å) rather than lipids. In addition, the position of A306 does not move toward to bilayer centre (**Figure 5.8B & 9**). The different between E305A and E306A behaviour may relate to their orientation in the secondary structure. The E305 points toward the water whereas E306 locates slightly higher than E305, and may therefore explain the unique properties of this residue.

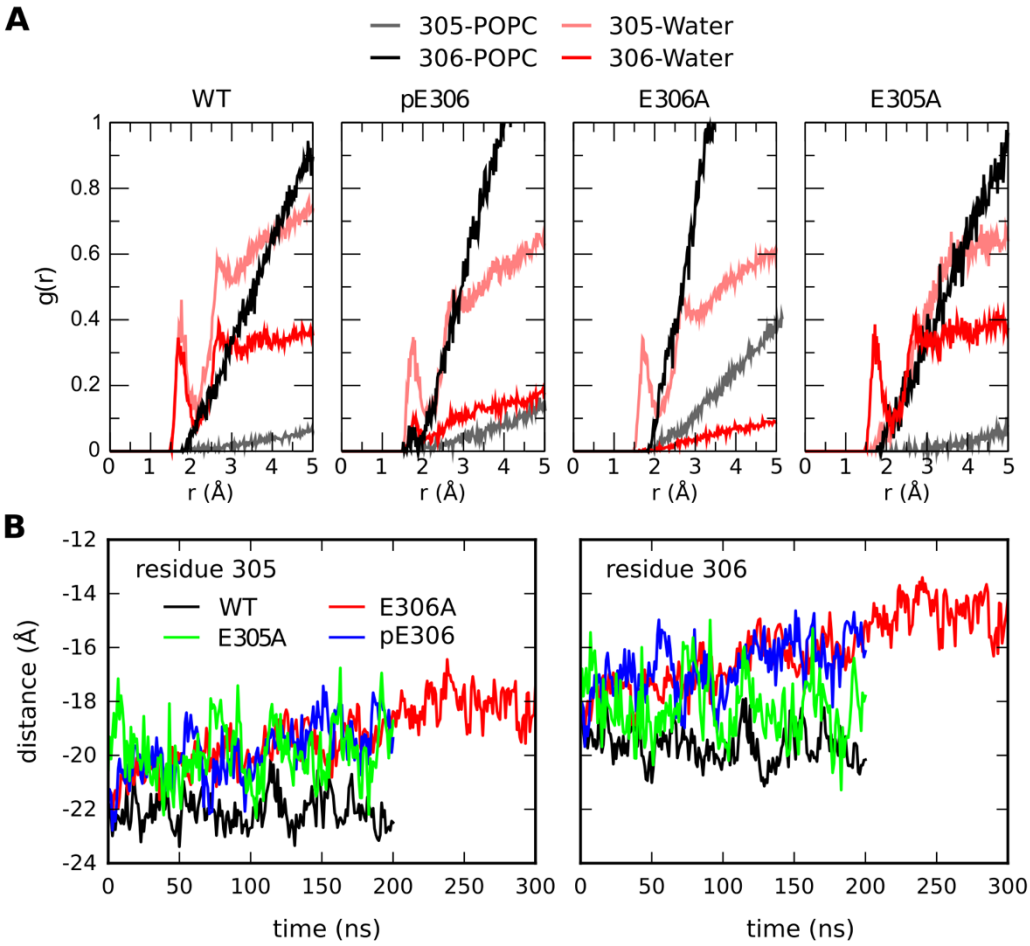


Figure 5.8 The local interactions about residue 305 and 306. *(A) RDF of residue 305 and 306. In WT both E305 and E306 are hydrated since there were water molecules surrounding (red and light-red line). E306A mutant and protonation of E306 made the first water shell disappear (red line). Hence, the residue 306 shifted to interact with lipid (black line). In E305A, the first water peak also disappeared (light-red line), nonetheless A305 preferred interaction with water rather than lipids (grey line). (B) Distance of residues 305 and 306 respected to the bilayer centre. E306A (red line) and pE306 (blue line) moved toward bilayer centre whereas WT (black line) and E305A (green line) remained to same location.*

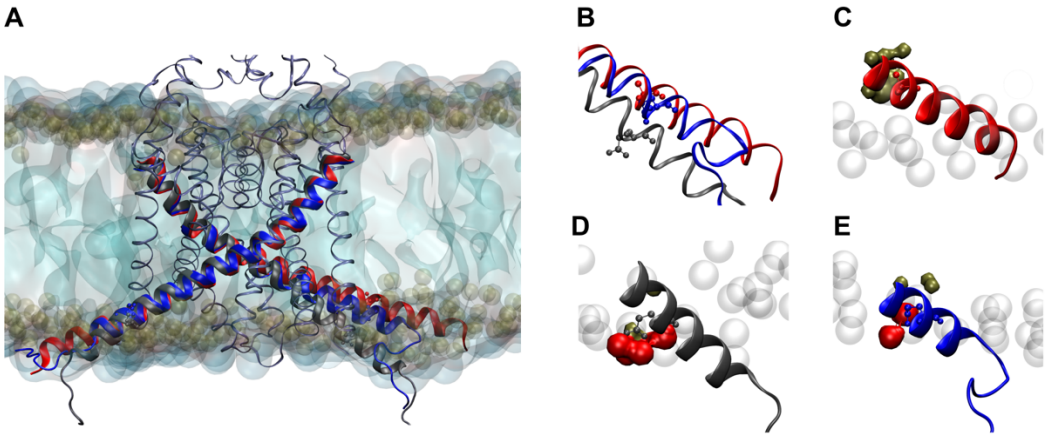


Figure 5.9 Structure overlay at 200 ns of the simulations. *(A) Overlay of TREK-1 E306A (red), pE306 (blue), WT (black). The pE306 was extended and protonated from WT simulation. (B) Zoom-in at the C-terminus. (C-E) Residue 306 (E306A (C), E306 (D), pE306 (E)) and its nearby atoms (within 3 Å) showing in surface representation. Lipids are brown, and water is red.*

5.4.3 E306A mutation and stretch activation

The previous studies[73,135,241] and Chapter 3 suggest that the 'up state' represents the membrane stretch activated state of TREK channels. Also, the E306A TREK-1 crystal structure appears locked in the 'up state'. However, the relation between pH and stretch activation is still unclear. Surprisingly, there is a fluctuation in APL of the POPC bilayer observed during the simulation (**Figure 5.10**). Interestingly, this only presented in E306A (2 of 3) and protonated E306 (1 of 2) simulations, but not in WT simulations. Moreover, there was some correlation with the movement of TM4. Because the movement of TM4 started before the expansion of the APL and the time scale is different from the 'down to up' transition caused by stretch protocol in Chapter 1, this implied that the TREK-1 with E306A may have an influence on the bilayer. This expansion is only seen in the re-modelled simulations and may relate to the structure of the C-terminus. However, there are still 2 possibilities: First, the 'up state' does not favour the no-stretch bilayer, therefore this then causes the fluctuation. Second, it is an artefact from the pressure coupling. Further investigation is needed. Unfortunately, we cannot do a stretch simulation from the 'down state' to the 'up state', because the structure already is in the 'up state'.

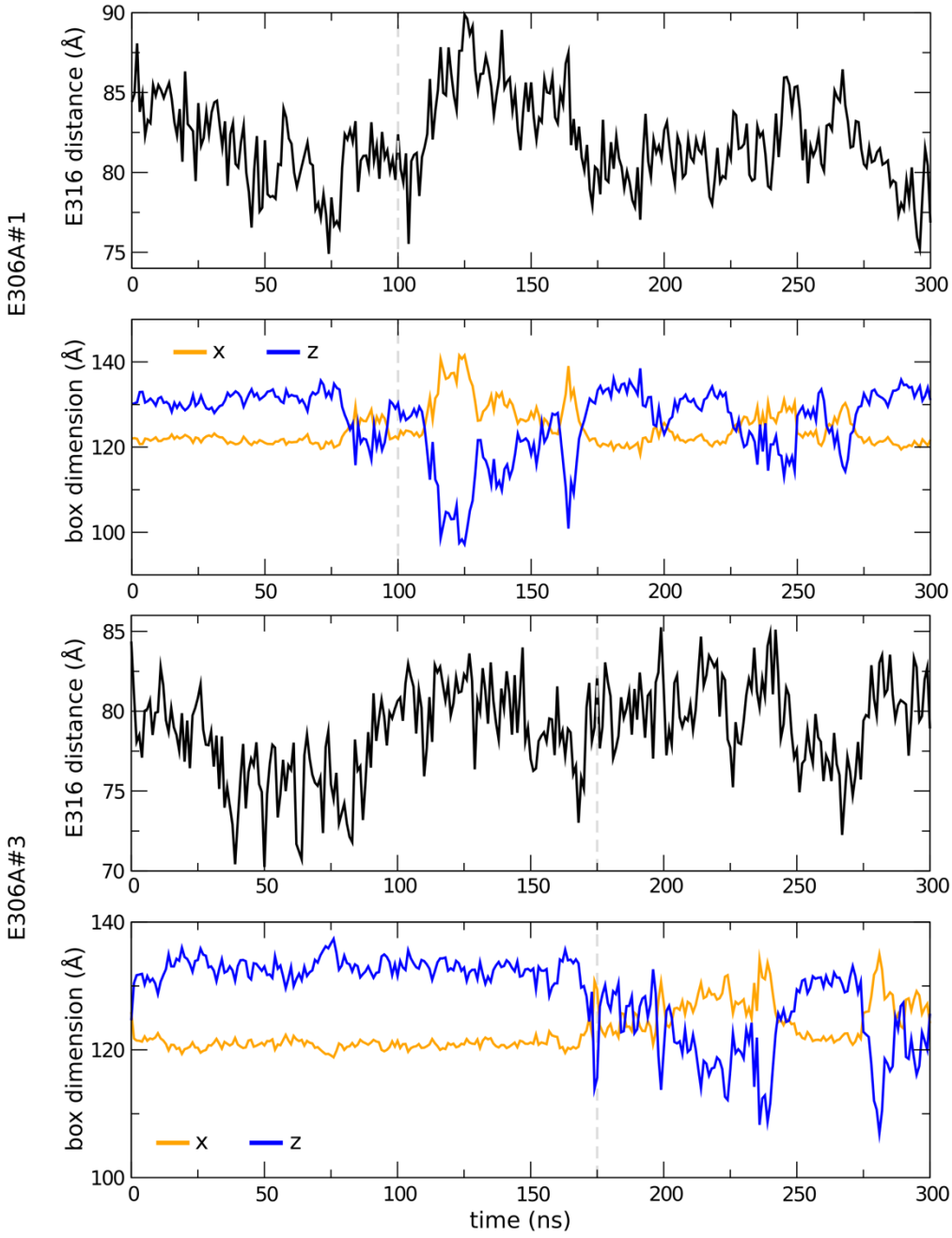


Figure 5.10 Effect of E306A mutation on lipid bilayer. *The E316 in-plane distance between two subunits represent the lateral expansion of TM4. The box dimension in x (orange) and z (blue) direction. Note that box dimension in x and y is equal because semi-isotropic pressure coupling. These two E306A simulations showed the fluctuation of the simulation box, in the other word, the fluctuation of area per lipid. There was some relation between the movement of TM4 and the fluctuation, since lateral expansion of TM4 (black line) related to the expansion in the bilayer plane (yellow line).*

5.5 Discussion

The MD simulation of the new TREK-1 provides insight how these E306 mutations mimics the protonated state of E306. Both have similar local interaction behaviour since they like to interact with lipid rather than water. This makes the C-terminus move slightly closer to the bilayer centre then lock TREK-1 in the 'up state'. The communication between C-terminus and selectivity filter was suggested to be facilitated by the TM4[271]. Therefore, intracellular acidification may activate TREK-1 by protonating glutamates leading to the 'down to up' transition and then signals from proximal C-terminus to the selectivity filter through these movements of TM4. The relation between mechanosensitivity and intracellular acidification is strongly suggested form MD simulation since both their activation states appear to correlate with the 'up state'. This could be the reason why neither E306A mutant nor pH-activated WT channel have significant further activation upon membrane stretch[131]. This is because intracellular acidification makes TREK-1 fully move to the conductive 'up state', and so the membrane stretch cannot drive any further structural transition. Knowledge of this behaviour of TREK-1 also leads to improving our understanding of TREK-2 because they are so structurally related, also it has been known that for TREK-2 there the mechanisms of mechanosensitivity and intracellular pH sensitivity are also very similar [267].

5.6 Summary

In this chapter, the influence of the TREK-1 E306A mutation, which mimics TREK-1 pH activation, is investigated using MD simulation. The stability of TREK-1 in a POPC bilayer was first determined followed by re-modelling of the C-terminal region. The results show that the E306A shifts its interaction from water towards lipid and makes the C-terminus moves up to position closer to the bilayer centre. A similar behaviour appears for the protonated state of E306, but not E305A. This may be related to the position of these two residues. The E306A potentially alters the bilayer and creates a stretch-like bilayer expansion without any additional pressure. This study shows insight from the molecular level of the E306A mutant contributes to our understanding of TREK internal pH sensitivity.

Chapter 6
Non-Bonded Force Distribution Analysis

6.1 Introduction

In the previous chapters, the mechanisms underlying stretch activation of TREK-2 were examined and discussed. However, the reason why only some K_{2P} channels are mechanosensitive and others (e.g. TWIK-1) are not is still unknown. One of the possible explanations is differences in how forces are distributed and transmitted between the protein and lipid bilayer. With the exception of the kink at the end of TM4 helix in TWIK-1, the overall structures of TREK-2 and TWIK-1 are quite similar, but their sequence similarity is very low. This may cause different patterns of protein-protein and protein-lipid interactions. Unfortunately, currently available tools are not sufficient to gather useful information. In this chapter, a new approach 'Non-Bonded Force Distribution Analysis' (NB-FDA) was developed and applied to this problem in an attempt to provide insight into how forces distribute/transmit between protein-lipids and also between protein helices. In addition, the allosteric pathway during the stretch activation was also investigated to explain how changes in the lower half of protein might be transmitted to the selectivity filter.

6.1.1 Perspectives and hypothesis

Mechanosensitivity of K_{2P} channels. As mentioned above, the main structural difference between TREK-2 and TWIK-1 is the kink at the end of TM4 (**Figure 6.1**). However, TWIK-1 and TREK-2 identity is relatively low at 17.8% and only 21.6% with TREK-1 (an alignment shown in **Figure 6.12**). The differences in the sequences of these proteins consequently cause differences in the protein-lipid interaction pattern and also affect the distribution of internal forces in the protein. This may explain why TREK channels are mechanosensitive whereas TWIK channels are not.

Allosteric pathways that communicate between changes in upper and lower half of the TREK-2 protein. The 'down to up' stretch activation model describes how TREK channels structurally respond to a membrane stretch. The further studies[254,255,272] of TREK channels strongly support the stretch activation gate located at selectivity filter. However, how changes in the lower half of the protein influence the selectivity filter, which is located in the upper half is still unclear. Electrophysiology studies[271,273] suggested there is coupling of TM2 and/or TM4 with the selectivity filter via movement of the helices at the conserved glycine hinges. Nevertheless, the details of the pathway remain unknown, i.e. whether it propagates along the helices and then through the loops which directly connected to the selectivity filter, or propagates through the pore lining helices and then affects the stability of selectivity filter.

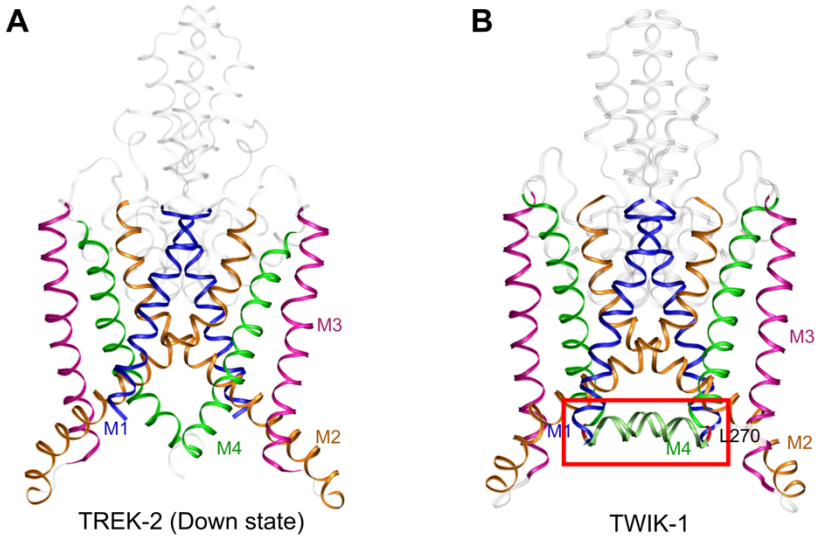


Figure 6.1 The difference between TREK and TWIK channel. *This figure shows the crystal structure of (A) TREK-2 and (B) TWIK-1. Overall, structures are quite similar. The major difference is the hinge (at L270) about the end of TM4 helix (red box).*

6.1.2 Available analysis tools

To investigate the above questions, there are currently available tools that can analyse the following 3 categories: (i) protein-lipid interactions, (ii) bilayer internal interactions and (iii) protein surface/internal interactions and conformational landscapes.

Protein-lipid interactions. There are three methods commonly used to analyse a homogeneous bilayer: radius distribution function (RDF), lipid contact analysis, and 2D-density map. These tools can also be used together. For example, using RDF to determine the interaction *cut-off* then calculating a lipid contact that counts the number of lipid molecules within the *cut-off* distance from a given residue and finally crosschecking with 2D-density map of protein and lipid. These provide the information where on the protein surface the lipid frequently visits hence indicating hot spots for lipid binding sites. These all are distance based analysis, and apart from performing potential mean force (PMF) calculation[274], there are currently no available tools to obtain any energetic information.

Protein surface/internal interactions and conformational landscapes. Computationally, to identify a critical residue for protein function, there are two different perspectives: (i) using evolutionary coupling information, or (ii) considering correlated motions (i.e. changes in corrective variable that correlated with the protein motion). The evolutionary coupling information approach assumes that evolutionarily coupled residues are likely to create a strong selective interaction for specific function. This method is based on predicting structures/models then performing simulations to expose the protein conformational landscapes[275–281]. In contrast, in the latter approach, the simulation is initially run to obtain collective variables (e.g. positions, distances), then comparing these variables with the protein motion to see if they have any correlation. This approach is also used to identify protein allosteric pathways[282,283]. Recently, Force Distribution Analysis (FDA)[284,285] was developed using forces as a collective variable to obtain not only dynamic, but also energetic information. Briefly, FDA computes pair-wise force between atom *i* and *j* from MD trajectory. However, for a given atom in a molecule in an MD simulation, the net force due to interactions with neighbouring atoms may be close to zero, therefore the '*punctual stress*' is defined as summation of force absolute values (equation 6.4) and used as collective variables.

Bilayer internal interactions. The distribution of forces within a lipid bilayer is complicated because a lipid bilayer is formed by many lipid molecules. Currently there are two approaches that attempt to represent this complexity. There are bilayer pressure profiles[19,235,237,286,287] (see section 2.4) and Lipid-Force Distribution Analysis (L-FDA) [288]. The L-FDA is based on the FDA[284,285], and optimised for lipids. Unfortunately, these tools are unable to provide the propagation of forces within the bilayer as a function of time.

6.1.3 Theory

In molecular dynamics (MD), there are two types of forces: bonded, and non-bonded (**Figure 6.2**, also see Chapter 2 for more detail). Interactions between molecules (e.g. protein-lipid interactions or protein inter-helix side-chain interactions) are only described by the non-bonded interactions which are Coulomb and Lennard-Jones (LJ) potentials. These are long-range interactions. The Coulomb force represents charge property, whereas LJ force is an approximate description of Pauli repulsion and Van der Waals forces. For convenience and unit compatibility, the calculation of Coulomb and LJ force is done by the equations 6.1 and 6.2, respectively. These equations are provided by GROMACS manual[142], and are compatible with the CHARMM36 forcefield[198] and reduced unit.

$$\boldsymbol{F}_i^C(\boldsymbol{r}_{ij}) = \frac{f q_i q_j}{\varepsilon_r r_{ij}^2} \frac{\boldsymbol{r}_{ij}}{r_{ij}} \tag{6.1}$$

Where f is $\frac{1}{4\pi\varepsilon_0}$ = 138.935485 in reduced unit, ε_r is dielectric constant, q_i and q_j is charges for an atom *i* and *j*, $\boldsymbol{r}_{ij}$ is a distance from an atom *i* to an atom *j*.

$$\boldsymbol{F}_i^{LJ}(\boldsymbol{r}_{ij}) = \left(\frac{12C_{ij}^{12}}{r_{ij}^{13}} - \frac{6C_{ij}^{6}}{r_{ij}^{7}}\right) \frac{\boldsymbol{r}_{ij}}{r_{ij}} \tag{6.2}$$

Where C_{ij}^6 and C_{ij}^{12} are constant regarding to a pair of atom *i* and atom j for r^6 and r^{12} (for potential, hence r^7 and r^{13} for force).

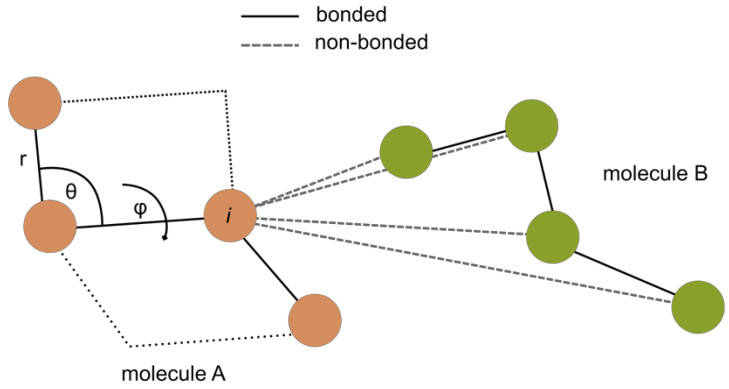


Figure 6.2 Bonded and Non-Bonded forces in MD simulations. *Bonded interactions describe interactions within molecule, for example bonded, angle, and dihedral. Non-bonded interactions are responsible for interaction between two molecules, in this case molecule A and molecule B. Bonded interactions are represented by solid line, non-bonded interactions on atom i of molecule A from atoms of molecule B represented by dashed line.*

6.1.4 Aims and direction

Aims of this study are (i) to examine the differences between the mechanosensitive K_{2P} channels (TREK-2) and the non-mechanosensitive channels (TWIK-1) and (ii) investigate allosteric pathway between the lower half of the TREK-2 and its selectivity filter in upper half. These were done by using considering correlated residue interaction with protein dynamics. Unfortunately, the currently available tools are not suitable for the following reasons.

(i) Tools for protein-lipid interaction only provide dynamic information but not energetic interactions which is important when considering force propagation between protein and lipid.

(ii) The FDA, which provides energetic information, is only available in either time-averaged punctual stress between residue pairs or time-dependent punctual stress on residues. However, to accurately investigate allosteric pathways the time-dependent punctual stress between residue pairs is needed.

I developed a new tool called Non-Bonded Force Distribution Analysis (NB-FDA) to fulfil this requirement. It is written in Python and based on FDA, but only considers the non-bonded interactions, because only non-bonded interactions play a significant role in interactions between molecules. This also reduces the complexity of 3-body and 4-body force decompositions and technically requires only simple non-bonded parameters. Apart from the above reasons, there are also other technical reasons to develop this new tool as follows: (i) the ability to fully control the output (e.g. level of details, format) that smooths overall analysis pipeline, (ii) to avoid issues in the installation process of GROMACS (GROMACS compatibility between each version is relatively low).

6.2 Development and implementation of NB-FDA

Although the NB-FDA concept is a relatively simple classical physics approach, the computational method is challenging. Since the electrostatic interaction is a pair-wise force, the number of interactions will be $N \times (N-1)$, for the system of N paricles. This means that for a TREK channel, with ~8,000 particles, this results in ~64 million interactions and hence is computationally expensive. For optimisation, the NB-FDA is written in 3 separate Python 2.7 scripts. There were optimised for protein internal interactions (e.g. interaction between helices), protein-lipid interactions, and lipid-lipid (bilayer) interaction. The overall algorithms are similar, but their searching selection and pre-calculation steps are slightly different. The first version of NB-FDA protein-protein (i.e. protein inter-helix interaction) took 6 minutes per frame for a CG TREK-2 simulation which had ~1,500 protein particles. It was therefore impossible to run this for an all-atom simulation with ~8,000 protein particles. In contrast, the current version takes less than 10 seconds per frame in CG and ~30 seconds per frame in all-atoms. To achieve this efficiency a number of computational techniques were used. The global algorithm is shown in (**Figure 6.3**). There are 5 main sections: i) setting up, ii) pre-calculation, iii) calculation, iv) statistical analysis, and v) output. The scripts and related tools can be found in GitHub (https://github.com/ViwanJ/Thesis). The related input and output files are provided for demonstration purposes. The technical details are all shown in **Table 6.1**.

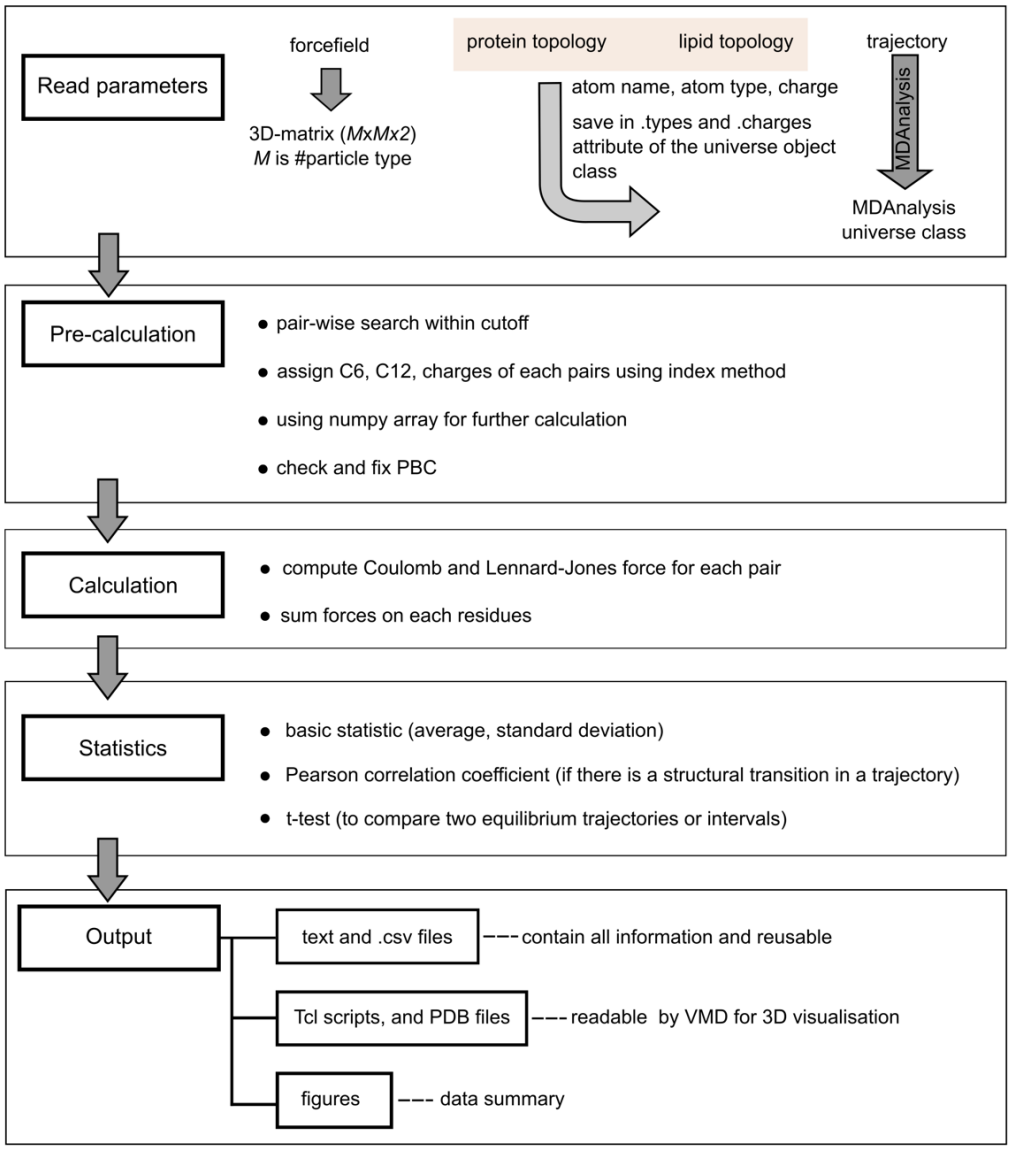


Figure 6.3 Global NB-FDA algorithm.

Table 6.1 *Technical details.*

Python Version	2.7
IDE	Ipython[289]
Standard library	sys, os, timeit, math, json, argparse, ast
Common Library	Numpy[290,291], Pandas[292,293], Scipy[294], Matplotlib[295]
MD library	MDAnalysis[226,227]
Output format	Data tables (.csv .json) and graphs, 3D-structure (.pdb) and associated Tcl script (for VMD)

6.2.1 Setting up

Initially, the script first sets up its environment for the calculation. There are 3 major parts: force-field, protein/lipid topology and their trajectory (coordinates), and user-defined parameters. To calculate interaction forces, all related parameters must be loaded (**Figure 6.4**). In this case, only non-bonded interactions are considered, therefore only non-bonded parameters (C_6, C_{12}, and charge) are loaded from the force-field using *Pandas* (a Python library) and put into a 3-dimensional matrix. If it is necessary, the combination rule is performed before putting the force-field into the matrix. For CHARMM force filed the combination rules are $\sigma_{ij} = {}^{1}/_{2}\left(\sigma_{ii} + \sigma_{jj}\right)$ and $\varepsilon_{ij} = \left(\varepsilon_{ii}\varepsilon_{jj}\right)^{1/2}$ [240]. The trajectory is read by using the MDAnalysis package and is kept in the universe class. Protein and lipid topology are loaded using *Pandas* and assigned to the attribute under the MDAnalysis universe class.

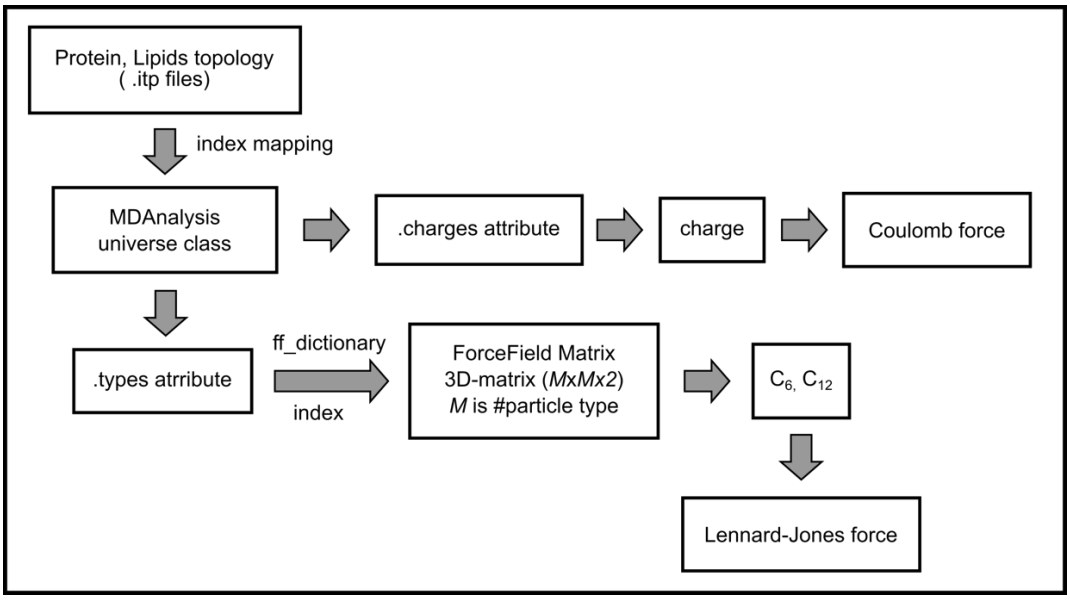


Figure 6.4 diagram describe read/call of non-bonded parameters. *Protein and lipid topologies were read and mapped into the MDAnalysis class using their indices. The atom charge and atom type property were save as .charges and .types attribute, respectively. This is to avoid the human errors that may be occur if using independent arrays. To call these parameters for the calculation, the charge of each particle can be called directly from .charges attribute, whereas C_6, C_{12} are called by using the combination of dictionary and indexing method through the atom type property. The .types attribute is called and fed into ff_dictionary, then translated to an index. Since it is pair-wise, therefore this will result in 2 indices that will map to the position of first 2-dimension in 3D ForceField Matrix. The 3rd dimension of the same position will result in C_6 and C_{12} of the pair.*

6.2.2 Pre-calculation

Pre-calculation is the most time-consuming step as it takes about two-thirds of the total computing time. To speed up the calculation and reduce the amount of required memory, a distance cut-off approach is used to reduce number of interaction pairs. This method is reasonable because only local interactions (i.e. first shell interaction) are considered and these are the forces suggested to play the most important roles. Atom pairs (two atoms where the distance between them are less than the *cut-off)* are searched by using an MDAnalysis selection method with the KB-tree algorithm. Their indices and all related parameters are put in the array format (**Figure 6.5**). Before preforming the calculation, the distance problem caused by PBC is fixed (see **Figures 6.6 & 6.7**).

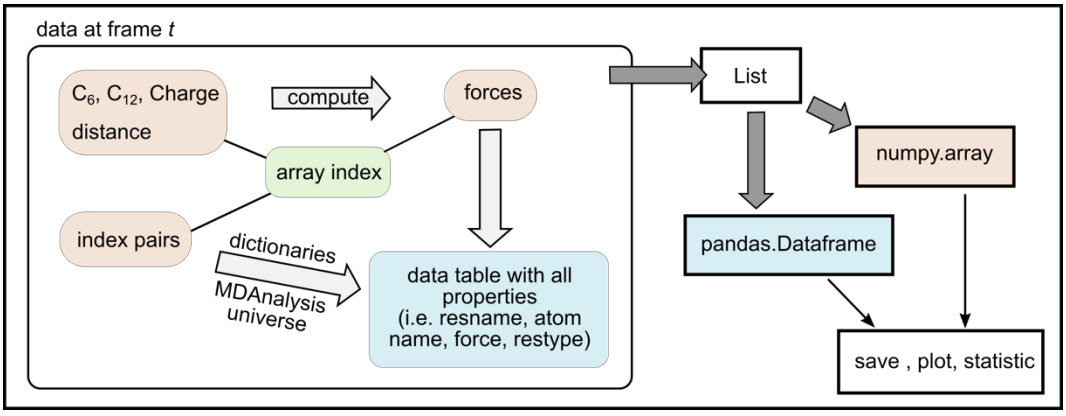


Figure 6.5 NB-FDA internal data structure. *The diagram shows how relevant parameters are kept internally. The majority of data sets (C_6, C_6, Charge, distance (r), forces, index pairs) are kept in the NumPy array. This is for memory (RAM) and calculation reason, since NumPy array occupies less memory than list and has elementwise operational method which ~80 times faster than normal for loop. All properties (resname, restype (polarity) and etc.) of each atom can be called through its index by using either dictionary or MDAnalysis. These properties and forces are collected in a pandas DataFrame as a table-like format. This benefits for data mining because of pandas DataFrame properties and method, e.g., summation of forces of each residue or average forces from each part of lipid on each amino acid type. The data of each frame (time step) is collected into a list than converted into a NumPy array and pandas DataFrame for later analysis.*

6.2.3 Calculation and statistical analysis

The Coulomb and Lennard-Jones forces are computed using equations 6.1 and 6.2. For Coulomb force, the dielectric constant is user-defined parameter which is 1 by default for all for all-atom. For each atom pair, the force on atom *i* from atom *j* (F_{ij}) is the summation of Coulomb and LJ force, equation 6.3. Using the basic of FDA[285], the '*punctual stress*', s_i, is defined as the summation of the magnitude of forces on an atom i, equation 6.4. This summation is done by the *Pandas* library. Then all statistics (i.e. time-average and standard deviation of '*punctual stress*') are computed by using *NumPy* and *Pandas* packages.

$$\boldsymbol{F}_{ij} = \boldsymbol{F}_C + \boldsymbol{F}_{LJ} \tag{6.3}$$

$$s_i = \sum_j |\boldsymbol{F_{ij}}| \tag{6.4}$$

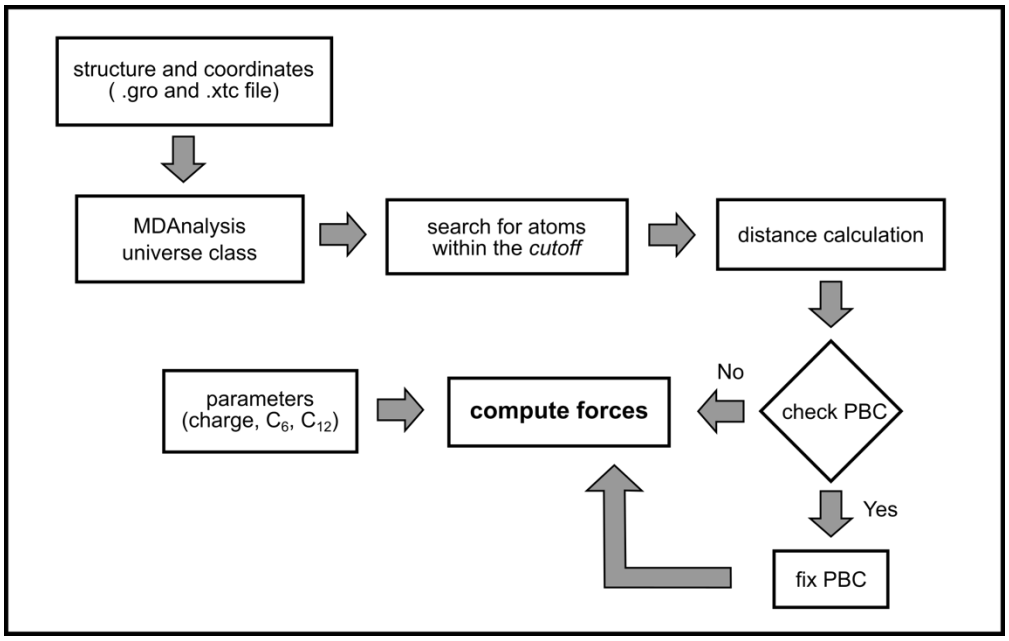


Figure 6.6 Diagram of the pre-calculation and forces calculations.

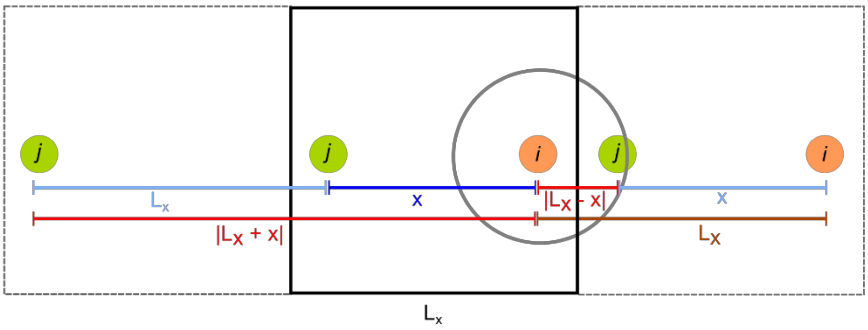


Figure 6.7 diagram of periodic boundary condition. *The solid line indicates the real system. The dash line indicates PBC images. The MDAnalysis selection includes PBC images, therefore it also gives the atom pairs where their image fall in the cut-off. However, coordinate attribute does not provide the image coordinates. For example, atom j image is in the cut-off distance of atom i. The distance calculated from coordinate attribute between atom i and atom j is x which is incorrect. The correct distance is* $L_x - x$ *which is the distance from the image of atom j. In general cases, the correct distance for force calculation is the shortest distance between atom i and atom j and its 2 images which is the minimum of the absolute values of three distances.*

6.2.4 Output

A considerable quantity of data is generated by the script. Saving this data is a challenge since it must be easy to reuse or readable by other visualisation softwares (i.e. VMD). The output consists of graphs and texts. Graphs are saved in SVG and PNG format and show the summary information. Texts are saved in either CSV or JSON format and have two functions: i) keep all details, ii) readable by other software, iii) reusable. Since the aims of NF-FDA is to get insight of each amino acid, the main output is time-dependent '*punctual stress*' on each residue or each molecule pairs. This information is also available in different scales (all-atom, coarse-grained, molecular, lipid-part, protein polarity). Because the information from all-atom level is extremely large and requires large amount of space (>20GB in the TREK channel case), by default, it is not printed out. The user-friendly level is molecular (e.g. *stress* shown on each residue or residue pair). Some examples of these NB-FDA outputs are shown in the Section 6.3 (protein-lipid) and 6.4 (internal protein side-chain). All results are from all-atom simulations that were performed in Chapter 3 unless otherwise specified.

6.3 Protein-lipid interaction

6.3.1 NB-FDA and traditional lipid contact analysis

To demonstrate the advantages of NB-FDA, I compared NB-FDA protein-lipid analysis with the traditional lipid contact analysis (LCA). In this case, LCA is separated into two parts: head and tail. The LCA-head is defined as a number of Phosphate (P) or Nitrogen (N) atoms within the cut-off. LCA-tail definition is an amount of lipid tail Carbon (C) atoms within the cut-off. Generally, the cut-off for most of contact analysis is determined by using the value of the first minimum of radius distribution function (RDF) between two reference groups. Therefore, RDF between protein and P, N, and C atoms was calculated and found that the first minimum is 3.42 Å for P or N atoms and 6.65 Å for C atoms (**Figure 6.8A**). Since the LCA result was expected to change upon changes in cut-off and that the presence of protein hydrogen atoms will obviously affect the RDF, this also was re-computed using only protein heavy atoms instead of including hydrogen atoms. Thus, the first minimum increased from 3.42 Å to 4.43 Å.

The LCA result (**Figure 6.8B & 6.9**) clearly shows that it is cut-off dependent since the results of all cut-offs were different. In the case of the LCA-head, an increase in cut-off radii results in a wider range of highlighted residues. However, they all highlighted the same lipid binding hot spots. Importantly, they emphasised high lipid contact residues at the same places, mostly arginine(s) and lysine(s). Similar changes also applied in the LCA-tail analysis. However, it also highlighted valine, isoleucine, leucine, proline, tryptophan, and phenylalanine. NB-FDA simultaneously combined the head and tail protein-lipid interactions. In addition, it demonstrated an ability to distinguish between a residue that indeed has interactions and a nearby residue. For example, A97, G184, and Y301 were dropped by NB-FDA.

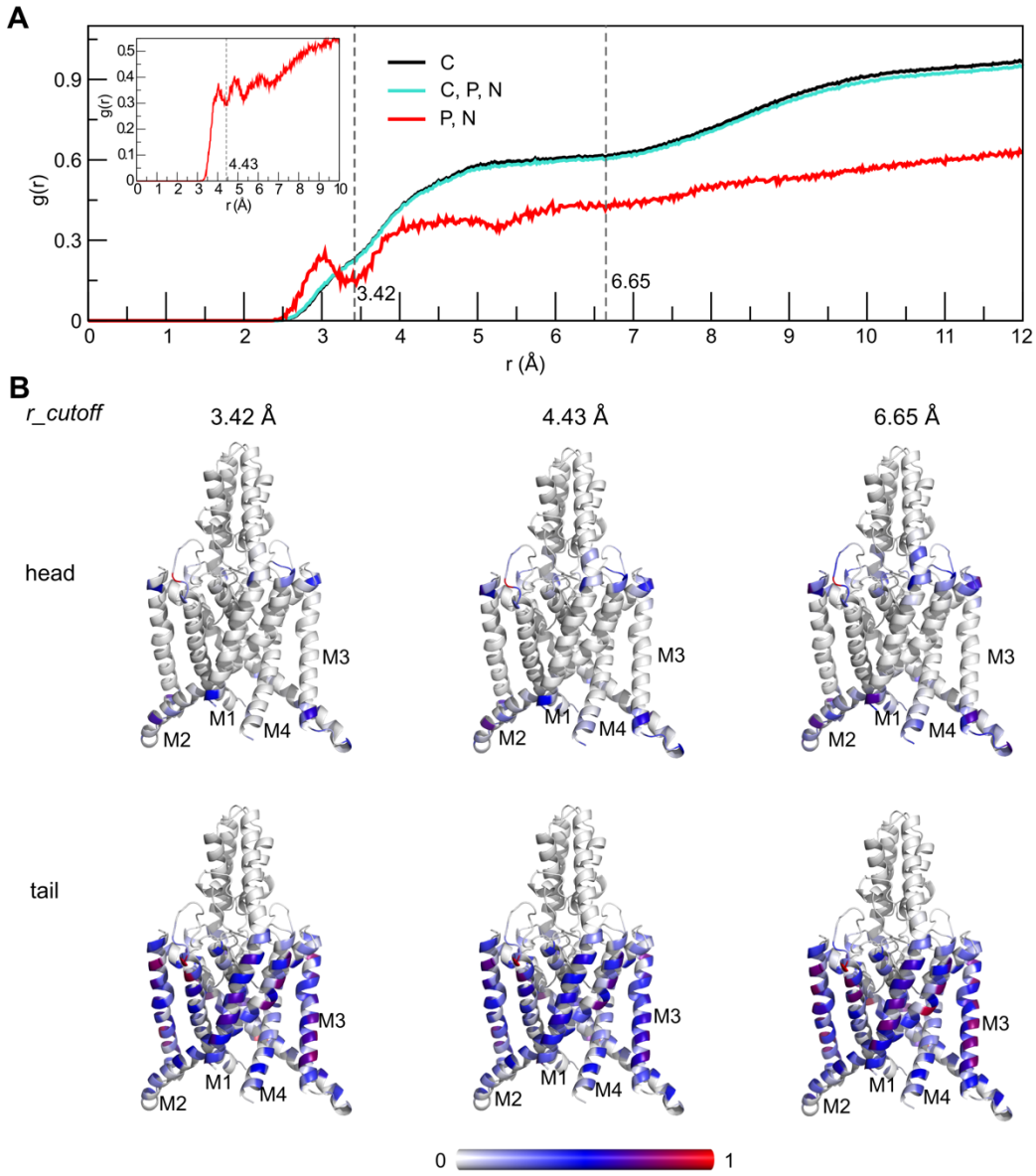


Figure 6.8 Lipid contact analysis. *(A) RDF between Phosphate (P), Nitrogen (N) or Carbon (C) atoms of lipids and protein. The first minimum for LCA-head is 3.42 Å and LCA-tail is 6.65 Å. Since this first minimum of LCA-tail is not obviously clear, it is only used for comparison reasons. The inset is RDF between P or N atom of lipids and protein without hydrogen atoms (i.e. protein heavy atoms). Without the hydrogen atoms, the RDF of P and N first minimum increased to 4.43 Å. (B) Lipid contact analysis of TREK-2 in no-stretch bilayer simulation at different cut-off: 3.42 Å, 4.43 Å, 6.65 Å. The results were averaged over 4 trajectories of 200 ns simulations. The colour scale ranges from white, blue, and red. It was normalised by the maximum number of lipid contact. For LCA-head, increase in cut-off radii results in wider highlighted lipid binding residues. However, they emphasised high lipid contact residues at the same places. Similar changes also show in the LCA-tail.*

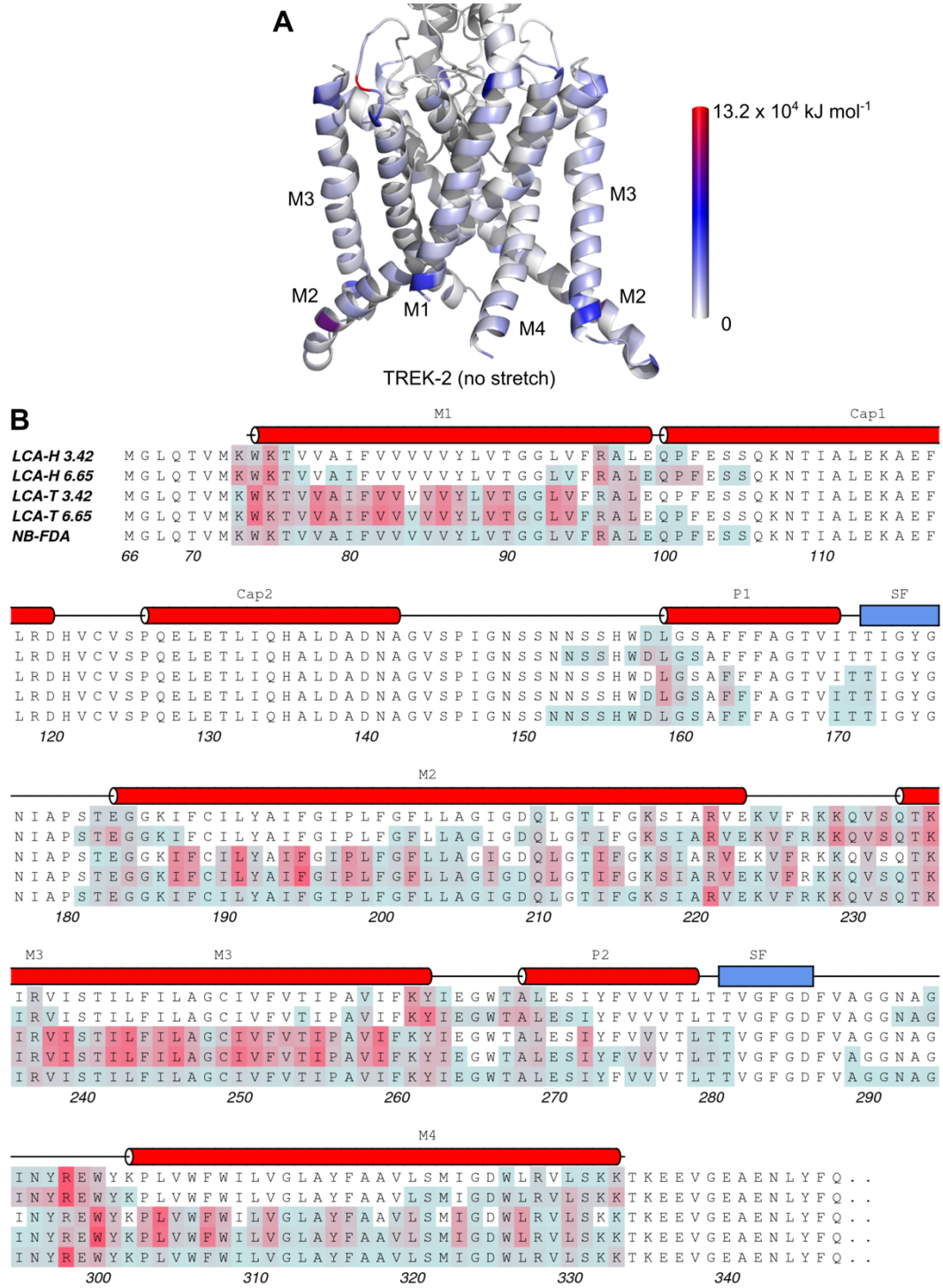


Figure 6.9 Lipid contact analysis and NB-FDA. *(A) The NB-FDA result map on the TREK-2 structure. The colour scale ranges from white to blue, to red. (B) LCA and NB-FDA mapped on the sequence of TREK-2 chain A. The colour scale ranges from light blue to red. This illustrates the effect of chosen radii on LCA. A short cut-off may not cover some of resides. In contrast, in LCA with a long cut-off, residues were over selected. NB-FDA simultaneously combined the head and tail protein-lipid interactions. It dropped some of residue (e.g. A79, A97, G184, C249) that highlighted by the long cut-off LCA. LCA-H/T stands for lipid contact analysis of head group and tails respectively; the followed numbers indicate the cut-off.*

6.3.2 General protein-lipid interactions in TREK-2 and TWIK

The information of TREK-2/POPC and TWIK-1/POPC interactions analysed by NB-FDA were summarised and shown at molecular level (**Figure 6.10 & 6.11**). This information shows that each amino acid has its own lipid preference. In the case of TREK-2 and TWIK-1, the strongest interaction is the interaction between arginine-lipid head group. This is related to the number of charged nitrogen atoms in the side-chain. The asparagine-lipid tail interaction seems to be the weakest in these two cases. This is obvious because most asparagine(s) are located in the extracellular loops, but near membrane, therefore they are not fully exposed to the lipid tails. Interestingly, histidine behaves differently in TREK-2 and TWIK-1. The reason is unclear, but may relate to the sequence and its position in the bilayer. Considering the normalised head/tail (H/T) score, asparagine has the highest score because its tail interaction is very small. As expected, apart from histidine, most of the acidic and basic polar amino acids have high scores. Methionine, glycine, and alanine all appeared in the middle. This is reasonable considering their short side-chain size. An increase of a hydrocarbon chain length (aspartate to glutamate, asparagine to glutamine) significantly increases the interaction with lipid tails.

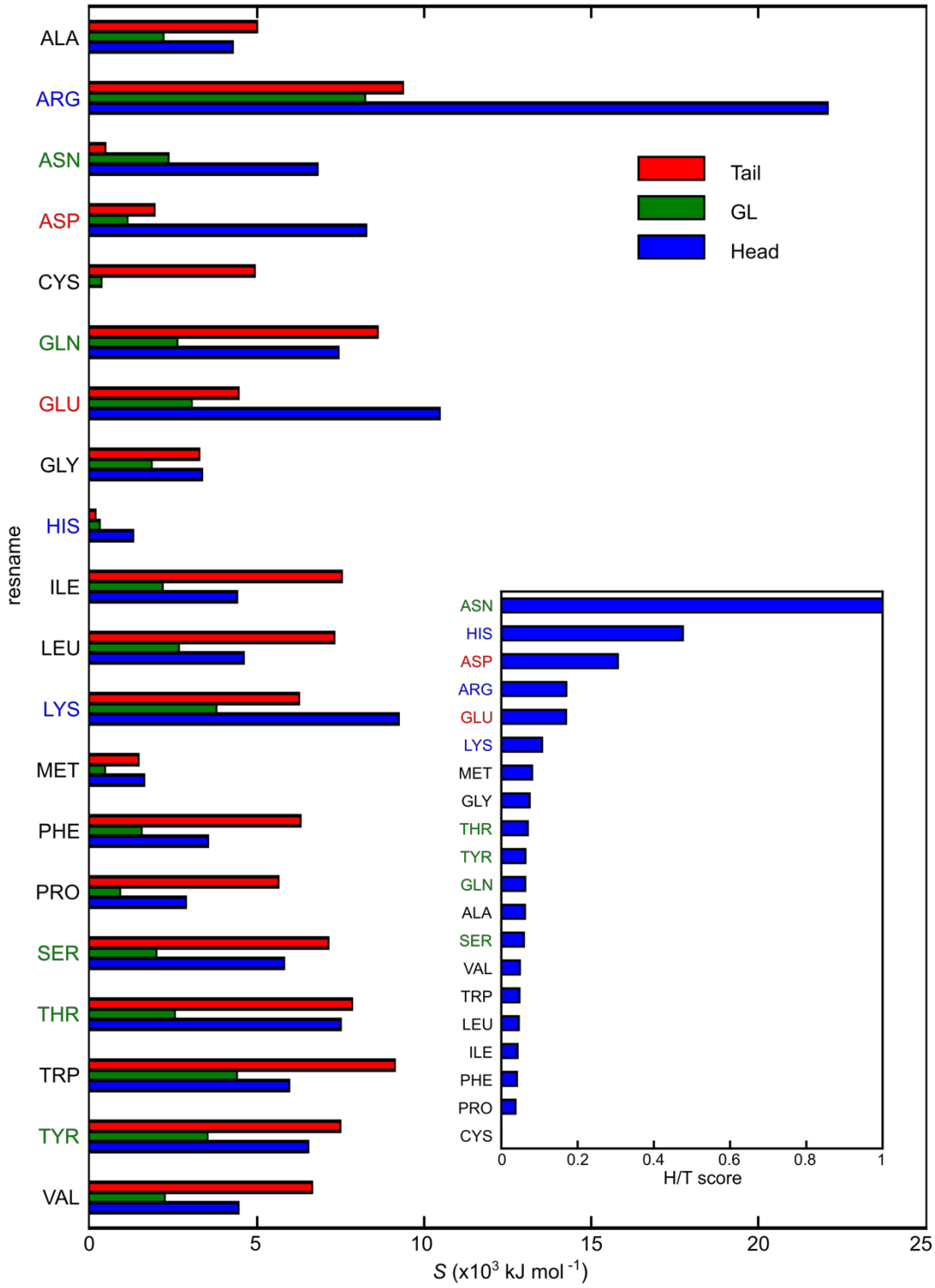


Figure 6.10 General Protein-lipid interaction of TREK-2. *The inset is normalised head/tail-preference score. Residue names are coloured by their polarity: black is non-polar, blue is basic, red is acidic, and green is polar.*

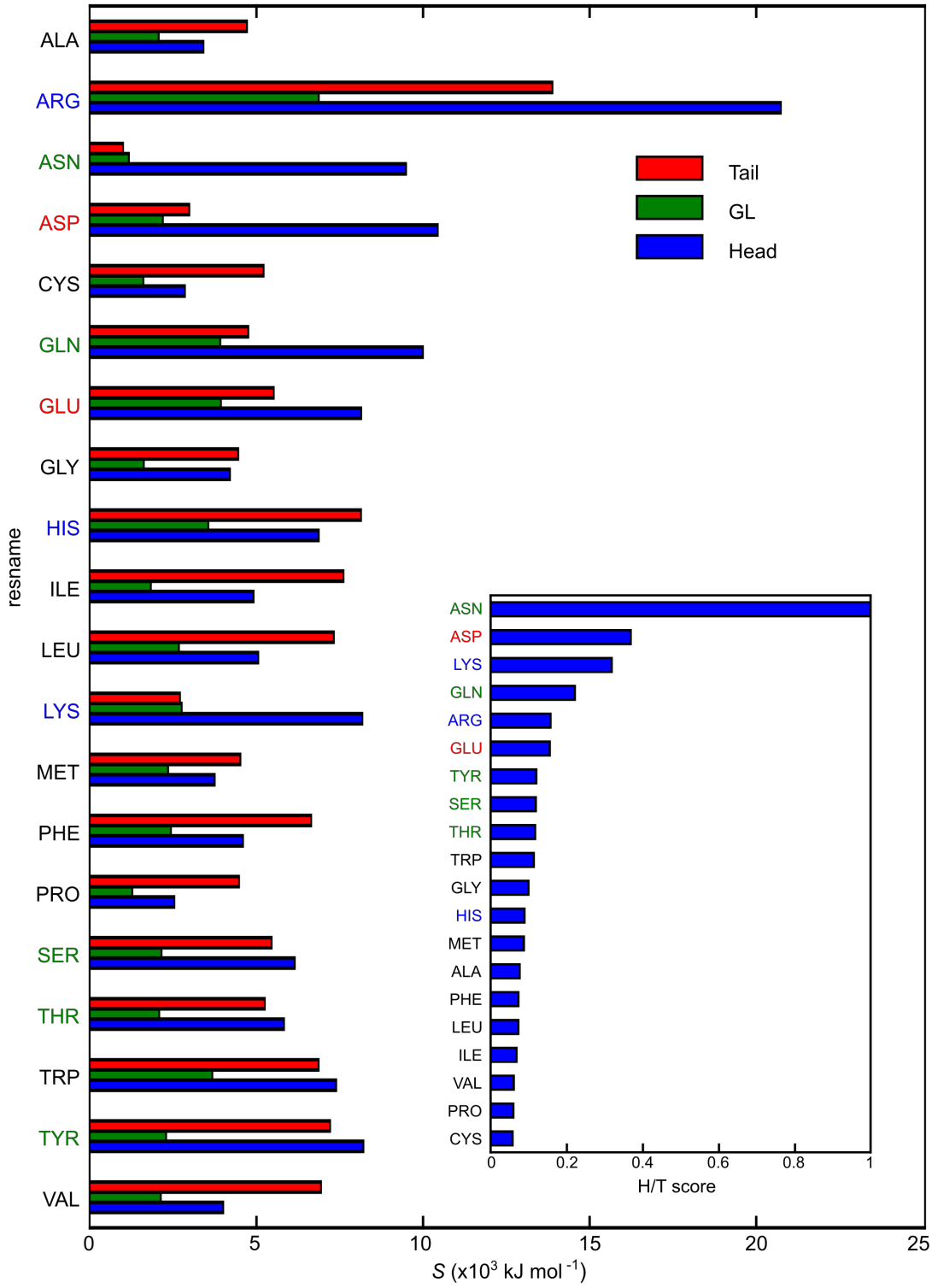


Figure 6.11 General Protein-lipid interaction of TWIK-1. *The inset is normalised head/tail-preference score. Residue names are coloured by their polarity: black is non-polar, blue is basic, red is acidic, and green is polar.*

6.3.3 State dependent protein-lipid interaction

After, the NB-FDA was tested, it was applied to both TREK-2 and TWIK-1 in non-stretched and stretched bilayers to investigate whether there are stretch-dependent protein-lipid interactions. The lipid interaction stretch-dependent score was defined as the absolute value of the differences of an averaged '*punctual stress*' in the no stretch and stretch simulations (i.e. $\left|s_{i,av}^{S} - s_{i,av}^{noS}\right|$). The results were then mapped onto the structures and sequences (**Figure 6.12**). This shows a different pattern between TREK-2 and TWIK-1, especially at the TM2-3 tips (TREK Q210-Q235, corresponding to TWIK-1 R155-Q185), the top of TM4 (TREK-2 G294-W300, corresponding to TWIK-1 N236-L245), and TWIK-1 H272 at the hinge at the end of TM4. As for TREK-2, most of highlighted residues were arginine and some lysines. Apart from these residues, interesting residues are F195, F202, T234, and Y261.

6.3.4 Force sensing residues

Although NB-FDA highlighted the residues that have stretch-dependent protein-lipid interactions in TREK-2 and TWIK-1, further investigation is required to ensure which residues are the force-sensing residues. Current studies suggest that protein interactions with lipid head groups are more likely to play a role in force sensing rather than the interaction with lipid tails primarily because the lipid head groups have very strong interactions with arginine and lysine. For TWIK-1, the amphipathic residues at TM2-3 tip help TWIK-1 to stabilise itself in the stretched membrane. In TREK-2, phenylalanines in TM2 may play a role in its mechanosensitivity. In addition, there were a small number of residues in TM helices that had no effect from the stretched bilayer; most are glycine and alanine (e.g. G91, A193, G212, G312, and A318).

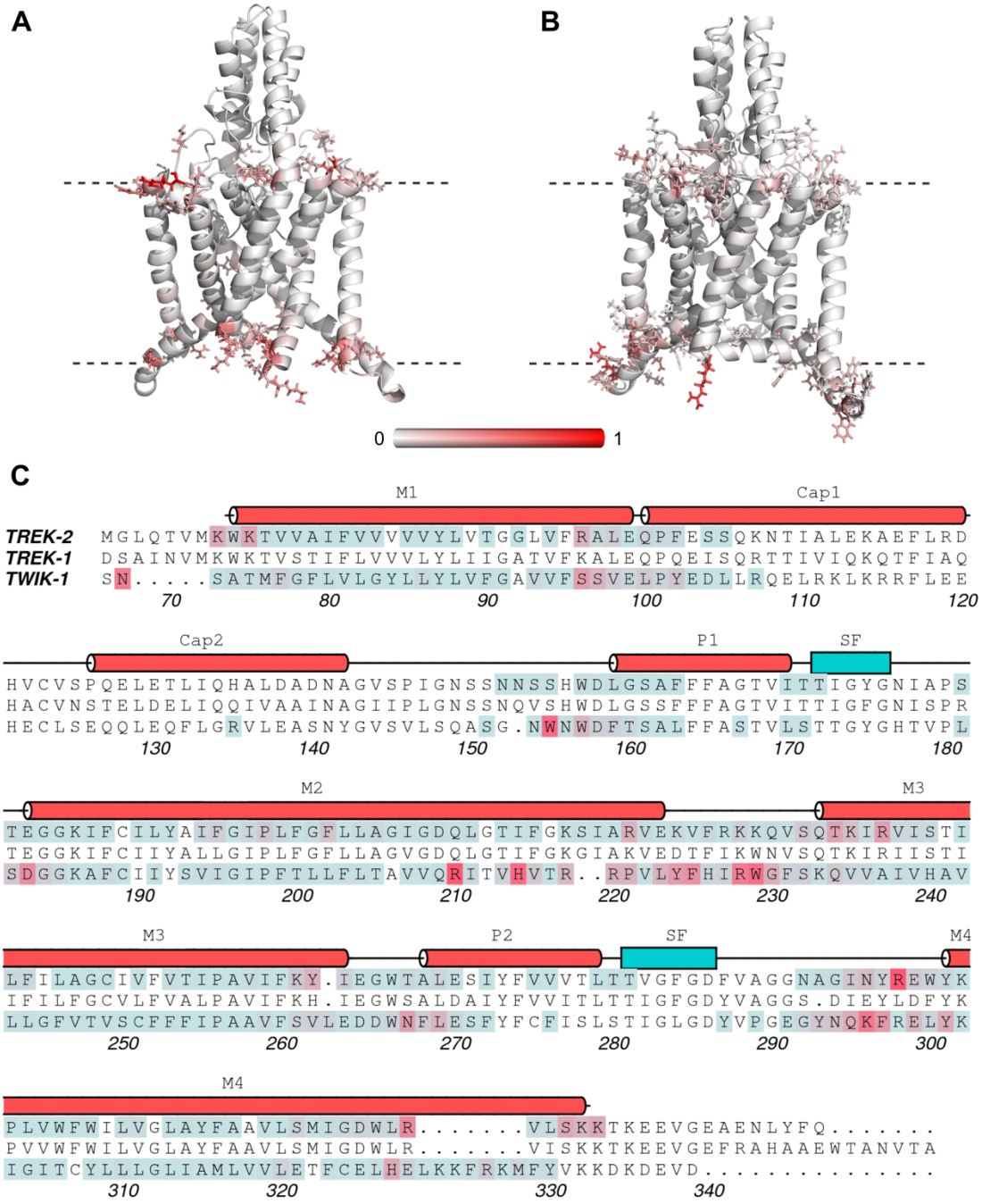


Figure 6.12 Protein-Lipid state dependent interaction. *(A-B) Lipid interaction stretch-dependent score ($\left|s^{S}_{i,av} - s^{nos}_{i,av}\right|$) mapped on the (A) TREK-2 and (B) TWIK-1 structure. (C) Lipid interaction stretch-dependent score mapped on the TREK-2 and TWIK-1 sequences. Colour ranges from light blue to red. Light blue indicates small difference between two states, whereas red indicate larger difference. White means no difference nor lipid interactions. There is no data for TREK-1, the sequence is just added as a visual guide. Sequences are taken from Uniprot id P97438 (TREK-1), P57789 (TREK-2), O00180 (TWIK-1) and aligned using Clustal Omega alignment program [296]. Note: TWIK-1 residue numbers are shifted from TREK-2 by -55.*

6.4 Internal protein interactions

In this section, the internal protein side-chain network of interactions was considered and analysed by using NB-FDA. All data was summarised on a residue-based level and shown in 3D visualisation using VMD and a Tcl script. There are multiple formats in which to represent the result. One can adjust with the visualisation options in VMD and the Tcl script to adjust colour or filter the network links. As shown in **Figure 6.13**, there are three samples of visualisation and each of them has their specific purpose. The network filter and colour range were determined by the distribution of S_{ij}. The representation A, showing all the existing network, mimics the contact analysis with a long cut-off radii. The representation B and C shows only filtered networks which represent significant interactions (e.g. hydrogen bonds, salt bridges). However, considering the objective of this chapter, the representation B is the most suitable in this case.

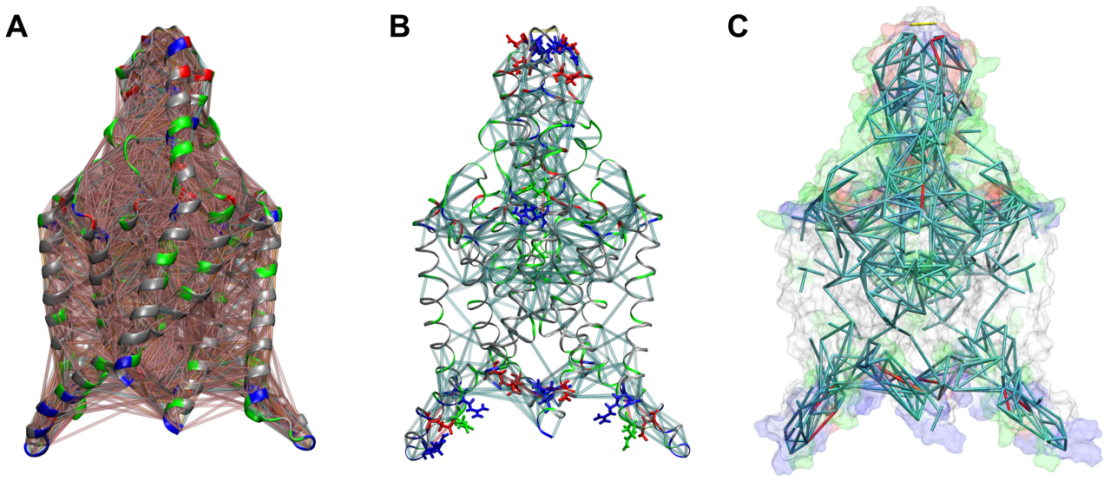


***Figure 6.13 TREK-2 Internal protein network**. Different forms of TREK-2 internal network representation. (A) Complete network without any filter shown as transparent and protein shown as cartoon. This representation fully shows the complexity of internal protein side-chain interaction. (B) filtered network shown as transparent and protein shown as ribbon. This shows only significant interaction and also presents some protein information. (C) Filtered network shown as opaque and protein shown as quick-surf and transparent. This mainly focus on the network and considers protein as a soft material. The network is coloured by S_{ij} as following: pink for $S_{ij} \leq 500$ kJ mol^{-1}, orange for 500 kJ mol^{-1} $< S_{ij} \leq 10^3$ kJ mol^{-1}, cyan for 10^3 kJ mol^{-1} $< S_{ij} <\leq 10^4$ kJ mol^{-1}, red for 10^4 kJ mol^{-1} $< S_{ij} \leq 10^5$ kJ mol^{-1}, yellow for 10^5 kJ mol^{-1} $< S_{ij}$.*

6.4.1 TREK-2 and TWIK-1 internal networks

To investigate how forces are distributed in the protein, TREK-2 and TWIK-1 inter helix interactions in no-stretch and stretched bilayers were analysed and shown in **Figure 6.14**. The data is averaged over last 50 ns of production run and across all repeats, 4 for TREK-2 and 2 for TWIK-1, for each condition. All of four structures have a strong network at the top region and around the selectivity filter indicating a high rigidity of this part of the protein. This is in agreement with simulation and functional results that the top part of TREK-2 does not have significant change during stretch activation[241]. However, in lower sections, TREK-2 and TWIK-1 exhibited clear differences. Compared with TREK-2, TWIK-1 has a greater number of networks, mostly because TWIK-1 has a major kink at the end of TM4 that produces the 'C-helix'. Moreover, the residues in the lower section of TM2, TM3 and TM4 are not conserved between TREK and TWIK-1 channels. This means that TWIK-1 has a unique network that will be described in the next section (6.4.2).

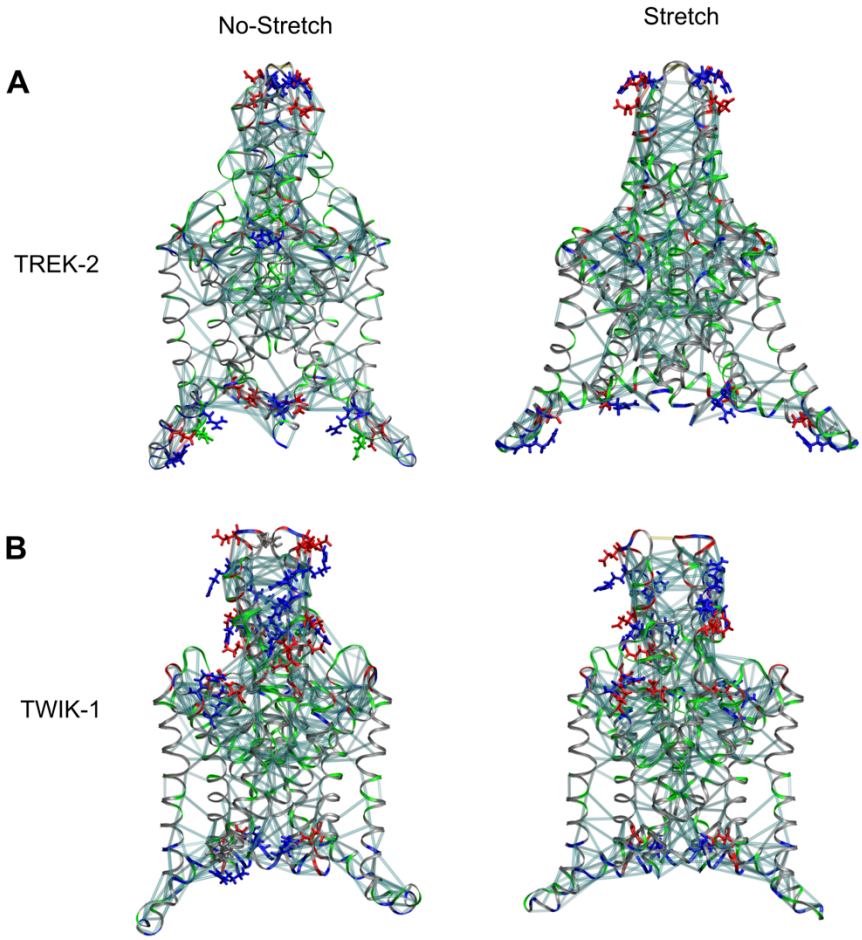


Figure 6.14 TREK-2 and TWIK-1 internal network. *(A) the internal network of TREK-2 in no-stretch (left, 'down-like' state) and stretched (right, 'up-like' state) bilayer. Structural transition and rearrangement of the networks mean the TREK-2 'up-like' state has a more supported network below selectivity filter. (B) the internal network of TWIK-1 in no-stretch (left) and stretched (right) bilayer. There is no significant different between the two conditions.*

6.4.2 The unique network in the non-mechanosensitive TWIK-1 channel

A clear difference in network distribution in the lower section of TREK-2 and TWIK-1 was observed. This network is centred around M4 and interacts with M2 and M3 (**Figure 6.15**). Compared to TREK-2, TWIK has a stronger network in this region as M2 and M4 residue creates a 'zip-like network' along the M4 (**Figure 6.15B & C**). This network is not found in TREK-2. This difference is the result of two factors: structure and sequence. Structurally, TWIK-1 has a special M4 structure as it has a small perpendicular 'C-helix' at the kinked end. This small kinked helix allows R227 and

F280 to form interactions with the back of M2 of another subunit. From sequence alignment (**Figure 6.12**), TWIK-1 has high similarity with TREK in the upper part of M2 (until TREK-2 P198, or TWIK-1 P143), whereas in the lower part of TM2, TWIK-1 has very low similarity. Interestingly, a 'zip-like' network is formed at this non-conserved region. Although, identity between TREK and TWIK-1 at TM4 is also very low, the network at the top part of both shows links between TM4, pore lining helices, and selectivity filter. Some of residues also show the same pattern, for example TREK-2 I309 and TWIK-1 L253 the both link to many of pore-lining helix residues. TREK-2 W208 and TWIK-1 Y252 links between TM4, TM3 and pore lining helixes.

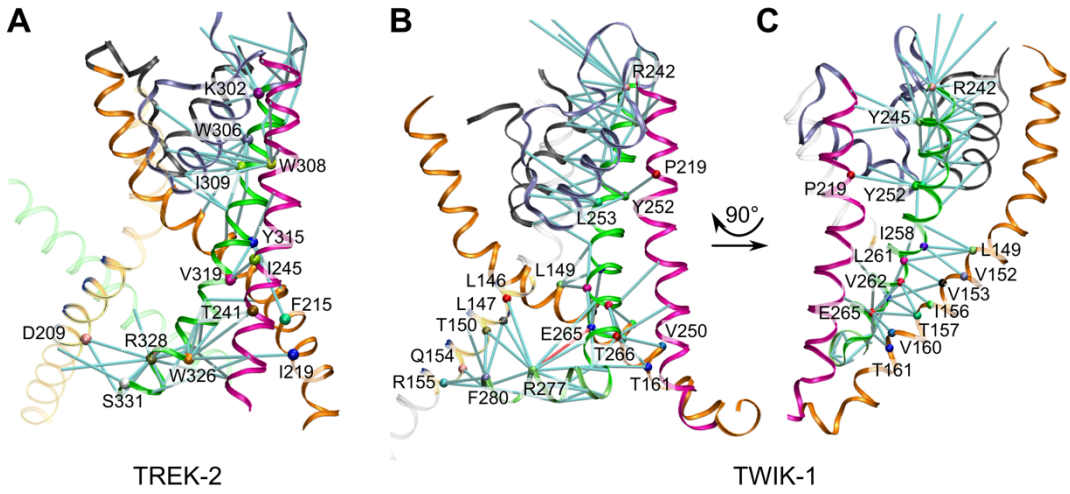


Figure 6.15 TM4 network of TREK-2 and TWIK-1. *(A) TREK-2 network of interaction around TM4. (B, C) TWIK-1 network of interaction around TM4. The 'zip-like' network connects M2 and M4.*

6.4.3 Unique network of the TREK-2 'down-like' state and the 'up-like' state

According to Chapter 2, TREK-2 was in the 'down-like' state when embedded in a non-stretched bilayer and in the 'up-like' state when in stretched bilayer, whereas TWIK-1 retains the same structure in both conditions. These networks are shown in **Figure 6.14**. Apparently, the network of TREK-2 in non-stretch bilayer is different from the network of TREK-2 when stretched. In contrast, there is no difference for TWIK-1. To examine these, the network of TREK-2 in no-stretch ('down-like' state) and stretch bilayer ('up-like' state) was compared using independent t-test (see **Figure 6.16** for graphical explanation). The network of TWIK-1 in no-stretch and stretch bilayer was analysed to compare. The data was obtained during last 50 ns of the production runs. The result is show in **Figure 6.17** with two criteria : P-score < 0.01 (99% confidence), and absolute value of the difference between average value of the network in stretch and no-stretch conditions, $\left|s_{ij,av}^{S} - s_{ij,av}^{noS}\right|$, is greater than 500 kJ mol^{-1}. Although, rearrangements of the force network were observed in both TREK-2 and TWIK-1, the TREK-2 network changes mainly occur in the lower section, whereas TWIK-1 changes presented in the top section. In TREK-2, the network at the end of M4 connected with the lower section of M2, M3, and M4 in another subunit is only shown in the 'down-like' state (**Figure 6.17A & C**). This network disappeared when TREK-2 moved to the 'up-like' state. The upward movement of M4 created a new set of networks below the selectivity filter and showed interactions with the pore-lining helices (**Figure 6.17B & D**). These connections may help to support the stability of selectivity filter and gating within the filter. This rearrangement of forces is expected to accompany with the 'down to up' structural transition. Unfortunately, there is no available supporting experimental data (e.g. site directed mutagenesis) to describe these changes. In TWIK-1, there were many changes in the cap region. In the lower section, there are only rearrangement of the interaction around the M2-M3 tips.

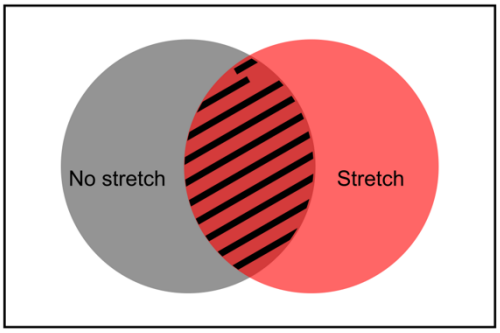


Figure 6.16 Venn diagram represents TREK-2 network. *TREK-2 was in the 'down-like' state when embedded in no-stretch bilayer and in the 'up-like' state when in stretch bilayer. In this figure, the networks of these two states are represented by a Venn diagram. Among these two states, there are the overlap network as highlighted. These overlap networks were removed by using t-test analysis, then therefore the figure 6.17 is only show the network that only exist in (left) no stretch and (right) stretch condition. The* $\left|s_{ij,av}^{S} - s_{ij,av}^{noS}\right|$*, is greater than 500 kJ mol*$^{-1}$ *was applied to filter out less significant pairs.*

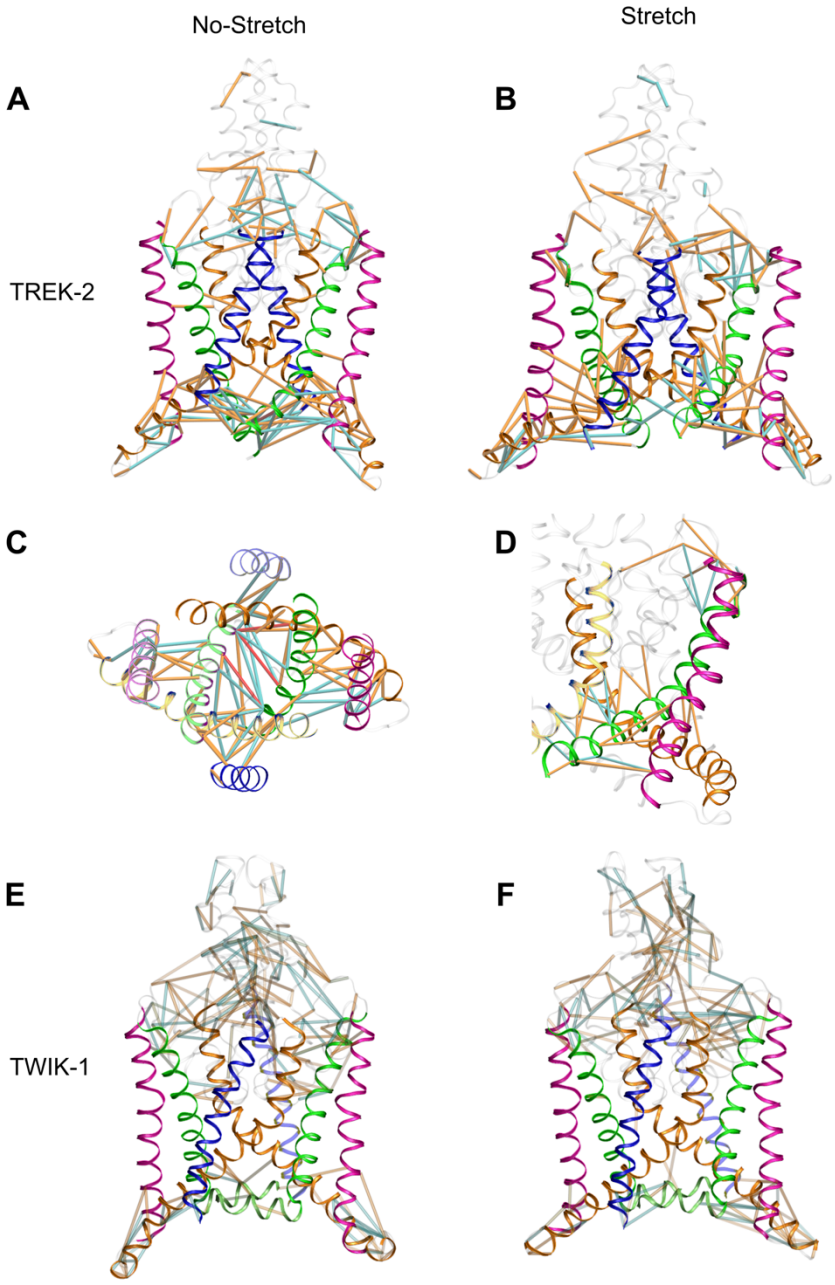


Figure 6.17 The network that changes during stretch protocol. *The network of TREK-2 (A-D) and TWIK-1(E, F) in no-stretch and stretch bilayer was compared using independent t-test. The data was obtained during last 50ns of the production runs. The result shows with two criteria: p-score < 0.01 (99% confident), and* $\left|s_{ij,av}^{S} - s_{ij,av}^{noS}\right|$ *> 500 kJ mol*$^{-1}$*. The network is coloured by* $\left|s_{ij,av}^{S} - s_{ij,av}^{noS}\right|$*: cyan is less than 1,000 kJ mol*$^{-1}$*, orange is greater than 1,000 kJ mol*$^{-1}$*. TREK-2 shows rearrangement of forces around M4 accompany with the structural transition. In TWIK-1, although there many changes in cap region and the some in upper section, there is no major change in the lower section network apart of rearrangement of interactions around the M2-M3 tips.*

6.4.4 Correlation of motion and allosteric pathway

After confirming that the down-like and the up-like states exhibited differences in their internal networks, the allosteric pathway for how these changes may be propagated to the upper part of the protein and affect channel gating was investigated. A correlation motion protocol was developed to track changes in the TREK-2 internal network during a simulation and compare with the protein dynamic. In this case, the protocol was designed to track the networks that change corresponding to the 'down to up' structural transition. This was done by considering the correlation between time-dependent RMSD and time-dependent S_{ij} of each residue pairs. The Pearson correlation was used as an initial study. Using the simulations performed in Chapters 3 and 4, the algorithm successfully captured the changes during the stretch activation. There was no change in 2 of 4 of TREK-2 in no-stretch bilayer and there were only less than 10 links in the other repeats. For TWIK-1, there were also only less than 10 residue pairs that were figured out whether in no-stretch or stretch bilayer condition. Importantly, it demonstrated changes of network in the lower section of TREK-2 during the simulation under stretch protocol and asymmetric protocol (**Figure 6.18**). These changes propagated along TM4 and affected the pore-lining helices. However, the algorithm was able to detect many more residue pairs in the asymmetric protocol. This difference in term of numbers may be related to the rate of structural transition that is different between these two stretch protocols, because the Pearson coefficient can only represent a linear relation.

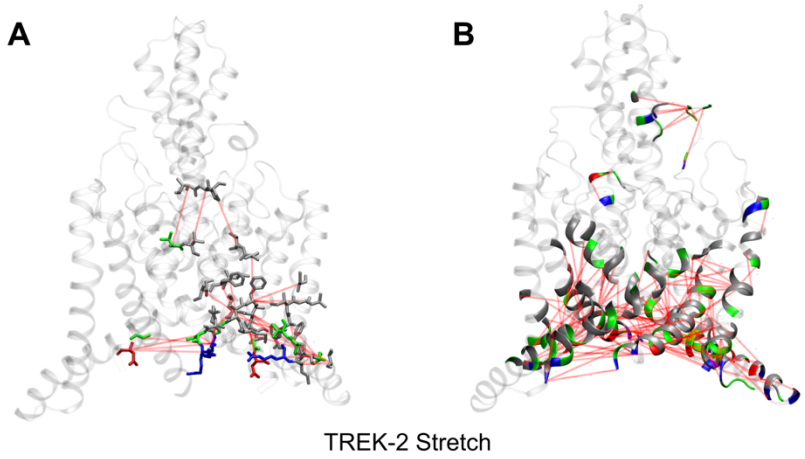


Figure 6.18 Network changing during stretch simulation. *(A) The network changed during the symmetric stretch protocol, Chapter 3. (B) The network changed during the asymmetric stretch protocol, Chapter 4. The different between these two may related to the structural transition rate because the Pearson coefficient works efficiently only for linear relationships.*

6.6 Discussion

6.6.1 Advantage and disadvantage of NB-FDA

NB-FDA protein-lipid interaction may be considered as a type of contact analysis that contains energetic information, i.e. NB-FDA is contact analysis with weights. It has an ability to distinguish molecules whether an adjacent region of a molecule is just nearby, or forms strong interactions, for example salt bridges and hydrogen bonds which are emphasized. Note that, the salt bridges are distinguished with $S_{ij} > 10^4$ kJ mol^{-1} , whereas the range of hydrogen bond is 10^3 kJ mol$^{-1} < S_{ij} < 10^4$ kJ mol^{-1}. These numbers were high because they were in summation of magnitude of all interactions between two residues. In terms of computing resources, it used ~1.32 computing time compared to LCA (for TREK-2/bilayer system, NB-FDA spent 29 seconds per frame whereas LCA spent 22 seconds). However, NB-FDA required a large amount of memory (RAM). In this case, the minimum of 16 GB RAM is required and 64GB RAM is recommended especially for analysing the bilayer interactions.

6.6.2 Cut-off sensitivity of contact analysis

All of the available contact analysis approaches are based on a cut-off, for example lipid contact analysis, protein contact analysis is based on distance cut-off, hydrogen bond analysis is based on distance and angle cut-off. In general, choosing an appropriate cut-off is straightforward (e.g. using first minimum of RDF). However, when comparing the interaction in two states, a small change in cut-off may cause changes in the results. This problem is even more critical when considering the local interactions especially for the distance between 3 -3.5 Å (hydrogen bond distance). As shown the section 6.3.1, too small a cut-off does not cover all features and makes the analysis too sensitive. In contrast, too large cut-off over selects the residues and make the analysis unable to detect changes in the different states. But NB-FDA does not have this cut-off sensitivity problem. There is only a cut-off rule that it needs to cover all interaction length, all non-interaction pairs will be filtered out by the algorithm.

6.6.3 Statistical approaches

In this study, the Pearson correlation was used and showed good results. However, other tools may also be suitable. The potential tools are Spearman rank correlation, clustering tools, kernel density estimation, or generalized correlation[297] which is designed for biomolecules. Spearman correlation provides whether two data sets is related since it compares a rank of data, therefore the relation is not required to be linear. Nonetheless, the efficiency of Spearman correlation is less when working with data with a high standard deviation. The fact that the system is a two-state model (down-like state and up-like state), clustering tools, and kernel density can be used to determine to distribution of data set whether it match with the two-state model i.e. has two peaks, or two clusters. However, since it is time-dependent, a time component should be considered. Since each approach has advantages and disadvantages, the effective approach is to develop a protocol that can combine two or more statistical tools.

6.6.5 Future work

Further developments in NB-FDA may be considered. These further developments can be in three directions: i) performance, ii) analysis method, and iii) visualisation. The performance can be efficiently increased by directly obtaining the distance from the MDAnalysis in the searching step. To do this one can implement the MDAnalysis source code or write the script do the KB-tree search by themselves. Other improvements can be done to optimise all functions in the script and maybe using new big data library, for example *dask*. For analysis, there are many available statistical tools, including machine learning, some of them may benefit in this project. Visualisation can be future developed by improving Tcl script for VMD or using JavaScript for interactive visualisation.

In addition, it may be possible to further develop the FDA script to investigate the forces distributed within a lipid bilayer. An example of the protocol output is shown in the **Figure 6.19**. It shows the punctual stress in each lipid molecule represented using Voronoi diagram and also its corresponding distribution histogram.

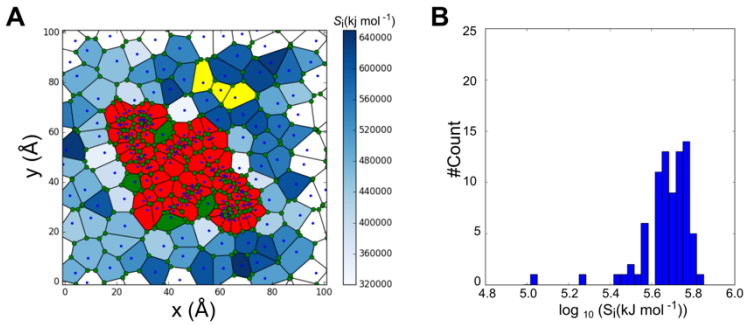


Figure 6.19 Force distribution in lipid bilayer*. (A) 2D-Voronoi tessellation representation of lipid molecules. Red is protein (i.e. TREK-2). Lipid molecules are coloured by their punctual stress as shown in the colour bar. Yellow and green highlight the lipid molecules have punctual stress excess or below the colour scale. that (B) A corresponding distribution histogram of punctual stress of lipids.*

6.7 Summary

In this chapter, the NB-FDA method is developed and applied to the mechanosensitive TREK-2 and non-mechanosensitive TWIK-1 ion channels. The protein-lipid interaction uncovered by both lipid contact analysis and NB-FDA shows strong lipid interactions with the arginine residues. NB-FDA shows advantages over the usual contact analysis as it has the ability to distinguish whether a molecule actually has a strong interaction or is just located nearby. It was also used to emphasise residues that have membrane stretch-dependent protein-lipid interaction. Comparison of protein internal networks, analysed by NB-FDA, revealed that TWIK-1 has the unique 'zip-like' network of connections between M2 and M4. This network is non-conserved in TREK-2 which exhibited different internal networks when it was in no-stretch and stretched bilayers. The correlation motion also showed a possible allosteric pathway between TM4, TM2 and the pore-lining helix.

Chapter 7
Summary

7.1 Stretch activation model

This thesis investigates the biophysical and structural mechanisms underlying the mechanosensitivity of K_{2P} potassium channels using computational approaches. First, the previously proposed models of stretch activation[73,134,135] were examined by applying symmetrical stretch on a TREK-2/bilayer system. The results supported the 'down to up' structural transition and also revealed how lipids may be involved in the stretch activation process, including the influence of hydrophobic mismatch. My initial CG simulations suggested that thinner bilayers (e.g. DLPC and DMPC) may help to drive the structural transition. However, the all-atom simulations indicated that changes in bilayer thickness itself are insufficient to drive the 'down to up' structural transition. It therefore appears that hydrophobic mismatch may assist in this process, but is not enough to cause the transition by itself.

7.2 Asymmetric response in membrane tension

When TREK-2 structurally switches from the down state to the up state in response to membrane stretch the majority of the changes occur in the lower half of the protein. This asymmetric structural change lead to an investigation of how TREK-2 responds under asymmetric bilayer tension. An asymmetric stretch protocol was developed using the relation between 'area per lipid' and membrane tension to create a mismatch - lipids were removed/added to induce monolayer tension in a particular leaflet. As predicted, the simulation results revealed that TREK-2 responded to the positive monolayer tension in the inner leaflet, but not in the outer leaflet. This highlights an ability of this eukaryotic MS channel to detect the direction of forces outside the plane of the bilayer. In addition, this study shows that, in this case (NPAT ensemble), bilayer torque and monolayer tension are different, with monolayer tension rather than bilayer torque playing the major role.

7.3 Intracellular pH sensitivity of TREK-1

Because the mechanisms underlying TREK-2 mechanosensitivity and intracellular pH sensitivity are known to be related[131], insights from understanding pH sensitivity may improve our understanding of its mechanosensitive properties. In TREK-1, the E306 residue has been suggested to act as the H^+ sensor with mutations at this position causing the channel to become almost fully open. To investigate this, MD simulations were performed using the recently solved crystal structure of TREK-1 with more information about the proximal C-terminus extension where this residue is located [138]. The results support the importance of this E306 residue in the intracellular pH activation. An analysis of protein-lipid-water interactions suggests that the E306A mutation mimics the protonated state of the E306 residue. However, its effects are stronger than for neutralisation of this residue. Although there is no 'up to down' structural transition

observed during the simulations, the simulation demonstrates the upward movement of E306 residue caused by either mutation or protonation. This implies that the intracellular pH activated state may be represented by the up state conformation of the channel. This explains why there is no further stretch activation of TREK channels when they are already activated by acidification. In other words, TREK channels already switched to the up state by pH can undergo no further movement caused by membrane stretch.

7.4 Internal protein interactions

The question of why some structurally related K_{2P} channels (e.g. TWIK-1) are not mechanosensitive was also addressed. Possible explanations may be how forces penetrate from lipid bilayer to the protein as well as the rigidity of the protein itself. Unfortunately, there are no available tools to examine these hypotheses. A non-bonded force distribution analysis (NB-FDA) method was therefore developed to probe these questions. It analysed the non-bonded interactions (Coulomb and LJ forces) between protein-lipid and also protein inter-helices interactions. Comparing to traditional lipid analysis, this NB-FDA approach provided more energetic details, but with an additional computational cost. In protein inter-helix interactions, it revealed a 'zip-like' network between TM2 and TM4 of the TWIK-1. This network securely prevented the movement of TM4 in TWIK-1. Interestingly, this network is unique for TWIK-1 when compared with TREK-1 and TREK-2. In addition, it showed that the network distribution in TREK-2 was different when embedded into unstretched vs and stretched bilayers, whereas they are quite similar in TWIK-1.

7.4 Further work

Although this thesis improves our understanding toward mechanism of K2P channel mechanosensitivity, there are several remaining questions related to my work:

Effect of bilayer thickness on the gating energy of TREK-2

Although my work indicates that the TREK-2 'down to up' structural transition is not induced by bilayer thickness alone, its influence on gating energy (or pressure required) has not been studied. The simulations of TREK-2 in DMPC and DLPC with low negative pressure have already been done. Surprisingly, only TREK-2/DMPC with the pressure of -40 bar initiated the 'down to up' transition within 100 ns whereas TREK-2 in a POPC bilayer required -50 bar and there was no the structural transition observed for TREK-2 a in DLPC bilayer, even near lytic tension. However, these results are not sufficient to conclude the influences of bilayer thickness on gating pressure. More simulations are required, especially for thicker bilayers to determine if any correlation.

The effect of small amphipathic molecules on the response of TREK-2

The asymmetric tension response of TREK-2 has now been shown in both computational and experimental studies. However, the effect of other relevant stimuli such as lysophosphatidylcholine (LPC) lipid or arachidonic acid is not examined. The interesting question is how these molecules affects the bilayer properties and activate the channels. Do they behave in same way as they activate the prokaryotic MscL channels?

The ‘down to up’ structural transition caused by intracellular acidification

Unfortunately, there is no available down state structure for TREK-1 (or TREK-2) that contains the extended proximal C-terminus (i.e. the pH-sensitive E306 residue), therefore our hypothesis that intracellular pH activation is also a ‘down to up’ structural transition is unable to directly tested. However, a possible way to test this is to use a homology model based on the TREK-2 down state or to simulate the up state in order to obtain a down-like state. Simulations that might manage to produce this would be extended simulation in the normal condition (with no additional pressure), but this may require >400ns to show a sign of the structural transition. Another one might be to use a compressed bilayer (i.e. applied positive pressure in xy-plane), this method is possible but initial attempts indicate that the TM1 N-terminus unfolds to interact with the TM4 helices.

Forces distribution within the lipid bilayer

In Chapter 6, how forces distribute within the bilayer is still a remaining question. The NB-FDA approach for bilayers still needs further development because it is necessary to have an ability to distinguish interactions between head group, glyceride, and tails. In addition, the Voronoi representation is also subjected for further development.

7.5 Conclusion

This thesis uses MD simulation and computational techniques to study the structural and biophysical mechanisms behind the mechanosensitivity of K2P potassium channels. It supports the ‘down to up’ structural transition as a stretch activation model and discovers that TREK-2 has an asymmetric response to membrane tension and primarily responds to the positive monolayer tension in the inner leaflet. Changes in bilayer thickness alone are not sufficient to drive the ‘down to up’ structural transition. The network analysis reveals the TWIK-1 has a unique network that stabilise the position of TM4. These results advance our overall understanding of these processes in eukaryotic potassium channels and emphasise their mechanistic complexity which underlies their role in physiological processes.

List of abbreviations

AA	arachidonic acid
APL	area per lipid
BB	Backbone
CG	Coarse-gained
DLPC	1,2-dilauroyl-sn-glycero-3-phosphocholine
DMPC	1,2-dimyristoyl-sn-glycero-3-phosphocholine
DPPC	1,2-dipalmitoyl-sn-glycero-3-phosphocholine
DSPC	1,2-distearoyl-sn-glycero-3-phosphocholine
FDA	Force Distribution Analysis
FFF	Force From Filament
FFL	Force From Lipid
IDE	Integrated Development Environment
LCA	Lipid Contact Analysis
LPC	Lysophospholipid
MD	Molecular Dynamics
MS	Mechanosensitive
NB-FDA	Non-bonded Force distribution analysis
PA	Phosphatidic acid
PC	phosphocholine
PE	Phosphatidylethanolamine
PIP	Phosphatidylinositol
PMF	Potential Mean Force
POPC	1-palmitoyl-2-oleoyl-sn-glycero-3-phosphocholine
POPE	1-palmitoyl-2-oleoyl-sn-glycero-3-phosphoethanolamine
POPS	1-palmitoyl-2-oleoyl-sn-glycero-3-phosphoserine
PUFA	poly-unsaturated fatty acid
RMSD	Root Mean Square Deviation
SF	Selectivity Filter
TALK	TWIK Related Alkaline pH-activated K^+ channels
TASK	TWIK Related Acid-Sensitive K^+ channels
THIK	Tandem pore domain Halothane Inhibited K^+ channels
TM	Transmembrane
TREK	TWIK Related K^+ channels
TRESK	TWIK Related Spinal cord K^+ channels
TWIK	Tandem of pore domains in a weak Inward rectifying K^+ channels

Bibliography

1. Bialecka-Fornal, M., Lee, H. J. & Phillips, R. The Rate of Osmotic Downshock Determines the Survival Probability of Bacterial Mechanosensitive Channel Mutants. *J. Bacteriol.* **197,** 231–237 (2015).
2. Hamilton, E. S., Schlegel, A. M. & Haswell, E. S. United in Diversity: Mechanosensitive Ion Channels in Plants. *Annu. Rev. Plant Biol.* **66,** 113–137 (2015).
3. Li, X.-Y. & Toyoda, H. Role of Leak Potassium Channels in Pain Signaling. *Brain Res. Bull.* **119,** 73–79 (2015).
4. Sukharev, S. & Sachs, F. Molecular Force Transduction by Ion Channels – Diversity and Unifying Principles. *J. Cell Sci.* **125,** 3075–3083 (2012).
5. Ranade, S. S., Syeda, R. & Patapoutian, A. Mechanically Activated Ion Channels. *Neuron* **87,** 1162–1179 (2015).
6. Sachs, F. Mechanical Transduction by Ion Channels: A Cautionary Tale. *World J. Neurol.* **5,** 74–87 (2015).
7. Singer, S. J. & Nicolson, G. L. The Fluid Mosaic Model of the Structure of Cell Membranes. *Science.* **175,** 720–731 (1972).
8. Engelman, D. M. Membranes Are More Mosaic than Fluid. *Nature* **438,** 578–580 (2005).
9. Fahy, E., Cotter, D., Sud, M. & Subramaniam, S. Lipid Classification, Structures and Tools. *Biochim. Biophys. Acta* **1811,** 637–47 (2011).
10. Israelachvili, J. N., Mitchell, D. J. & Ninham, B. W. Theory of Self-Assembly of Lipid Bilayers and Vesicles. *Biochim. Biophys. Acta - Biomembr.* **470,** 185–201 (1977).
11. Frolov, V. A., Shnyrova, A. V. & Zimmerberg, J. Lipid Polymorphisms and Membrane Shape. *Cold Spring Harb. Perspect. Biol.* **3,** a004747–a004747 (2011).
12. Franklin, B. Of the Stilling of Waves by Means of Oil. *Philos. Trans. R. Soc.* **64,** 445–460 (1774).
13. Wang, D.-N., Stieglitz, H., Marden, J. & Tamm, L. K. Benjamin Franklin, Philadelphia's Favorite Son, Was a Membrane Biophysicist. *Biophys. J.* **104,** 287–91 (2013).
14. Harayama, T. & Riezman, H. Understanding the Diversity of Membrane Lipid Composition. *Nat. Rev. Mol. Cell Biol.* **19,** 281 (2018).
15. Van Meer, G., Voelker, D. R. & Feigenson, G. W. Membrane Lipids: Where They Are and How They Behave. *Nature Reviews Molecular Cell Biology* **9,** 112–124 (2008).
16. Harayama, T., Eto, M., Shindou, H., Kita, Y., Otsubo, E., Hishikawa, D., Ishii, S., Sakimura, K., Mishina, M. & Shimizu, T. Lysophospholipid Acyltransferases Mediate Phosphatidylcholine Diversification to Achieve the Physical Properties Required In Vivo. *Cell Metab.* **20,** 295–305 (2014).
17. Sezgin, E., Levental, I., Mayor, S. & Eggeling, C. The Mystery of Membrane Organization: Composition, Regulation and Roles of Lipid Rafts. *Nat. Rev. Mol. Cell Biol.* **18,** 361–374 (2017).
18. Kučerka, N., Nieh, M. P. & Katsaras, J. Fluid Phase Lipid Areas and Bilayer Thicknesses of Commonly Used Phosphatidylcholines as a Function of Temperature. *Biochim. Biophys. Acta - Biomembr.* **1808,** 2761–2771 (2011).
19. Cantor, R. S. Lipid Composition and the Lateral Pressure Profile in Bilayers. *Biophys. J.* **76,** 2625–2639 (1999).

20. Verkhratsky, A., Krishtal, O. A. & Petersen, O. H. From Galvani to Patch Clamp: The Development of Electrophysiology. *Pflügers Arch. - Eur. J. Physiol.* **453,** 233–247 (2006).

21. Sigg, D. Modeling Ion Channels: Past, Present, and Future. *J. Gen. Physiol.* **144,** 7–26 (2014).

22. Cobb, M. Exorcizing the Animal Spirits: Jan Swammerdam on Nerve Function. *Nat. Rev. Neurosci.* **3,** 395–400 (2002).

23. Piccolino, M. Luigi Galvani and Animal Electricity: Two Centuries after the Foundation of Electrophysiology. *Trends Neurosci.* **20,** 443–8 (1997).

24. Nernst, W. Die Elektromotorische Wirksamkeit Der Ionen. *Z. Phys. Chem.* **4,** 129–181 (1889).

25. Hodgkin, A. L. & Huxley, A. F. A Quantitative Description of Membrane Current and Its Application to Conduction and Excitation in Nerve. *J. Physiol.* **117,** 500–44 (1952).

26. Neher, E. & Sakmann, B. Single-Channel Currents Recorded from Membrane of Denervated Frog Muscle Fibres. *Nature* **260,** 799–802 (1976).

27. Diebler, H., Eigen, M., Ilgenfritz, G., Maass, G. & Winkler, R. Kinetics and Mechanism of Reactions of Main Group Metal Ions with Biological Carriers. *Pure Appl. Chem.* **20,** 93–116 (1969).

28. Narahashi, T., Moore, J. W. & Scott, W. R. Tetrodotoxin Blockage Of Sodium Conductance Increase In Lobster Giant Axons. *J. Gen. Physiol.* **47,** 965–74 (1964).

29. Armstrong, C. M., Bezanilla, F. & Rojas, E. Destruction of Sodium Conductance Inactivation in Squid Axons Perfused with Pronase. *J. Gen. Physiol.* **62,** 375–91 (1973).

30. Goldman, D. E. POTENTIAL, IMPEDANCE, AND RECTIFICATION IN MEMBRANES. *J. Gen. Physiol.* **27,** 37–60 (1943).

31. Hille, B. *Ion Channels of Excitable Membranes*. (Sinauer, 2001).

32. Gough, J., Karplus, K., Hughey, R. & Chothia, C. Assignment of Homology to Genome Sequences Using a Library of Hidden Markov Models That Represent All Proteins of Known Structure. *J. Mol. Biol.* **313,** 903–919 (2001).

33. Finn, R. D., Bateman, A., Clements, J., Coggill, P., Eberhardt, R. Y., Eddy, S. R., Heger, A., Hetherington, K., Holm, L., Mistry, J., Sonnhammer, E. L. L., Tate, J. & Punta, M. Pfam: The Protein Families Database. *Nucleic Acids Res.* **42,** D222-30 (2014).

34. Murzin, A. G., Brenner, S. E., Hubbard, T. & Chothia, C. SCOP: A Structural Classification of Proteins Database for the Investigation of Sequences and Structures. *J. Mol. Biol.* **247,** 536–540 (1995).

35. Yates, B., Braschi, B., Gray, K. A., Seal, R. L., Tweedie, S. & Bruford, E. A. Genenames.Org: The HGNC and VGNC Resources in 2017. *Nucleic Acids Res.* **45,** D619–D625 (2017).

36. Zheng, J. & Trudeau, M. C. *Handbook of Ion Channels*. *CRC Press* (CRC Press, 2015).

37. Millar, I. D., Bruce, J. I. & Brown, P. D. Ion Channel Diversity, Channel Expression and Function in the Choroid Plexuses. *Cerebrospinal Fluid Res.* **4,** 8 (2007).

38. Yu, F. H. & Catterall, W. A. The VGL-Chanome: A Protein Superfamily Specialized for Electrical Signaling and Ionic Homeostasis. *Sci. Signal.* **2004,** re15-re15 (2004).

39. Doyle, D. A., Cabral, J. M., Pfuetzner, R. A., Kuo, A., Gulbis, J. M., Cohen, S. L., Chait, B. T. & MacKinnon, R. The Structure of the Potassium Channel: Molecular Basis of K^+ Conduction and Selectivity. *Science.* **280,** 69 (1998).

40. Shrivastava, I. H., Peter Tieleman, D., Biggin, P. C. & Sansom, M. S. P. K+ versus Na+ Ions in a K Channel Selectivity Filter: A Simulation Study. *Biophys. J.* **83,** 633–645 (2002).

41. Köpfer, D. A., Song, C., Gruene, T., Sheldrick, G. M., Zachariae, U. & De Groot, B. L. Ion Permeation in K+channels Occurs by Direct Coulomb Knock-On. *Science.* **346,** 352–355 (2014).

42. Cuello, L. G., Jogini, V., Cortes, D. M. & Perozo, E. Structural Mechanism of C-Type Inactivation in K+ Channels. *Nature* **466,** 203–208 (2010).

43. Baker, K. A., Tzitzilonis, C., Kwiatkowski, W., Choe, S. & Riek, R. Conformational Dynamics of the KcsA Potassium Channel Governs Gating Properties. *Nat. Struct. Mol. Biol.* **14,** 1089–95 (2007).

44. Capener, C. E., Shrivastava, I. H., Ranatunga, K. M., Forrest, L. R., Smith, G. R. & Sansom, M. S. P. Homology Modeling and Molecular Dynamics Simulation Studies of an Inward Rectifier Potassium Channel. *Biophys. J.* **78,** 2929–2942 (2000).

45. Liu, H.-L. & Lin, J.-C. A Set of Homology Models of Pore Loop Domain of Six Eukaryotic Voltage-Gated Potassium Channels Kv1.1-Kv1.6. *Proteins Struct. Funct. Bioinforma.* **55,** 558–567 (2004).

46. Milac, A., Anishkin, A., Fatakia, S. N., Chow, C. C., Sukharev, S. & Guy, H. R. Structural Models of TREK Channels and Their Gating Mechanism. *Channels (Austin).* **5,** 23–33 (2011).

47. Enyedi, P. & Czirják, G. Molecular Background of Leak K^+ Currents: Two-Pore Domain Potassium Channels. *Physiol. Rev.* **90,** 559–605 (2010).

48. Goldstein, S. A. N., Bockenhauer, D., O'Kelly, I. & Zilberberg, N. Potassium Leak Channels and the KCNK Family of Two-p-Domain Subunits. *Nat. Rev. Neurosci.* **2,** 175–184 (2001).

49. Lesage, F., Guillemare, E., Fink, M., Duprat, F., Lazdunski, M., Romey, G. & Barhanin, J. TWIK-1, a Ubiquitous Human Weakly Inward Rectifying K+ Channel with a Novel Structure. *EMBO J.* **15,** 1004–11 (1996).

50. Duprat, F., Lesage, F., Fink, M., Reyes, R., Heurteaux, C. & Lazdunski, M. TASK, a Human Background K+ Channel to Sense External PH Variations near Physiological PH. *EMBO J.* **16,** 5464–5471 (1997).

51. Kim, Y., Bang, H. & Kim, D. TASK-3, a New Member of the Tandem Pore K(+) Channel Family. *J. Biol. Chem.* **275,** 9340–7 (2000).

52. Kim, D. & Gnatenco, C. TASK-5, a New Member of the Tandem-Pore K+channel Family. *Biochem. Biophys. Res. Commun.* **284,** 923–930 (2001).

53. Reyes, R., Duprat, F., Lesage, F., Fink, M., Salinas, M., Farman, N. & Lazdunski, M. Cloning and Expression of a Novel PH-Sensitive Two Pore Domain K+ Channel from Human Kidney. *J. Biol. Chem.* **273,** 30863–9 (1998).

54. Rajan, S., Wischmeyer, E., Karschin, C., Preisig-Müller, R., Grzeschik, K.-H., Daut, J., Karschin, A. & Derst, C. THIK-1 and THIK-2, a Novel Subfamily of Tandem Pore Domain K^+ Channels. *J. Biol. Chem.* **276,** 7302–7311 (2001).

55. Lesage, F., Maingret, F. & Lazdunski, M. Cloning and Expression of Human TRAAK, a Polyunsaturated Fatty Acids-Activated and Mechano-Sensitive K(+) Channel. *FEBS Lett.* **471,** 137–40 (2000).

56. Bang, H., Kim, Y. & Kim, D. TREK-2, a New Member of the Mechanosensitive Tandem-Pore K+ Channel Family. *J. Biol. Chem.* **275,** 17412–9 (2000).

57. Sano, Y., Inamura, K., Miyake, A., Mochizuki, S., Kitada, C., Yokoi, H., Nozawa, K., Okada, H., Matsushime, H. & Furuichi, K. A Novel Two-Pore Domain K^+ Channel, TRESK, Is Localized in the Spinal Cord. *J. Biol. Chem.* **278,** 27406–27412 (2003).

58. Chavez, R. A., Gray, A. T., Zhao, B. B., Kindler, C. H., Mazurek, M. J., Mehta, Y., Forsayeth, J. R. & Yost, C. S. TWIK-2, a New Weak Inward Rectifying Member of the Tandem Pore Domain Potassium Channel Family. *J. Biol. Chem.* **274,** 7887–92 (1999).

59. Salinas, M., Reyes, R., Lesage, F., Fosset, M., Heurteaux, C., Romey, G. & Lazdunski, M. Cloning of a New Mouse Two-P Domain Channel Subunit and a Human Homologue with a Unique Pore Structure. *J. Biol. Chem.* **274,** 11751–60 (1999).

60. Honoré, E. The Neuronal Background K2P Channels: Focus on TREK1. *Nat. Rev. Neurosci.* **8,** 251–261 (2007).

61. Fink, M., Duprat, F., Lesage, F., Reyes, R., Romey, G., Heurteaux, C. & Lazdunski, M. Cloning, Functional Expression and Brain Localization of a Novel Unconventional Outward Rectifier K+ Channel. *EMBO J.* **15,** 6854–62 (1996).

62. Lesage, F., Terrenoire, C., Romey, G. & Lazdunski, M. Human TREK2, a 2P Domain Mechano-Sensitive K+Channel with Multiple Regulations by Polyunsaturated Fatty Acids, Lysophospholipids, and Gs, Gi, and GqProtein-Coupled Receptors. *J. Biol. Chem.* **275,** 28398–28405 (2000).

63. Meadows, H. J., Benham, C. D., Cairns, W., Gloger, I., Jennings, C., Medhurst, A. D., Murdock, P. & Chapman, C. G. Cloning, Localisation and Functional Expression of the Human Orthologue of the TREK-1 Potassium Channel. *Pflügers Arch. - Eur. J. Physiol.* **439,** 714–722 (2000).

64. Kang, D. TREK-2 (K2P10.1) and TRESK (K2P18.1) Are Major Background K+ Channels in Dorsal Root Ganglion Neurons. *AJP Cell Physiol.* **291,** C138–C146 (2006).

65. Decher, N., Kiper, A. K. & Rinné, S. Stretch-Activated Potassium Currents in the Heart: Focus on TREK-1 and Arrhythmias. *Prog. Biophys. Mol. Biol.* **130,** 223–232 (2017).

66. Noël, J., Sandoz, G. & Lesage, F. Molecular Regulations Governing TREK and TRAAK Channel Functions. *Channels (Austin).* **5,** 402–9 (2011).

67. Patel, A. J. & Honoré, E. Properties and Modulation of Mammalian 2P Domain K+ Channels. *Trends in Neurosciences* **24,** 339–346 (2001).

68. Miller, A. & Long, S. Crystal Structure of the Human Two – Pore Domain Potassium Channel K2P1. *Science.* **335,** 432 (2012).

69. Brohawn, S. G., Del Mármol, J. & MacKinnon, R. Crystal Structure of the Human K2P TRAAK, a Lipid- and Mechano-Sensitive K+ Ion Channel. *Science.* **335,** 436–441 (2012).

70. Piechotta, P. L., Rapedius, M., Stansfeld, P. J., Bollepalli, M. K., Ehrlich, G., Erhlich, G., Andres-Enguix, I., Fritzenschaft, H., Decher, N., Sansom, M. S. P., Tucker, S. J. & Baukrowitz, T. The Pore Structure and Gating Mechanism of K2P Channels. *EMBO J.* **30,** 3607–19 (2011).

71. Uysal, S., Cuello, L. G., Cortes, D. M., Koide, S., Kossiakoff, A. A. & Perozo, E. Mechanism of Activation Gating in the Full-Length KcsA K+ Channel. *Proc. Natl. Acad. Sci. U. S. A.* **108,** 11896–9 (2011).

72. Aryal, P., Abd-Wahab, F., Bucci, G., Sansom, M. S. P. & Tucker, S. J. Influence of Lipids on the Hydrophobic Barrier within the Pore of the TWIK-1 K2P Channel. *Channels* **9,** (2015).

73. Brohawn, S. G., Campbell, E. B. & MacKinnon, R. Physical Mechanism for Gating and Mechanosensitivity of the Human TRAAK K+ Channel. *Nature* **516,** 126–130 (2014).

74. Schewe, M., Nematian-Ardestani, E., Sun, H., Musinszki, M., Cordeiro, S., Bucci, G., de Groot, B. L., Tucker, S. J., Rapedius, M. & Baukrowitz, T. A Non-Canonical Voltage-Sensing Mechanism Controls Gating in K2P K(+) Channels. *Cell* **164,** (2016).

75. Rose, A. S., Bradley, A. R., Valasatava, Y., Duarte, J. M., Prlić, A., Rose, P. W. & Valencia, A. NGL Viewer: Web-Based Molecular Graphics for Large Complexes. *Bioinformatics* (2018). doi:10.1093/bioinformatics/bty419

76. Katz, B. Depolarization of Sensory Terminals and the Initiation of Impulses in the Muscle Spindle. *J. Physiol.* **111,** 261–282 (1950).

77. Guharay, F. & Sachs, F. Stretch-Activated Single Ion Channel Currents in Tissue-Cultured Embryonic Chick Skeletal Muscle. *J. Physiol.* **352,** 685–701 (1984).

78. Sachs, F. Stretch-Activated Ion Channels: What Are They? *Physiology (Bethesda).* **25,** 50–6 (2010).

79. Battle, A. R., Ridone, P., Bavi, N., Nakayama, Y., Nikolaev, Y. A. & Martinac, B. Lipid-Protein Interactions: Lessons Learned from Stress. *Biochimica et Biophysica Acta - Biomembranes* **1848,** 1744–1756 (2015).

80. Gustin, M. C., Zhou, X. L., Martinac, B. & Kung, C. A Mechanosensitive Ion Channel in the Yeast Plasma Membrane. *Science.* **242,** 762 LP-765 (1988).

81. Sokabe, M. & Sachs, F. The Structure and Dynamics of Patch-Clamped Membranes: A Study Using Differential Interference Contrast Light Microscopy. *J. Cell Biol.* **111,** 599–606 (1990).

82. Sackin, H. A Stretch-Activated K+ Channel Sensitive to Cell Volume. *Proc. Natl. Acad. Sci. U. S. A.* **86,** 1731–5 (1989).

83. Niggel, J., Sigurdson, W. & Sachs, F. Mechanically Induced Calcium Movements in Astrocytes, Bovine Aortic Endothelial Cells and C6 Glioma Cells. *J. Membr. Biol.* **174,** 121–134 (2000).

84. Hammami, S., Willumsen, N. J., Olsen, H. L., Morera, F. J., Latorre, R. & Klaerke, D. A. Cell Volume and Membrane Stretch Independently Control K^+ Channel Activity. *J. Physiol.* **587,** 2225–2231 (2009).

85. Huang, D. & Yu, B. Recent Advance and Possible Future in TREK-2: A Two-Pore Potassium Channel May Involved in the Process of NPP, Brain Ischemia and Memory Impairment. *Med. Hypotheses* **70,** 618–624 (2008).

86. Murthy, S., Dubin, A., Whitwam, T., Jojoa Cruz, S., Cahalan, S., Mosavi, S. A. R., Ward, A. & Patapoutian, A. OSCA/TMEM63 Are an Evolutionarily Conserved Family of Mechanically Activated Ion Channels. *bioRxiv* (2018).

87. Hamill, O. P. & McBride, D. W. Induced Membrane Hypo/Hyper-Mechanosensitivity:A Limitation of Patch-Clamp Recording. *Annu. Rev. Physiol.* **59,** 621–631 (1997).

88. Markin, V. S. & Hudspeth, A. J. Gating-Spring Models of Mechanoelectrical Transduction by Hair Cells of the Internal Ear. *Annu. Rev. Biophys. Biomol. Struct.* **24,** 59–83 (1995).

89. Xiong, W., Grillet, N., Elledge, H. M., Wagner, T. F. J., Zhao, B., Johnson, K. R., Kazmierczak, P. & Müller, U. TMHS Is an Integral Component of the Mechanotransduction Machinery of Cochlear Hair Cells. *Cell* **151,** 1283–1295 (2012).

90. Kung, C. A Possible Unifying Principle for Mechanosensation. *Nature* **436,** 647–654 (2005).

91. Teng, J., Loukin, S., Anishkin, A. & Kung, C. The Force-from-Lipid (FFL) Principle of Mechanosensitivity, at Large and in Elements. *Pflugers Arch. Eur. J. Physiol.* **467,** 27–37 (2014).

92. Martinac, B. Bacterial Mechanosensitive Channels as a Paradigm for Mechanosensory Transduction. *Cell. Physiol. Biochem.* **28,** 1051–1060 (2011).

93. Martinac, B., Adler, J. & Kung, C. Mechanosensitive Ion Channels of E. Coli Activated by Amphipaths. *Nature* **348,** 261–263 (1990).

94. Berrier, C., Pozza, A., De Lacroix De Lavalette, A., Chardonnet, S., Mesneau, A., Jaxel, C., Maire, M. Le & Ghazi, A. The Purified Mechanosensitive Channel TREK-1 Is Directly Sensitive to Membrane Tension. *J. Biol. Chem.* (2013). doi:10.1074/jbc.M113.478321

95. Brohawn, S. G., Su, Z. & MacKinnon, R. Mechanosensitivity Is Mediated Directly by the Lipid Membrane in TRAAK and TREK1 K + Channels. *Proc. Natl. Acad. Sci.* **111,** 3614–3619 (2014).

96. Syeda, R., Florendo, M. N., Cox, C. D., Kefauver, J. M., Santos, J. S., Martinac, B. & Patapoutian, A. Piezo1 Channels Are Inherently Mechanosensitive. *Cell Rep.* **17,** 1739–1746 (2016).

97. Cox, C. D., Bae, C., Ziegler, L., Hartley, S., Nikolova-Krstevski, V., Rohde, P. R., Ng, C.-A., Sachs, F., Gottlieb, P. A. & Martinac, B. Removal of the Mechanoprotective Influence of the Cytoskeleton Reveals PIEZO1 Is Gated by Bilayer Tension. *Nat. Commun.* **7,** 10366 (2016).

98. Brohawn, S. G. How Ion Channels Sense Mechanical Force: Insights from Mechanosensitive K2P Channels TRAAK, TREK1, and TREK2. *Ann. N. Y. Acad. Sci.* **1352,** 20–32 (2015).

99. Martinac, B. The Ion Channels to Cytoskeleton Connection as Potential Mechanism of Mechanosensitivity. *Biochim. Biophys. Acta - Biomembr.* **1838,** 682–691 (2014).

100. Cox, C. D., Bavi, N. & Martinac, B. Origin of the Force: The Force-From-Lipids Principle Applied to Piezo Channels. *Curr. Top. Membr.* **79,** 59–96 (2017).

101. Bavi, N., Nikolaev, Y. A., Bavi, O., Ridone, P., Martinac, A. D., Nakayama, Y., Cox, C. D. & Martinac, B. Principles of Mechanosensing at the Membrane Interface. in *The Biophysics of Cell Membranes: Biological Consequences* (eds. Epand, R. M. & Ruysschaert, J.-M.) 85–119 (Springer Singapore, 2017). doi:10.1007/978-981-10-6244-5_4

102. Hamill, O. P. & Martinac, B. Molecular Basis of Mechanotransduction in Living Cells. *Physiol. Rev.* **81,** 685–740 (2001).

103. Nilius, B. & Honoré, E. Sensing Pressure with Ion Channels. *Trends in Neurosciences* **35,** 477–486 (2012).

104. Martinac, B. Mechanosensitive Ion Channels: Molecules of Mechanotransduction. *J. Cell Sci.* **117,** 2449–60 (2004).

105. Perozo, E. & Rees, D. C. Structure and Mechanism in Prokaryotic Mechanosensitive Channels. *Current Opinion in Structural Biology* **13,** 432–442 (2003).

106. Anishkin, A., Loukin, S. H., Teng, J. & Kung, C. Feeling the Hidden Mechanical Forces in Lipid Bilayer Is an Original Sense. *Proc. Natl. Acad. Sci.* **111,** 7898–7905 (2014).

107. Naismith, J. H. & Booth, I. R. Bacterial Mechanosensitive Channels--MscS: Evolution's Solution to Creating Sensitivity in Function. *Annu. Rev. Biophys.* **41,** 157–77 (2012).

108. Bootha, I. R. & Blount, P. The MscS and MscL Families of Mechanosensitive Channels Act as Microbial Emergency Release Valves. *Journal of Bacteriology* **194,** 4802–4809 (2012).

109. Markin, V. S. & Sachs, F. Thermodynamics of Mechanosensitivity. *Phys. Biol.* **1,** 110–124 (2004).

110. Reeves, D., Ursell, T., Sens, P., Kondev, J. & Phillips, R. Membrane Mechanics as a Probe of Ion-Channel Gating Mechanisms. *Phys. Rev. E. Stat. Nonlin. Soft Matter Phys.* **78,** 041901 (2008).

111. Nielsen, C., Goulian, M. & Andersen, O. S. Energetics of Inclusion-Induced Bilayer Deformations. *Biophys. J.* **74,** 1966–83 (1998).

112. Bavi, O., Vossoughi, M., Naghdabadi, R. & Jamali, Y. The Combined Effect of Hydrophobic Mismatch and Bilayer Local Bending on the Regulation of Mechanosensitive Ion Channels. *PLoS One* **11,** e0150578 (2016).

113. Morris, R. G. Signatures of Mechanosensitive Gating. *Biophys. J.* **112,** 3–9 (2017).

114. Wiggins, P. & Phillips, R. Analytic Models for Mechanotransduction: Gating a Mechanosensitive Channel. *Proc. Natl. Acad. Sci. U. S. A.* **101,** 4071–6 (2004).

115. Perozo, E., Kloda, A., Cortes, D. M. & Martinac, B. Physical Principles Underlying the Transduction of Bilayer Deformation Forces during Mechanosensitive Channel Gating. *Nat. Struct. Biol.* **9,** 696–703 (2002).

116. Martinac, B., Buechner, M., Delcour, A. H., Adler, J. & Kung, C. Pressure-Sensitive Ion Channel in Escherichia Coli. *Proc. Natl. Acad. Sci. U. S. A.* **84,** 2297–301 (1987).

117. Booth, I. R. & Louis, P. Managing Hypoosmotic Stress: Aquaporins and Mechanosensitive Channels in Escherichia Coli. *Curr. Opin. Microbiol.* **2,** 166–9 (1999).

118. Sukharev, S. I., Blount, P., Martinac, B., Blattner, F. R. & Kung, C. A Large-Conductance Mechanosensitive Channel in E. Coli Encoded by MscL Alone. *Nature* **368,** 265–268 (1994).

119. Bass, R. B., Strop, P., Barclay, M. & Rees, D. C. Crystal Structure of Escherichia Coli MscS, a Voltage-Modulated and Mechanosensitive Channel. *Science.* **298,** 1582–1587 (2002).

120. Sukharev, S. Purification of the Small Mechanosensitive Channel of Escherichia Coli (MscS): The Subunit Structure, Conduction, and Gating Characteristicsin Liposomes. *Biophys. J.* **83,** 290–298 (2002).

121. Vásquez, V., Cortes, D. M., Furukawa, H. & Perozo, E. An Optimized Purification and Reconstitution Method for the MscS Channel: Strategies for Spectroscopical Analysis†. (2007). doi:10.1021/BI700322K

122. Moe, P. & Blount, P. Assessment of Potential Stimuli for Mechano-Dependent Gating of MscL: Effects of Pressure, Tension, and Lipid Headgroups. *Biochemistry* **44,** 12239–12244 (2005).

123. Perozo, E., Cortes, D. M., Sompornpisut, P., Kloda, A. & Martinac, B. Open Channel Structure of MscL and the Gating Mechanism Ofmechanosensitive Channels. *Nature* **418,** 942–948 (2002).

124. Mukherjee, N., Jose, M. D., Birkner, J. P., Walko, M., Ingólfsson, H. I., Dimitrova, A., Arnarez, C., Marrink, S. J. & Koçer, A. The Activation Mode of the Mechanosensitive Ion Channel, MscL, by Lysophosphatidylcholine Differs from Tension-Induced Gating. *FASEB J.* **28,** 4292–302 (2014).

125. Bavi, N., Cortes, D. M., Cox, C. D., Rohde, P. R., Liu, W., Deitmer, J. W., Bavi, O., Strop, P., Hill, A. P., Rees, D., Corry, B., Perozo, E. & Martinac, B. The Role of MscL Amphipathic N Terminus Indicates a Blueprint for Bilayer-Mediated Gating of Mechanosensitive Channels. *Nat. Commun.* **7,** 11984 (2016).

126. Ollila, O. H. S., Louhivuori, M., Marrink, S. J. & Vattulainen, I. Protein Shape Change Has a Major Effect on the Gating Energy of a Mechanosensitive Channel. *Biophys. J.* **100,** 1651–1659 (2011).

127. Nomura, T., Cranfield, C. G., Deplazes, E., Owen, D. M., Macmillan, A., Battle, A. R., Constantine, M., Sokabe, M. & Martinac, B. Differential Effects of Lipids and Lyso-Lipids on the Mechanosensitivity of the Mechanosensitive Channels MscL and MscS. *Proc. Natl. Acad. Sci.* **109,** 8770–8775 (2012).

128. Coste, B., Mathur, J., Schmidt, M., Earley, T. J., Ranade, S., Petrus, M. J., Dubin, A. E. & Patapoutian, A. Piezo1 and Piezo2 Are Essential Components of Distinct Mechanically Activated Cation Channels. *Science.* **330,** 55–60 (2010).

129. Murthy, S. E., Dubin, A. E. & Patapoutian, A. Piezos Thrive under Pressure: Mechanically Activated Ion Channels in Health and Disease. *Nat. Rev. Mol. Cell Biol.* **18,** 771–783 (2017).

130. Wu, J., Lewis, A. H. & Grandl, J. Touch, Tension, and Transduction - The Function and Regulation of Piezo Ion Channels. *Trends Biochem. Sci.* **42,** 57–71 (2017).

131. Maingret, F., Patel, A. J., Lesage, F., Lazdunski, M. & Honoré, E. Mechano- or Acid Stimulation, Two Interactive Modes of Activation of the TREK-1 Potassium Channel. *J. Biol. Chem.* **274,** 26691–6 (1999).

132. Patel, A. J., Honoré, E., Maingret, F., Lesage, F., Fink, M., Duprat, F. & Lazdunski, M. A Mammalian Two Pore Domain Mechano-Gated S-like K+ Channel. *EMBO J.* **17,** 4283–90 (1998).

133. Maingret, F., Patel, A. J., Lesage, F., Lazdunski, M. & Honoré, E. Lysophospholipids Open the Two-Pore Domain Mechano-Gated K(+) Channels TREK-1 and TRAAK. *J. Biol. Chem.* **275,** 10128–33 (2000).

134. Lolicato, M., Riegelhaupt, P. M., Arrigoni, C., Clark, K. A. & Minor, D. L. Transmembrane Helix Straightening and Buckling Underlies Activation of Mechanosensitive and Thermosensitive K_{2P} Channels. *Neuron* **84,** 1198–1212 (2014).

135. Dong, Y. Y. *et al.* K2P Channel Gating Mechanisms Revealed by Structures of TREK-2 and a Complex with Prozac. *Science.* **347,** 1256–1259 (2015).

136. Laganowsky, A., Reading, E., Allison, T. M., Ulmschneider, M. B., Degiacomi, M. T., Baldwin, A. J. & Robinson, C. V. Membrane Proteins Bind Lipids Selectively to Modulate Their Structure and Function. *Nature* **510,** 172–175 (2014).

137. Marcelja, S. Lipid-Mediated Protein Interaction in Membranes. *Biochim. Biophys. Acta* **455,** 1–7 (1976).

138. Lolicato, M., Arrigoni, C., Mori, T., Sekioka, Y., Bryant, C., Clark, K. A. & Minor, D. L. K2P2.1 (TREK-1)-Activator Complexes Reveal a Cryptic Selectivity Filter Binding Site. *Nature* **547,** 364–368 (2017).

139. Yefimov, S., van der Giessen, E., Onck, P. R. & Marrink, S. J. Mechanosensitive Membrane Channels in Action. *Biophys. J.* **94,** 2994–3002 (2008).

140. Colombo, G., Marrink, S. J. & Mark, A. E. Simulation of MscL Gating in a Bilayer under Stress. *Biophys. J.* **84,** 2331–2337 (2003).

141. Yuan, C., Li, S., Zou, Q., Ren, Y. & Yan, X. Multiscale Simulations for Understanding the Evolution and Mechanism of Hierarchical Peptide Self-Assembly. *Phys. Chem. Chem. Phys.* **19,** 23614–23631 (2017).

142. van der Spoel, D., Lindahl, B., Hess, B. & the GROMACS development team. *GROMACS User Manual Version 4.6.7*. (2014).

143. Swope, W. C., Andersen, H. C., Berens, P. H. & Wilson, K. R. A Computer Simulation Method for the Calculation of Equilibrium Constants for the Formation of Physical Clusters of Molecules: Application to Small Water Clusters. *J. Chem. Phys.* **76,** 637–649 (1982).

144. Verlet, L. Computer "Experiments" on Classical Fluids. I. Thermodynamical Properties of Lennard-Jones Molecules. *Phys. Rev.* **159,** 98–103 (1967).

145. Berendsen, H. J. C. & Van Gunsteren, W. F. Practical Algorithms for Dynamic Simulations. in *Molecular dynamics Simulation of Statistical Mechanical Systems. Proceedings of the Enrico Fermi Summer School, Varenna* 43–65 (1986).

146. Ryckaert, J.-P., Ciccotti, G. & Berendsen, H. J. . Numerical Integration of the Cartesian Equations of Motion of a System with Constraints: Molecular Dynamics of n-Alkanes. *J. Comput. Phys.* **23,** 327–341 (1977).

147. Hess, B., Bekker, H., Berendsen, H. J. C. & Fraaije, J. G. E. M. LINCS: A Linear Constraint Solver for Molecular Simulations. *J. Comput. Chem.* **18,** 1463–1472 (1997).

148. Miyamoto, S. & Kollman, P. A. Settle: An Analytical Version of the SHAKE and RATTLE Algorithm for Rigid Water Models. *J. Comput. Chem.* **13,** 952–962 (1992).

149. Darden, T., York, D. & Pedersen, L. Particle Mesh Ewald: An $N \cdot \log(N)$ Method for Ewald Sums in Large Systems. *J. Chem. Phys.* **98,** 10089–10092 (1993).

150. Berendsen, H. J. C., Postma, J. P. M., van Gunsteren, W. F., DiNola, A. & Haak, J. R. Molecular Dynamics with Coupling to an External Bath. *J. Chem. Phys.* **81,** 3684–3690 (1984).

151. Nosé, S. A Molecular Dynamics Method for Simulations in the Canonical Ensemble. *Mol. Phys.* **52,** 255–268 (1984).

152. Hoover, W. G. Canonical Dynamics: Equilibrium Phase-Space Distributions. *Phys. Rev. A* **31,** 1695–1697 (1985).

153. Bussi, G., Donadio, D. & Parrinello, M. Canonical Sampling through Velocity Rescaling. *J. Chem. Phys.* **126,** 014101 (2007).

154. Parrinello, M. & Rahman, A. Polymorphic Transitions in Single Crystals: A New Molecular Dynamics Method. *J. Appl. Phys.* **52,** 7182–7190 (1981).

155. Monticelli, D. P. T. and J. L. M. and W. L. A. and C. K. and Z. X. and L. Membrane Protein Simulations with a United-Atom Lipid and All-Atom Protein Model: Lipid–Protein Interactions, Side Chain Transfer Free Energies and Model Proteins. *J. Phys. Condens. Matter* **18,** S1221 (2006).

156. Ulmschneider, J. P. & Ulmschneider, M. B. United Atom Lipid Parameters for Combination with the Optimized Potentials for Liquid Simulations All-Atom Force Field. *J. Chem. Theory Comput.* **5,** 1803–1813 (2009).

157. Trick, J. L., Chelvaniththilan, S., Klesse, G., Aryal, P., Wallace, E. J., Tucker, S. J. & Sansom, M. S. P. Functional Annotation of Ion Channel Structures by Molecular Simulation. *Structure* **24,** 2207–2216 (2016).

158. Choi, S. M., Sokkar, P. & Rhee, Y. M. Simple Method for Hybrid All-Atom and Coarse-Grained Molecular Dynamics Simulations and Its Applications. *Biophys. J.* **106,** 413a (2014).

159. Stansfeld, P. J. & Sansom, M. S. P. From Coarse Grained to Atomistic: A Serial Multiscale Approach to Membrane Protein Simulations. *J. Chem. Theory Comput.* **7,** 1157–1166 (2011).

160. Wassenaar, T. A., Pluhackova, K., Böckmann, R. A., Marrink, S. J. & Tieleman, D. P. Going Backward: A Flexible Geometric Approach to Reverse Transformation from Coarse Grained to Atomistic Models. *J. Chem. Theory Comput.* **10,** 676–690 (2014).

161. Hornak, V., Abel, R., Okur, A., Strockbine, B., Roitberg, A. & Simmerling, C. Comparison of Multiple Amber Force Fields and Development of Improved Protein Backbone Parameters. *Proteins* **65,** 712–25 (2006).

162. Maier, J. A., Martinez, C., Kasavajhala, K., Wickstrom, L., Hauser, K. E. & Simmerling, C. Ff14SB: Improving the Accuracy of Protein Side Chain and Backbone Parameters from Ff99SB. *J. Chem. Theory Comput.* **11,** 3696–3713 (2015).

163. Huang, J., Rauscher, S., Nawrocki, G., Ran, T., Feig, M., de Groot, B. L., Grubmüller, H. & MacKerell, A. D. CHARMM36m: An Improved Force Field for Folded and Intrinsically Disordered Proteins. *Nat. Methods* **14,** 71–73 (2017).

164. Robertson, M. J., Tirado-Rives, J. & Jorgensen, W. L. Improved Peptide and Protein Torsional Energetics with the OPLS-AA Force Field. *J. Chem. Theory Comput.* **11,** 3499–3509 (2015).

165. Oostenbrink, C., Villa, A., Mark, A. E. & Van Gunsteren, W. F. A Biomolecular Force Field Based on the Free Enthalpy of Hydration and Solvation: The GROMOS Force-Field Parameter Sets 53A5 and 53A6. *J. Comput. Chem.* **25,** 1656–1676 (2004).

166. Reif, M. M., Hünenberger, P. H. & Oostenbrink, C. New Interaction Parameters for Charged Amino Acid Side Chains in the GROMOS Force Field. *J. Chem. Theory Comput.* **8,** 3705–3723 (2012).

167. Lyubartsev, A. P. & Rabinovich, A. L. Force Field Development for Lipid Membrane Simulations. *Biochim. Biophys. Acta - Biomembr.* **1858,** 2483–2497 (2016).

168. Pluhackova, K., Kirsch, S. A., Han, J., Sun, L., Jiang, Z., Unruh, T. & Böckmann, R. A. A Critical Comparison of Biomembrane Force Fields: Structure and Dynamics of Model DMPC, POPC, and POPE Bilayers. *J. Phys. Chem. B* **120,** 3888–3903 (2016).

169. Poger, D., Caron, B. & Mark, A. E. Validating Lipid Force Fields against Experimental Data: Progress, Challenges and Perspectives. *Biochim. Biophys. Acta - Biomembr.* **1858,** 1556–1565 (2016).

170. Sandoval-Perez, A., Pluhackova, K. & Böckmann, R. A. Critical Comparison of Biomembrane Force Fields: Protein-Lipid Interactions at the Membrane Interface. *J. Chem. Theory Comput.* **13,** 2310–2321 (2017).

171. Lindorff-Larsen, K., Maragakis, P., Piana, S., Eastwood, M. P., Dror, R. O. & Shaw, D. E. Systematic Validation of Protein Force Fields against Experimental Data. *PLoS One* **7,** e32131 (2012).

172. Beauchamp, K. A., Lin, Y.-S., Das, R. & Pande, V. S. Are Protein Force Fields Getting Better? A Systematic Benchmark on 524 Diverse NMR Measurements. *J. Chem. Theory Comput.* **8,** 1409–1414 (2012).

173. Robustelli, P., Piana, S. & Shaw, D. E. Developing a Molecular Dynamics Force Field for Both Folded and Disordered Protein States. *Proc. Natl. Acad. Sci. U. S. A.* **115,** E4758–E4766 (2018).

174. Smith, M. D., Rao, J. S., Segelken, E. & Cruz, L. Force-Field Induced Bias in the Structure of Aβ $_{21–30}$: A Comparison of OPLS, AMBER, CHARMM, and GROMOS Force Fields. *J. Chem. Inf. Model.* **55,** 2587–2595 (2015).

175. Piana, S., Lindorff-Larsen, K. & Shaw, D. E. How Robust Are Protein Folding Simulations with Respect to Force Field Parameterization? *Biophys. J.* **100,** L47–L49 (2011).

176. Cino, E. A., Choy, W.-Y. & Karttunen, M. Comparison of Secondary Structure Formation Using 10 Different Force Fields in Microsecond Molecular Dynamics Simulations. *J. Chem. Theory Comput.* **8,** 2725–2740 (2012).

177. Siwy, C. M., Lockhart, C. & Klimov, D. K. Is the Conformational Ensemble of Alzheimer's Aβ10-40 Peptide Force Field Dependent? *PLoS Comput. Biol.* **13,** e1005314 (2017).

178. Gumbart, J. C., Ulmschneider, M. B., Hazel, A., White, S. H. & Ulmschneider, J. P. Computed Free Energies of Peptide Insertion into Bilayers Are Independent of Computational Method. *J. Membr. Biol.* **251,** 345–356 (2018).

179. Martin, M. G. Comparison of the AMBER, CHARMM, COMPASS, GROMOS, OPLS, TraPPE and UFF Force Fields for Prediction of Vapor–Liquid Coexistence Curves and Liquid Densities. *Fluid Phase Equilib.* **248,** 50–55 (2006).

180. Huang, J. & Mackerell, A. D. CHARMM36 All-Atom Additive Protein Force Field: Validation Based on Comparison to NMR Data. *J. Comput. Chem.* **34,** 2135–2145 (2013).

181. Klauda, J. B., Venable, R. M., Freites, J. A., O'Connor, J. W., Tobias, D. J., Mondragon-Ramirez, C., Vorobyov, I., MacKerell, A. D. & Pastor, R. W. Update of the CHARMM All-Atom Additive Force Field for Lipids: Validation on Six Lipid Types. *J. Phys. Chem. B* **114,** 7830–7843 (2010).

182. Klauda, J. B., Monje, V., Kim, T. & Im, W. Improving the CHARMM Force Field for Polyunsaturated Fatty Acid Chains. *J. Phys. Chem. B* **116,** 9424–9431 (2012).

183. Riniker, S. Fixed-Charge Atomistic Force Fields for Molecular Dynamics Simulations in the Condensed Phase: An Overview. *Journal of Chemical Information and Modeling* **58,** 565–578 (2018).

184. Guvench, O. & MacKerell, A. D. Comparison of Protein Force Fields for Molecular Dynamics Simulations. in *Molecular Modeling of Proteins* **443,** 63–88 (Humana Press, 2008).

185. Lopes, P. E. M., Guvench, O., MacKerell, A. D. & Jr. Current Status of Protein Force Fields for Molecular Dynamics Simulations. *Methods Mol. Biol.* **1215,** 47–71 (2015).

186. Cornell, W. D., Cieplak, P., Bayly, C. I., Gould, I. R., Merz, K. M., Ferguson, D. M., Spellmeyer, D. C., Fox, T., Caldwell, J. W. & Kollman, P. A. A Second Generation Force Field for the Simulation of Proteins, Nucleic Acids, and Organic Molecules. *J. Am. Chem. Soc.* **117,** 5179–5197 (1995).

187. Duan, Y., Wu, C., Chowdhury, S., Lee, M. C., Xiong, G., Zhang, W., Yang, R., Cieplak, P., Luo, R., Lee, T., Caldwell, J., Wang, J. & Kollman, P. A Point-Charge Force Field for Molecular Mechanics Simulations of Proteins Based on Condensed-Phase Quantum Mechanical Calculations. *J. Comput. Chem.* **24,** 1999–2012 (2003).

188. Wang, J., Wolf, R. M., Caldwell, J. W., Kollman, P. A. & Case, D. A. Development and Testing of a General Amber Force Field. *J. Comput. Chem.* **25,** 1157–1174 (2004).

189. Salomon-Ferrer, R., Case, D. A. & Walker, R. C. An Overview of the Amber Biomolecular Simulation Package. *Wiley Interdiscip. Rev. Comput. Mol. Sci.* **3,** 198–210 (2013).

190. Jorgensen, W. L., Maxwell, D. S. & Tirado-Rives, J. Development and Testing of the OPLS All-Atom Force Field on Conformational Energetics and Properties of Organic Liquids. *J. Am. Chem. Soc.* **118,** 11225–11236 (1996).

191. Kaminski, G. A., Friesner, R. A., Tirado-Rives, J. & Jorgensen, W. L. Evaluation and Reparametrization of the OPLS-AA Force Field for Proteins via Comparison with Accurate Quantum Chemical Calculations on Peptides. *J. Phys. Chem. B* **105,** 6474–6487 (2001).

192. Jorgensen, W. L. & Tirado-Rives, J. The OPLS [Optimized Potentials for Liquid Simulations] Potential Functions for Proteins, Energy Minimizations for Crystals of Cyclic Peptides and Crambin. *J. Am. Chem. Soc.* **110,** 1657–1666 (1988).

193. Sakae, Y. & Okamoto, Y. Optimisation of OPLS–UA Force-Field Parameters for Protein Systems Using Protein Data Bank. *Mol. Simul.* **36,** 1148–1156 (2010).

194. Chiu, S.-W., Pandit, S. A., Scott, H. L. & Jakobsson, E. An Improved United Atom Force Field for Simulation of Mixed Lipid Bilayers. *J. Phys. Chem. B* **113,** 2748–2763 (2009).

195. Schuler, L. D., Daura, X. & van Gunsteren, W. F. An Improved GROMOS96 Force Field for Aliphatic Hydrocarbons in the Condensed Phase. *J. Comput. Chem.* **22,** 1205–1218 (2001).

196. Soares, T. A., Hünenberger, P. H., Kastenholz, M. A., Kräutler, V., Lenz, T., Lins, R. D., Oostenbrink, C. & van Gunsteren, W. F. An Improved Nucleic Acid Parameter Set for the GROMOS Force Field. *J. Comput. Chem.* **26,** 725–737 (2005).

197. Schmid, N., Eichenberger, A. P., Choutko, A., Riniker, S., Winger, M., Mark, A. E. & van Gunsteren, W. F. Definition and Testing of the GROMOS Force-Field Versions 54A7 and 54B7. *Eur. Biophys. J.* **40,** 843–856 (2011).

198. Best, R. B., Zhu, X., Shim, J., Lopes, P. E. M., Mittal, J., Feig, M. & MacKerell, A. D. Optimization of the Additive CHARMM All-Atom Protein Force Field Targeting Improved Sampling of the Backbone ϕ, ψ and Side-Chain χ_1 and χ_2 Dihedral Angles. *J. Chem. Theory Comput.* **8,** 3257–3273 (2012).

199. MacKerell, A. D., Feig, M. & Brooks, C. L. Improved Treatment of the Protein Backbone in Empirical Force Fields. *J. Am. Chem. Soc.* **126,** 698–699 (2004).

200. De Jong, D. H., Singh, G., Bennett, W. F. D., Arnarez, C., Wassenaar, T. A., Schäfer, L. V., Periole, X., Tieleman, D. P. & Marrink, S. J. Improved Parameters for the Martini Coarse-Grained Protein Force Field. *J. Chem. Theory Comput.* **9,** 687–697 (2013).

201. Monticelli, L., Kandasamy, S. K., Periole, X., Larson, R. G., Tieleman, D. P. & Marrink, S.-J. The MARTINI Coarse-Grained Force Field: Extension to Proteins. *J. Chem. Theory Comput.* **4,** 819–834 (2008).

202. Marrink, S. J., Risselada, H. J., Yefimov, S., Tieleman, D. P. & Vries, A. H. de. The MARTINI Force Field: Coarse Grained Model for Biomolecular Simulations. (2007). doi:10.1021/JP071097F

203. Wassenaar, T. A., Ingólfsson, H. I., Böckmann, R. A., Tieleman, D. P. & Marrink, S. J. Computational Lipidomics with *Insane* : A Versatile Tool for Generating Custom Membranes for Molecular Simulations. *J. Chem. Theory Comput.* **11,** 2144–2155 (2015).

204. Boonstra, S., Onck, P. R. & Van Der Giessen, E. CHARMM TIP3P Water Model Suppresses Peptide Folding by Solvating the Unfolded State. *J. Phys. Chem. B* **120,** 3692–3698 (2016).

205. Jorgensen, W. L. Transferable Intermolecular Potential Functions for Water, Alcohols, and Ethers. Application to Liquid Water. *J. Am. Chem. Soc.* **103,** 335–340 (1981).

206. Jorgensen, W. L., Chandrasekhar, J., Madura, J. D., Impey, R. W. & Klein, M. L. Comparison of Simple Potential Functions for Simulating Liquid Water. *J. Chem. Phys.* **79,** 926–935 (1983).

207. Mahoney, M. W. & Jorgensen, W. L. A Five-Site Model for Liquid Water and the Reproduction of the Density Anomaly by Rigid, Nonpolarizable Potential Functions. *J. Chem. Phys.* **112,** 8910–8922 (2000).

208. Zhang, H., Yin, C., Jiang, Y. & van der Spoel, D. Force Field Benchmark of Amino Acids: I. Hydration and Diffusion in Different Water Models. *J. Chem. Inf. Model.* **58,** 1037–1052 (2018).

209. Onufriev, A. V. & Izadi, S. Water Models for Biomolecular Simulations. *Wiley Interdisciplinary Reviews: Computational Molecular Science* **8,** e1347 (2018).

210. Gromacs - Gromacs. Available at: http://www.gromacs.org/. (Accessed: 26th September 2018)

211. NAMD. Available at: https://www.ks.uiuc.edu/Research/namd/. (Accessed: 26th September 2018)

212. The Amber Molecular Dynamics Package. Available at: http://ambermd.org/. (Accessed: 26th September 2018)

213. LAMMPS Molecular Dynamics Simulator. Available at: https://lammps.sandia.gov. (Accessed: 3rd October 2018)

214. OpenMM. Available at: http://openmm.org/. (Accessed: 26th September 2018)

215. Shirts, M. R., Klein, C., Swails, J. M., Yin, J., Gilson, M. K., Mobley, D. L., Case, D. A. & Zhong, E. D. Lessons Learned from Comparing Molecular Dynamics Engines on the SAMPL5 Dataset. *J. Comput. Aided. Mol. Des.* **31,** 147–161 (2017).

216. Duarte, F., Amrein, B. A., Blaha-Nelson, D. & Kamerlin, S. C. L. Recent Advances in QM/MM Free Energy Calculations Using Reference Potentials. *Biochim. Biophys. Acta* **1850,** 954–965 (2015).

217. van der Kamp, M. W. & Mulholland, A. J. Combined Quantum Mechanics/Molecular Mechanics (QM/MM) Methods in Computational Enzymology. *Biochemistry* **52,** 2708–2728 (2013).

218. Domański, J., Sansom, M. S. P., Stansfeld, P. J. & Best, R. B. Balancing Force Field Protein–Lipid Interactions To Capture Transmembrane Helix–Helix Association. *J. Chem. Theory Comput.* **14,** 1706–1715 (2018).

219. Li, H., Chowdhary, J., Huang, L., He, X., MacKerell, A. D. & Roux, B. Drude Polarizable Force Field for Molecular Dynamics Simulations of Saturated and Unsaturated Zwitterionic Lipids. *J. Chem. Theory Comput.* **13,** 4535–4552 (2017).

220. Shi, Y., Xia, Z., Zhang, J., Best, R., Wu, C., Ponder, J. W. & Ren, P. The Polarizable Atomic Multipole-Based AMOEBA Force Field for Proteins. *J. Chem. Theory Comput.* **9,** 4046–4063 (2013).

221. Zhang, C., Lu, C., Jing, Z., Wu, C., Piquemal, J.-P., Ponder, J. W. & Ren, P. AMOEBA Polarizable Atomic Multipole Force Field for Nucleic Acids. *J. Chem. Theory Comput.* **14,** 2084–2108 (2018).

222. Wang, Z.-X., Zhang, W., Wu, C., Lei, H., Cieplak, P. & Duan, Y. Strike a Balance: Optimization of Backbone Torsion Parameters of AMBER Polarizable Force Field for Simulations of Proteins and Peptides. *J. Comput. Chem.* **27,** 781–790 (2006).

223. Baker, C. M. Polarizable Force Fields for Molecular Dynamics Simulations of Biomolecules. *Wiley Interdiscip. Rev. Comput. Mol. Sci.* **5,** 241–254 (2015).

224. Humphrey, W., Dalke, A. & Schulten, K. VMD: Visual Molecular Dynamics. *J. Mol. Graph.* **14,** 33–38 (1996).

225. Schrödinger LLC. *The PyMOL Molecular Graphics System, Version~1.8*. (2015).

226. Michaud-Agrawal, N., Denning, E. J., Woolf, T. B. & Beckstein, O. MDAnalysis: A Toolkit for the Analysis of Molecular Dynamics Simulations. *J. Comput. Chem.* **32,** 2319–27 (2011).

227. Gowers, R. J., Linke, M., Barnoud, J., Reddy, T. J. E., Melo, M. N., Seyler, S. L., Domański, J., Dotson, D. L., Buchoux, S., Kenney, I. M. & Beckstein, O. MDAnalysis: A Python Package for the Rapid Analysis of Molecular Dynamics Simulations. 98–105 (2016).

228. McGibbon, R. T., Beauchamp, K. A., Harrigan, M. P., Klein, C., Swails, J. M., Hernández, C. X., Schwantes, C. R., Wang, L.-P., Lane, T. J. & Pande, V. S. MDTraj: A Modern Open Library for the Analysis of Molecular Dynamics Trajectories. *Biophys. J.* **109,** 1528–32 (2015).

229. Camilloni, C. & Pietrucci, F. Advanced Simulation Techniques for the Thermodynamic and Kinetic Characterization of Biological Systems Introduction : Key Problems. *Adv. Phys. X* **3,** 1–40 (2018).

230. Lukat, G., Krüger, J. & Sommer, B. APL@Voro: A Voronoi-Based Membrane Analysis Tool for GROMACS Trajectories. *J. Chem. Inf. Model.* **53,** 2908–2925 (2013).

231. Kučerka, N., Nagle, J. F., Sachs, J. N., Feller, S. E., Pencer, J., Jackson, A. & Katsaras, J. Lipid Bilayer Structure Determined by the Simultaneous Analysis of Neutron and X-Ray Scattering Data. *Biophys. J.* **95,** 2356–2367 (2008).

232. Unsay, J. D., Cosentino, K. & García-Sáez, A. J. Atomic Force Microscopy Imaging and Force Spectroscopy of Supported Lipid Bilayers. *J. Vis. Exp.* e52867 (2015). doi:10.3791/52867

233. Vermeer, L. S., de Groot, B. L., Réat, V., Milon, A. & Czaplicki, J. Acyl Chain Order Parameter Profiles in Phospholipid Bilayers: Computation from Molecular Dynamics Simulations and Comparison with 2H NMR Experiments. *Eur. Biophys. J.* **36,** 919–931 (2007).

234. Piggot, T. J., Allison, J. R., Sessions, R. B. & Essex, J. W. On the Calculation of Acyl Chain Order Parameters from Lipid Simulations. *J. Chem. Theory Comput.* (2017). doi:10.1021/acs.jctc.7b00643

235. Ollila, O. H. S., Risselada, H. J., Louhivuori, M., Lindahl, E., Vattulainen, I. & Marrink, S. J. 3D Pressure Field in Lipid Membranes and Membrane-Protein Complexes. *Phys. Rev. Lett.* **102,** 078101 (2009).

236. Gullingsrud, J. & Schulten, K. Lipid Bilayer Pressure Profiles and Mechanosensitive Channel Gating. *Biophys. J.* **86,** 3496–509 (2004).

237. Vanegas, J. M., Torres-Sánchez, A. & Arroyo, M. Importance of Force Decomposition for Local Stress Calculations in Biomembrane Molecular Simulations. *J. Chem. Theory Comput.* **10,** 691–702 (2014).

238. Hess, B., Kutzner, C., Van Der Spoel, D. & Lindahl, E. GRGMACS 4: Algorithms for Highly Efficient, Load-Balanced, and Scalable Molecular Simulation. *J. Chem. Theory Comput.* **4,** 435–447 (2008).

239. Abraham, M. J., Murtola, T., Schulz, R., Páll, S., Smith, J. C., Hess, B. & Lindahl, E. GROMACS: High Performance Molecular Simulations through Multi-Level Parallelism from Laptops to Supercomputers. *SoftwareX* **1–2,** 19–25 (2015).

240. Abraham, M. J., van der Spoel, D., Lindahl, E., Hess, B. & the GROMACS development team. *GROMACS User Manual Version 5.1*. (2015).

241. Aryal, P., Jarerattanachat, V., Clausen, M. V., Schewe, M., McClenaghan, C., Argent, L., Conrad, L. J., Dong, Y. Y., Pike, A. C. W., Carpenter, E. P., Baukrowitz, T., Sansom, M. S. P. & Tucker, S. J. Bilayer-Mediated Structural Transitions Control Mechanosensitivity of the TREK-2 K2P Channel. *Structure* **25,** 708–718.e2 (2017).

242. Eswar, N., Webb, B., Marti-Renom, M. A., Madhusudhan, M. S., Eramian, D., Shen, M.-Y., Pieper, U. & Sali, A. Comparative Protein Structure Modeling Using Modeller. *Curr. Protoc. Bioinforma.* **Chapter 5,** Unit-5.6 (2006).

243. Periole, X., Cavalli, M., Marrink, S.-J. & Ceruso, M. A. Combining an Elastic Network With a Coarse-Grained Molecular Force Field: Structure, Dynamics, and Intermolecular Recognition. *J. Chem. Theory Comput.* **5,** 2531–2543 (2009).

244. Lee, J. *et al.* CHARMM-GUI Input Generator for NAMD, GROMACS, AMBER, OpenMM, and CHARMM/OpenMM Simulations Using the CHARMM36 Additive Force Field. *J. Chem. Theory Comput.* **12,** 405–413 (2016).

245. Jo, S., Lim, J. B., Klauda, J. B. & Im, W. CHARMM-GUI Membrane Builder for Mixed Bilayers and Its Application to Yeast Membranes. *Biophys. J.* **97,** 50–8 (2009).

246. Jo, S., Kim, T., Iyer, V. G. & Im, W. CHARMM-GUI: A Web-Based Graphical User Interface for CHARMM. *J. Comput. Chem.* **29,** 1859–1865 (2008).

247. Jo, S., Kim, T. & Im, W. Automated Builder and Database of Protein/Membrane Complexes for Molecular Dynamics Simulations. *PLoS One* **2,** e880 (2007).

248. Maksaev, G., Milac, A., Anishkin, A., Guy, H. R. & Sukharev, S. Analyses of Gating Thermodynamics and Effects of Deletions in the Mechanosensitive Channel TREK-1: Comparisons with Structural Models. *Channels (Austin).* **5,** 34–42 (2011).

249. Perez, D., Uberuaga, B. P., Shim, Y., Amar, J. G. & Voter, A. F. Chapter 4 Accelerated Molecular Dynamics Methods: Introduction and Recent Developments. *Annu. Rep. Comput. Chem.* **5,** 79–98 (2009).

250. Barducci, A., Bonomi, M. & Parrinello, M. Metadynamics. *Wiley Interdiscip. Rev. Comput. Mol. Sci.* **1,** 826–843 (2011).

251. Sugita, Y. & Okamoto, Y. Replica-Exchange Molecular Dynamics Method for Protein Folding. *Chem. Phys. Lett.* **314,** 141–151 (1999).

252. Mori, T., Miyashita, N., Im, W., Feig, M. & Sugita, Y. Molecular Dynamics Simulations of Biological Membranes and Membrane Proteins Using Enhanced Conformational Sampling Algorithms. *Biochim. Biophys. Acta - Biomembr.* **1858,** 1635–1651 (2016).

253. Rapedius, M., Schmidt, M. R., Sharma, C., Stansfeld, P. J., Sansom, M. S. P., Baukrowitz, T. & Tucker, S. J. State-Independent Intracellular Access of Quaternary Ammonium Blockers to the Pore of TREK-1. *Channels (Austin).* **6,** 473–8 (2012).

254. McClenaghan, C., Schewe, M., Aryal, P., Carpenter, E. P., Baukrowitz, T. & Tucker, S. J. Polymodal Activation of the TREK-2 K2P Channel Produces Structurally Distinct Open States. *J. Gen. Physiol.* **147,** 497–505 (2016).

255. Brennecke, J. T. & de Groot, B. L. Mechanism of Mechanosensitive Gating of the TREK-2 Potassium Channel. *Biophys. J.* **114,** 1336–1343 (2018).

256. Vásquez, V., Sotomayor, M., Cordero-Morales, J., Schulten, K. & Perozo, E. A Structural Mechanism for MscS. *Science.* **321,** 1210–14 (2008).

257. Yoo, J. & Cui, Q. Curvature Generation and Pressure Profile Modulation in Membrane by Lysolipids: Insights from Coarse-Grained Simulations. *Biophys. J.* **97,** 2267–2276 (2009).

258. Maingret, F., Fosset, M., Lesage, F., Lazdunski, M. & Honoré, E. TRAAK Is a Mammalian Neuronal Mechano-Gated K+ Channel. *J. Biol. Chem.* **274,** 1381–7 (1999).

259. Patel, A. J., Honoré, E., Lesage, F., Fink, M., Romey, G. & Lazdunski, M. Inhalational Anesthetics Activate Two-Pore-Domain Background K+ Channels. *Nat. Neurosci.* **2,** 422–426 (1999).

260. Clausen, M. V, Jarerattanachat, V., Carpenter, E. P., Sansom, M. S. P. & Tucker, S. J. Asymmetric Mechanosensitivity in a Eukaryotic Ion Channel. *Proc. Natl. Acad. Sci. U. S. A.* 201708990 (2017). doi:10.1073/pnas.1708990114

261. Braun, G., Lengyel, M., Enyedi, P. & Czirják, G. Differential Sensitivity of TREK-1, TREK-2 and TRAAK Background Potassium Channels to the Polycationic Dye Ruthenium Red. *Br. J. Pharmacol.* **172,** (2015).

262. Perlmutter, J. D. & Sachs, J. N. Interleaflet Interaction and Asymmetry in Phase Separated Lipid Bilayers: Molecular Dynamics Simulations. *J. Am. Chem. Soc.* **133,** 6563–6577 (2011).

263. Fowler, P. W., Williamson, J. J., Sansom, M. S. P. & Olmsted, P. D. Roles of Interleaflet Coupling and Hydrophobic Mismatch in Lipid Membrane Phase-Separation Kinetics. *J. Am. Chem. Soc.* **138,** 11633–11642 (2016).

264. Honoré, E., Maingret, F., Lazdunski, M. & Patel, A. J. An Intracellular Proton Sensor Commands Lipid- and Mechano-Gating of the K+ Channel TREK-1. *EMBO J.* **21,** 2968–2976 (2002).

265. Vivier, D., Bennis, K., Lesage, F. & Ducki, S. Perspectives on the Two-Pore Domain Potassium Channel TREK-1 (TWIK-Related K^+ Channel 1). A Novel Therapeutic Target? *J. Med. Chem.* **59,** 5149–5157 (2016).

266. Chemin, J., Patel, A. J., Duprat, F., Lauritzen, I., Lazdunski, M. & Honoré, E. A Phospholipid Sensor Controls Mechanogating of the K+ Channel TREK-1. *EMBO J.* **24,** 44–53 (2005).

267. Kim, Y., Gnatenco, C., Bang, H. & Kim, D. Localization of TREK-2 K + Channel Domains That Regulate Channel Kinetics and Sensitivity to Pressure, Fatty Acids and PH I. *Pflügers Arch. Eur. J. Physiol.* **442,** 952–960 (2001).

268. Woo, J., Jun, Y. K., Zhang, Y.-H., Nam, J. H., Shin, D. H. & Kim, S. J. Identification of Critical Amino Acids in the Proximal C-Terminal of TREK-2 K+ Channel for Activation by Acidic PHi and ATP-Dependent Inhibition. *Pflügers Arch. - Eur. J. Physiol.* **470,** 327–337 (2018).

269. Pike, A. C. W. *et al.* Crystal Structure of Human Two Pore Domain Potassium Ion Channel TREK1 (K2P2.1). *Protein Data Bank* (2014). doi:10.2210/PDB4TWK/PDB

270. Murbartián, J., Lei, Q., Sando, J. J. & Bayliss, D. A. Sequential Phosphorylation Mediates Receptor- and Kinase-Induced Inhibition of TREK-1 Background Potassium Channels. *J. Biol. Chem.* **280,** 30175–84 (2005).

271. Zhuo, R. G., Peng, P., Zheng, J. Q., Zhang, Y. long, Wen, L., Wei, X. li & Ma, X. Y. The Glycine Hinge of Transmembrane Segment 2 Modulates the Subcellular Localization and Gating Properties in TREK Channels. *Biochem. Biophys. Res. Commun.* **490,** 1125–1131 (2017).

272. Harrigan, M. P., McKiernan, K. A., Shanmugasundaram, V., Denny, R. A. & Pande, V. S. Markov Modeling Reveals Novel Intracellular Modulation of the Human TREK-2 Selectivity Filter. *Sci. Rep.* **7,** 632 (2017).

273. Zhuo, R. G., Peng, P., Liu, X. Y., Yan, H. T., Xu, J. P., Zheng, J. Q., Wei, X. L. & Ma, X. Y. Allosteric Coupling between Proximal C-Terminus and Selectivity Filter Is Facilitated by the Movement of Transmembrane Segment 4 in TREK-2 Channel. *Sci. Rep.* **6,** 21248 (2016).

274. Hedger, G. & Sansom, M. S. P. Lipid Interaction Sites on Channels, Transporters and Receptors: Recent Insights from Molecular Dynamics Simulations. *Biochim. Biophys. Acta - Biomembr.* **1858,** 2390–2400 (2016).

275. Shamsi, Z., Moffett, A. S. & Shukla, D. Enhanced Unbiased Sampling of Protein Dynamics Using Evolutionary Coupling Information. *Sci. Rep.* **7,** 12700 (2017).

276. Marks, D. S., Colwell, L. J., Sheridan, R., Hopf, T. A., Pagnani, A., Zecchina, R. & Sander, C. Protein 3D Structure Computed from Evolutionary Sequence Variation. *PLoS One* **6,** e28766 (2011).

277. Ovchinnikov, S., Kamisetty, H. & Baker, D. Robust and Accurate Prediction of Residue–Residue Interactions across Protein Interfaces Using Evolutionary Information. *Elife* **3,** (2014).

278. Hopf, T. A., Schärfe, C. P. I., Rodrigues, J. P. G. L. M., Green, A. G., Kohlbacher, O., Sander, C., Bonvin, A. M. J. J. & Marks, D. S. Sequence Co-Evolution Gives 3D Contacts and Structures of Protein Complexes. *Elife* **3,** (2014).

279. Wang, Y. & Barth, P. Evolutionary-Guided de Novo Structure Prediction of Self-Associated Transmembrane Helical Proteins with near-Atomic Accuracy. *Nat. Commun.* **6,** 7196 (2015).

280. Dos Santos, R. N., Morcos, F., Jana, B., Andricopulo, A. D. & Onuchic, J. N. Dimeric Interactions and Complex Formation Using Direct Coevolutionary Couplings. *Sci. Rep.* **5,** 13652 (2015).

281. Lakhani, B., Thayer, K. M., Hingorani, M. M. & Beveridge, D. L. Evolutionary Covariance Combined with Molecular Dynamics Predicts a Framework for Allostery in the MutS DNA Mismatch Repair Protein. *J. Phys. Chem. B* **121,** 2049–2061 (2017).

282. Ricci, C. G., Silveira, R. L., Rivalta, I., Batista, V. S. & Skaf, M. S. Allosteric Pathways in the PPARγ-RXRα Nuclear Receptor Complex. *Sci. Rep.* **6,** 19940 (2016).

283. Daily, M. D., Upadhyaya, T. J. & Gray, J. J. Contact Rearrangements Form Coupled Networks from Local Motions in Allosteric Proteins. *Proteins Struct. Funct. Bioinforma.* **71,** 455–466 (2008).

284. Stacklies, W., Seifert, C. & Graeter, F. Implementation of Force Distribution Analysis for Molecular Dynamics Simulations. *BMC Bioinformatics* **12,** 101 (2011).

285. Costescu, B. I. & Gräter, F. Time-Resolved Force Distribution Analysis. *BMC Biophys.* **6,** 5 (2013).

286. Essex, M. O. and J. M. and J. W. Coarse-Grain Modelling of DMPC and DOPC Lipid Bilayers. *J. Phys. Condens. Matter* **22,** 155106 (2010).

287. Lai, K., Wang, B., Zhang, Y. & Zhang, Y. High Pressure Effect on Phase Transition Behavior of Lipid Bilayers. *Phys. Chem. Chem. Phys.* **14,** 5744–5752 (2012).

288. Ray, A., Gräter, F. & Thukral, L. Probing Molecular Forces in Multi-Component Physiological Membranes. *Phys. Chem. Chem. Phys.* **20,** 2155–2161 (2018).

289. Pérez, F. & Granger, B. E. IPython: A System for Interactive Scientific Computing. *Comput. Sci. Eng.* **9,** 21–29 (2007).

290. NumPy — NumPy. Available at: http://www.numpy.org/. (Accessed: 5th October 2018)

291. Oliphant, T. E. *Guide to NumPy*. (CreateSpace Independent Publishing Platform, 2015).

292. Python Data Analysis Library — Pandas: Python Data Analysis Library. Available at: https://pandas.pydata.org/index.html. (Accessed: 5th October 2018)

293. McKinney, W. Data Structures for Statistical Computing in Python. *Proc. 9th Python Sci. Conf.* **1697900,** 51–56 (2010).

294. Jones, E., Oliphant, T., Peterson, P. & Others. SciPy:Open Source Scientific Tools for Python. (2001).

295. Hunter, J. D. Matplotlib: A 2D Graphics Environment. *Comput. Sci. Eng.* **9,** 99–104 (2007).

296. Sievers, F., Wilm, A., Dineen, D., Gibson, T. J., Karplus, K., Li, W., Lopez, R., McWilliam, H., Remmert, M., Söding, J., Thompson, J. D. & Higgins, D. G. Fast, Scalable Generation of High-Quality Protein Multiple Sequence Alignments Using Clustal Omega. *Mol. Syst. Biol.* **7,** 539 (2011).

297. Lange, O. F. & Grubmüller, H. Generalized Correlation for Biomolecular Dynamics. *Proteins Struct. Funct. Bioinforma.* **62,** 1053–1061 (2005).